
Electronic Thesis and Dissertation Repository

8-21-2015 12:00 AM


X-ray Absorption Fine Structure Studies of Calcium Silicate Hydrate Biomaterials in Drug Delivery

Xiaoxuan Guo
The University of Western Ontario

Supervisor
Tsun-Kong Sham
The University of Western Ontario

Graduate Program in Chemistry
A thesis submitted in partial fulfillment of the requirements for the degree in Doctor of Philosophy
© Xiaoxuan Guo 2015

Follow this and additional works at: <https://ir.lib.uwo.ca/etd>

 Part of the [Analytical Chemistry Commons](#), [Materials Chemistry Commons](#), and the [Physical Chemistry Commons](#)

Recommended Citation

Guo, Xiaoxuan, "X-ray Absorption Fine Structure Studies of Calcium Silicate Hydrate Biomaterials in Drug Delivery" (2015). *Electronic Thesis and Dissertation Repository*. 3082.
<https://ir.lib.uwo.ca/etd/3082>

This Dissertation/Thesis is brought to you for free and open access by Scholarship@Western. It has been accepted for inclusion in Electronic Thesis and Dissertation Repository by an authorized administrator of Scholarship@Western. For more information, please contact wlsadmin@uwo.ca.

X-RAY ABSORPTION FINE STRUCTURE STUDIES OF CALCIUM SILICATE
HYDRATE BIOMATERIALS IN DRUG DELIVERY

(Thesis format: Integrated Article)

by

Xiaoxuan Guo

Graduate Program in Chemistry

A thesis submitted in partial fulfillment
of the requirements for the degree of
Doctor of Philosophy

The School of Graduate and Postdoctoral Studies
The University of Western Ontario
London, Ontario, Canada

© Xiaoxuan Guo 2015

Abstract

Calcium silicate hydrate (CSH), a new type of bioceramics, has gained significant attention in hard tissue restoration because of their impressive role in the stimulation of osteoblast proliferation and differentiation *in vitro*. The further development of mesoporous bioceramics opens up new opportunities for drug delivery in hard tissue therapies. In this thesis, interaction mechanisms of drug molecules with CSH of different morphologies and CSH/polymer composites, imaging of drug distributions in CSH carriers in nanoscale, and the biomineralization mechanisms of CSH *in vitro* during drug release are extensively investigated using X-ray absorption near edge structure (XANES) and scanning transmission X-ray microscopy (STXM).

The interactions between different drug molecules and CSH with different morphologies are investigated using XANES. It is found that the morphology and the presence of hydrates of drug carriers influence the drug loading capacities (DLCs). CSH provides active linkage sites (Ca-OH and Si-OH groups) for the acidic functional groups of drug molecules via electrostatic interactions. Besides, it is also found that the stoichiometric ratio of Ca²⁺ ions of CSH carriers to the functional groups of drug molecules will significantly influence the DLCs. The mapping of an individual CSH microsphere, which was synthesized by a sonochemical method, before and after the loading of ibuprofen (IBU) is recorded by STXM. This STXM-XANES study illustrates the integrity and the homogeneously distribution of drug molecules in these drug carriers.

The biomineralization of the drug carrier, CSH microspheres upon IBU release, are monitored with XANES and STXM. The biomineralization mechanisms for CSH microspheres loaded with IBU in the SBF solution, which were still controversial before, emerge via STXM mapping, spectral comparisons and fitting analysis.

Finally, CSH/polymer composites were synthesized using a controlled precipitation reaction between calcium salt and silicate salt, followed by the addition of various polymer solutions

at room temperature. The interactions between different polymers and CSH, the interactions between drug molecule IBU and these polymer composites have been extensively studied by XANES. We find that the polymers alter the structure of CSH to various degrees, and that this behaviour further influences the DLCs and drug release kinetics.

Keywords

biomineralization *in vitro*, calcium silicate hydrate, calcium silicate hydrate/polymer composites, drug-carrier interactions, scanning transmission X-ray microscopy, X-ray absorption near edge structure

Co-Authorship Statement

This thesis contains materials from previously published manuscripts. Dr. Tsun-Kong Sham is co-authored on all published papers and he played a major role in editing and revising the content presented in this thesis.

Calcium silicate hydrate nanomaterials were prepared by Dr. Jin Wu or synthesized by Xiaoxuan Guo under the supervision of Dr. Jin Wu and Dr. Ying-Jie Zhu from Shanghai Institute of Ceramics, Chinese Academy of Sciences.

Guo collected all of the X-ray absorption near-edge structure (XANES) data, with the exception of those of Ca and P K-edge XANES spectra of calcium standard samples in Chapter 6, which was obtained by Jun Li; C K-edge fast scan spectra of drug molecules in Chapter 5 were collected by Dr. Zhiqiang Wang. Preliminary scanning transmission X-ray microscopy (STXM) data were collected by Dr. Zhiqiang Wang, and further detailed analysis was made by Guo with the discussion to Dr. Wang. Modellings of crystal structures of calcium silicate hydrate using FEFF program were performed by Dr. Yun-Mui Yiu.

Technical support with synchrotron spectroscopy measurements at the Canadian Light Source (CLS) were provided by the following people: Dr. Yongfeng Hu for the experiments on the Soft X-ray Microcharacterization Beamline (SXRMB) at the CLS, Dr. Jian Wang for the experiments on the Soft X-ray Spectromicroscopy (SM) beamline, Dr. Tom Regier and Dr. Jay Dynes for the experiments on the Spherical Grating Monochromator (SGM) beamline at the CLS.

Transmission electron microscopy (TEM) graphs were taken with the assistance from Dr. Richard Gardiner at Biotron, University of Western Ontario. Fourier transform infrared (FTIR) spectroscopy, UV-Vis spectroscopy, and thermalgravimetric analysis (TGA) were conducted with assistance from Chao Qi; and X-ray diffraction (XRD) data were collected in Shanghai Institute of Ceramics, Chinese Academy of Sciences.

To my loving family

Acknowledgments

First of all, I would like to thank my supervisor Dr. Tsun-Kong Sham for his exceptional supervision, encouragement and support during my five-year graduate study. I am grateful for having this opportunity to study and work under the guidance of him who is a world-class expert in the field of synchrotron X-ray absorption spectroscopy. He is not only a mentor but also is a kindly friend, who is willing to provide any help he could. His passion and enthusiasm on science will always inspire me.

Second, I would like thank my collaborator, Dr. Ying-Jie Zhu for his unconditional support when I went to Shanghai Institute of Ceramics for research every summer, without which my graduate studies would not have been finished so smoothly.

I also thank members of Dr. Sham's research group, past and present, Dr. Yun-Mui Yiu, Dr. Zhiqiang Wang, Dr. Matthew Ward, Dr. Lijia Liu, Dr. Dongniu Wang, Dr. Michael Murphy, Dr. Fuyan Zhao, Dr. Dong Zhao, Dr. Olga Lobacheva, Dr. Dejian Hou, Ms. Biqiong Wang, Ms. Madalena Kozachuk, Mr. Ankang Zhao, Mr. Jun Li, and Mr. Wei Xiao for all of their helpful discussion and constructive feedbacks.

Moreover, I am grateful to the all the technical support from beamline scientists at synchrotron facilities: Dr. Yongfeng Hu (CLS), Dr. Jian Wang (CLS), Dr. Lucia Zuin (CLS), Dr. Tom Regier (CLS), Dr. Qunfeng Xiao (CLS), Dr. Jinghua Guo (ALS), and Dr. Robert Gordon (APS). Their expertise and assistance on data collections and interpretations made synchrotron experiments more hands-on and interesting.

I acknowledge the assistance from ASPIRE Awards and all of the funding support for my research at University of Western Ontario (Natural Science and Engineering Research Council of Canada (NSERC), Canada Foundation for Innovation (CFI) and the Ontario Innovation Trust (OIT)) and Shanghai Institute of Ceramics (National Natural Science Foundation of China (51172260) and Science and Technology Commission of Shanghai (11nm0506600, 12ZR1452100)), respectively.

Finally, I would like to thank my parents and my wife for their support and encouragement during my graduate studies. I would also like to thank my friends at University of Western Ontario. I am lucky to have all of them when I am alone in a foreign country, my life will not be that colorful without them.

Table of Contents

Abstract	ii
Co-Authorship Statement.....	iv
Dedication	v
Acknowledgments.....	vi
Table of Contents	viii
List of Tables	xv
List of Figures	xvi
List of Schemes.....	xxiv
List of Abbreviations:	xxv
Chapter 1	1
1 Introduction	1
1.1 Biomaterials	1
1.1.1 General Background	1
1.1.2 Metallic Biomaterials.....	2
1.1.3 Ceramics Biomaterials	3
1.1.4 Composite Biomaterials.....	3
1.1.5 Nano-bioceramics and Drug Delivery	4
1.1.6 Calcium Silicate Bioceramics	6
1.2 X-ray Absorption Spectroscopy.....	8
1.2.1 X-ray Absorption Fine Structure	8
1.2.2 De-excitation Processes	11
1.3 Overview of Synchrotron Radiation	12

1.4 Research Motivations and Thesis Outline	17
1.5 References.....	18
Chapter 2.....	24
2 Experimental Facilities and Methodologies.....	24
2.1 Experimental Facilities	24
2.1.1 Shanghai Institute of Ceramics	24
2.1.2 Canadian Light Source.....	24
2.2 Beamlines.....	25
2.2.1 Spherical Grating Monochromator (SGM) Beamline.....	25
2.2.2 Soft X-ray Microcharacterization Beamline (SXRMB)	27
2.2.3 Soft X-ray Spectromicroscopy (SM) Beamline	28
2.3 Detection Modes	30
2.4 FEFF Simulations	32
2.5 Linear Combination Fitting (LCF).....	33
2.6 Other Characterization Techniques.....	34
2.6.1 Brunauer-Emmett-Teller (BET) Theory	34
2.6.2 Thermalgravimetric Analysis (TGA).....	35
2.6.3 Inductively Coupled Plasma Optical Emission Spectrometry (ICP-OES) Analysis.....	36
2.7 References.....	36
Chapter 3.....	39
3 Drug-Carrier Interaction - Tracking the Local Structure of Calcium Silicate upon Ibuprofen Loading with X-ray Absorption Near Edge Structure (XANES).....	39
3.1 Introduction.....	39

3.2	Experimental.....	40
3.2.1	Synthesis of Materials.....	40
3.2.2	IBU Drug Loading	41
3.2.3	BET Specific Surface Areas (SSAs) Measurements	41
3.2.4	UV-Vis Experiments.....	41
3.2.5	Fourier Transform Infrared (FTIR) Measurements	41
3.2.6	<i>In Vitro</i> IBU Drug Release	41
3.2.7	X-ray Absorption Near Edge Spectroscopy (XANES) Experiments	42
3.2.8	Real Space Multiple Scattering Theory - Calculation by FEFF9	42
3.3	Results and Discussion	43
3.3.1	Morphologies of Calcium Silicate Samples.....	43
3.3.2	Ibuprofen Loading in CSH Drug Carriers	43
3.3.3	XANES Studies of the Interactions between CSH and IBU.....	45
3.3.4	FTIR Spectroscopy of CSH Carriers Before and After IBU Loading	55
3.3.5	<i>In Vitro</i> CSH-IBU Release.....	57
3.4	Conclusions.....	58
3.5	References.....	59
	Chapter 4.....	62
4	Imaging of Drug Loading Distributions in Individual Microsphere of Calcium Silicate Hydrate - An X-ray Spectromicroscopic Study	62
4.1	Introduction.....	62
4.2	Experimental.....	64
4.2.1	Preparation of CSH Mesoporous Microspheres	64
4.2.2	IBU Drug Loading	64

4.2.3	Characterization	64
4.2.4	STXM Measurement.....	64
4.3	Results and Discussion	65
4.3.1	IBU Loading in CSH Microspheres.....	65
4.3.2	Morphology of Individual CSH Microsphere Before and After IBU Loading	66
4.3.3	STXM Analysis of Individual CSH Microsphere Before and After IBU Loading	67
4.3.4	Thickness Mapping of Individual CSH Microsphere Before and After IBU Loading	80
4.4	Conclusions.....	85
4.5	References.....	86
Chapter 5	90
5	Tracking Drug Loading Capacities of Calcium Silicate Hydrate Carrier Loaded with Various Drugs: A Comparative X-ray Absorption Near Edge Structures Study.....	90
5.1	Introduction.....	90
5.2	Experimental	92
5.2.1	Preparation of Mesoporous Spheres of CSH (MS-CSH).....	92
5.2.2	Ibuprofen (IBU), Alendronate Sodium (ALN), and Gentamicin Sulfate (GS) Drug Incorporations into MS-CSH	93
5.2.3	Characterizations.....	93
5.2.4	XANES Measurements.....	93
5.2.5	FEFF Calculation	94
5.3	Results and Discussion	95
5.3.1	Morphologies of MS-CSH Loaded with Different Drug Molecules	95
5.3.2	Stabilities of Drug Molecules under the Collimated X-ray Beam.....	96

5.3.3	Studies of Interactions between MS-CSH and Different Drug Molecules by XANES	99
5.3.4	Studies of Interactions between MS-CSH and Different Drug Molecules by FTIR Spectroscopy	108
5.3.5	Relationship between Drug Loading Capacities and Interactions of CSH and Different Drug Molecules	109
5.4	Conclusions.....	111
5.5	References.....	112
Chapter 6.....		117
6	Tracking the Transformations of Mesoporous Microspheres of Calcium Silicate Hydrate in Nanoscale upon Ibuprofen Release: An XANES and STXM Study	117
6.1	Introduction.....	117
6.2	Experimental.....	119
6.2.1	Preparation of Mesoporous CSH Microspheres	119
6.2.2	IBU Drug Loading	119
6.2.3	<i>In Vitro</i> Test	119
6.2.4	Characterization	120
6.2.5	XANES Measurements.....	120
6.2.6	STXM Measurements	121
6.3	Results and Discussion	121
6.3.1	Morphologies of CSH Microspheres Before and After IBU Loading	121
6.3.2	IBU Loading Capacity of CSH Microspheres	122
6.3.3	Morphologies Changes of CSH Microspheres in SBF upon IBU Release	123
6.3.4	XRD Study of CSH Microspheres Phase Transformations in SBF upon IBU Release	124

6.3.5	XANES Study of CSH Microspheres Phase Transformations in SBF upon IBU Release	125
6.3.6	STXM Analysis of CSH-IBU System after Having Soaked in SBF for Five Hours.....	132
6.3.7	Changes of Ca, Si and P during the Biomineralization	138
6.4	Conclusions.....	139
6.5	References.....	140
Chapter 7.....		145
7	Effects of Polymers on the Drug Loading Capacities and Drug Release of Calcium Silicate Hydrates: An X-ray Absorption Near Edge Structures (XANES) Study	145
7.1	Introduction.....	145
7.2	Experimental.....	147
7.2.1	Materials	147
7.2.2	Preparation of CSH/polymer Composites.....	148
7.2.3	IBU Drug Loading and <i>In Vitro</i> Release	148
7.2.4	Characterization	148
7.2.5	XANES Measurement	149
7.2.6	FEFF Simulation.....	149
7.3	Results and Discussion	150
7.3.1	Morphologies of CSH Nanosheets, CSH/polymer Composites and CSH/polymer-IBU	150
7.3.2	Studies of Interactions between CSH and Different Block Polymers	151
7.3.3	Studies of Interactions between CSH/polymer Composites and IBU Molecules.....	158
7.3.4	Effects of Different Polymer Incorporations on Drug Loading Capacities and Drug Release Kinetics.....	163

7.4 Conclusions.....	165
7.5 References.....	166
Chapter 8.....	169
8 Summary, Conclusions, and Future Work.....	169
8.1 Summary and Conclusions	169
8.2 Future Work.....	171
8.3 References.....	173
Appendix A: Copyright Release from The Royal Society of Chemistry.....	174
Appendix B: Copyright Release from The American Chemical Society	177
Curriculum Vitae	178

List of Tables

Table 3-1 Atomic coordinates of rankinite.	42
Table 3-2 BET specific surface areas (SSAs) of CSH carriers without and with IBU loading and the IBU loading capacities.	45
Table 4-1 ΔL_3 and ΔL_2 of CSH microspheres before and after IBU loading*	78
Table 4-2 Thickness and thickness ratio of CSH to IBU in different regions*	84
Table 5-1 Atomic coordinates of rankinite.	94
Table 5-2 Ca K-edge linear combination fitting results of MS-CSH loaded with IBU, ALN and GS drug.	102
Table 5-3 Drug loading capacities for MS-CSH drug delivery systems.	110
Table 5-4 Sensitivities of Ca-OH, Si-OH groups to different functional groups of drug molecules.	112
Table 6-1 Ion concentrations of SBF and human blood plasma (mmol/L)	120
Table 6-2 Ca K-edge linear combination fitting results of samples after soaked in SBF solution in the first 4 hours.	127
Table 6-3 P K-edge linear combination fitting results of samples after soaked in SBF solution in the first 3 hours.	129
Table 6-4 Thickness of SiO ₂ and HAp in different regions.	138
Table 7-1 Atomic coordinates of tobermorite.	150

List of Figures

Figure 1-1 Crystal structures of (a) rankinite and (b) tobermorite.....	7
Figure 1-2 Log-log plot of the mass photoabsorption cross section of silver as a function of X-ray photon energy [66].....	9
Figure 1-3 Illustration of outgoing photoelectron wave produced by a diatomic system upon X-ray absorption [67].....	10
Figure 1-4 Diagram of de-excitation progresses after core-electron excitation (solid dots: electrons; hollow dot: electron core-hole).	12
Figure 1-5 Schematic layout of synchrotron radiation facility (focussing magnets are left out for clarity).	14
Figure 1-6 Emission pattern of bending magnet (a), wiggler (b) and undulator (c) (l/γ is the opening angle, and N is the number of magnets) [68].....	15
Figure 1-7 Duration of the light pulse produced by a single electron in an ideal orbit seen by an observer [68].	16
Figure 2-1 Schematic layout of the CLS beamlines (courtesy of Canadian Light Source Inc.) [3].....	25
Figure 2-2 Layout of SGM beamline at CLS [6].....	26
Figure 2-3 Schematic illustration of (a) plane grating monochromator and (b) double crystal monochromator (DCM).	27
Figure 2-4 Layout of SXRMB at CLS [7].	28
Figure 2-5 Layout of SM beamlines at CLS (courtesy of Canadian Light Source Inc.) [10].	29

Figure 2-6 Schematic illustration of STXM.	29
Figure 2-7 Illustration of XAFS detection modes: (a) transmission, (b) electron and X-ray fluorescence yield (TEY is detected by monitoring the sample neutralization current).....	31
Figure 3-1 Morphologies of calcium silicate hydrate: (a) amorphous CSH, (b) CSH nanosheets, (c) CSH mesoporous microspheres.	43
Figure 3-2 UV-Vis absorption spectra of the IBU hexane solution diluted 50 times before and after the IBU loading with different carriers.....	44
Figure 3-3 (a) TEY XANES spectra of calcium silicate hydrate and anhydrous calcium silicate carriers with different morphologies, comparison with FEFF calculation; (b) Crystal structure of rankinite simulated by FEFF (green, red and beige spheres stand for Ca, O and Si atoms, respectively).	46
Figure 3-4 Ca K-edge XANES spectra of calcium silicate hydrate and anhydrous calcium silicate carriers with different morphologies, without (a) and with (b) loading of IBU.	48
Figure 3-5 (a) TEY XANES spectra and (b) first derivative spectra of calcium silicate hydrate and anhydrous calcium silicate carriers with different morphologies, with and without loading of IBU.	49
Figure 3-6 Comparison of drug-loaded CSH and CS carriers with calcium acetate monohydrate powder; (a) Ca K-edge XANES total electron yield (TEY) of CSH and CS carriers with IBU drug molecules, and (b) first derivative spectra of CSH mesoporous microspheres before and after IBU loading.	51
Figure 3-7 Si K-edge XANES total electron yield (TEY) spectra of calcium silicate hydrate and anhydrous calcium silicate nanocarriers with different morphologies, without (a) and with (b) IBU loading.....	53

Figure 3-8 (a) Si K-edge XANES and (b) first derivative spectra of calcium silicate hydrate and anhydrous calcium silicate carriers with different morphologies, with and without IBU.	54
Figure 3-9 Si K-edge XANES total electron yield (TEY) spectra of calcium silicate hydrate mesoporous microspheres with and without IBU, compared with SiO ₂ powder.	55
Figure 3-10 FTIR spectra of different CSH carriers with and without IBU drug loading; the FTIR spectrum of pure IBU is also shown for comparison.	57
Figure 3-11 IBU drug release profiles of different IBU-CSH drug delivery systems in the PBS medium.	58
Figure 4-1 UV-Vis absorption spectra of the IBU hexane solution diluted 50 times before and after the IBU loading in CSH mesoporous microspheres.	66
Figure 4-2 TEM images of CSH mesoporous microspheres before (a) and after (b) IBU loading.....	67
Figure 4-3 (a) STXM images of CSH microspheres before IBU loading: two ROIs were selected which represented different CSH microspheres; Red: Sphere-1, Blue: Sphere-2. Scale bar in (a) is 1µm. (b, c) XANES spectra from each ROI displayed at the Ca L _{3,2} -edge (b) and the Si K-edge (c).....	68
Figure 4-4 (a) STXM images of CSH microspheres after IBU loading: 10 ROIs were selected which represented different CSH microspheres. Scale bar in (a) is 1µm. XANES spectra from each ROI displayed at (b) the C K-edge, (c) the Ca L _{3,2} -edge and (d) the Si K-edge.	69
Figure 4-5 STXM images and XANES spectra of individual CSH microsphere before IBU loading, (a) STXM image of individual CSH microsphere (average: 346-1890 eV); (b) 4 ROIs taken from the CSH microsphere: Red: ROI-1, Cyan: ROI-2, Blue: ROI-3, Green: ROI-	

4. Scale bars in (a) and (b) are 600 nm; (c), (d), (e) are isolated XANES spectra of each ROIs displayed in (b) at Ca L_{3,2}-edge , O K-edge and Si K-edge, respectively..... 71

Figure 4-6 STXM images of an individual CSH microsphere: (a) before and (b) after IBU loading taken at the Ca L_{3,2}-edge (E = 352.5 eV); (c) STXM image of an individual CSH microsphere (average at all edges); (d) 4 ROIs taken from an individual CSH microsphere; Red: ROI-1, Cyan: ROI-2, Blue: ROI-3, Green: ROI-4. Scale bars in (c) and (d) are 500 nm; (e) XANES spectra from each ROI displayed in (d) at the C K-edge. 73

Figure 4-7 XANES spectra of individual CSH microsphere after IBU loading at Ca L_{3,2}-edge (a), Si K-edge (b) and O K-edge (c). (ROI 1-4 are the same regions as shown in Fig. 4-6(d)). 75

Figure 4-8 Comparison of average XANES spectra before (a) and after (b) IBU loading at (c) Ca L_{3,2}-edge, (d) Si K-edge and (e) O K-edge..... 77

Figure 4-9 XANES spectra comparisons of individual mesoporous CSH microsphere before/after IBU loading and SiO₂..... 80

Figure 4-10 Reference spectra and elemental linear X-ray absorption profiles of CSH and IBU. (a) and (b) CSH Si K-edge before and after IBU loading (black profile: optical density spectrum of 1 nm thickness based on formula CaSiO₃; red profile: elemental linear X-ray absorption profile); (c) IBU C K-edge (black profile: optical density spectrum of 1 nm thickness based on formula C₁₂H₁₈O₂; red profile: elemental linear X-ray absorption profile). 82

Figure 4-11 Thickness distribution of individual CSH microsphere at the Si K-edge; the vertical color bar illustrates the thickness of the microsphere. 83

Figure 4-12 Thickness distribution maps of an individual CSH microsphere after IBU loading at (a) the Si K-edge and (b) the C K-edge. The vertical bar illustrates the color code of the material thickness..... 85

Figure 5-1 TEM images of CSH before/after drug loading: (a) mesoporous spheres of CSH (MS-CSH); (b) MS-CSH-IBU; (c) MS-CSH-ALN; (d) MS-CSH-GS; contrast change means the thickness increase of CSH microspheres, indicating the drug incorporations (scale bar = 500 nm).	96
Figure 5-2 (a) Fast scan XANES spectra of ALN and GS drug molecules at the C K-edge (spectra were obtained sequentially), and (b) C K-edge XANES comparisons before and after the loading of IBU, ALN and GS into CSH mesoporous microspheres (feature “a” at 290.3 eV is for CO ₂ adsorption in CSH; “b” at 285.2 eV is the feature of aryl ring of IBU; “c” at 288.5 eV is 1s- π* transition from carboxylic acid as in the case of IBU; “d” and “e” at around 289 eV is from C 1s-σ* (C-OH/C-NH ₂) of ALN and GS drug molecules, respectively).....	98
Figure 5-3 Crystal structure of CSH (green, beige and red dots represent for Ca, Si and O atoms, respectively; α=90 ⁰ , β=119.586 ⁰ , and γ=90 ⁰).....	99
Figure 5-4 Comparisons of Ca K-edge TEY and FY XANES spectra of MS-CSH loaded with different drug molecules.	100
Figure 5-5 Ca K-edge total electron yield (TEY) XANES spectra (a) and linear combination fitting (b to d) of MS-CSH loaded with IBU, ALN and GS.	101
Figure 5-6 XANES (a, c, e) and their first derivative (b, d, f) spectra comparisons of MS-CSH before, after loaded with ibuprofen (IBU), alendronate sodium (ALN) and gentamicin sulfate (GS) and relative standard samples.	103
Figure 5-7 Si K-edge total electron yield (TEY) (a) fluorescence yield (FLY) (b) XANES spectra of MS-CSH and MS-CSH loaded with different types of drug molecules.	106
Figure 5-8 FTIR spectra of CSH mesoporous microspheres before and after loading of different drug molecules, and pure IBU, ALN, GS are also shown for comparisons (magenta arrows: Si-O-C stretching; navy arrow: P=O stretching vibration; cyan arrows: P-O	

stretching; dark cyan arrows: major representative absorption peaks of pure GS; green arrow: bands of sulfate ions).	109
Figure 5-9 TG curves of MS-CSH and MS-CSH-Drug delivery systems (more weight change observed after loading, more drugs are incorporated into CSH).	110
Figure 6-1 TEM images of mesoporous CSH microspheres before (a) and after (b) IBU loading.....	122
Figure 6-2 TG curves of mesoporous CSH microspheres and CSH loaded with IBU.	123
Figure 6-3 TEM micrographs of CSH-IBU microspheres soaked in SBF solution for different time: (a) 1 hours, (b) 5 hours, (c) 24 hours, and (d) 48 hours.	124
Figure 6-4 XRD patterns of CSH-IBU powder soaked in SBF solution for different time..	125
Figure 6-5 Ca (a), P (b) and Si (c) K-edge XANES spectra of CSH-IBU microspheres soaked in SBF solution for various time.	126
Figure 6-6 Comparison of Ca K-edge XANES spectra and linear combination fitting in the first 4 hours.	128
Figure 6-7 Comparison of P K-edge XANES spectra and linear combination fitting in the first 3 hours.	130
Figure 6-8 Si K-edge FLY XANES spectra of CSH-IBU microspheres soaked in SBF solution for various time periods.	131
Figure 6-9 The cumulative IBU release of mesoporous CSH microspheres in SBF.....	132
Figure 6-10 (a) STXM optical density image of CSH-IBU sample soaked in SBF for 5h (averaged from 280 to 2190 eV); (b) ROIs taken from the CSH-IBU sample: Red: ROI-1, Magenta: ROI-2, Orange: ROI-3, Green: ROI-4, Blue: ROI-5 and Cyan: ROI-6; (c) XANES spectra taken from each ROI displayed in (b) at the C K-edge.	133

Figure 6-11 Thickness distribution maps of CSH-IBU sample soaked in SBF for 5h at (a) the Si K-edge and (b) the P K-edge. The vertical bar illustrates the color code of the material thickness; XANES spectra of CSH-IBU sample soaked in SBF for 5h at the Si K-edge (c) and P K-edge (d) (ROI 1-6 are the same regions as shown in Figure 6-10(b)).	135
Figure 6-12 Reference spectra and elemental linear X-ray absorption profiles of SiO ₂ (a) (black profile: optical density spectrum of 1 nm thickness based on formula SiO ₂ ; red profile: elemental linear X-ray absorption profile) and HAp (b) (black profile: optical density spectrum of 1 nm thickness based on formula Ca ₅ (PO ₄) ₃ (OH); red profile: elemental linear X-ray absorption profile).	137
Figure 6-13 Concentration changes of Ca, P and Si after soaking CSH-IBU in SBF for different period of time.	139
Figure 6-14 Illustration of the proposed mechanisms for the IBU (black dots) release from mesoporous CSH microspheres and biomineralization.	140
Figure 7-1 TEM images of CSH nanosheets and CSH/polymer composites before and after IBU loading: (a) CSH, (b) CSH-IBU, (c) CSH/PDDA, (d) CSH/PDDA-IBU, (e) CSH/mPEG-PLGA, (f) CSH/mPEG-PLGA-IBU, (g) CSH/PVA, (h) CSH/PVA-IBU.	151
Figure 7-2 FTIR spectra of CSH nanosheets, and different CSH/polymer composites.	152
Figure 7-3 XRD patterns of CSH nanosheets and different CSH/polymer composites.	153
Figure 7-4 (a) Ca K-edge XANES total electron yield (TEY) and (b) fluorescence yield (FLY) spectra of CSH/polymer composites and their first derivative spectra (c) and (d), respectively (dashed arrows in (c) and (d) indicate the changes of CSH/PVA composites compared with CSH nanosheets).	154
Figure 7-5 Crystal structure of 1.4 nm tobermorite (green, red and beige spheres stand for Ca, O and Si atoms, respectively; $\alpha=90^{\circ}$, $\beta=90^{\circ}$, and $\gamma=123.25^{\circ}$).	156

Figure 7-6 (a) Si K-edge XANES total electron yield (TEY) and (b) fluorescence yield (FLY) spectra of CSH/polymer composites.....	157
Figure 7-7 Schematic illustration of the interactions between CSH and different polymers (navy triangle, orange rectangle, green trapezoid stand for PVA, mPEG-PLGA and PDDA, respectively; and green, beige and red dots represent calcium, silicon and oxygen atoms, respectively).....	158
Figure 7-8 Comparisons of (a) Ca K-edge XANES total electron yield (TEY) and (b) fluorescence yield (FLY) spectra of CSH/polymer composites before and after IBU loading and their first derivative spectra (c) and (d), respectively.	160
Figure 7-9 Comparisons of (a) Si K-edge XANES total electron yield (TEY) and (b) fluorescence yield (FLY) spectra of CSH/polymer composites after IBU loading.....	162
Figure 7-10 Comparisons of FTIR spectra of CSH nanosheets, CSH/polymer composites before and after IBU drug loading.....	163
Figure 7-11 Drug loading capacities (DLCs) of different CSH/polymer composites (the DLC of CSH nanosheets for comparison).	164
Figure 7-12 Drug release profiles of different CSH/polymer composites.....	165

List of Schemes

Scheme 1-1 Chemical structures of ibuprofen, alendronate sodium and gentamicin sulfate. . .	6
Scheme 3-1 Possible interactions between calcium ions and IBU.	50
Scheme 3-2 Possible interactions between calcium ions and IBU.	50
Scheme 3-3 Possible interaction between silanol groups and IBU.....	54
Scheme 4-1 Interaction between CSH and IBU at the Ca local environment.	78
Scheme 4-2 Interaction between CSH and IBU at the Si local environment.	79
Scheme 5-1 Chemical structures of ibuprofen (IBU), alendronate sodium (ALN) and gentamicin sulfate (GS).	92
Scheme 5-2 Electrostatic interactions between Ca-OH groups and different drug molecules.	104
Scheme 5-3 Electrostatic interactions between silanol groups and different drug molecules on the surface.	107
Scheme 7-1 Chemical structures of different polymers and ibuprofen.	147
Scheme 7-2 Interactions between CSH, IBU and PVA on the local structure of Ca in the interlayer of CSH.	159
Scheme 7-3 Interactions between CSH, IBU and polymers on the local structure of silicate on the surface.	161

List of Abbreviations:

3D:	Three Dimensional
ALN:	Alendronate Sodium
aXis2000	Analysis of X-ray Images and Spectra 2000
BET:	Brunauer-Emmett-Teller
BG:	Bioactive Glasses
CaP:	Calcium Phosphate
CLS:	Canadian Light Source
CS:	Calcium Silicate
CSH:	Calcium Silicate Hydrate
CXRO:	Center for X-ray Optics
DCM:	Double Crystal Monochromator
DLCs:	Drug Loading Capacities
DSC:	Differential Scanning Calorimetry
DTX:	Destruxin
EA:	Endstation
EDX:	Energy-Dispersive X-ray Spectrometry
EXAFS:	Extended X-ray Absorption Fine Structure

FLY (FY):	Fluorescence Yield
FTIR:	Fourier Transform Infrared Spectroscopy
GS:	Gentamicin Sulfate
HAp:	Hydroxyapatite
HDPE:	High-density Polyethylene
HEG:	High Energy Grating
IBU:	Ibuprofen
ICP-OES:	Inductively Coupled Plasma Optical Emission Spectrometry
IPFY:	Inversion Partial Fluorescence Yield
LCF:	Linear Combination Fitting
LEG:	Low Energy Grating
LINAC:	Linear Accelerator
LUMO:	Lowest Unoccupied Molecular Orbitals
MCM-41:	Mobil Composition of Matter No. 41
MEG:	Medium Energy Grating
Mw:	Molecular Weight
NBOs:	Non-Bridging Oxygens
NMR:	Nuclear Magnetic Resonance

OD:	Optical Density
PBS:	Phosphate Buffered Saline
PDDA:	Poly(DiallylDimethylAmmonium Chloride)
PDLLA:	Poly-DL-Lactide
PE	PolyEthylene
PLGA:	Poly(Lactic-co-Glycolic Acid)
PLGA-mPEG:	Poly(Lactide-co-Glycolic Acid) - methoxy Poly(Ethylene Glycol)
PLLA:	Poly-L-Lactide
PVA:	PolyVinyl Alcohol
RF:	Radio Frequency
ROIs:	Regions of Interests
SBF:	Simulated Body Fluid
SEM:	Scanning Electron Microscopy
SGM:	Spherical Grating Monochromator
SICCAS:	Shanghai Institute of Ceramics of Chinese Academy of Sciences
SM:	Soft X-ray Spectromicroscopy
SPRing-8:	Super Photon Ring – 8 GeV
SSAs:	Specific Surface Areas

STXM:	Scanning Transmission X-ray Microscopy
SXRMB:	Soft X-ray Microcharacterization Beamline
TEM:	Transmission Electron Microscopy
TEOS:	Tetraethyl Orthosilicate
TEY:	Total Electron Yield
TGA:	Thermalgravimetric Analysis
UV-Vis:	Ultraviolet–Visible Spectroscopy
XAFS:	X-ray Absorption Fine Structure
XANES:	X-ray Absorption Near Edge Structure
XAS:	X-ray Absorption Spectroscopy
XEOL:	X-ray Excited Optical Luminescence
X-PEEM:	X-ray Photoemission Electron Microscopy
XPS:	X-ray Photoelectron Spectroscopy
XRD:	X-ray Diffraction

Chapter 1

1 Introduction

1.1 Biomaterials

1.1.1 General Background

Bone not only is a hard form of supportive organ, but also keeps the essential inorganic elements for human beings, particularly calcium and phosphate. Bone consists of minerals (mainly hydroxyapatite, HAp), collagen, water, noncollagenous proteins, lipids, vascular elements and cells [1, 2]. Besides HAp, a few trace elements for different metabolic functions are enriched in minerals, such as carbonate, citrate, sodium, fluoride *etc.* Organic phases provide tensile strength and flexibility while the minerals which are embedded onto collagens to strengthen the bone. Hence, a healthy skeletal system is essential to overall health and quality of human life.

However, according to the report of the U.S. Department of Health and Human Services (2004), annually, 1.5 million Americans suffered wrist, spine, and hip fractures which are due to bone diseases [3]. One of the most common bone diseases is osteoporosis (low bone mass), leading to the deterioration of bone structure [4]. Other bone diseases include Paget's disease (skeletal deformities and fractures) and osteogenesis imperfect (inherited bone disorder). Under these circumstances, surgical treatment to repair or replace damaged bone is inevitable. Traditionally, autograft (graft is implanted from the same patient) has been used for a long time, but the source of autograft is limited; another ways are allograft or xenograft (from another individual or animals), nevertheless, they suffered from pathogen transfer and graft rejection [2]. As a result, people tried to utilize synthetic materials which have the same ability to repair or replace the defective bone system. These kinds of synthetic or biologically derived materials are called biomaterials.

The first use of biomaterials for hard tissue treatment can be dated back to ancient Egypt; they used elephant's tusks to replace bone or missing teeth [5]. However, the practical use of biomaterials for hard-tissue treatment was unsuccessful until the development of aseptic surgical technique in 1860s, because most of previous failures were due to

infection [6]. The development of modern biomaterials for bone treatment started from the 1960s and 1970s, when the first generation of biomaterials called prostheses were invented. Since then, there were more than 50 implanted devices in clinical use made from 40 different materials, however, none of them was bioactive or bioresorbable [7]. By 1984, a second generation of biomaterials which was to be either bioactive or bioresorbable had been engineered [8]. By the mid-1980s, bioactive materials including various bioactive glasses, ceramics and composites had been applied in clinical use. The third generation of biomaterials has made further progresses; they are designed to stimulate specific cellular responses at the molecular level [9]; bioactive materials are being made resorbable while bioresorbable polymers are being designed to be bioactive. Currently, biomaterials which should be biocompatible, nontoxic, sterilisable *etc.*, have improved the quality of human life year after year. In 2000, the biomaterials market was valued around \$30 billion USD, the demand for biomaterials to repair or replace bone tissue continued to increase during the last decade [2, 10].

So far, biomaterials can be classified into metallic biomaterials, ceramic biomaterials, polymeric biomaterials and composite biomaterials. Normally, metals and ceramics are applied in hard tissues treatment, while polymers are used in soft tissue applications. Since the studies in this thesis are focused on the biomaterials applied in hard-tissue engineering, metallic, ceramic biomaterials and composite biomaterials will be introduced below.

1.1.2 Metallic Biomaterials

Since early 1900s, metals have been used as biomaterials because of their excellent electrical and thermal conductivity, as well as mechanical properties. They served as substitutes such as hip or knee joints for fracture healing implants. Until now, stainless steels [11], cobalt-chromium alloys [12, 13], titanium and Ti-based alloys [14, 15] have been used as biomaterials. The major advantages of these metals and alloys are their biocompatibility, impressive mechanical properties and reasonable cost. Ti and its alloys gain more preferences right now since they are lighter and have superior corrosion resistance. In addition, some noble metals (Au, Pt, Pd. *etc.*) and amalgam have been also utilized as biomaterials to replace tooth roots for dental applications [16].

Although these metallic biomaterials have been applied in hard-tissue treatment successfully, they are still lack of mechanical compatibility with natural bone to some extent. Moreover, metals do not have the ability to interact with human tissue, leading to the limited integration with the bone. To overcome this issue, hydroxyapatite coated metallic implants are introduced in most of treatments [17].

1.1.3 Ceramics Biomaterials

Ceramics in the form of pottery or concrete have been used by humans for thousands of years. People did not realize that ceramics could be also used to bone tissues augmentation and repair until 1920 [18]. Thus, these ceramics used in hard-tissue applications are categorized as ceramic biomaterials or bioceramics. Around 60% of the bone graft substitutes on the market are related to bioceramics [10]. They can also be classified as non-absorbable (relative inert), bioactive or surface reactive [19] and biodegradable or bioresorbable [20].

Relatively inert bioceramics maintain their physical and mechanical properties while they are implanted in the host. Aluminium oxides and zirconia ceramics are the typical examples of these bioceramics [21, 22]. Based on their characteristics, they are used as structural-support implants. Bioactive or surface reactive bioceramics such as bioglass [23] are very important for the application in the coating of metal prostheses because of their strong bonding with adjacent tissue once implanted in the host. Calcium phosphate (CaP) based bioceramics are another representative examples of bioceramics. They have a long history of bone repair since 1920 [24], some of them like β -tricalcium phosphates are biodegradable materials, nevertheless, their degradation rate is not satisfactory [25]. Moreover, although CaP bioceramics possess the ability of bone growth on the materials surface, they lack the ability of recruitment of immature cells and the stimulation of these cells to develop into pre-osteoblasts. Another common disadvantages of all bioceramics are that they are brittle, lower toughness and not resilient.

1.1.4 Composite Biomaterials

Currently, the development of composite biomaterials (ceramics/polymer) is attractive because the advantages of two or more kinds of materials can be combined and the

shortcomings of a single phase biomaterial, such as poor mechanical property for bioceramics and poor bioactivity of polymeric biomaterials, can be overcome simultaneously [26]. For example, Bonfield *et al.* first introduced the bone analog concept using HAp particulate-reinforced high-density polyethylene (HDPE) composites in 1981 [27]. Until now, nanocomposite biomaterials have been applied into various biomedical applications as a new and versatile class of biomaterials for hard tissue repair and regeneration. Poly(lactic-co-glycolic acid) (PLGA), poly-L-lactide (PLLA), poly-DL-lactide (PDLLA) *etc.* have been successfully combined with amorphous CaP, bioglass and HAp to form composite biomaterials with high porous structures [28-30]. Besides, the incorporation of biomolecules (proteins) by surface modification accelerated local bone growth and healing [31].

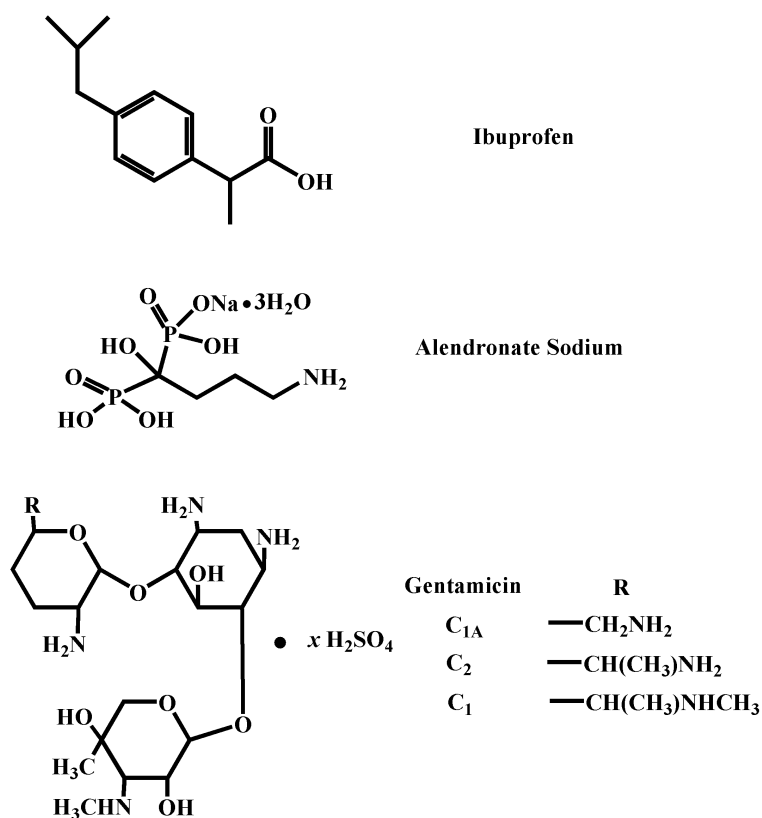
Although nanocomposite biomaterials have shown some promising advantages in particular hard tissues treatment, the use of composite biomaterials is still at an early stage: the mechanical properties are still lower than those of bone; for example the Young's modulus and tensile strength of glass-ceramic/polyethylene (PE) are 2.84 GPa and 14.84 MPa, respectively; while the natural mechanical properties of normal cortical bone are around 30 GPa and 150 MPa, respectively [2]. In addition, more *in vitro* and *in vivo* studies are necessary before they are applied in clinical treatment.

1.1.5 Nano-bioceramics and Drug Delivery

With the development of nanotechnology, bioceramics currently are designed at the nanoscale to obtain gene- and cell-activating functions to meet the requirement of third generation biomaterials [32]. There are four main methods which are currently used to synthesize nano-bioceramics: sol-gel method, hydrothermal method, chemical precipitation, and solid-reaction [10].

Nowadays, open bone fractures are more and more common, even though the development of the aseptic surgical technique, the association of bone infections after the surgery are reported to be 7% [33], and the following treatments are more difficult. Repeated operations to remove dead bone tissue cannot be avoided which leads to more medical spending, more pains and higher health risks to the patients [34]. The

conventional intake of antibiotics and anti-inflammatory drugs (oral and injection) for prophylaxis are not effective because the perfusion rate to diseased bone site is poor. Hence, new requirements for bioceramics, which possess the ability to deliver drugs to local diseased bone site in order to increase the effectiveness of therapy, are increasing [35]. After the successful application of ordered mesoporous silica in drug delivery [36] (Vallet-Regi *et al.* loaded ibuprofen (IBU) into Mobil composition of matter No. 41 (MCM-41), which is a type of mesoporous silicate and aluminosilicate material [37]), highly ordered structures, high surface area, and larger pore size have been regarded as the key factors to increase the possibilities to trap both small and large drug molecules into the bioceramics. Since then, many new types of porous bioceramics with different functionalities have been investigated [38, 39]; until now, a wide range of drugs (antibiotics [40], anticancer drug [41], anti-inflammatory drug [42] and proteins [43] *etc.*) have been successfully loaded into bioceramics drug carriers. In this thesis, three kinds of drugs molecules are utilized to study the drug-carrier interactions: ibuprofen, which is an anti-inflammatory drug, is daily used to reduce fever and treat pain or inflammation caused by many conditions; alendronate sodium, a bisphosphonate drug, inhibits bone resorption by osteoclasts [44] and gentamicin sulfate, a typical antibiotic drug that is extremely effective in treating bone infections [45]. Their chemical structures are shown in Scheme 1-1.



Scheme 1-1 Chemical structures of ibuprofen, alendronate sodium and gentamicin sulfate.

1.1.6 Calcium Silicate Bioceramics

Although silicate bioceramics was first proposed as $\text{SiO}_2\text{-CaO-Na}_2\text{O-P}_2\text{O}_5$ glass by Hench *et al.* in the early 1970s [46], they are still regarded as a new family of biomaterials, because silicon which is one of the trace element in human body, is found to be located on the active calcification sites in bones and directly participated in the biomineralization processes in simulated body fluid (SBF) [47, 48]. What are more important, previous studies have shown that Ca and Si are found to stimulate osteoblast proliferation and differentiation *in vitro* [49, 50]. Besides, the mechanical properties of silicate bioceramics are higher than those of HAP ceramics; for example, the bending strength and fracture toughness of HAP are 195 MPa and $1.3 \text{ MPa}\cdot\text{m}^{1/2}$, respectively; while these mechanical properties of dicalcium silicate are 293 MPa and $3.0 \text{ MPa}\cdot\text{m}^{1/2}$, respectively [51]. Hence, silicate bioceramics belong to the third generation of biomaterials and gained more research attentions during the past few years.

Calcium silicates (CS), which are normally regarded as a main component of cement, have not been used as bioceramics until the last two decade. There are three kinds of calcium silicate with different Ca/Si ratios: monocalcium, dicalcium, and tricalcium silicate, and dicalcium silicates have five polymorphs [52]. When hydrated, the silicate phases undergo physicochemical reactions resulting in the formation of calcium silicate hydrates (CSH) and a soluble fraction of calcium hydroxide [53]. CSH microspheres studied in this thesis have the crystal structure of rankinite, while CSH nanosheets possess the crystal structure of 1.4 nm tobermorite, whose unit cells are shown in Figure 1-1. Figure 1-1(a) is the unit cell of rankinite; the calcium atoms which have seven nearest neighbours of oxygens, are placed among the Si_2O_7 paired linked tetrahedra [54]. Figure 1-1 (b) shows the structure of tobermorite; it is formed by a central Ca-O sheet (Ca is in octahedral structure which have six nearest neighbour oxygens), which flanked on each side of silicates' "dreierketten" chains: the silicate tetrahedra share oxygen atoms with the Ca-O layer or neighbouring bridge silicate tetrahedra. Hydrates can either adsorb on the surface or in the interlayer spaces [55-57]. The concentrations of Ca-OH and Si-OH groups on CSH surface are extremely important because they not only determine the nanostructure of CSH, but also are the bioactive sites for bone attachment. Ca-OH groups located at the interlayer site or at the surface will be dominant only at high Ca/Si ratios [56, 58].

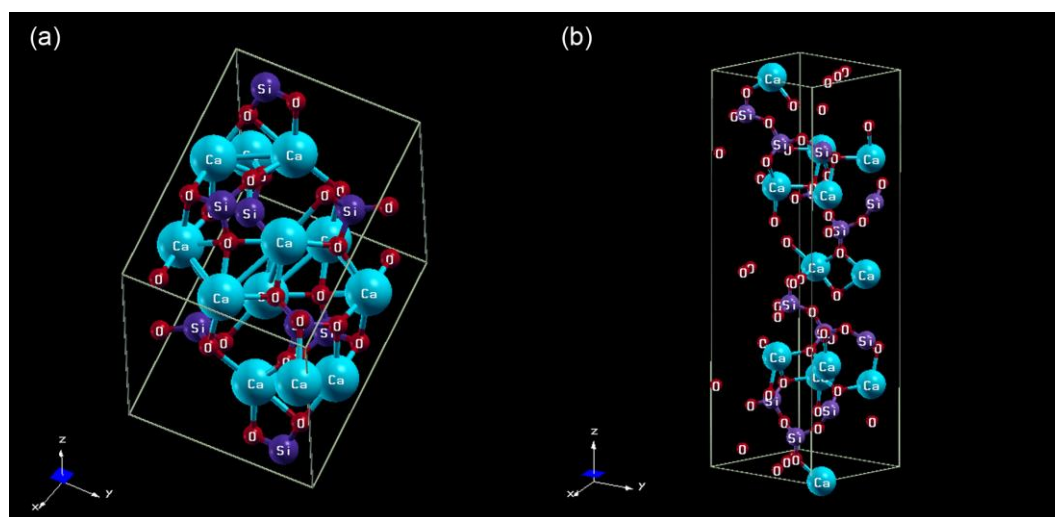


Figure 1-1 Crystal structures of (a) rankinite and (b) tobermorite.

Until now, CS can be fabricated into microspheres, nanowires, nanobelts *etc.* and all of them have shown good biocompatibility, bioactivity, and excellent marginal adaptation and sealing ability, hence they are primarily applied as dental repair materials [59], and the CS application in bone treatment is still ongoing. More recently, Wu *et al.* successfully incorporated drug molecules, protein and metal ions into CSH nanosheets [60]; they found that the release rates of anticancer drug doxorubicin (DOX) in CSH/mPEG-PLGA nanoparticles in phosphate buffered saline are different at different pH, which is promising for cancer therapy [61]. Fan *et al.* [62] and Kang *et al.* [63] used as Eu³⁺ and Tb³⁺ doped CS as drug carriers, which illustrate the current development of multifunction bioceramics (drug delivery and imaging). All these results demonstrate that CS/CSH is a type of great potential biomaterials for drug delivery.

1.2 X-ray Absorption Spectroscopy

1.2.1 X-ray Absorption Fine Structure

X-ray absorption fine structure (XAFS) spectroscopy is an elemental specific technique which provides much information of the local structure of materials, and XAFS is not limited to crystalline sample, it works for non-crystalline, liquid or gas phases.

Information such as formal oxidation state, coordination number, bond length, *etc.* can be obtained from XAFS.

When X-ray photons are absorbed by materials, their intensities are attenuated in an exponential function:

$$I_t = I_0 e^{-\mu t} \quad (1 - 1)$$

where I_0 is the incident X-ray intensity, I_t is the transmitted X-ray intensity, t is the thickness of the sample and the μ is the absorption coefficient [64, 65]. XAFS measurements are made by monitoring the absorption coefficient (μ in cm^{-1}) as a function of the X-ray energy (E) of a specific element across an absorption edge of the element of interest. Elemental specificity comes about since each atom has core level electrons with unique energy thresholds. When the incident X-ray energy reaches the energy threshold of a core electron, X-ray energy will be absorbed due to the increase of absorption cross

section (σ in cm^2/g) resulting in a sharp rise of μ (absorption edge). Hence, the absorption coefficient can be written as a function of the X-ray absorption cross section as

$$\mu = \sigma \cdot \rho \quad (1 - 2)$$

where ρ is the density of sample (g/cm^3). Figure 1-2 shows the atomic mass photoabsorption cross section of silver metal as a function of X-ray energy. There are several absorption edges, labeled L_3 , L_2 , L_1 and K corresponding to core level electron at different energy levels being excited. K-edge refers to the excitation of the $1s$ core electrons at threshold, L_1 -edge is the energy at which the $2s$ core electrons are excited, and $L_{3,2}$ -edge is the excitation of the $2p_{3/2}$ and $2p_{1/2}$ electrons.

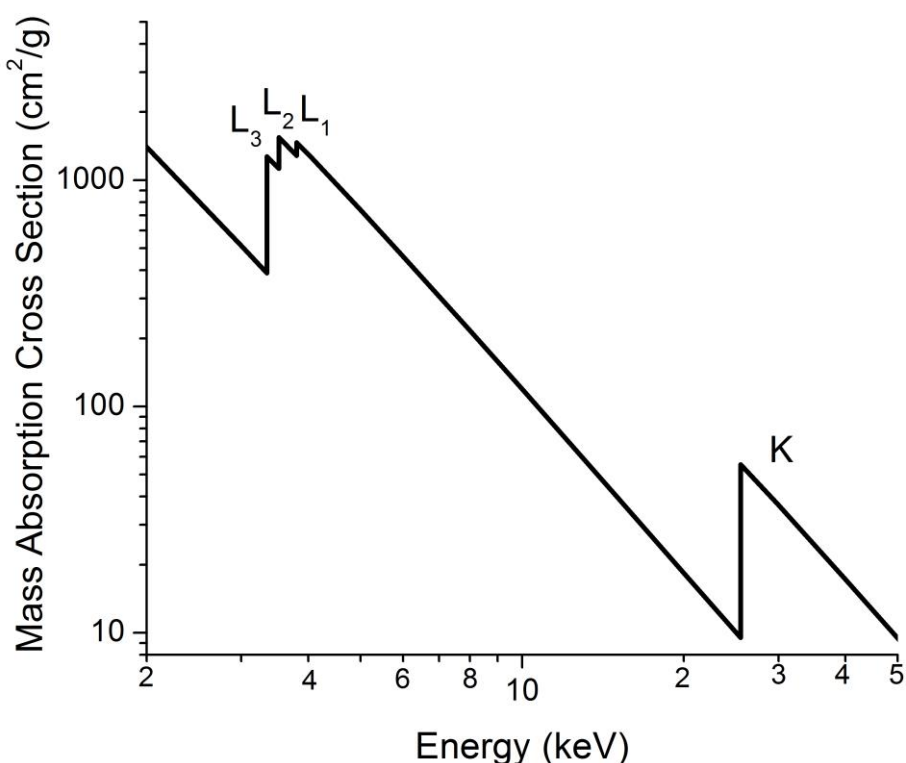


Figure 1-2 Log-log plot of the mass photoabsorption cross section of silver as a function of X-ray photon energy [66].

When the absorbing atom is surrounded by a neighbouring atom, the ejected photoelectron can be scattered from the electrons of the neighbouring atom, and return to the absorbing atom, in the form of a wave with the wave number ($2\pi/\lambda$) proportional to

the $(E-E_0)^{1/2}$. The outgoing and backscattering wave interfere with each other by modulating the absorption coefficient ($\mu(E)$). We call this modulation the XAFS. It should be noted that in a free atom, there is no neighboring atom, hence no XAFS (Figure 1-3).

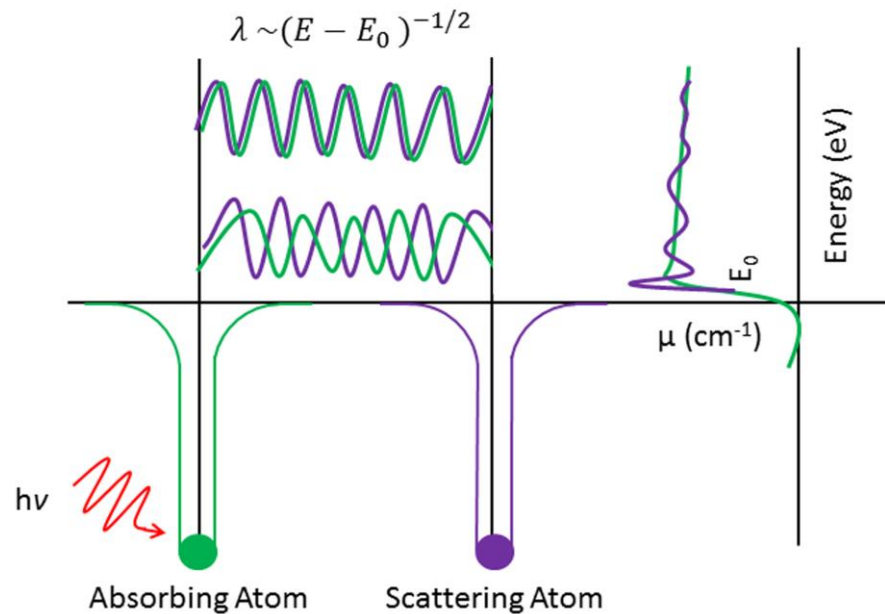


Figure 1-3 Illustration of outgoing photoelectron wave produced by a diatomic system upon X-ray absorption [67].

An XAFS spectrum is typically divided into two regimes, X-ray absorption near-edge structure (XANES) and extended X-ray fine structure (EXAFS), which are dependent on the behaviours of electrons scattering related to the kinetic energy of electrons [68]. In this thesis, researches are only focused on the XANES region, generally from 20 eV below to 50 eV above the absorption edge. There are two sources for the XANES intensity; one is the probability of a transition from initial state to a final state, which can be described by Fermi's golden rule; the other is the density of states (ρ) where the excited state is embedded:

$$\mu(E) \propto |\langle \varphi_i | H | \varphi_f \rangle|^2 \rho \quad (1 - 3)$$

where φ_i and φ_f are the initial and final state wave function, respectively; H is the interaction Hamiltonian, which includes the electric field vector of X-ray (ε) and electron vector (r). Hence, Equation 1-3 can be rewritten as:

$$\mu(E) \propto |\langle \varphi_i | \varepsilon \cdot r | \varphi_f \rangle|^2 \rho' \quad (1 - 4)$$

It should be noted that the quantum states which the electrons can be excited to should have not only the right energy, but also have the right angular momentum; hence all the allowed transition probability is followed by dipole transition selection rule ($\Delta l = \pm 1$, $\Delta j = 0, \pm 1$). For example, core electrons from s orbitals can be only excited to the p final state and p core-level is excited to either d or s states, although p to d transition is normally a dominant process, and electrons from $2p_{3/2, 1/2}$ ($l = 1, j = 1/2, 3/2$) may be excited to $3d_{5/2, 3/2}$ ($l = 2, j = 3/2, 5/2$) [69-71].

In the XANES region, a quantitative interpretation is not often involved because the low kinetic energy photoelectrons are more inclined to the multiple scattering phenomena. However, materials with different structures or compositions have their unique XANES spectra at specific absorption edges; take bioceramics as specific examples, calcium silicate hydrate (CSH), amorphous calcium phosphate, HAp and CaCO_3 show different XANES features at the Ca K-edge, by which qualitative analysis is very reliable by spectral “fingerprint” [72, 73].

1.2.2 De-excitation Processes

After a core electron is excited to a previously unoccupied state, which could be the lowest unoccupied molecule orbital in molecules, states just above Fermi level in metals, or bottom of the conduction band of semiconductors, *etc.*, a core-hole will be created, and several de-excitation processes will take place to fill this core-hole. There are two main mechanisms for the de-excitation processes, Auger electron and X-ray fluorescence ejection (Figure 1-4). After an electron from higher energy electron level drops to fill the core-hole, the excess energy can be released by either ejection of another electron to continuum (Auger electron) or by emission of an X-ray fluorescence photon. In either case, a new core-hole will be created at shallower energy level, and the cascade of

subsequent de-excitation will continue until the system is fully relaxed. These two de-excitation processes occur simultaneously however, X-ray fluorescence emission will be dominant in the hard X-ray regime (> 10 keV), while Auger electron emission is more likely to happen in the soft X-ray region. Major detection methods will be based on these de-excitation processes, which will be introduced in details in Chapter 2.

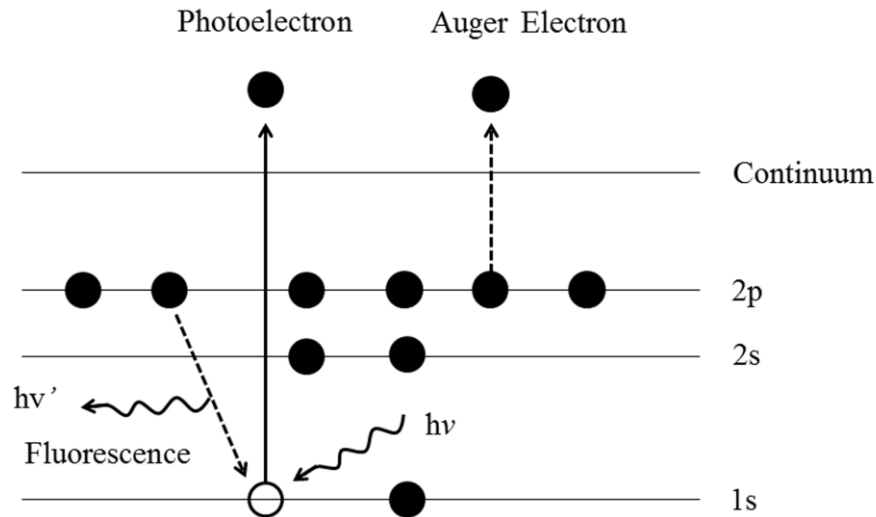


Figure 1-4 Diagram of de-excitation progresses after core-electron excitation (solid dots: electrons; hollow dot: electron core-hole).

1.3 Overview of Synchrotron Radiation

In order to conduct XAFS measurements, a tuneable X-ray source is essential, which can be provided by synchrotron radiation. When high energy electrons are moving in a circular orbit at near the speed of light, they will emit electromagnetic radiation tangential to the orbit. This kind of radiation is called synchrotron radiation or synchrotron light [68, 74]. The electromagnetic radiation power (P) generated by high speed electrons when changing directions can be expressed by Equation 1-5:

$$P = \frac{2 e^2 c E^4}{3 (m_0 c^2)^4 \rho^2} \quad (1 - 5)$$

where e is the electron charge, c is the speed of light, E is the energy of the electron in GeV, m_0 is the rest mass of the particle, and ρ is the radius of the curvature of the electron orbit. The higher the electron energy (E), the higher power of synchrotron light can be generated. The energy loss ΔE , per electron per turn to synchrotron radiation can be shown as

$$\Delta E[\text{keV}] = 88.5 \frac{E^4 [\text{GeV}]}{\rho [\text{m}]} \quad (1 - 6)$$

From Equation 1-6, the energy loss per electron per turn is around one fourth power of the electron energy. Hence, most of synchrotron facilities are built at the energies of the order of GeV.

The first generation synchrotron facilities were originally built for high energy physics research until the mid-1970s, the second generation synchrotron facilities were designed specifically as light sources, where most of beamlines are from bending magnets. Later with the introduction of insertion devices (undulators and wigglers), the third generation of synchrotron facilities provide higher brightness synchrotron light. So far, most of synchrotron facilities all round the world are in third generation, like Canadian Light Source (Canada), Advanced Photon Source (USA), and SPring-8 (Japan) [74]. A schematic layout of a synchrotron light source is shown in Figure 1-5.

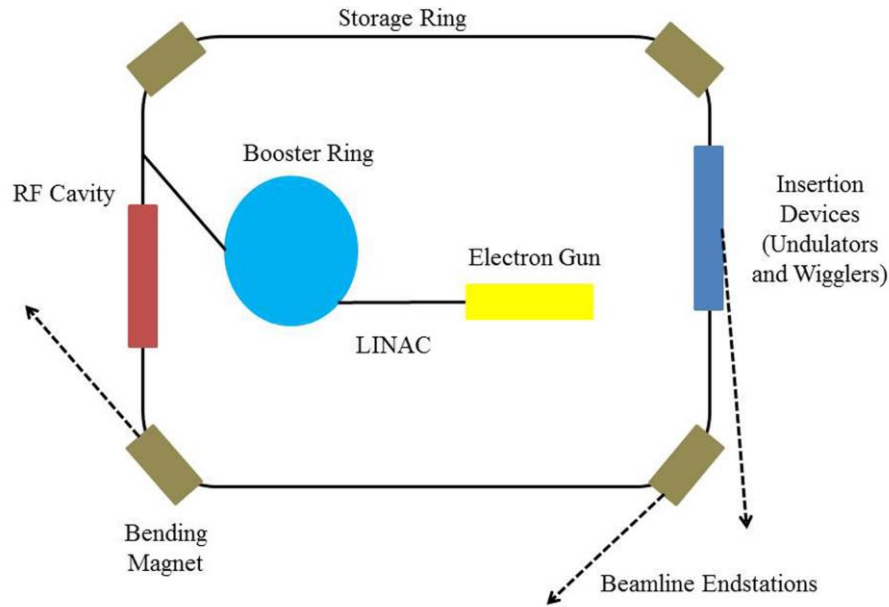


Figure 1-5 Schematic layout of synchrotron radiation facility (focussing magnets are left out for clarity).

First of all, bunches of electrons are generated by a heated metal oxide cathode (electron gun), and then, they are injected into the linear accelerator (LINAC), which can accelerate the electrons to 99.9998% of the speed of light with the energy to the order of MeV. After that, electrons are injected into the booster ring. Dipole magnets are used to direct electrons travelling around the booster ring, while quadrupole magnets can focus and defocus the electrons and keep them in the desired orbit and maintain the stability of the electron beam. After the electrons get enough energy (GeV), they are transferred into the storage ring, where the electrons will circulate for several hours at nearly the speed of light. In the third generation storage rings, two kinds of insertion devices, known as wigglers and undulators were further developed. Basically, they consist of many periods of alternating magnets to deflect the directions of high energy electrons rapidly. The wiggler can produce a continuum of radiation that can be regarded as the superposition of the bending magnet radiation with higher flux, whereas the undulator takes advantage of the phasing/interference effects to produce more collimated, synchrotron light (Figure 1-6). Hence, electromagnetic radiation will be produced either by the bending magnets (tangential to the orbit) or by insertion devices at straight sections. Moreover, a radio

frequency (RF) cavity in the straight section is applied to restore the energy loss of synchrotron radiation [68].

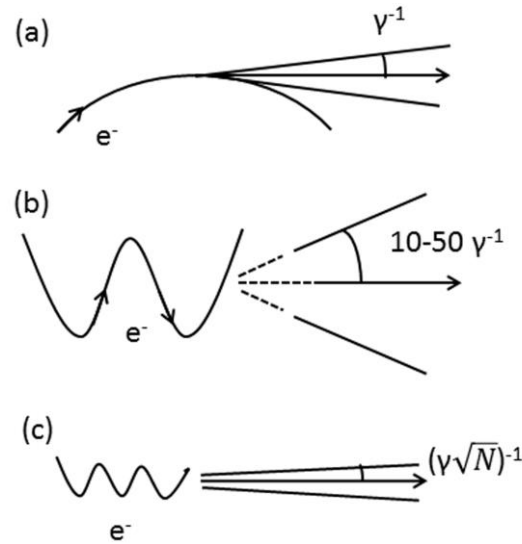


Figure 1-6 Emission pattern of bending magnet (a), wiggler (b) and undulator (c) ($1/\gamma$ is the opening angle, and N is the number of magnets) [68].

Under the Lorentz force of bending magnet or insertion devices, the synchrotron light is emitted by the trajectory altered high energy electron, with a spatial distribution, defined by opening angle (γ^{-1}), where γ is the ratio of the mass of a relativistic electron to its rest mass.

$$\gamma = \frac{m}{m_0} = \frac{E}{m_0 c^2} = 1957E \text{ (GeV)} \quad (1 - 7)$$

The reason why synchrotron radiation is energy tuneable is because of the broad energy spread (ΔE_{SR}) of the photon spectrum, which can be explained by using an approximation based on Heisenberg's uncertainty principle. As mentioned above, when the trajectory of high energy electrons are bended by magnet, electromagnetic radiation is emitted with a pulse of duration Δt . The length of pulse can be determined by a consideration shown in Figure 1-7.

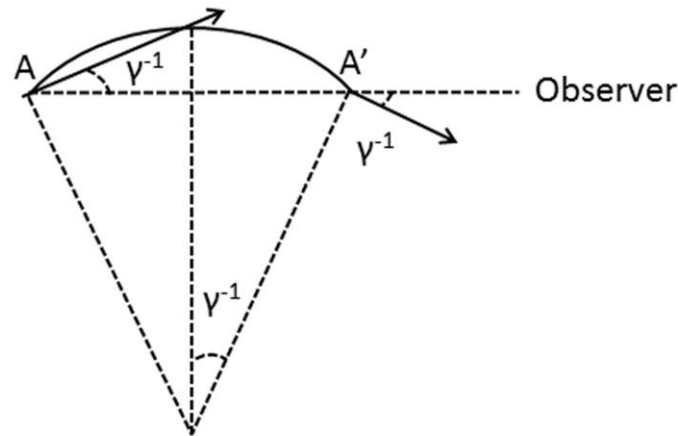


Figure 1-7 Duration of the light pulse produced by a single electron in an ideal orbit seen by an observer [68].

The light is first seen at point A where the electron is at an angle of $1/\gamma$ to the observer. At point A', light is last seen the angle is $-1/\gamma$. So the pulse length of radiation is the time difference between the electron (t_e) and photon (t_γ) going from point A to A' (equation 1-8). According to Heisenberg's uncertainty principle, Equation 1-11 can be derived; and thus, for a typical GeV synchrotron facility, the energy spread is around keV. Hence, this wide energy range provides the tunability of synchrotron radiation from a bending magnet.

$$\Delta t = t_e - t_\gamma = \frac{2\rho}{\beta\gamma c} - \frac{2\rho \sin\left(\frac{1}{\gamma}\right)}{c} \approx \frac{4\rho}{3c\gamma^3} \quad (1-8)$$

$$\beta = v/c \quad (1-9)$$

$$\Delta E_{SR} \cdot \Delta t \geq \hbar/2 \quad (1-10)$$

$$\Delta E_{SR} \geq \frac{3\hbar c\gamma^3}{8\rho} \quad (1-11)$$

Besides tunable energy (energy ranges from IR to hard X-ray) and highly collimated light (very narrow opening angle $1/\gamma$), compared with conventional characterization techniques, synchrotron radiation has a couple of advantages which make synchrotron radiation more powerful in materials analysis despite they are not utilized in this thesis. First is the polarization. Synchrotron light can be linearly polarized in the orbit plane, and elliptically polarized out of the orbit plane. Hence, polarization is a very important property of synchrotron radiation; it provides possibilities for the study of magnetic and optical circular and linear dichroism. Second is the time structure of the synchrotron light. Because of the use of radio frequency cavity to replenish the energy loss of electrons in the storage ring, it produces bunches of electrons whose length determines the pulse width of the synchrotron light (in nanoseconds). For example, the Canadian Light Source ring has a 35 ps pulse width with a repetition rate of 570 ns. This unique property allows for conducting time-resolved experiments [68, 75].

1.4 Research Motivations and Thesis Outline

Despite the reported studies of bioceramics in drug delivery, enhancing drug loading capacities of drug carriers and controlling drug release kinetics are still challenges in the drug delivery field, which would be largely influenced by the interaction between drug molecules and drug carriers. Currently, only a few researches have been systematically carried out on the interaction study between drug molecules and drug carriers on the molecular level, which is due to the limitation of conventional characterization techniques. Moreover, although many characterization methods have been used in the study of the transformation mechanisms from CS to HAp, the mechanism of biomineralization of CS is still not completely clear so far because some of the initial products are amorphous and in a low amount. From the introduction of XAFS described above, it is certain that XAFS is a powerful tool in the investigation of ceramic biomaterials in drug delivery applications because XAFS is elemental specific and sensitive to the subtle changes of chemical environment of absorbing atoms. For example, changes of the electronic structures of the bioceramics before and after drug loading can be tracked by comparison of the XANES spectra, thus a more comprehensive understanding of how drug molecules interact with different functional groups in drug

carriers will be obtained. This information will provide foresights into the functionalization and engineering of bioceramics to enhance drug loading capacities.

The thesis outline is as follows: Chapter 1 provides a general introduction of biomaterials, bioceramics, descriptions of X-ray absorption fine structure, and overview of synchrotron radiation. Chapter 2 provides the synchrotron radiation instrumentations, detection methods, XANES modelling processes, and related analysis techniques which were used in the research. Chapter 3 discusses the interactions between calcium silicate hydrate (CSH) with different morphologies and ibuprofen (IBU) molecules by using X-ray absorption near edge structure (XANES) spectroscopy. In Chapter 4, mapping of an individual mesoporous CSH microsphere before and after the loading of IBU and the interaction between individual drug carrier and drug molecules are presented simultaneously by scanning transmission X-ray microscopy (STXM). Chapter 5 reports a systematic and comparative study to investigate the interactions between CSH drug carriers and different drug molecules in order to reveal the relationship of interactions and drug loading capacities. Chapter 6 presents the XANES and STXM studies of biomineralization mechanisms of CSH microspheres upon IBU release in SBF. In Chapter 7, the effects of block copolymer on drug loading capacities of CSH/polymer composites are studied using XANES spectroscopy. Chapter 8 contains the summaries from Chapter 3 to 7 and a description of proposed future work.

1.5 References

1. Murugan, R. and Ramakrishna, S., *Compos. Sci. Technol.* **2005**, *65*, 2385-2406.
2. Ramakrishna, S., Ramalingam, M., Kumar, T.S., and Soboyejo, W.O., *Biomaterials: a nano approach.* **2010**: CRC Press.
3. United States. Public Health Service, Office of the Surgeon, *Bone health and osteoporosis: a report of the Surgeon General.* **2004**, U.S. Dept. of Health and Human Services, Public Health Service, Office of the Surgeon General: Washington, D.C; Rockville, MD.
4. Percival, M., Bone health & osteoporosis. *Appl. Nutr. Sci. Rep.* **1999**, *5*, 1-5.

5. Williams, D.F. and Cunningham, J., *Materials in clinical dentistry*. **1979**: Oxford University Press.
6. Wong, J.Y. and Bronzino, J.D., *Biomaterials* **2007**: CRC Press.
7. Hench, L.L., *Science* **1980**, 208, 826-831.
8. Hench, L.L. and Wilson, J., *Science* **1984**, 226, 630-636.
9. Hench, L.L. and Polak, J.M., *Science* **2002**, 295, 1014-1017.
10. Wu, C.T. and Chang, J., *Biomed. Mater.* **2013**, 8, 032001.
11. Disegi, J. and Eschbach, L., *Injury* **2000**, 31, D2-D6.
12. Granchi, D., Ciapetti, G., Stea, S., Savarino, L., Filippini, F., Sudanese, A., Zinghi, G., and Montanaro, L., *Biomaterials* **1999**, 20, 1079-1086.
13. Park, J.B. and Bronzino, J.D., *Biomaterials: principles and applications*. **2003**: CRC Press.
14. Geetha, M., Singh, A., Asokamani, R., and Gogia, A., *Prog. Mater. Sci.* **2009**, 54, 397-425.
15. Li, L.-H., Kong, Y.-M., Kim, H.-W., Kim, Y.-W., Kim, H.-E., Heo, S.-J., and Koak, J.-Y., *Biomaterials* **2004**, 25, 2867-2875.
16. Wataha, J.C., *J. Prosthet. Dent.* **2000**, 83, 223-234.
17. Habibovic, P., Barrere, F., Blitterswijk, C.A., Groot, K., and Layrolle, P., *J. Am. Ceram. Soc.* **2002**, 85, 517-522.
18. Albee, F.H. and Morrison, H.F., *Am. J. Med. Sci.* **1920**, 159, 40-52.
19. Hench, L.L., *J. Am. Ceram. Soc.* **1991**, 74, 1487-1510.

20. Park, J., Lakes, R.S., *Biomaterials: An Introduction*. **2007**: Springer Science and Business Media LLC.
21. De Aza, A., Chevalier, J., Fantozzi, G., Schehl, M., and Torrecillas, R., *Biomaterials* **2002**, *23*, 937-945.
22. Piconi, C., Maccauro, G., Muratori, F., and Prever, E., *J. Appl. Biomater. Biomech.* **2003**, *1*, 19-32.
23. Kokubo, T., *Biomaterials* **1991**, *12*, 155-163.
24. Kossler, W. and Fuchs, J., *Bioceramics: properties, preparation, and applications*. **2009**: Nova Biomedical Books.
25. Xu, S., Lin, K., Wang, Z., Chang, J., Wang, L., Lu, J., and Ning, C., *Biomaterials* **2008**, *29*, 2588-2596.
26. Rezwani, K., Chen, Q., Blaker, J., and Boccaccini, A.R., *Biomaterials* **2006**, *27*, 3413-3431.
27. Bonfield, W., Grynopas, M., Tully, A., Bowman, J., and Abram, J., *Biomaterials* **1981**, *2*, 185-186.
28. Khan, Y.M., Katti, D.S., and Laurencin, C.T., *J. Biomed. Mater. Res. A* **2004**, *69*, 728-737.
29. Zhang, R. and Ma, P.X., *J. Biomed. Mater. Res.* **1999**, *44*, 446-455.
30. Verrier, S., Blaker, J.J., Maquet, V., Hench, L.L., and Boccaccini, A.R., *Biomaterials* **2004**, *25*, 3013-3021.
31. Jansen, J., Vehof, J., Ruhe, P., Kroeze-Deutman, H., Kuboki, Y., Takita, H., Hedberg, E., and Mikos, A., *J. Control. Release* **2005**, *101*, 127-136.
32. Traykova, T., Aparicio, C., Ginebra, M.P., and Planell, J.A., *Nanomedicine* **2006**, *1*, 91-106.

33. Patzakis, M.J. and Wilkins, J., *Clin. Orthop. Relat. Res.* **1989**, 243, 36-40.
34. Jain, A.K. and Panchagnula, R., *Int. J. Pharm.* **2000**, 206, 1–12.
35. Dhanikula, A.B. and Panchagnula, R., *Int. J. Pharm.* **1999**, 183, 85-100.
36. Kresge, C., Leonowicz, M., Roth, W., Vartuli, J., and Beck, J., *Nature* **1992**, 359, 710-712.
37. Vallet-Regi, M., Rámila, A., del Real, R.P., and Pérez-Pariente, J., *Chem. Mater.* **2001**, 13, 308-311.
38. Wang, S.B., *Micropor. Mesopor. Mater.* **2009**, 117, 1-9.
39. Wu, C., Chang, J., and Xiao, Y., *Advanced bioactive inorganic materials for bone regeneration and drug delivery.* **2013**: CRC Press.
40. Zhu, Y.F. and Shi, J.L., *Micropor. Mesopor. Mater.* **2007**, 103, 243-249.
41. Zhu, Y.F., Ikoma, T., Hanagata, N., and Kaskel, S., *Small* **2010**, 6, 471-478.
42. Otsuka, M., Nakahigashi, Y., Matsuda, Y., Fox, J.L., Higuchi, W.I., and Sugiyama, Y., *J. Control. Release* **1998**, 52, 281-289.
43. Blom, E.J., Klein-Nulend, J., Wolke, J.G.C., Kurashina, K., van Waas, M.A.J., and Burger, E.H., *Biomaterials* **2002**, 23, 1261-1268.
44. Balas, F., Manzano, M., Horcajada, P., and Vallet-Regi, M., *J. Am. Chem. Soc.* **2006**, 128, 8116-8117.
45. Sivakumar, M. and Panduranga Rao, K., *Biomaterials* **2002**, 23, 3175-3181.
46. Hench, L.L., *J. Mater. Sci. Mater. Med.* **2006**, 17, 967-978.
47. Rodriguez-Lorenzo, L.M., Garcia-Carrodeguas, R., Rodriguez, M.A., De Aza, S., Jimenez, J., Lopez-Bravo, A., Fernandez, M., and Roman, J.S., *J. Biomed. Mater. Res. A* **2009**, 88A, 53-64.

48. Carlisle, E.M., *Science* **1970**, *167*, 279-280.
49. Gough, J.E., Jones, J.R., and Hench, L.L., *Biomaterials* **2004**, *25*, 2039-2046.
50. Valerio, P., Pereira, M.M., Goes, A.M., and Leite, M.F., *Biomaterials* **2004**, *25*, 2941-2948.
51. Wu, C.-T. and Chang, J., *J. Inorgan. Mater.* **2013**, *28*, 29-39.
52. Toraya, H. and Yamazaki, S., *Acta Crystallogr. B* **2002**, *58*, 613-621.
53. Hughes, E., Yanni, T., Jamshidi, P., and Grover, L., *Adv. Appl. Ceram.* **2015**, *114*, 65-76.
54. Kusachi, I., Henmi, C., Kawahara, A., and Henmi, K., *Mineral. J.* **1975**, *8*, 38-47.
55. Nonat, A., *Cem. Concr. Res.* **2004**, *34*, 1521-1528.
56. Cong, X.D. and Kirkpatrick, R.J., *Adv. Cem. Based Mater.* **1996**, *3*, 144-156.
57. Bonaccorsi, E., Merlino, S., and Kampf, A.R., *J. Am. Ceram. Soc.* **2005**, *88*, 505-512.
58. Chen, J.J., Thomas, J.J., Taylor, H.F.W., and Jennings, H.M., *Cem. Concr. Res.* **2004**, *34*, 1499-1519.
59. Taddei, P., Tinti, A., Gandolfi, M.G., Rossi, P.L., and Prati, C., *J. Raman Spectros.* **2009**, *40*, 1858-1866.
60. Wu, J., Zhu, Y.-J., and Chen, F., *Small* **2013**, *9*, 2911-2925.
61. Wu, J., Zhu, Y.-J., Chen, F., Zhao, X.Y., Zhao, J., and Qi, C., *Dalton Trans.* **2013**, *42*, 7032-7040.
62. Fan, Y., Huang, S.S., Jiang, J.H., Li, G.G., Yang, P.P., Lian, H.Z., Cheng, Z.Y., and Lin, J., *J. Colloid Interf. Sci.* **2011**, *357*, 280-285.

63. Kang, X.J., Huang, S.S., Yang, P.P., Ma, P.A., Yang, D.M., and Lin, J., *Dalton Trans.* **2011**, 40, 1873-1879.
64. Bunker, G., *Introduction to XAFS: a practical guide to X-ray absorption fine structure spectroscopy.* **2010**: Cambridge University Press.
65. Newville, M., *Rev. Mineral. Geochem.* **2014**, 78, 33-74.
66. Hubbell, J.H. and Seltzer, S.M., *Tables of X-ray mass attenuation coefficients and mass energy-absorption coefficients 1 keV to 20 MeV for elements Z= 1 to 92 and 48 additional substances of dosimetric interest.* **1995**, National Inst. of Standards and Technology-PL.
67. Newville, M., *Fundamentals of XAFS. Consortium for Advanced Radiation Sources.* **2004**: University of Chicago.
68. Henderson, G. and Baker, D.R., *Synchrotron radiation: earth, environmental and materials sciences applications.* **2002**: Mineralogical Association of Canada.
69. De Groot, F. and Kotani, A., *Core level spectroscopy of solids.* **2008**: CRC Press.
70. De Groot, F., *Chem. Rev.* **2001**, 101, 1779-1808.
71. Willmott, P., *An introduction to synchrotron radiation: techniques and applications.* **2011**: Wiley.
72. Stöhr, J., *NEXAFS spectroscopy.* **1992**: Springer Science & Business Media.
73. Naftel, S.J., Sham, T.-K., Yiu, Y.M., and Yates, B.W., *J. Synchrotron Radiat.* **2001**, 8, 255-257.
74. Winick, H., *Synchrotron radiation sources: a primer.* **1994**: World Scientific.
75. Sham, T.-K. and Rivers, M.L., *Rev. Mineral. Geochem.* **2002**, 49, 117-147.

Chapter 2

2 Experimental Facilities and Methodologies

2.1 Experimental Facilities

2.1.1 Shanghai Institute of Ceramics

Shanghai Institute of Ceramics of the Chinese Academy of Sciences (SICCAS) which locates in Shanghai, China, was founded in 1959 under Chinese Academy of Sciences (CAS), while the history of SICCAS can be dated back to 1928 when the Engineering Institute of the National Central Academy was founded. Its main research areas are focused on high performance ceramics and superfine microstructures, structural ceramics and composites, inorganic functional materials and devices *etc.* So far, SICCAS has won 49 national-level awards, applied 650 patents [1]. In this thesis, all the samples preparations and parts of characterizations (such as XRD, FTIR *etc.*) are conducted in SICCAS under the supervision and support of our collaborator Prof. Ying-Jie Zhu.

2.1.2 Canadian Light Source

Canadian Light Source (CLS) which is a third generation synchrotron light source is located at the University of Saskatchewan, Saskatoon, SK, Canada. It is assembled by a 250 MeV electron linear accelerator (LINAC), a booster ring to increase the electron beam energy to 2.9 GeV, and the main storage ring which operates at the energy of 2.9 GeV and the current of 500 mA. The radio frequency (RF) cavity which operates at 500 MHz is installed to restore the electrons energy loss [2]. Figure 2-1 shows the schematic layout of the CLS beamlines. Currently 14 operating beamlines which provide photon energy range from Far IR to hard X-ray are designed to meet specific experimental techniques. In this thesis, three beamlines, Spherical Grating Monochromator (SGM) beamline, Soft X-ray Spectromicroscopy (SM) beamline and Soft X-ray Microcharacterization Beamline (SXRMB) are used for XANES and STXM experiments.

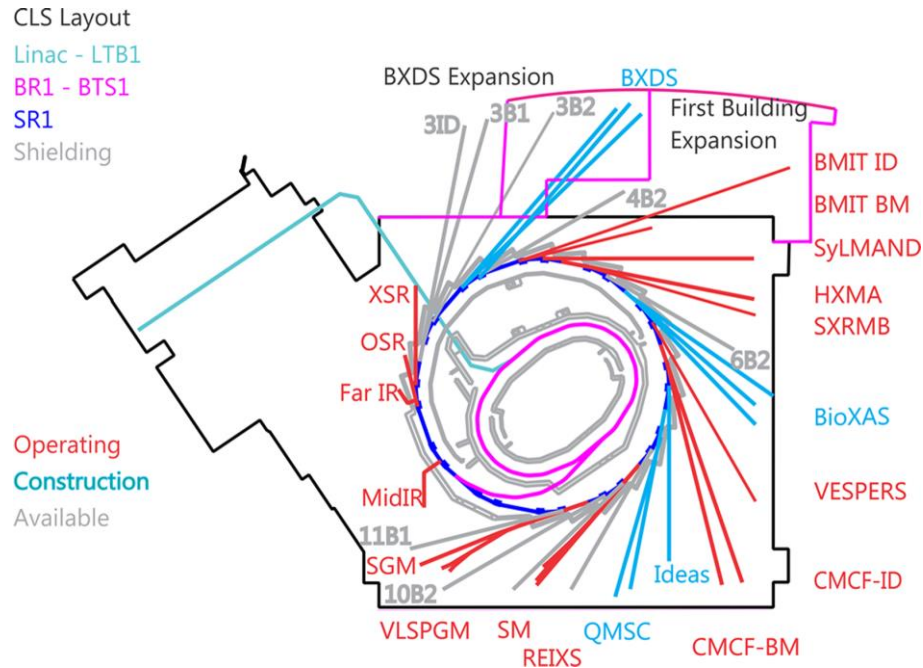


Figure 2-1 Schematic layout of the CLS beamlines (courtesy of Canadian Light Source Inc.) [3].

2.2 Beamlines

2.2.1 Spherical Grating Monochromator (SGM) Beamline

The SGM beamline (11ID-1) at CLS is an undulator based beamline, which covers the energy range from 250 eV-2000 eV. It is a dragon-shape beamline which is based on Chen's design [4], and its layout is shown in Figure 2-2. Three gratings are available to choose for the desired energy range: low energy grating (LEG): 250-700 eV, medium energy grating (MEG): 450-1250 eV and high energy grating (HEG): 740-2000 eV. The energy resolution ($E/\Delta E$) is greater than 5000 at energy below 1500 eV with spot size of $1000 \mu\text{m} \times 100 \mu\text{m}$ (Horizontal x Vertical). The beamline flux (normalized to 100 mA) is greater than 10^{12} at 250 eV and exceeds 10^{11} up to 1900 eV [5]. The beamline contains two endstations, noted as the EA₁ and EA₂, respectively. EA₁ is designed for photoemission studies, and EA₂ is for X-ray absorption measurement. All the XAFS experiments at SGM beamline in this thesis are conducted in endstation 2 (EA₂).

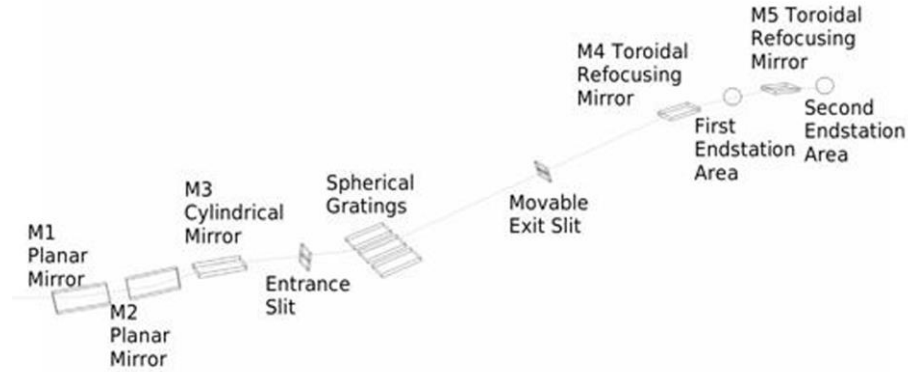


Figure 2-2 Layout of SGM beamline at CLS [6].

The SGM operates on the principle of grating diffraction,

$$n\lambda = d(\sin \alpha + \sin \beta) \quad (2 - 1)$$

$$d = \frac{W}{N} \quad (2 - 2)$$

where n is the order of the diffraction; α and β are the incidence and diffraction angles, respectively; d is the distance between the grating lines; W is the ruled width and N is the number of grating lines. Hence, the incident non-monochromatic light hits the grating at a grazing angle (α), and different energy gets diffracted at different angles (β), and X-ray photon energy is selected by rotation of the grating monochromator in order to make the exit beam to a fixed angle (Figure 2-3(a)). This beamline is well suited for the XANES spectroscopy of low Z element K-edges, such as carbon, nitrogen, oxygen, and the L-edge of the first row (3d) transition metals.

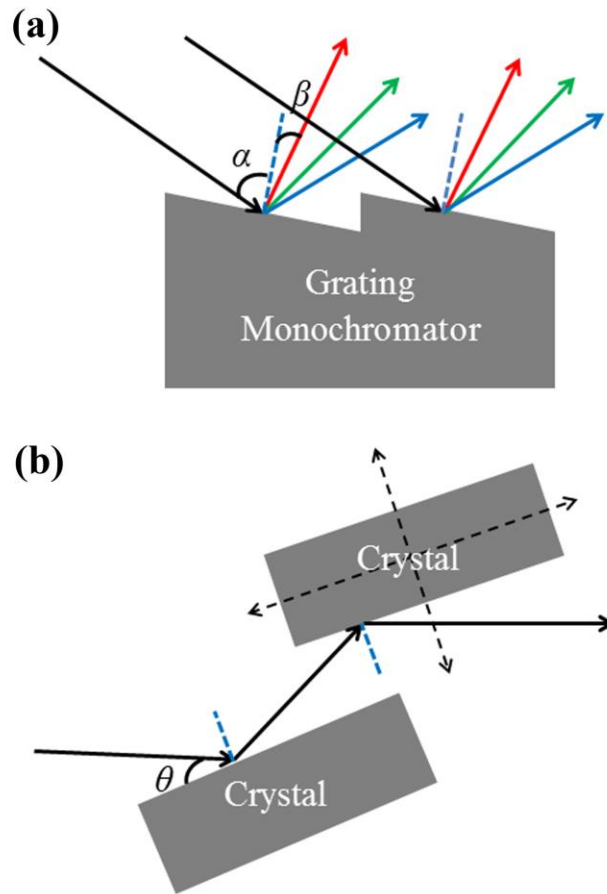


Figure 2-3 Schematic illustration of (a) plane grating monochromator and (b) double crystal monochromator (DCM).

2.2.2 Soft X-ray Microcharacterization Beamline (SXRMB)

The SXRMB (06B1-1) is a bending magnet based beamline, with an energy range from 1.7 to 10 keV and the spot size (Horizontal vs. Vertical) of $300 \mu\text{m} \times 300 \mu\text{m}$ (Figure 2-4).

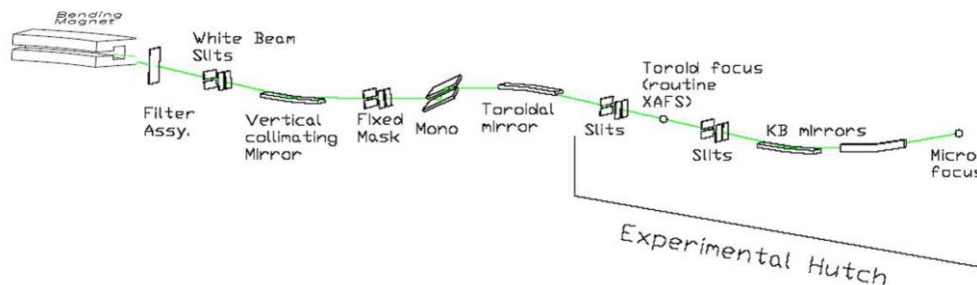


Figure 2-4 Layout of SXRMB at CLS [7].

The energy selection is based on Bragg's law by using double-crystal monochromators (DCM).

$$n\lambda = 2d \sin \theta \quad (2 - 3)$$

where n is the order of the diffraction; λ is the wavelength of the light; θ is the scattering angle; d is the lattice spacing of a crystal, which is determined by the crystal plane (Miller index (h, l, k)) (Equation 2-4).

$$d = \frac{1}{\sqrt{h^2 + k^2 + l^2}} \quad (2 - 4)$$

Two same perfect crystals are installed parallel to each other, and there are two sets of crystals equipped in SXRMB (Figure 2-3(b)): InSb (111) crystals are used for photon energy below 3.7 keV; and Si (111) crystals are used for energy up to 10 keV. The energy is selected by rotating and translating of both crystals to keep the outgoing beam is at a fixed angle. The energy resolutions ($E/\Delta E$) of two sets of crystals are different: InSb(111) has a resolution around 3000; while Si(111) has a resolution of 10,000 [8]. SXRMB is ideal for the XANES of the K-edge of many elements, specifically Si, P and Ca K-edge in this research; and L-edge and M-edge of the 4d and 5d transition metals.

2.2.3 Soft X-ray Spectromicroscopy (SM) Beamline

The SM beamline (10ID-1) is a spectromicroscopy beamline based on a collimated plane grating monochromator optimized for 130-2500 eV range and the normal spectral resolution ($E/\Delta E$) is 3000 (can be higher than 10,000) (Figure 2-5). Similar to the SGM

beamline, it is split into two endstations: scanning transmission X-ray microscope (STXM) and roll-in X-ray photoemission electron microscopy (X-PEEM). This beamline covers C, N, O, Si, P, and Al K-edge and L-edges of all the 3d transition metals; hence it is essential for the biological, environmental science [9]. In this thesis, all the synchrotron experiments are conducted at the STXM endstation.



Figure 2-5 Layout of SM beamlines at CLS (courtesy of Canadian Light Source Inc.) [10].

In STXM endstation, a Fresnel zone plate is used to further focus monochromatic X-rays to a small spot size (~30 nm) (Figure 2-6). To generate an image, the specimen is raster-scanned in the focused X-ray under the control of computer. The transmitted photons are collected by X-ray detector behind the specimen. Micro-spectra are measured by holding the beam at the spot of interest on the sample while the photon energy is scanned.

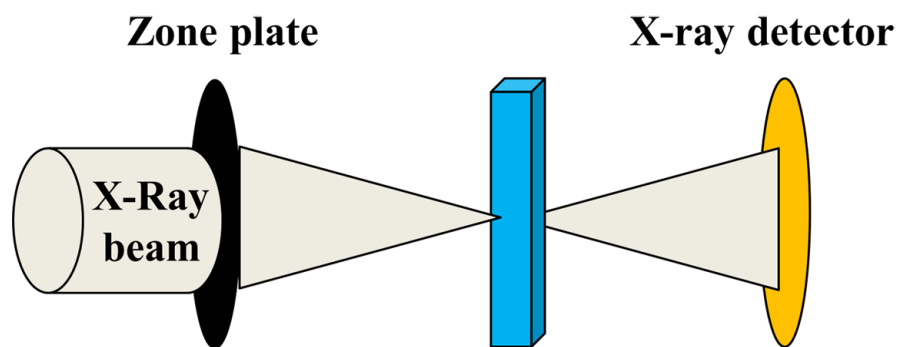


Figure 2-6 Schematic illustration of STXM.

For quantitative analysis, XANES spectra were obtained by converting the transmitted signal to optical density (OD) based on Beer-Lambert Law:

$$OD = -\ln\left(\frac{I_t}{I_0}\right) = \mu \cdot \rho \cdot t \quad (2-5)$$

where I_0 and I_t are the incident and transmitted X-ray photon flux (photons), respectively. μ is the energy dependent mass absorption coefficient (cm^2/g), ρ is the density (g/cm^3) of the material, and t is the sample thickness (nm). Then these spectra were converted to absolute linear absorbance scales (optical density per nm thickness sample). The elemental linear X-ray absorption, which neglects interactions such as bonding among the atoms, is calculated by aXis2000 using Equation (2-5) and (2-6):

$$\mu = \frac{N_A}{MM} \sum_i x_i \cdot \sigma_{ai} \quad (2 - 6)$$

where N_A is the Avogadro's number, MM is the molecular weight of a compound containing x_i atoms of type i , σ_{ai} is the atomic photo-absorption cross section (cm^2/atom) for type i atom. Then, the thickness was obtained by comparing the OD of each pixel in a STXM image and reference spectra [11].

2.3 Detection Modes

There are several detection modes to measure XAFS spectra, shown in Figure 2-7: transmission mode, total electron yield (TEY) mode and fluorescence yield (FLY) mode.

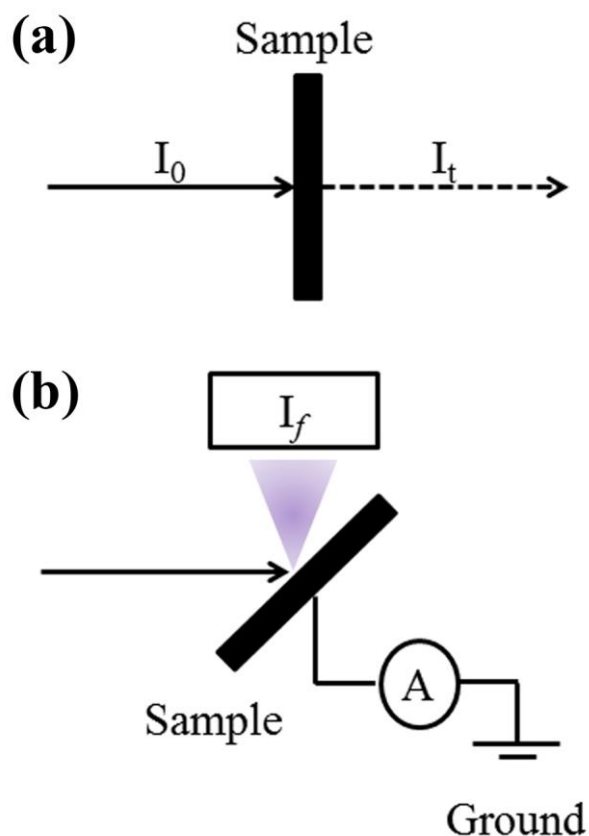


Figure 2-7 Illustration of XAFS detection modes: (a) transmission, (b) electron and X-ray fluorescence yield (TEY is detected by monitoring the sample neutralization current).

In transmission mode measurement, the intensities of the incident and transmitted X-rays are typically measured using ionization chambers which are filled with N_2 gas before and after the sample, respectively, and the absorption coefficient as a function of excitation energy, $\mu(E)$ is calculated directly from the ratio of I_0 to I_t using Beer's Law (See Equation 1-1). However, the thickness of sample cannot be too thick; otherwise all the photons will be adsorbed by the samples themselves, and concentration of element of interest cannot be too low (must be larger than 10% wt.), or the absorption is not constant throughout the sample. Thus transmission mode is suitable for the measurement of uniform samples which can be made into thin films (such as metal foils or pure minerals) [12].

If the samples cannot be made thin enough for transmission, as is often the case for low Z elements or the element concentration is too low, electron or fluorescence yields are alternative preferred detection modes for measuring XAFS. As mentioned in Section 1.2.2 of Chapter 1, several de-excitation processes (Auger electron process, secondary electron process and X-ray fluorescence process) take place simultaneously in order to fill the electron core-hole. TEY measures all the electrons ejected from the samples, including photoelectrons, Auger electrons and secondary electrons. It is detected by monitoring the sample neutralization current (to ground) and is proportional to the absorption coefficient [13]. It should be noted that TEY is a surface sensitive technique, usually detecting a sample surface with a few nm deep because the electron escape depth as a function of their energy is quite small [14].

In FY measurement, the absorption coefficient is also directly proportional to the intensity of X-ray fluorescence photons. There are several types of detectors that have been used for collecting X-ray fluorescence, such as multi-channel plates, solid state detectors and Si drift detectors. Compared with TEY, the attenuation length of the fluorescence X-ray is quite larger compared to that of an Auger or secondary electron, allowing the bulk of the sample to be probed. However, the self-absorption effect which suppresses or inverts the peaks in the spectra and makes FY nonlinear to the absorption coefficient is commonly seen at the soft X-ray region for low Z elements or the sample is too concentrated. It often occurs when the penetration depth of the X-rays varies strongly near an X-ray absorption edge. Recently, this effect can be partially overcome with the development of inversion partial fluorescence yield (IPFY) by using energy-dispersive fluorescence detector [15].

2.4 FEFF Simulations

FEFF is a computer code based on Real Space Multiple Scattering Theory-it allows the mathematical modeling of XANES and EXAFS. It originated from Prof. John Rehr's group at the University of Washington and has been upgraded to the present version-FEFF9 over a period of more than three decades. FEFF is commonly accepted in the literature. This theory can be derived from the real-space Green's function approach [16].

The amplitude of XAFS is given by Equation 2-7 (similar to the origin of EXAFS equation) [17]:

$$\chi(k) = S_0^2 \sum_R \frac{|f_{eff}(k)|}{kR^2} \sin(2kR + \Phi_k) e^{-2R/\lambda_k} e^{-2\sigma^2 k^2} \quad (2-7)$$

where S_0^2 is the amplitude reduction; k is the wave-vector of the photo-electron and f_{eff} is the effective scattering amplitude. The structural parameters include the atomic radius R . The dependence of the oscillatory structure on atomic radius and energy is reflected by the sine function. The decay of the wave due to the mean free path or core-hole life time of the photoelectron is described by the exponential term $e^{-2R/\lambda}$. The Debye-Waller factor is given by $e^{-2\sigma^2 k^2}$, which is due to thermal and static effects and is negligible in XANES when $\sigma^2 k^2 \leq 1$. This equation has been calculated including options in the FEFF code and is used to analyze XAFS data.

To set up a calculation, the positions of the atomic positions are needed to be input into the FEFF software. The clusters can be generated by the crystal parameters, including the space group, unit cell parameters, and the atomic coordination in the unit cell, *etc.* A FEFF calculation starts with two basic tasks: calculation of the potentials, followed by calculation of the scattering phase shifts. Using these phase shifts, scattering paths are found and their scattering amplitudes can be calculated. For XANES calculation, it can be approached by full multiple scattering. Finally, these scattering amplitudes are combined and generate the calculated XAFS spectra [18].

2.5 Linear Combination Fitting (LCF)

ATHENA is a graphical front end to Matt Newville's IFEFFIT library written entirely in the Perl programming language and using the PGPLOT graphical library for data display. It is designed to provide high quality analysis with a highly usable interface. It has many capabilities to process and plot large quantities of data, including energy calibration, k-, R- space transformation, peak fitting, *etc.*, among which, linear combination fitting (LCF) of standard to XANES data is one of the unique functions. This fitting can be done using normalized $\mu(E)$ spectra. This analysis could help interpret the kinetics of a series of

spectra measured during a chemical reaction. By fitting each intermediate spectrum as a linear combination of the different standard spectra, one can determine the species and the relative amount of standards in a heterogeneous sample. In order to have a best result, spectra normalization is very important, including background removal, energy threshold determination $\mu_0(E)$, and pre- and post-edge selection.

LCF is based on a non-linear, least-squares minimization procedure. After fitting, the fitting result parameters will be shown along with the R-factor, which should be smaller than 1. The R-factor reported in the text box is:

$$R = \frac{\text{Sum} ((data - fit)^2)}{\text{Sum} (data^2)} \quad (2 - 8)$$

where the sums are over the data points in the fitting region.

Interpretation of the statistical parameters requires the knowledge about the system which is measuring. The results of sample fractions must be meaningful in the context of any external knowledge about the system [19].

2.6 Other Characterization Techniques

2.6.1 Brunauer-Emmett-Teller (BET) Theory

This theory was first established in 1938 [20], and so far it has been widely used to determine the specific surface areas of materials. It uses the adsorption of chemically inert gases, such as helium, nitrogen, to measure the total surface area contained in or on micropores, mesopores, macropores and flat surfaces. The BET equation can be expressed as

$$\frac{1}{v[(p_0/p) - 1]} = \frac{c - 1}{v_m} \frac{p}{p_0} + \frac{1}{v_m c} \quad (2 - 9)$$

where p and p_0 are the equilibrium and saturation pressures of the gas, respectively; v is the volume of the adsorbed gas; v_m is the volume of gas adsorbed when the entire adsorbent surface is covered with a complete unimolecular layer; c is the constant. Hence,

Equation 2-9 can be plotted as a straight line (y-axis: $1/v[(p_0/p)-1]$ and x-axis: p/p_0). Thus, v_m and c can be calculated based the linear relationship and surface area of the solid can be calculated based on the value of v_m :

$$S = \frac{v_m N \sigma}{V} \quad (2 - 10)$$

where V is the molar volume of the gas, N is the Avogadro number and σ the area covered by one layer gas molecules [21].

2.6.2 Thermalgravimetric Analysis (TGA)

TGA is a thermal analysis method in which changes of materials mass are measured as a function of increasing temperature (at a constant heating rate). It can provide many physical and chemical phenomena of samples, such as vaporization, adsorption, dehydration, decomposition *etc.* [22]. It can be applied into measurement of weight of organic component; determine the purity or compositions of minerals; and some kinetic reactions involving weight loss. There are several features in the TGA curve:

1. The horizontal or plateau portion of the curve indicates the constant weight.
2. The curved portion means the weight loss; the steepness of the curve indicates the rate of weight loss
3. An inflection (minimum of dw/dt , but not zero) may imply an intermediate compound formation.

A TGA instrument consists of a sample pan that is supported by a precision balance, and a furnace is heated during the experiment. The mass of the sample is monitored during the experiment. In this thesis, TGA was utilized to compare the weight loss before and after drug loading to calculate the drug loading capacities in CSH drug carriers.

2.6.3 Inductively Coupled Plasma Optical Emission Spectrometry (ICP-OES) Analysis

ICP-OES is an analytical technique used for the detection of trace elements. It is based on the spontaneous emission of photons from atoms or ions that have been excited in a radio frequency discharge. Inductively coupled plasma (ICP) has a temperature of approximately 10,000 K, so the aerosol which is converted from the sample, is quickly vaporized. Liquid and gas samples can be injected into the plasma directly, while solid samples require acid dissolution. Elements are easily liberated as free atoms in the gaseous phase and further excited by the plasma. The excess energy is going to be released by the emission of photons which have unique energies. Thus the wavelength of the photons can be used to identify the elements from which they originated. The total number of photons is directly proportional to the concentration of the originating element in the sample [23]. The number of elements that can be measured by ICP-OES is around 70, including alkaline and alkaline earth elements, rare earth elements, transition metals and some low *Z* elements (B, C, N, Si, P, Cl *etc.*). In this thesis, ICP-OES is used to determine the Ca, P, Si concentration during the CSH biomineralization upon ibuprofen (IBU) release in Chapter 6.

2.7 References

1. Hull, M., *Powder Metall.* **2006**, *49*, 203-205.
2. Dallin, L., Blomqvist, I., De Jong, M., Lowe, D., and Silzer, R. *Proceedings of the Particle Accelerator Conference* **2003**, *1*, 220-223.
3. http://www.lightsource.ca/beamlines/images/CLS_Experimental_Hall_2011.png.
4. Chen, C.T., *Nucl. Instrum. Meth. A* **1987**, *256*, 595-604.
5. <http://exshare.lightsource.ca/sgm/Pages/Beamline.aspx>.
6. Regier, T., Paulsen, J., Wright, G., Coulthard, I., Tan, K., Sham, T.-K., and Blyth, R.I.R., *AIP Conference Proceedings* **2007**, *879*, 473-476.

7. Hu, Y.F., Coulthard, I., Chevrier, D., Wright, G., Igarashi, R., Sitnikov, A., Yates, B.W., Hallin, E.L., Sham, T.-K., and Reininger, R., *AIP Conference Proceedings* **2010**, *1234*, 343-346.
8. <http://www.lightsource.ca/beamlines/sxrmb.php>.
9. Kaznatcheev, K.V., Karunakaran, C., Lanke, U.D., Urquhart, S.G., Obst, M., and Hitchcock, A.P., *Nucl. Instrum. Meth. A* **2007**, *582*, 96-99.
10. <http://exshare.lightsource.ca/sm/Pages/Beamline.aspx>.
11. Wang, Z., Wang, J., Sham, T.-K., and Yang, S., *J. Phys. Chem. C* **2012**, *116*, 10375-10381.
12. Newville, M., *Rev. Mineral. Geochem.* **2014**, *78*, 33-74.
13. Stöhr, J., *NEXAFS spectroscopy*. **1992**: Springer Science & Business Media.
14. Tanuma, S., Powell, C.J., and Penn, D.R., *Surf. Interf. Anal.* **2011**, *43*, 689-713.
15. Achkar, A.J., Regier, T.Z., Wadati, H., Kim, Y.J., Zhang, H., and Hawthorn, D.G., *Phys. Rev. B* **2011**, *83*, 081106.
16. Rehr, J.J. and Albers, R.C., *Rev. Mod. Phys.* **2000**, *72*, 621-654.
17. Rehr, J.J., Kas, J.J., Prange, M.P., Sorini, A.P., Takimoto, Y., and Vila, F., *C. R. Phys.* **2009**, *10*, 548-559.
18. http://www.feffproject.org/feff/Docs/feff9/feff90/feff90_users_guide.pdf.
19. Ravel, B., *ATHENA user's guide*
<http://cars9.uchicago.edu/~ravel/software/doc/Athena/html/athena.pdf>.
20. Brunauer, S., Emmett, P.H., and Teller, E., *J. Am. Chem. Soc.* **1938**, *60*, 309-319.
21. Leofanti, G., Padovan, M., Tozzola, G., and Venturelli, B., *Catal. Today* **1998**, *41*, 207-219.

22. Coats, A.W. and Redfern, J.P., *Analyst* **1963**, 88, 906-924.
23. Hou, X. and Jones, B.T., *Inductively Coupled Plasma-Optical Emission Spectrometry, Encyclopedia of Analytical Chemistry* **2000**, 9468–9485, John Wiley & Sons, Ltd.

Chapter 3

3 Drug-Carrier Interaction - Tracking the Local Structure of Calcium Silicate upon Ibuprofen Loading with X-ray Absorption Near Edge Structure (XANES)

3.1 Introduction

Ceramic devices are generally suitable candidates for biological and medical applications due to their compatibility with human tissues [1]. For example, calcium phosphate [2], hydroxyapatite [3], alumina [4], zirconia [5] *etc.* have been studied extensively and these studies have made significant contributions to bone tissue engineering and drug delivery. Although calcium silicate hydrates (CSH) were just regarded formerly as simple components of glass, they have been shown recently to be excellent candidates for the application of bone regeneration due to their good bioactivity, biocompatibility and biodegradability [6-9].

Despite the interest, most of the researches concentrate on the development of new types of drug carriers, innovative synthesis methods [3, 6, 10] and drug release kinetics [10, 11], little is known or have researches been carried out on the interactions between drug molecules and drug carriers on the molecular level. Undoubtedly, the interactions between drug molecules and their carriers are fundamental and valuable for drug carriers engineering optimizations. Using differential scanning calorimetry (DSC), powder X-ray diffraction (PXRD) and Fourier transform infrared spectroscopy (FTIR), Madieh *et al.* [12] reported that silanol groups on the surface could interact with functional groups of drug molecules via hydrogen bonding, and Wu *et al.* [10, 13] noted that calcium ions could possibly interact with the carboxyl groups of ibuprofen molecules.

* A version of this chapter has been published in *Phys. Chem. Chem. Phys.* **2013**, *15*, 15033-15040. Reproduced by permission of the PCCP Owner Societies. DOI:

[10.1039/C3CP50699A](https://doi.org/10.1039/C3CP50699A)

XANES is now a well-established element and chemical specific technique and can also be modelled with theory. Thus, we can track the changes of the electronic structure of the drug delivery materials before, during and after drug loading by investigating the local environment of the atoms of interest using XANES, such as Si and Ca in this case, and gain a more comprehensive understanding of how drug molecules interact with different functional groups in drug carriers and their implications on local structure of the carrier framework and their drug loading capacities. In this chapter, we report the XANES study at both the Ca and Si K-edge of the interactions between a model drug, ibuprofen (IBU) and calcium silicate hydrate carriers with different morphologies.

3.2 Experimental

3.2.1 Synthesis of Materials

Calcium silicate hydrate (CSH) mesoporous microspheres formed by self-assembly of nanosheets were prepared according to a sonochemical method [10]. Briefly, 5 mL of a 4 M NaOH aqueous solution and 2.0 mL of tetraethyl orthosilicate (TEOS) were added into 500 mL of a 0.03 M $\text{Ca}(\text{NO}_3)_2$ aqueous solution under magnetic stirring at room temperature. The resulting mixture was ultrasonically irradiated for 1 h under ambient conditions with a high-intensity ultrasonic probe with the power of 200 W (Ti-horn, 27 kHz, Hangzhou Success, China) immersed directly in the solution.

The CSH nanosheets were synthesized using a controlled precipitation reaction between calcium salt and silicate salt [13]. 3.0 mmol $\text{Na}_2\text{SiO}_3 \cdot 9\text{H}_2\text{O}$ was dissolved in 50 mL deionized water, into which 5.0 mL of a 0.6 M $\text{Ca}(\text{NO}_3)_2$ aqueous solution was injected at a constant addition rate of $2.5 \text{ mL} \cdot \text{h}^{-1}$ at room temperature under magnetic stirring. The resulting reaction system was aged at room temperature under stirring for 3 h. Then the product was centrifuged, washed with deionized water and absolute ethanol several times, and dried at 60°C . The amorphous CSH nanoparticles were synthesized by using a rapid precipitation reaction between calcium salt and silicate salt.

For the preparation of the anhydrous calcium silicate (CS) counterparts, the as-synthesized CSH powder was heated at a rate of $2^\circ\text{C}/\text{min}$ from room temperature to 700°C

°C, and maintained at this temperature for 2 h, then cooled at the same rate to room temperature.

3.2.2 IBU Drug Loading

The carrier (0.67 g) was added to 50 mL IBU hexane solution ($\sim 40 \text{ mg mL}^{-1}$) in a flask at room temperature. The flask was immediately sealed to prevent hexane from evaporation, and the mixture was treated by ultrasound for several minutes. Then the flask was oscillated at a constant rate of 160 rpm at 37 °C for 24 h. The product was separated by centrifugation, washed with hexane once, and dried at 60 °C.

3.2.3 BET Specific Surface Areas (SSAs) Measurements

The specific surface areas (SSAs) of CSH carriers before and after IBU loading were measured with a surface area and porosimetry instrument (Gold APP, V-Sorb 2800P).

3.2.4 UV-Vis Experiments

The IBU hexane solutions before and after the IBU loading with different carriers were analysed by UV-Vis absorption at the wavelength of 263 nm. The UV-Vis absorption spectra were performed on a spectrophotometer (Techcomp, UV2300).

3.2.5 Fourier Transform Infrared (FTIR) Measurements

Fourier transform infrared (FTIR) spectra were recorded using the KBr technique on a FTIR spectrometer (FTIR-7600, Lambda, Australia).

3.2.6 *In Vitro* IBU Drug Release

The as-prepared IBU-loaded carriers were compacted into disks (0.1 g each, $d = 13 \text{ mm}$) at a pressure of 3 MPa. Then each disk was immersed in 200 mL phosphate buffered saline (PBS) at 37 °C under shaking at a constant rate of 140 rpm. The IBU release medium (2.0 mL) was extracted for UV-Vis analysis at the wavelength of 263 nm at given time intervals and replaced with the same volume of fresh PBS which was preheated to 37 °C.

3.2.7 X-ray Absorption Near Edge Spectroscopy (XANES) Experiments

XANES measurements were conducted at the Canadian Light Source using the Soft X-ray Microcharacterization Beamline (SXRMB), which is equipped with a double crystal monochromator with two sets of interchangeable crystals operating with an energy range of 1.7 to 10 keV. The InSb (111) crystals were used for the Si K-edge XANES measurements while the Si (111) was used for the Ca K-edge XANES. The detection modes are total electron yield (TEY) and X-ray fluorescence yield (FLY), tracking surface and bulk sensitivity, respectively. Herein we only use TEY XANES for the discussions because both TEY and FLY are the same since the specimens are homogeneous and optically thin and FLY shows no detectable thickness effects.

3.2.8 Real Space Multiple Scattering Theory - Calculation by FEFF9

The crystal structure of $\text{Ca}_3\text{Si}_2\text{O}_7$ is modelled to have the structure of rankinite [14], and have space group symmetry of $P_{21/a}$ with lattice constants of $a=10.557\text{\AA}$, $b=8.885\text{\AA}$, and $c=7.858\text{\AA}$, $\alpha=90^\circ$, $\beta=119.586^\circ$, $\gamma=90^\circ$. The locations of the atoms in $\text{Ca}_3\text{Si}_2\text{O}_7$ are shown in Table 3-1.

Table 3-1 Atomic coordinates of rankinite.

Site	x	y	z
Ca ₁	0.0071	0.0552	0.2893
Ca ₂	0.1677	0.5745	0.2083
Ca ₃	0.3403	0.9034	0.2839
Si ₁	0.2948	0.2357	0.4314
Si ₂	0.0903	0.2145	0.9843
O ₁	0.3579	0.4038	0.4229
O ₂	0.1782	0.2344	0.5033
O ₃	0.4105	0.1016	0.5523
O ₄	0.2007	0.1629	0.2120
O ₅	0.0970	0.3857	0.9810
O ₆	0.1451	0.1487	0.8437
O ₇	0.9299	0.1536	0.9394

The XANES (X-ray Absorption Near Edge Structure) spectra of the cluster of the $\text{Ca}_3\text{Si}_2\text{O}_7$ compounds with this crystal models have been calculated by the multiple

scattering theory using the FEFF9 code [15]. This theory is based on the real-space Green's function approach [16].

3.3 Results and Discussion

3.3.1 Morphologies of Calcium Silicate Samples

All calcium silicate samples were characterized by transmission electron microscopy (TEM, Philips CM-10 Transmission Electron Microscope) at the Biotron, University of Western Ontario (Figure 3-1). Here, only the TEM images of amorphous CSH (Figure 3-1(a)), CSH nanosheets (Figure 3-1(b)) and CSH mesoporous microspheres (Figure 3-1(c)) are shown because no significant differences either from anhydrous samples or from the samples with IBU can be observed.

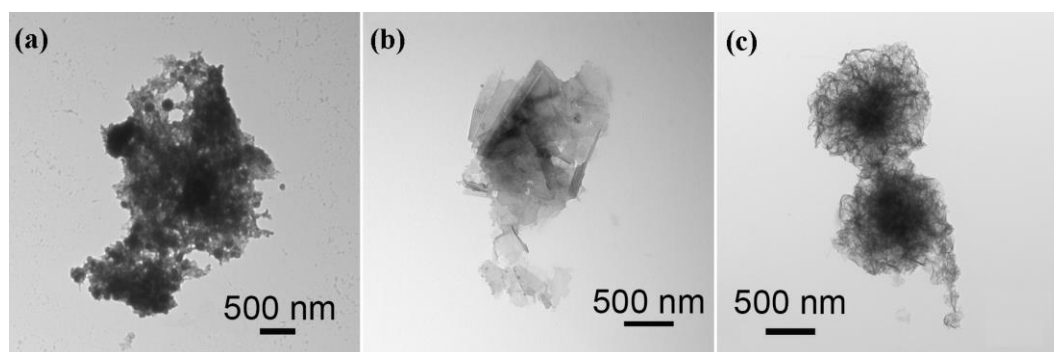


Figure 3-1 Morphologies of calcium silicate hydrate: (a) amorphous CSH, (b) CSH nanosheets, (c) CSH mesoporous microspheres.

3.3.2 Ibuprofen Loading in CSH Drug Carriers

The UV-Vis absorption spectra of the hexane solution containing ibuprofen before and after ibuprofen loading in different carriers are shown in Figure 3-2. One can see that the absorption spectra of ibuprofen in hexane solution show the characteristic absorption peaks, for example, at 263 nm, which are similar to those reported in the literature [17]. The significant decrease in the absorbance after the drug loading indicates that the drug has been loaded into the carriers with a high drug loading capacity.

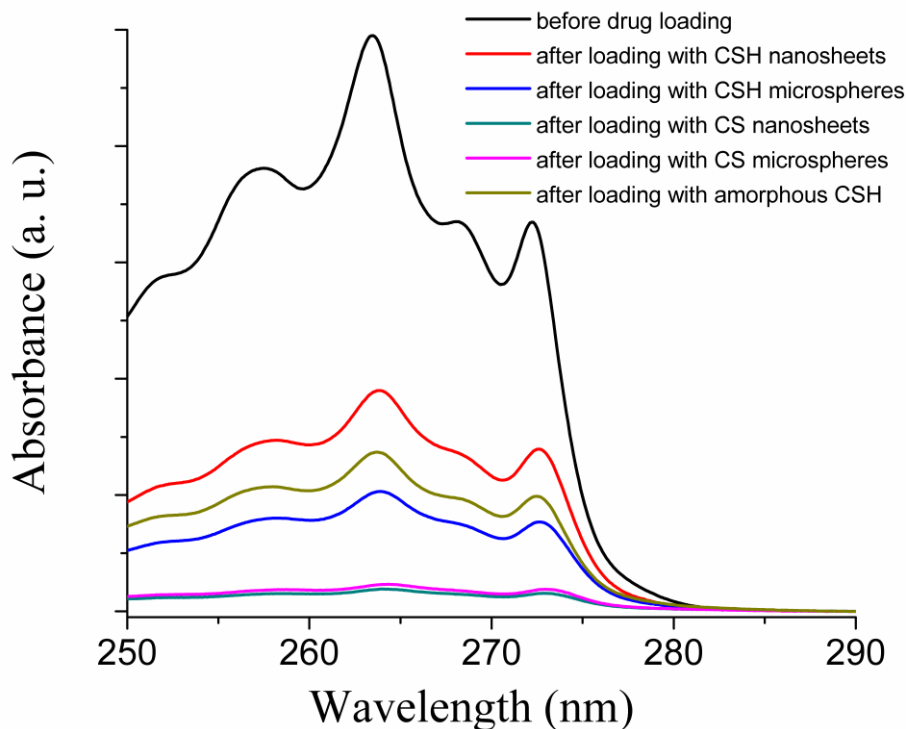


Figure 3-2 UV-Vis absorption spectra of the IBU hexane solution diluted 50 times before and after the IBU loading with different carriers.

To further illustrate that IBU has been loaded into CSH carriers successfully, the BET specific surface areas (SSAs) of the CSH carriers without and with the IBU loading are listed in Table 3-2. The SSA of CSH nanosheets is measured to be $462 \text{ m}^2/\text{g}$, which is ultrahigh for calcium silicate materials, and it is even higher than that of mesoporous wollastonite calcium silicate ($405 \text{ m}^2/\text{g}$) reported previously [18]. It can be seen that the SSAs of CSH carriers greatly decrease after the IBU drug loading, indicating that the drug IBU has been successfully loaded into the nanocarriers. The IBU drug loading capacities of the CSH nanocarriers, obtained from the UV-Vis absorption analysis, are also listed in Table 3-2. One can see that the IBU drug loading capacities of the CSH carriers are very high, which are usually higher than those reported in the literature [19-21]. The IBU drug loading capacities of the CSH carriers, expressed in the unit of mg/m^2 , are also presented in Table 3-2.

Table 3-2 BET specific surface areas (SSAs) of CSH carriers without and with IBU loading and the IBU loading capacities.

CSH carriers	SSA without IBU loading (m ² /g)	SSA with IBU loading (m ² /g) ^[a]	IBU loading capacity (g _{IBU} /g _{carrier}) ^[b]	IBU loading capacity (mg _{IBU} /m ² _{carrier})
CSH nanosheets	462	12	~1.7	~3.7
CSH microspheres	253	22	~2.2	~8.7
Amorphous CSH	107	17	~2.0	~18.7

^[a] It stands for the SSA of the CSH-IBU nanocarrier drug delivery system other than the single nanocarrier.

^[b] IBU loading capacity is obtained from the UV-Vis absorption analysis using the method of the standard concentration curve at the absorbance of 263 nm.

3.3.3 XANES Studies of the Interactions between CSH and IBU

In order to have a comprehensive image of the interactions between calcium, silicate ions and IBU on the molecular level, it is necessary to understand the crystal structure of calcium silicate hydrate drug carriers. According to the study of Wu *et al.* [10], the crystal structure of CSH mesoporous microspheres is rankinite (Ca₃Si₂O₇·6H₂O), and the FEFF XANES simulation is consistent with a rankinite structure. (Figure 3-3): the XANES spectra for all the specimens are similar to a rankinite structure. The rankinite structure has a layered structure, in which the silicate tetrahedra share oxygen atoms with Ca-O layer or neighboring bridge silicate tetrahedra. Hydrates can either adsorb on the surface or in the interlayer spaces.

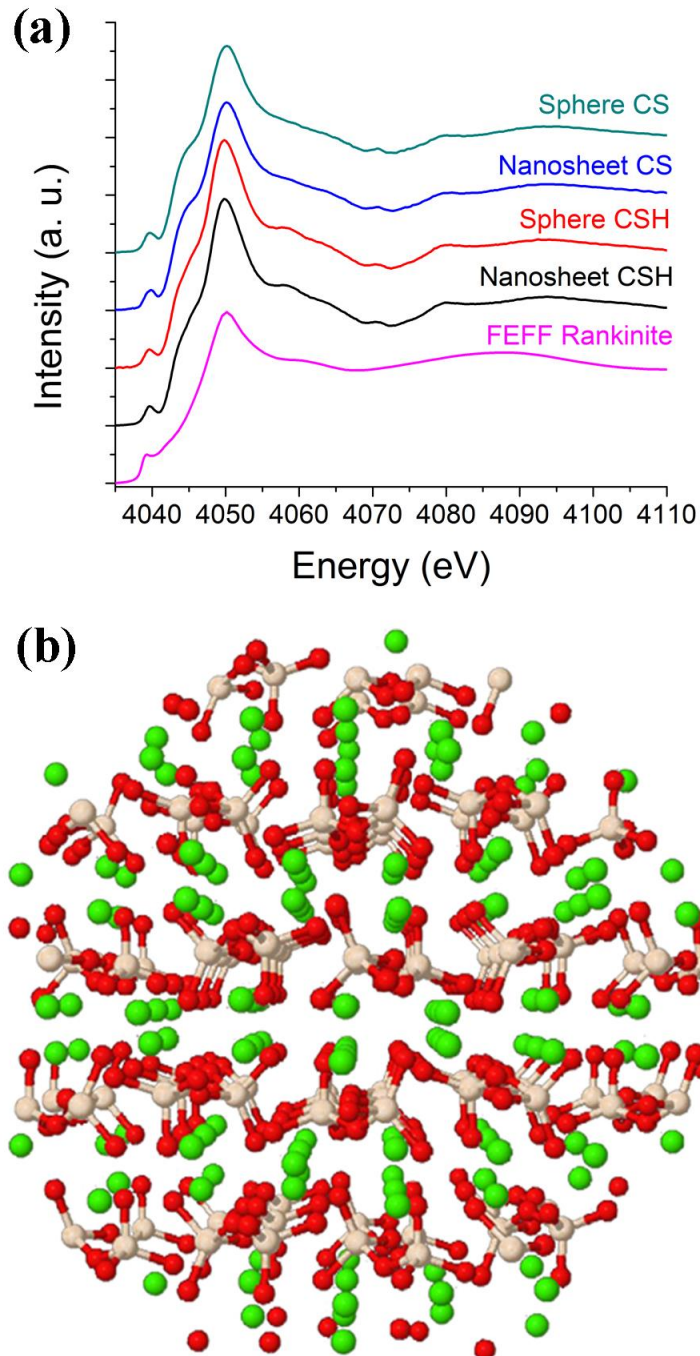


Figure 3-3 (a) TEY XANES spectra of calcium silicate hydrate and anhydrous calcium silicate carriers with different morphologies, comparison with FEFF calculation; (b) Crystal structure of rankinite simulated by FEFF (green, red and beige spheres stand for Ca, O and Si atoms, respectively).

Figure 3-4 shows the Ca K-edge XANES of carriers of calcium silicate hydrate and anhydrous calcium silicate with different morphologies, before (a) and after (b) IBU loading and a standard calcium silicate hydrate. CSH and CS henceforth denote calcium silicate with and without hydrate, respectively. From the XANES of the specimens before IBU loading, there are four discernible XANES features, labelled from A to D as the energy increases. The most intense peak (labelled C) is due to $1s \rightarrow np$ transition. This is the principal peak which follows the dipole transition selection rules. The first small feature at the pre-edge (labelled A) can be ascribed to $1s \rightarrow 3d$ transition, which is commonly observed in the K-edge spectra of the first row transition metals. Shoulder B is assigned to the $1s \rightarrow 4s$ transition. Although formally dipole forbidden, both A and B can still be observed due to hybridization of Ca 3d with ligand p-character states [22-24]. The shoulder after the main resonance (labelled D) is mainly from multiple scattering processes, it is very sensitive to the immediate surroundings of Ca.

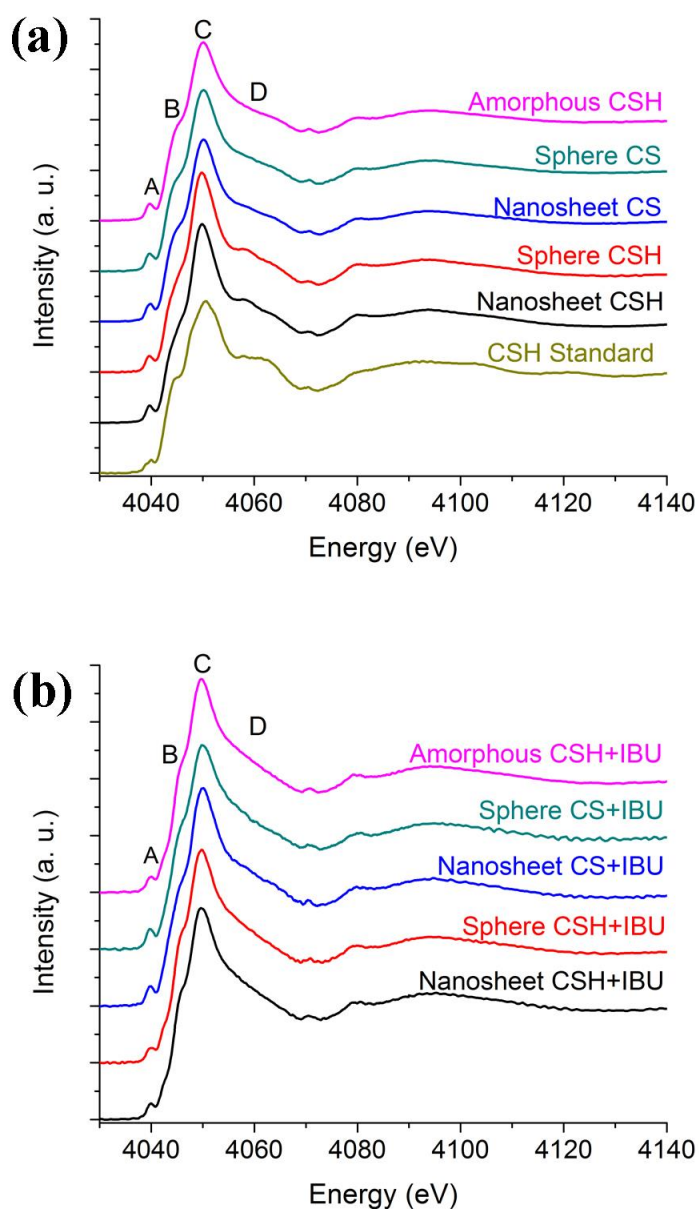


Figure 3-4 Ca K-edge XANES spectra of calcium silicate hydrate and anhydrous calcium silicate carriers with different morphologies, without (a) and with (b) loading of IBU.

The most discernible differences from XANES spectra can be observed from Figure 3-5 when we compare the drug carriers in different morphology with and without IBU individually. First of all, we assign feature D to be closely related to the hydrates in the

system because the feature D is not prominent from the anhydrous samples (Figure 3-4(a), except amorphous CSH, which is due to poor crystallinity). For the change of feature D in Figure 3-5, which smear out in all the spectra after IBU loading, the explanation is given as follows. The loading of IBU replaced the hydrates on the surface or in the interlayer, changes the local ordering and then alters the multiple scattering pathways.

Besides, close examination of the data for the IBU-loaded drug delivery system reveals a subtle though clearly noticeable change in the edge jump region (labelled B) which becomes more apparent in the first derivative of the spectrum (Figure 3-5(b)). What is the most interesting is that, before drug loading (solid lines), there are only two peaks between 4040-4050 eV but three peaks appear after the drug is loaded (dash lines); which means the B resonance is now split into a doublet. Moreover, the change of feature D can be also observed in the derivative spectra of CSH samples between 4055-4060 eV, which also supports our previous discussion.

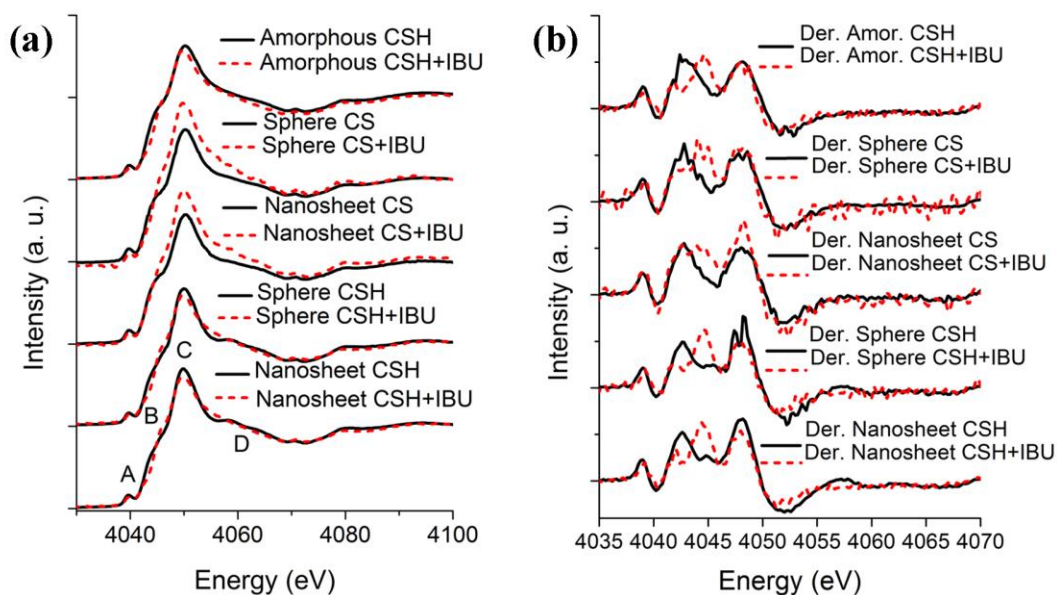
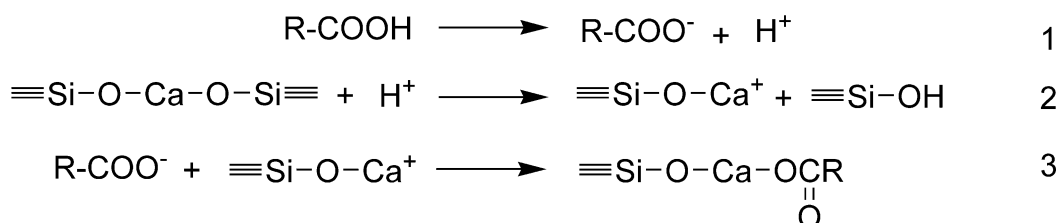


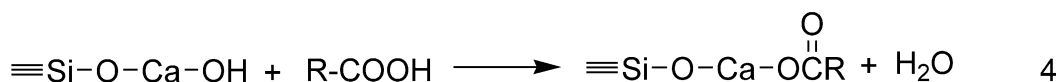
Figure 3-5 (a) TEY XANES spectra and (b) first derivative spectra of calcium silicate hydrate and anhydrous calcium silicate carriers with different morphologies, with and without loading of IBU.

The possible explanation for the change of feature B is the interaction between calcium ions and ibuprofen; the electrostatic bonding between Ca^{2+} and the carboxyl groups from the IBU drug molecules lowers the local symmetry. We propose that the following chemical reactions take place (Scheme 3-1).



Scheme 3-1 Possible interactions between calcium ions and IBU.

The H^+ ions which are provided by carboxyl groups will break up the calcium silicate structure [25]; forming silanol groups and releasing coordination deficient Ca ions simultaneously (Scheme 3-1, 1 and 2). Calcium ions then react with R-COO^- and generate carboxylate salt (Scheme 3-1, 3). The other possibility is that the Ca-OH groups which locate on the surface or interlayer sites [14, 26-28] react with carboxyl groups directly (Scheme 3-2).



Scheme 3-2 Possible interactions between calcium ions and IBU.

In either case, the local environment of Ca will somewhat similar to those in calcium acetate ($\text{Ca}(\text{Ac})_2$) after IBU is loaded. This notion is supported by the observation that drug-loaded CSH and CS carriers exhibit very similar Ca K-edge XANES as that of calcium acetate, shown in Figure 3-6. From Figure 3-6(a), all of the TEY XANES of drug-loaded calcium silicate samples are nearly identical to that of $\text{Ca}(\text{Ac})_2$ monohydrate except the shoulder D, which is from the hydrates in calcium acetate. From Figure 3-6(b), the derivative of CSH mesoporous microspheres with IBU (dash line) is almost the same as that of calcium acetate monohydrate (dot line) except the difference in 4055-4060 eV.

Both the observations suggest that there is a loss of hydrates during the IBU drug loading processes.

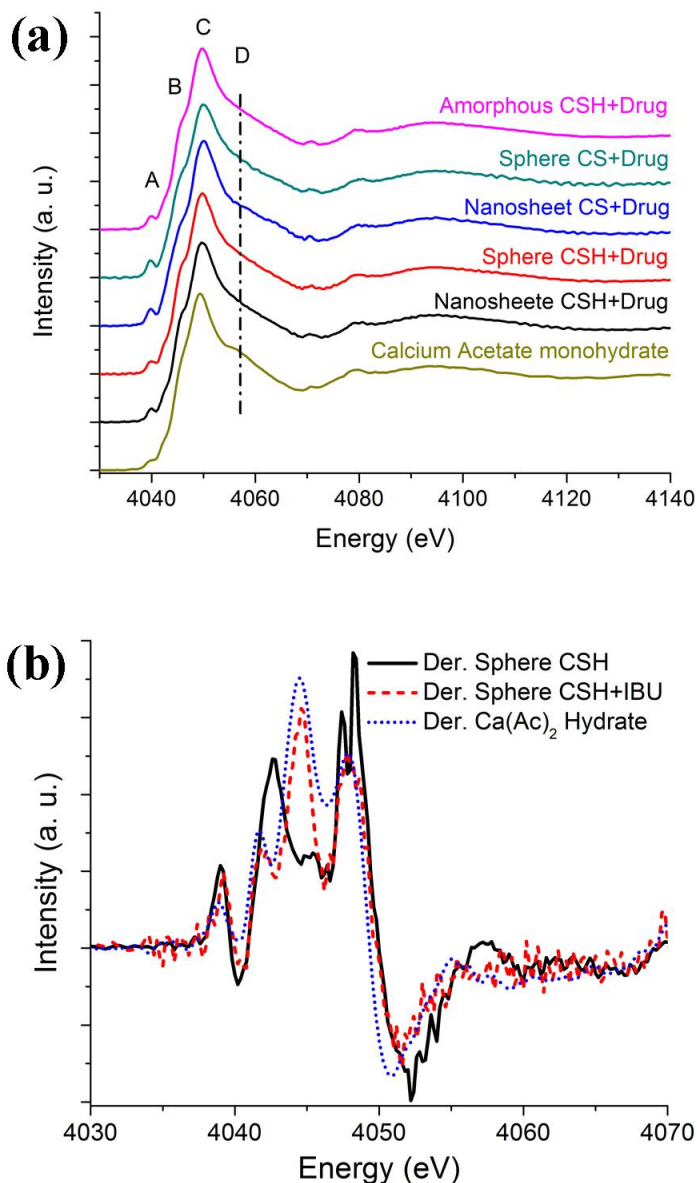


Figure 3-6 Comparison of drug-loaded CSH and CS carriers with calcium acetate monohydrate powder; (a) Ca K-edge XANES total electron yield (TEY) of CSH and CS carriers with IBU drug molecules, and (b) first derivative spectra of CSH mesoporous microspheres before and after IBU loading.

We now turn to the Si K-edge (Figure 3-7); all the spectra of the CSH carriers with different morphologies without IBU are almost identical. There is only one prominent peak (labelled A) which is identified as the Si 1s to 3p transition for silicon (IV) in a tetrahedral oxygen ligand environment [23, 29]. This peak however is very broad, which can be associated with chemical inhomogeneity owing to a distribution of Si (IV) sites in chemically slight different environments. The most amazing observation is that after the drug is loaded, a small feature (labelled B) emerges at ~2 eV below the main resonance which sharpens considerably as if the IBU loading induces “crystallization” (ordering).

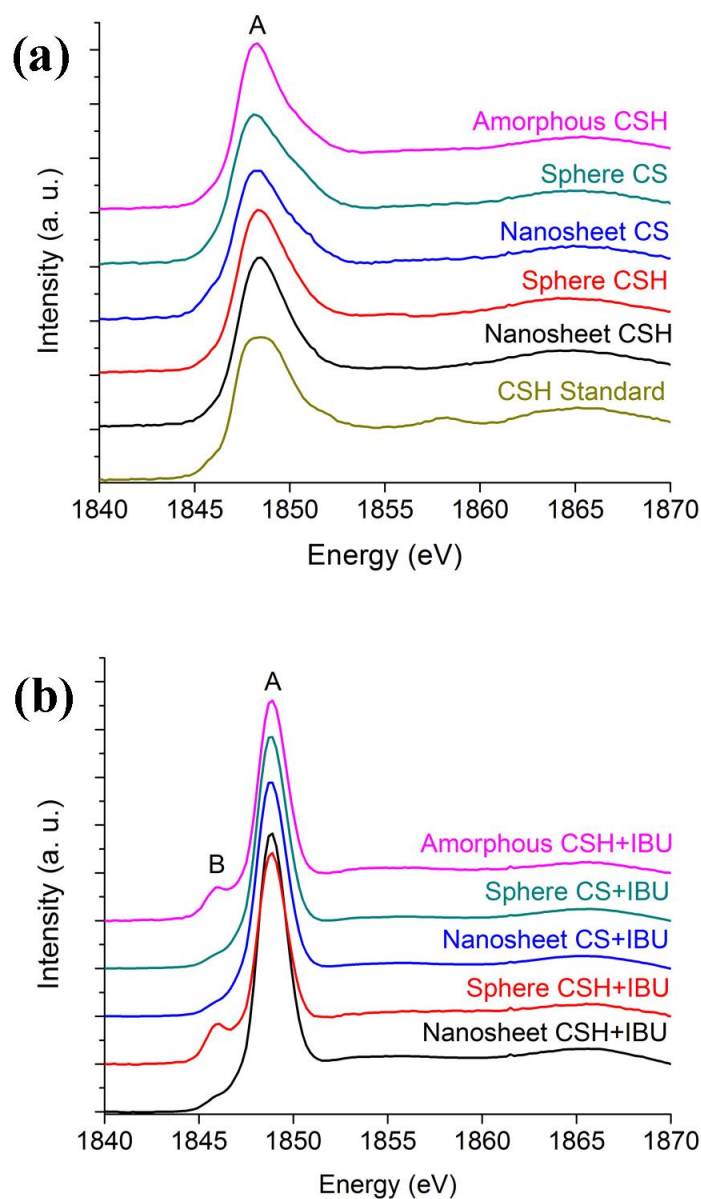


Figure 3-7 Si K-edge XANES total electron yield (TEY) spectra of calcium silicate hydrate and anhydrous calcium silicate nanocarriers with different morphologies, without (a) and with (b) IBU loading.

Interestingly, compared with Figure 3-7, the main resonance not only becomes sharper but also shifts to a higher energy (by ~ 0.5 eV) after IBU loading (Figure 3-8(a)). Besides, the peak B in the spectra of the drug loaded carriers with hydrates (CSH) has higher intensity (Dash lines in Figure 3-8(a₁), (a₃) and (a₂), (a₄)). Moreover, the intensity

of peak B for the mesoporous microsphere carriers is higher than that of nanosheet samples (Dash lines in Figure 3-8 (a₁), (a₂)). For the CS samples, although the presence of B is less apparent, we can still reveal their presence from the derivative spectra (Figure 3-8(b) vertical dash dot lines).

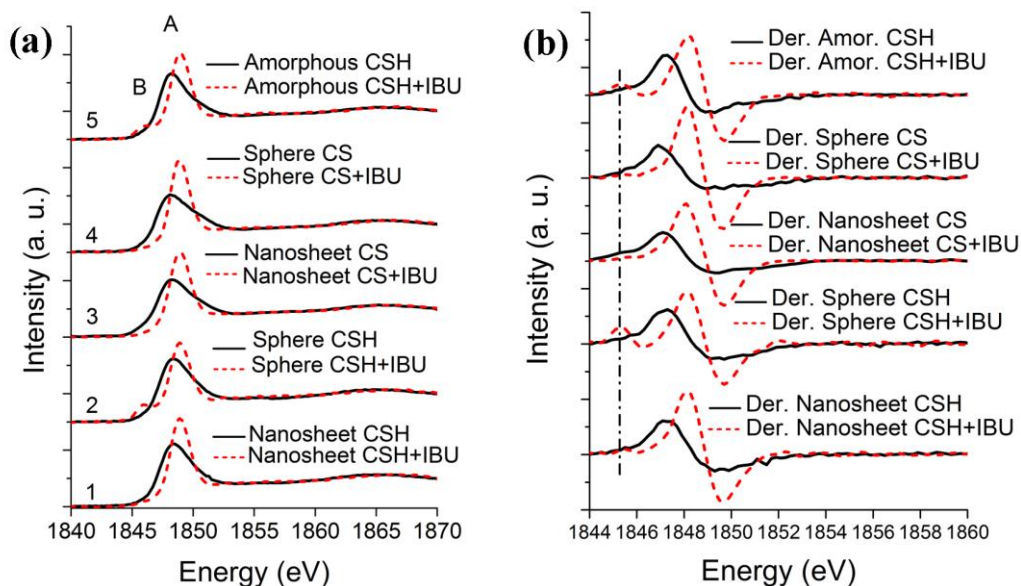


Figure 3-8 (a) Si K-edge XANES and (b) first derivative spectra of calcium silicate hydrate and anhydrous calcium silicate carriers with different morphologies, with and without IBU.

These observations suggest that the samples with hydrates form more silanol groups (Si-OH) on the material surface [18-21], where the IBU molecules attach to the drug carriers. This is why the spectra of drug carriers with hydrates have a more prominent peak B. The interaction is an esterification-like reaction (Scheme 3-3).



Scheme 3-3 Possible interaction between silanol groups and IBU.

Due to the presence of the alkyl groups, which are known to be excellent electron density donors, in the structure (Si-O-C bonds) [30] providing better shielding, and hence we can

observe a small peak B shifted to the lower photon energy, indicating the formation of Si-OOC-R groups. However, most of the Si atoms of calcium silicate in the bulk are still in a SiO_4 tetrahedral environment and after drug loading, most of the silanol groups on the surface probably have been reacted with carboxyl groups. As the result of this interaction, the crystallinity of the system improves and rest of the Si atoms find themselves in a more “regular” SiO_4 like environment. That is why the main resonance turns sharper and shifts to a higher energy (Figure 3-9).

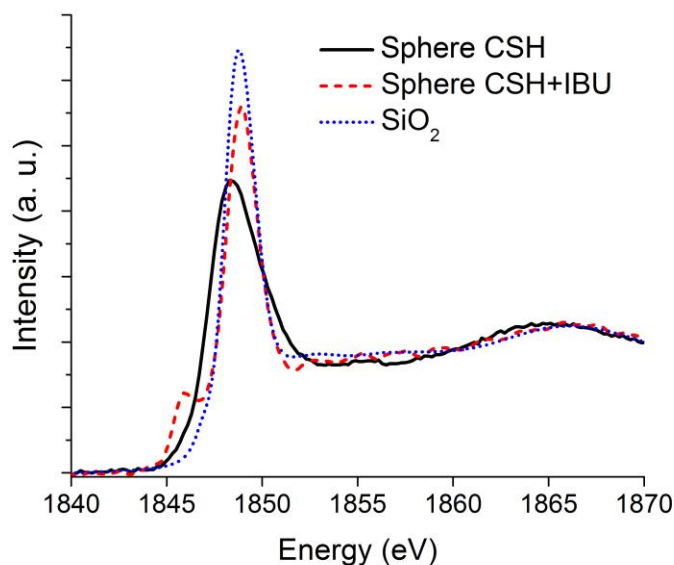


Figure 3-9 Si K-edge XANES total electron yield (TEY) spectra of calcium silicate hydrate mesoporous microspheres with and without IBU, compared with SiO_2 powder.

3.3.4 FTIR Spectroscopy of CSH Carriers Before and After IBU Loading

To further support the existence of the interaction between drug molecules and carriers, the FTIR spectra of the CSH carriers without and with the IBU loading are shown in Figure 3-10. For the carriers after IBU loading, the appearance of C–H, C=O and C–O stretching vibration peaks indicates that IBU has been loaded on the carriers. The blue shift of Si–O stretching vibration from 975 to 1083 cm^{-1} and the red shift of C=O

stretching vibration from 1724 to 1560 cm^{-1} indicate the chemical interactions between the $-\text{Si}-\text{O}-\text{Ca}-$ groups of the carrier and $-\text{COOH}$ groups of IBU drug molecules. However, almost no shift of the $\text{C}-\text{O}$ stretching vibration in IBU molecules suggests that the chemical surrounding of $\text{C}-\text{O}$ in the $-\text{COOH}$ group is little changed after the drug loading. Thus, it is inferred that there is a coordination reaction between the Ca (II) of the carriers and the $\text{C}=\text{O}$ group of IBU molecules during the drug loading process. The formation of $-\text{Si}-\text{O}-\text{Ca}\leftarrow\text{O}=\text{C}-\text{OH}$ can increase the polarity of the $\text{Si}-\text{O}$ group while reduce the polarity of the $\text{C}=\text{O}$ group, which results in the blue and red shifts in the FTIR spectra mentioned above.

For the carriers before IBU loading, the absorption at around 1630 cm^{-1} is assigned to the bending vibration of the adsorbed water. It can be seen that this bending vibration of $\text{H}-\text{O}-\text{H}$ disappears after the IBU loading, implying that there may be a replacement of hydrates during IBU loading processes. In the case of CSH nanosheets and CSH microspheres, the absorption at 3614 cm^{-1} appears after IBU loading, which is assigned to the stretching vibration of the $-\text{O}-\text{H}$ groups of IBU molecules, free from the hydrogen bonds (the IBU molecules in pure IBU crystals exist in the form of dimers due to hydrogen bonding between the $\text{O}-\text{H}$ groups) [31].

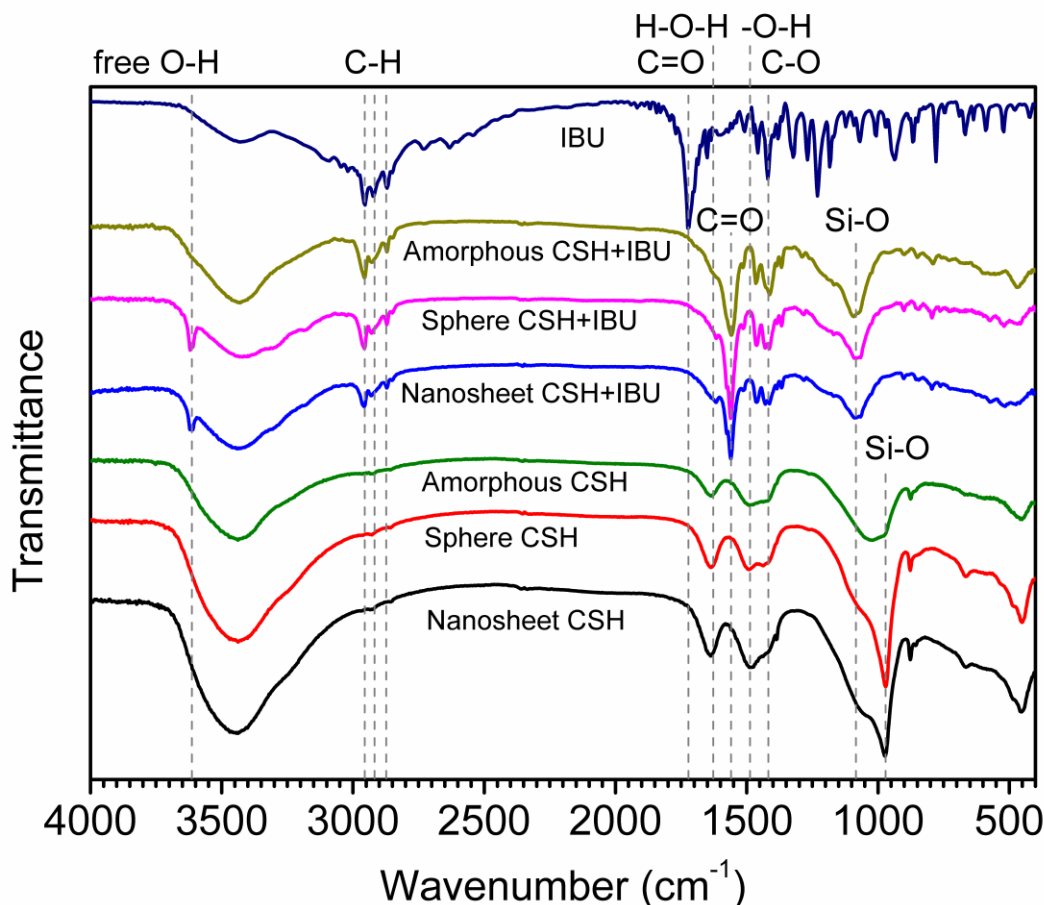


Figure 3-10 FTIR spectra of different CSH carriers with and without IBU drug loading; the FTIR spectrum of pure IBU is also shown for comparison.

3.3.5 *In Vitro* CSH-IBU Release

Figure 3-11 shows the IBU drug release profiles of the IBU-CSH carrier drug delivery systems in the PBS medium. For the CSH mesoporous microsphere drug delivery system, 63% of the loaded IBU was released in PBS in the first 24 h and nearly 100% was released in a time period of 175 h. The IBU drug release curves of both CSH nanosheet and amorphous CSH drug delivery systems are similar. For these two drug delivery systems, ~43% of the loaded IBU was released in PBS in the first 24 h and then the drug release slowed down, and the total drug release time lasted as long as 293 h. The excellent sustained drug release behaviors of CSH drug delivery systems are promising for applications in various biomedical fields.

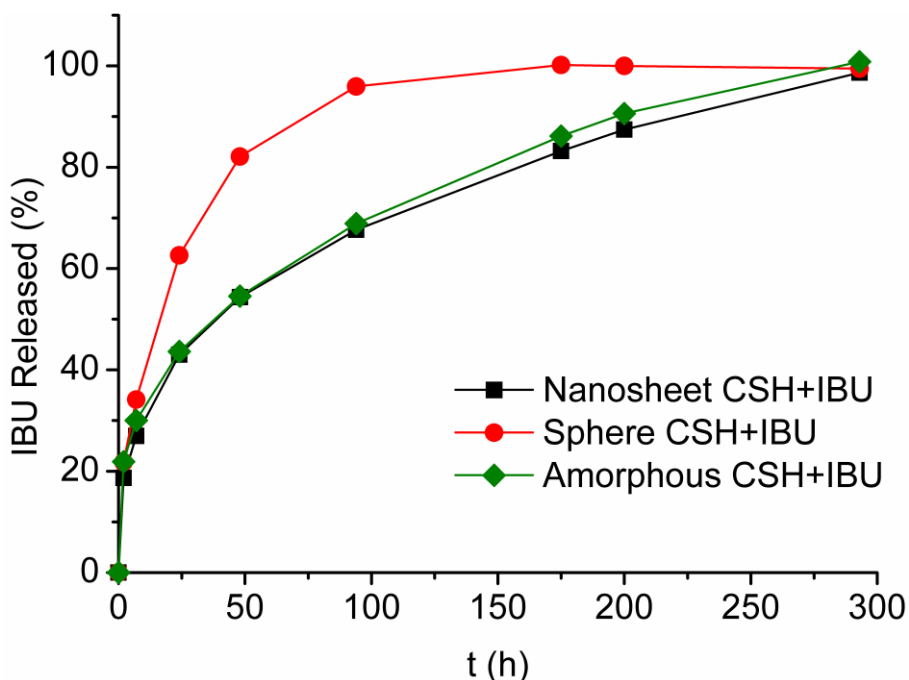


Figure 3-11 IBU drug release profiles of different IBU-CSH drug delivery systems in the PBS medium.

3.4 Conclusions

In summary, we have shown that IBU can be loaded into CSH drug carriers successfully and that there are significant interactions of the drug molecules with the carriers from XANES spectra, accompanied by the local ordering of the system.

- Calcium ions interact with carboxyl groups, generating calcium acetate like compounds.
- Besides hydrogen bonding between silicates and drug molecules, the most amazing observation is the stronger interaction between silicates and carboxylic groups, forming Si-O-C bonds via esterification-like reaction. Moreover, drug loading leads to better ordering of silicates locally.
- Moreover, the CSH drug delivery systems exhibit high drug loading capacities and excellent sustained drug release behaviors, which can be potentially applied in various biomedical fields.

Finally, we have demonstrated that the morphology and the presence of hydrates of drug carriers may influence the drug loading capacities. XANES is a sensitive tool to track these effects and opens up future possibilities for the study of drug delivery, drug targeting and drug release.

3.5 References

- 1 Paul, W. and Sharma, C.P., *J. Biomater. Appl.* **2003**, *17*, 253-264.
- 2 Kalita, S.J., Bhardwaj, A., and Bhatt, H.A., *Mater. Sci. Eng. C* **2007**, *27*, 441-449.
- 3 Ma, M.Y., Zhu, Y.J., Li, L., and Cao, S.W., *J. Mater. Chem.* **2008**, *18*, 2722-2727.
- 4 Bertoluzza, A., Simoni, R., Tinti, A., Morocutti, M., Ottani, V., and Ruggeri, A., *J. Biomed. Mater. Res.* **1991**, *25*, 23-38.
- 5 Liu, B., Cao, Y., Chen, D., Kong, J., and Deng, J., *Analytica. Chimica. Acta* **2003**, *478*, 59-66.
- 6 Wu, J. and Zhu, Y.-J., *Mater. Lett.* **2009**, *63*, 761-763.
- 7 Rodriguez-Lorenzo, L.M., Garcia-Carrodeguas, R., Rodriguez, M.A., De Aza, S., Jimenez, J., Lopez-Bravo, A., Fernandez, M., and Roman, J.S., *J. Biomed. Mater. Res. A* **2009**, *88A*, 53-64.
- 8 Siriphannon, P., Kameshima, Y., Yasumori, A., Okada, K., and Hayashi, S., *J. Biomed. Mater. Res.* **2002**, *60*, 175-185.
- 9 Long, L.H., Chen, L.D., Bai, S.Q., Chang, J., and Lin, K.L., *J. Eur. Ceram. Soc.* **2006**, *26*, 1701-1706.
- 10 Wu, J., Zhu, Y.-J., Cao, S.W., and Chen, F., *Adv. Mater.* **2010**, *22*, 749-753.
- 11 Ginebra, M.P., Traykova, T., and Planell, J.A., *J. Control. Release* **2006**, *113*, 102-110.

- 12 Madieh, S., Simone, M., Wilson, W., Mehra, D., and Augsburger, L., *J. Pharm. Sci.* **2007**, *96*, 851-863.
- 13 Wu, J., Zhu, Y.-J., and Chen, F., *Small* **2013**, *9*, 2911-2925.
- 14 Kusachi, I., Henmi, C., Kawahara, A., and Henmi, K., *Mineral. J.* **1975**, *8*, 38-47.
- 15 Rehr, J.J., Kas, J.J., Prange, M.P., Sorini, A.P., Takimoto, Y., and Vila, F., *C. R. Phys.* **2009**, *10*, 548-559.
- 16 Rehr, J.J. and Albers, R.C., *Rev Mod Phys.* **2000**, *72*, 621-654.
- 17 Zhu, Y.F., Shi, J.L., Li, Y.S., Chen, H.R., Shen, W.H., and Dong, X.P., *Micropor. Mesopor. Mater.* **2005**, *85*, 75-81.
- 18 Wei, J., Chen, F.P., Shin, J.W., Hong, H., Dai, C.L., Su, J.C., and Liu, C.S., *Biomaterials* **2009**, *30*, 1080-1088.
- 19 Vallet-Regi, M., Rámila, A., del Real, R.P., and Pérez-Pariente, J., *Chem. Mater.* **2000**, *13*, 308-311.
- 20 Muñoz, B., Rámila, A., Pérez-Pariente, J., Díaz, I., and Vallet-Regí, M., *Chem. Mater.* **2002**, *15*, 500-503.
- 21 Zhu, Y.F., Shi, J.L., Shen, W.H., Dong, X.P., Feng, J.W., Ruan, M.L., and Li, Y.S., *Angew. Chem. Int. Edit.* **2005**, *44*, 5083-5087.
- 22 Eichert, D., Salome, M., Banu, M., Susini, J., and Rey, C., *Spectrochim. Acta B* **2005**, *60*, 850-858.
- 23 Demirkiran, H., Hu, Y., Zuin, L., Appathurai, N., and Aswath, P.B., *Mate. Sci. Eng. C* **2011**, *31*, 134-143.
- 24 Cormier, L. and Neuville, D.R., *Chem. Geol.* **2004**, *213*, 103-113.
- 25 Xue, W., Bandyopadhyay, A., and Bose, S., *Acta Biomater.* **2009**, *5*, 1686-1696.

- 26 Nonat, A., *Cem. Concr. Res.* **2004**, *34*, 1521-1528.
- 27 Cong, X.D. and Kirkpatrick, R.J., *Adv. Cem. Based Mater.* **1996**, *3*, 144-156.
- 28 Chen, J.J., Thomas, J.J., Taylor, H.F.W., and Jennings, H.M., *Cem. Concr. Res.* **2004**, *34*, 1499-1519.
- 29 Li, D., Bancroft, G.M., Kasrai, M., Fleet, M.E., Feng, X.H., Tan, K.H., and Yang, B.X., *Solid State Commun.* **1993**, *87*, 613-617.
- 30 Hu, Y.F., Boukherroub, R., and Sham, T.-K., *J. Electron Spectros. Related Pheno.* **2004**, *135*, 143-147.
- 31 Stuart, B.H., *Infrared spectroscopy: fundamentals and applications.* **2004**: Wiley.

Chapter 4

4 Imaging of Drug Loading Distributions in Individual Microsphere of Calcium Silicate Hydrate - An X-ray Spectromicroscopic Study

4.1 Introduction

The calcium silicate based materials are promising for applications in biomedical fields with the advantages of having excellent biocompatibility and biodegradability [1-4]. Hence, calcium silicate hydrate (CSH) can be applied in periodontal repair and bone augmentation because of their stimulatory effect on osteogenic differentiation of stem cells [5]. For clinical applications, drug incorporation using CSH drug carrier allows for not only the repair of bone defects, but also bone therapies, such as bone anti-infection, fracture consolidation and tumor treatment [6]. Insufficient drug dose, however, is one of the most common issues in drug delivery systems, thus it is important to ensure the successful incorporation of drug molecules, and to determine the drug loading capacities for the next step. Although there are many conventional methods, such as UV-Vis, thermogravimetric analysis *etc.*, to measure the drug loading amount in the drug carriers, the integrity and distributions of drug molecules, which are essential to the drug delivery and further drug release, cannot be revealed based on the conventional techniques. Besides, the interactions between drug molecules and carriers also play a crucial role on drug loading capacities and drug release kinetics [7, 8]. To realize this goal, it is necessary to image the variations of the local chemical composition in an individual drug carrier before and after drug loading. However, very few techniques can provide this unique information.

* A version of this chapter has been published in *Nanoscale* **2015**, 7, 6767–6773.

Reproduced by permission of The Royal Society of Chemistry. DOI:

[10.1039/C4NR07471H](https://doi.org/10.1039/C4NR07471H)

Scanning transmission X-ray microscopy (STXM) [9, 10] records the X-ray absorption features at an absorption edge of an element in a chemical environment in the transmission mode using a nano size X-ray beam. It provides spectromicroscopy information; thus both chemical images and detailed absorption spectroscopic features in the near edge region of a single nanostructure can be revealed, this technique is especially good for the low Z elements (such as C, O and N). More importantly, STXM can also measure the absolute thickness of the specimen. It has been successfully applied to study the iron-based Fischer–Tropsch catalyst [11], individual multi-walled carbon nanotube [12], graphene [13], single ZnS/ZnO nano-heterostructure [14] and individual hybrid TiO₂ particles [15] by providing unique composition of nanomaterials without significant beam damage. X-ray absorption near edge structure (XANES) spectroscopy provides information about the structure and bonding intimately associated with the absorbing atom and the immediate surroundings of the absorbing atom [16]. It is very sensitive to the slight changes of surrounding environment of target atoms via the noticeable changes of spectral features (peak energy shift, peak intensity variations, and dis/appearance of new features, *etc.*) [17-19]. As a matter of fact, STXM-XANES is also suitable for drug delivery study. For example, it is desirable to know the integrity of drug molecules, bonding information and their distributions after loading processes. The normal area of beam on the samples is around mm²; consequently, the information from the XANES spectra is an average of a large area which may contain impurities from the substrate, especially for the organic materials. The improvement of spatial resolution of STXM overcomes the shortcoming above and provides information of isolated or individual structures of nanomaterials. In this chapter, we report the application of STXM combined with XANES in the chemical imaging of individual CSH mesoporous microsphere loaded with model drug ibuprofen (IBU). The electronic and chemical structure of selected sample regions of sub-micron dimension were obtained by spatially-resolved XANES at the C, O, Si K-edges and the Ca L_{3,2}-edge.

4.2 Experimental

4.2.1 Preparation of CSH Mesoporous Microspheres

CSH mesoporous microspheres formed by the self-assembly of CSH nanosheets were prepared via a sonochemical method [20]. 5 mL of a 4 M NaOH aqueous solution and 2 mL of tetraethyl orthosilicate (TEOS) were added into 500 mL of 0.03 M $\text{Ca}(\text{NO}_3)_2$ aqueous solution under magnetic stirring at room temperature. The resulting mixture was ultrasonically irradiated for 1 hour under ambient conditions using a high-intensity ultrasonic probe with the power of 200 W (Ti-horn, 27 kHz, Hangzhou Success, China) immersed directly in the solution. The product was centrifuged (6000 rpm for 2 min) and washed with deionised water and absolute ethanol three times, respectively. Then, the powder was dried in air at 60 °C overnight.

4.2.2 IBU Drug Loading

The as-synthesized powder (1.0 g of CSH mesoporous microspheres) was added to a 50 mL IBU hexane solution ($\sim 40 \text{ mg mL}^{-1}$) in a flask at room temperature. The flask was immediately sealed to prevent hexane from evaporation, and the mixture was treated by ultrasound for 2 minutes. Then the flask was oscillated at a constant rate of 160 rpm at 37 °C for 24 hours. The product was separated by centrifugation (6000 rpm for 2 min), washed with hexane, and dried in air at 60 °C overnight.

4.2.3 Characterization

The IBU hexane solutions before and after the IBU loading were analysed by UV-Vis absorption (Techcomp, UV2300) at the wavelength of 263 nm. Transmission electron microscopy (TEM) images were obtained at the Biotron, University of Western Ontario (Philips CM-10 TEM).

4.2.4 STXM Measurement

STXM measurement was conducted at the Soft X-ray Spectromicroscopy (SM) beamline at the Canadian Light Source (CLS); SM beamline is equipped with a 25 nm outermost-zone zone plate (CXRO, Berkeley Lab). The diffraction-limited spatial resolution for this zone plate is 30 nm with a spectral resolution of 0.05 eV. Image sequence (stack) scans

over a range of photon energies were acquired for the same sample region at the Ca L_{3,2}-edge, and Si, O and C K-edges, respectively. A few mg of the sample was dispersed in deionised water by brief sonication, and then deposited on a copper grid to allow it to dry in air before transferring into the STXM chamber. STXM data were analyzed using the aXis2000 software package, which allows for detailed interactive processing of the images and fitting the image stacks with the X-ray absorption spectra.

4.3 Results and Discussion

4.3.1 IBU Loading in CSH Microspheres

The UV-Vis absorption spectra of the hexane solution containing IBU before and after IBU loading in CSH mesoporous microspheres are shown in Figure 4-1. One can see that the absorption spectra of IBU in hexane show the characteristic absorption peaks of IBU, e.g. the most intense feature at 263 nm, which are consistent with the literature [21]. After IBU loading, a significant decrease in the absorbance of IBU in hexane solution (red profile) indicates that the IBU drug molecules have been loaded into the drug carriers with a high drug loading capacity.

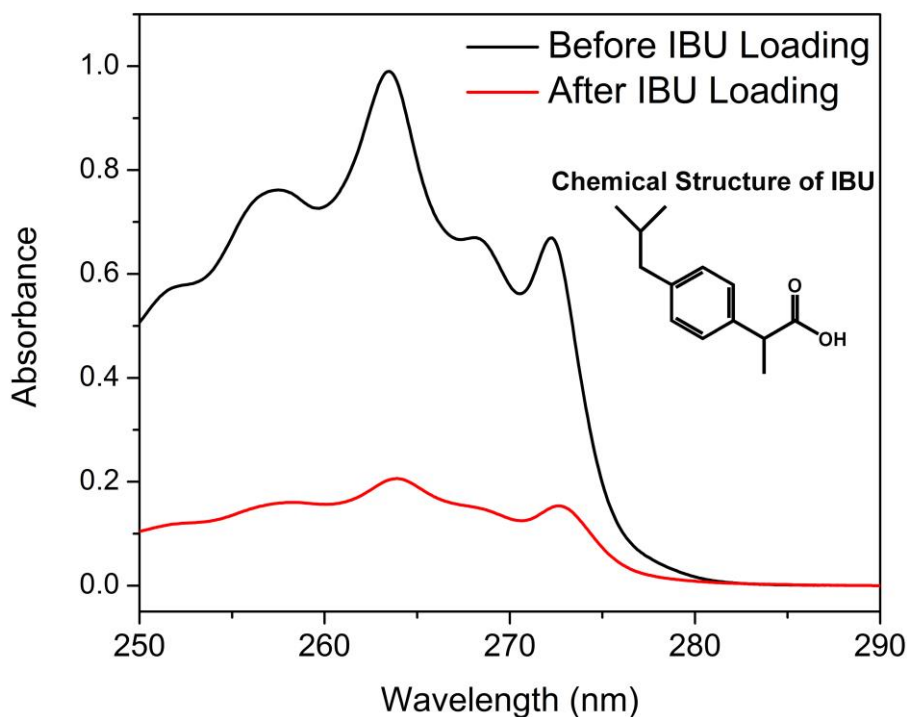


Figure 4-1 UV-Vis absorption spectra of the IBU hexane solution diluted 50 times before and after the IBU loading in CSH mesoporous microspheres.

4.3.2 Morphology of Individual CSH Microsphere Before and After IBU Loading

The morphology of the CSH mesoporous microspheres before and after IBU loading was characterized by TEM. As shown in Figure 4-2(a), the sample before IBU loading is composed of mesoporous microspheres formed by self-assembly of nanosheets with diameters around 1 μm . The three-dimensional interconnected nanosheets lead to the formation of a large number of mesopores. It should be noted that the CSH mesoporous microspheres after IBU loading (see Figure 4-2 (b)) show a similar morphology to that before IBU loading. Thus, TEM results clearly reveal that the morphology of CSH mesoporous microspheres remains intact after IBU loading, and it would be significant if we can identify the locations and distributions of IBU in the carriers.

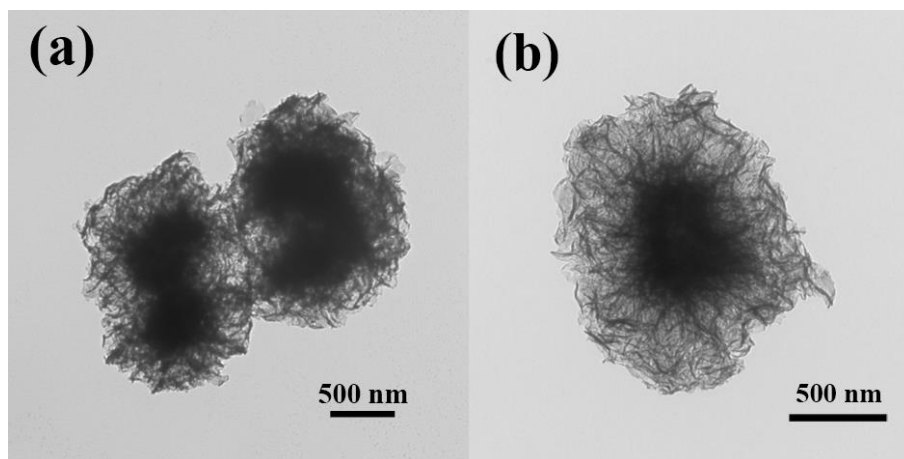


Figure 4-2 TEM images of CSH mesoporous microspheres before (a) and after (b) IBU loading.

4.3.3 STXM Analysis of Individual CSH Microsphere Before and After IBU Loading

The STXM images of CSH microspheres before and after IBU loading (Figure 4-3 and 4-4) are in good agreement with the TEM micrographs: no significant morphology changes are observed from the CSH microspheres before and after IBU loading. Moreover, except for the variations of intensities, which is due to the sample thickness, there are no noticeable spectral differences from different CSH microspheres at Ca $L_{3,2}$ -edge, Si K-edge (the peak at ~ 1862 eV is not real, is due to the I_0 glitch) and C K-edge, respectively, indicating the uniformity of CSH microspheres. As a result, we selected individual mesoporous microsphere for a more detailed analysis in the following study.

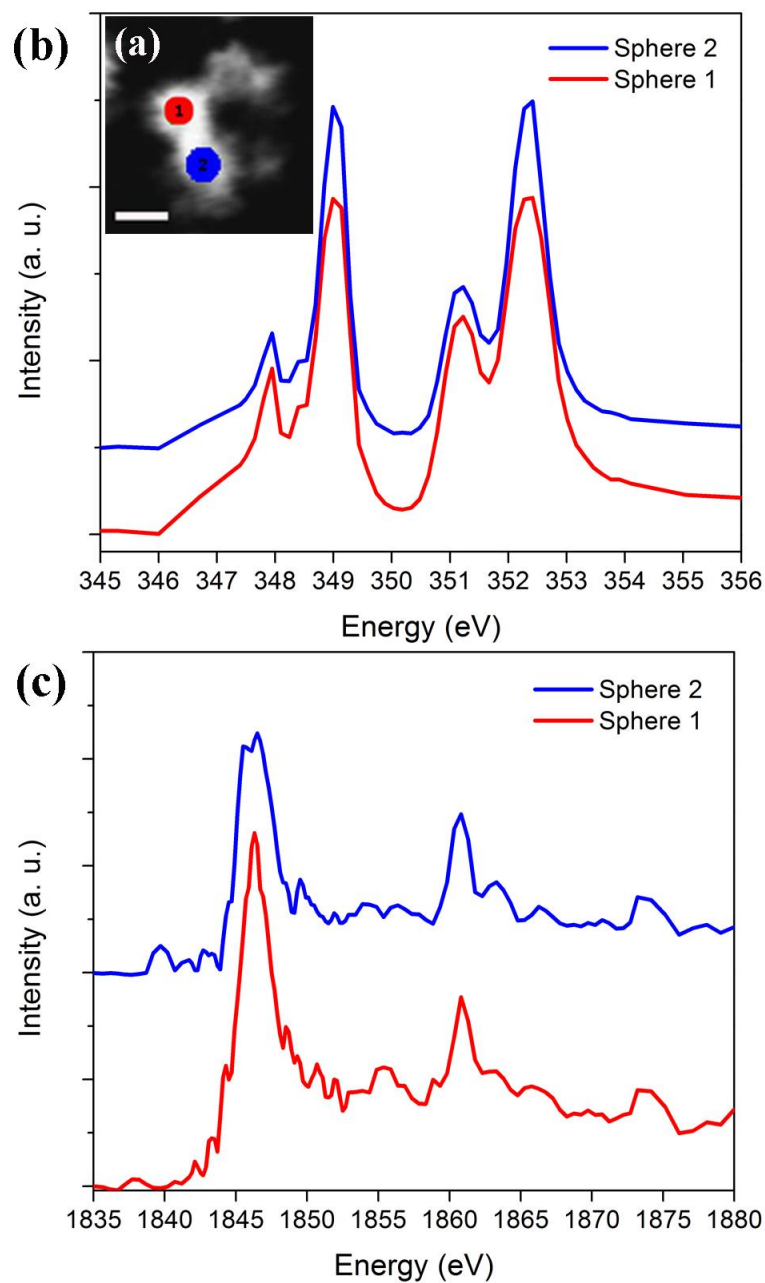


Figure 4-3 (a) STXM images of CSH microspheres before IBU loading: two ROIs were selected which represented different CSH microspheres; Red: Sphere-1, Blue: Sphere-2. Scale bar in (a) is 1 μ m. (b, c) XANES spectra from each ROI displayed at the Ca L_{3,2}-edge (b) and the Si K-edge (c).

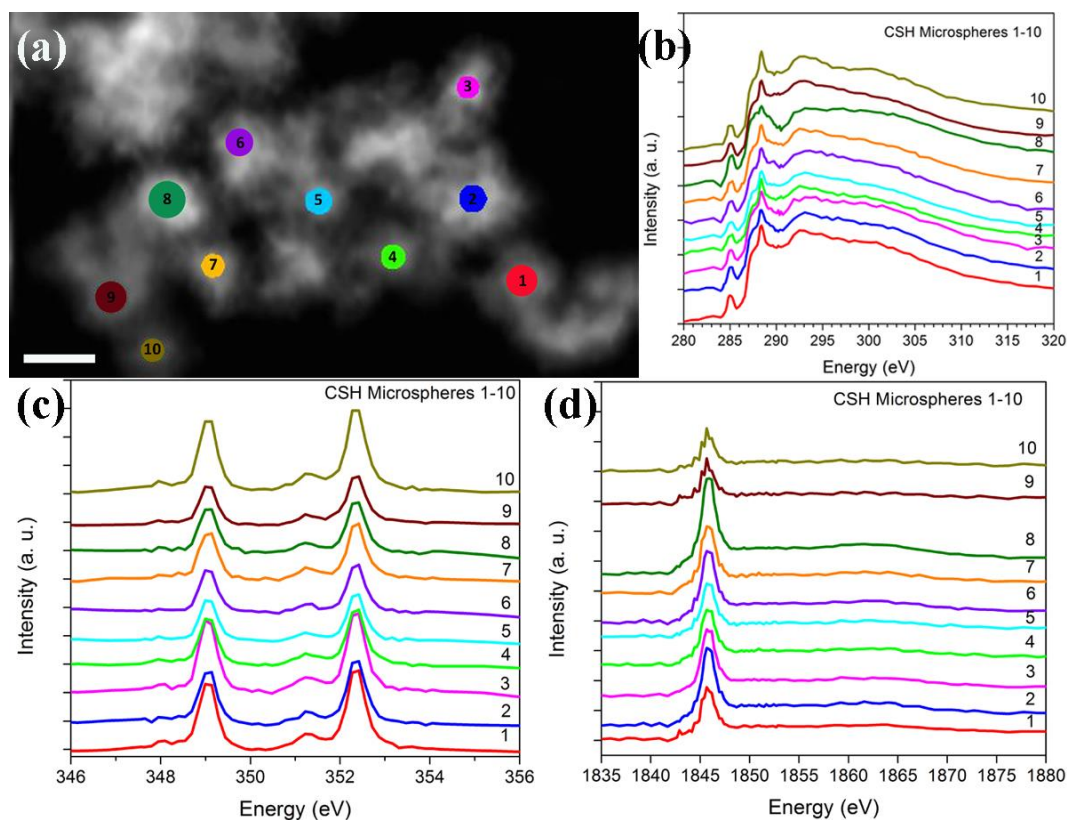


Figure 4-4 (a) STXM images of CSH microspheres after IBU loading: 10 ROIs were selected which represented different CSH microspheres. Scale bar in (a) is 1 μ m. XANES spectra from each ROI displayed at (b) the C K-edge, (c) the Ca L_{3,2}-edge and (d) the Si K-edge.

Figure 4-5 shows the STXM images and XANES spectra taken from different regions of interests (ROIs) of individual CSH microsphere before IBU loading at the Ca L_{3,2}-edge, O K-edge and Si K-edge. Several interesting features are apparent. First, at the Ca L_{3,2}-edge (Figure 4-5(c)), no significant changes were observed in the XANES spectra of different ROIs, except that the peaks taken in the thick region (ROI-4) are broadened and the intensity ratios of a_1/a_2 and b_1/b_2 increase a lot due to the thickness effects (saturation phenomenon). The spin-orbit related L₃ (a_2) and L₂ (b_2) peaks before IBU loading (Figure 4-5(c)), which are located around 349.1 and 352.4 eV respectively, are due to transitions from 2p_{3/2} and 2p_{1/2} electrons to the empty 3d states of Ca²⁺. The weak multiple peaks at lower energies are due to crystal field splitting from the first coordination sphere surrounding Ca²⁺ [22-26]. Thus Ca L-edge is sensitive to changes of the magnitude of

crystal field and coordination of Ca^{2+} . Figure 4-5(d) shows the XANES spectra at the O K-edge. There are two discernible features, labelled “a” and “b”. The pre-edge peak “a” is due to the Ca–O crystal field effects. The main resonance “b” at around 538 eV is from transition from O 1s to 2p antibonding states hybridized with orbitals of the cations which O is bound [27-29]. The Si K-edge XANES spectra are shown in Figure 4-5(e). All spectra show the same features. The main resonance is identified as the Si 1s to 3p transition for silicon (IV) in a tetrahedral oxygen ligand environment [30, 31]. At all the edges, we do not observe any significant changes in spectral features in the spectra of different ROIs, indicating that there are no chemical differences in the condensed and the relatively thin areas.

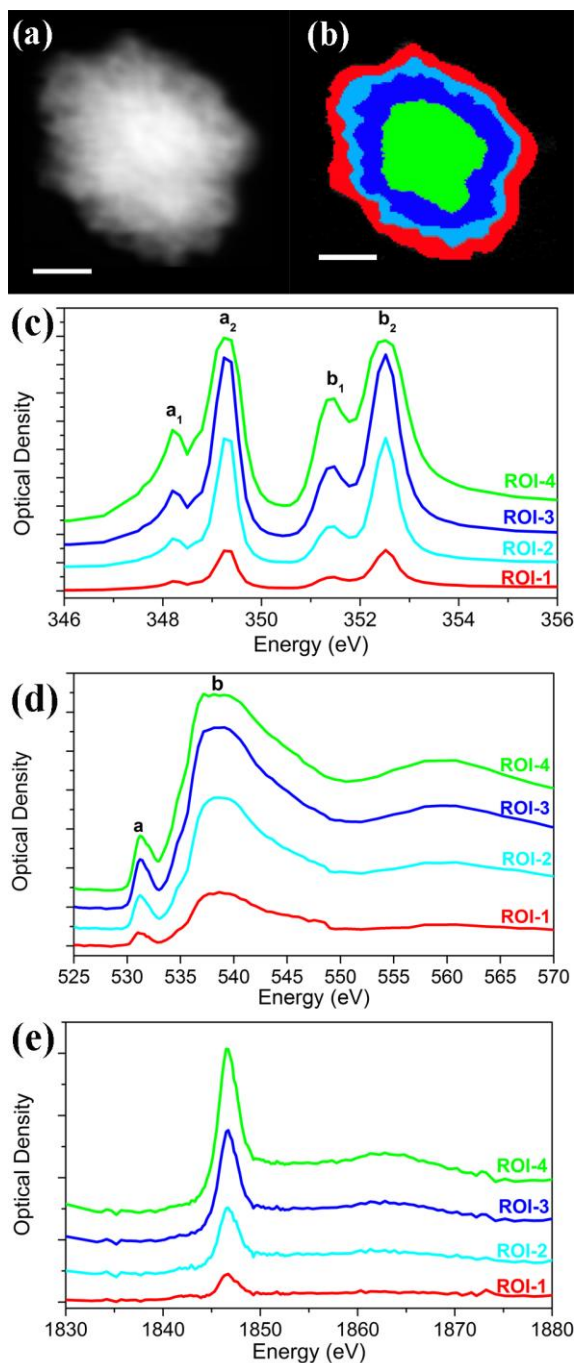


Figure 4-5 STXM images and XANES spectra of individual CSH microsphere before IBU loading, (a) STXM image of individual CSH microsphere (average: 346-1890 eV); (b) 4 ROIs taken from the CSH microsphere: Red: ROI-1, Cyan: ROI-2, Blue: ROI-3, Green: ROI-4. Scale bars in (a) and (b) are 600 nm; (c), (d), (e) are isolated XANES spectra of each ROIs displayed in (b) at Ca L_{3,2}-edge , O K-edge and Si K-edge, respectively.

The analysis reported below for IBU-loaded CSH mesoporous microspheres is based on the CSH microsphere traced in red dot circle shown in Figure 4-6(b) (taken at the Ca $L_{3,2}$ -edge ($E = 352.5$ eV)). Since STXM can provide high quality images as well as high quality absorption spectra at the C K-edge, it has been successfully applied to the studies of carbon nanomaterials [19, 32, 33]. Therefore, it will provide chemical information of the IBU drug molecules from the perspective of the carbon site. Figures 4-6(c) to (e) show the STXM images and the C K-edge XANES taken from different regions of interests (ROIs) of an individual CSH microsphere after IBU loading. As shown in Figure 4-6(e), the spectra obtained from different ROIs have identical features. The sharp peak “a” located at 285 eV is from the carbon 1s to π^* transition for the aryl rings of IBU molecules; the peak “b” located at 288.3 eV is from the carbon 1s to π^* transition for carboxylic functional groups of IBU; the weak peak “c” located around 290 eV is assigned to the transition from carbon 1s to σ^* of the C-OH moiety of the carboxylic group [27, 34-36]. Compared with the spectrum of IBU powder (black profile), there is no significant change or beam damage to the IBU molecules, except that peak “c” is less apparent after IBU loading. Based on the STXM and XANES spectra at the C K-edge, it is certain that IBU has been successfully loaded into CSH mesoporous microspheres. We will discuss below in details the chemistry that took place between CSH and IBU during the drug loading process.

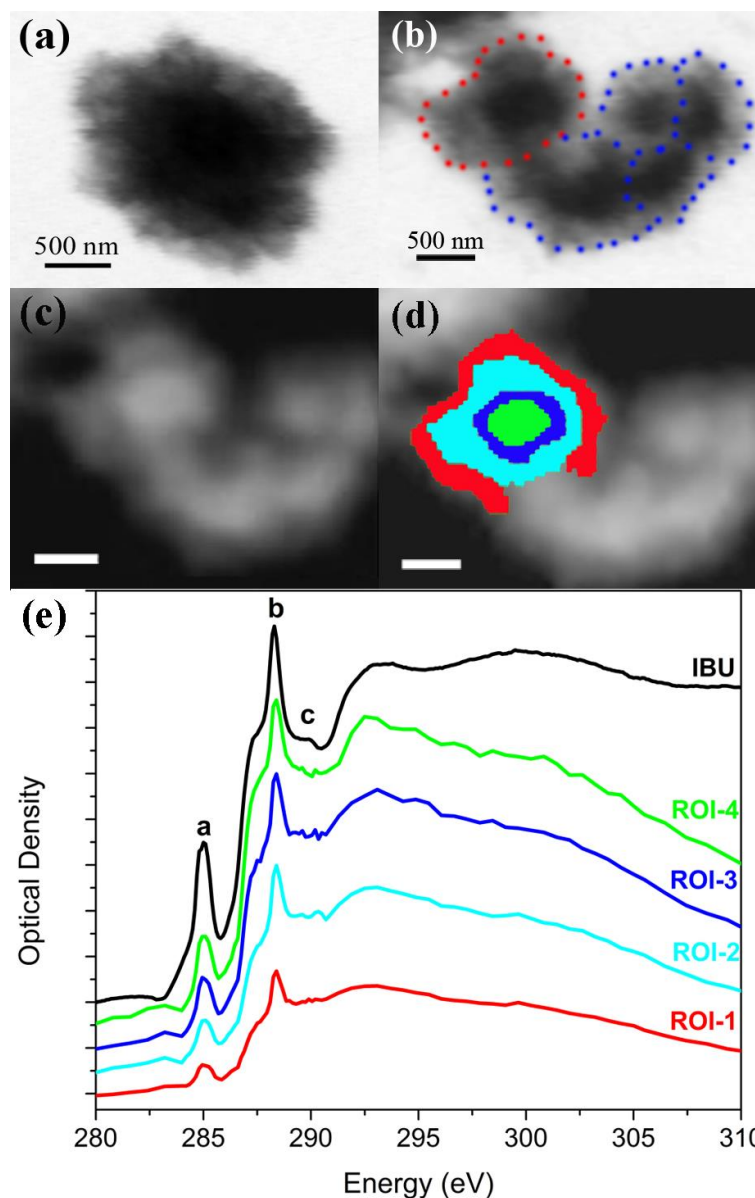


Figure 4-6 STXM images of an individual CSH microsphere: (a) before and (b) after IBU loading taken at the Ca $L_{3,2}$ -edge ($E = 352.5$ eV); (c) STXM image of an individual CSH microsphere (average at all edges); (d) 4 ROIs taken from an individual CSH microsphere; Red: ROI-1, Cyan: ROI-2, Blue: ROI-3, Green: ROI-4. Scale bars in (c) and (d) are 500 nm; (e) XANES spectra from each ROI displayed in (d) at the C K-edge.

XANES spectra of the individual CSH microsphere after IBU loading in different ROIs at the Ca L_{3,2}-edge, Si K-edge and O K-edge, respectively are shown in Figure 4-7(a), 7(b) and 7(c).

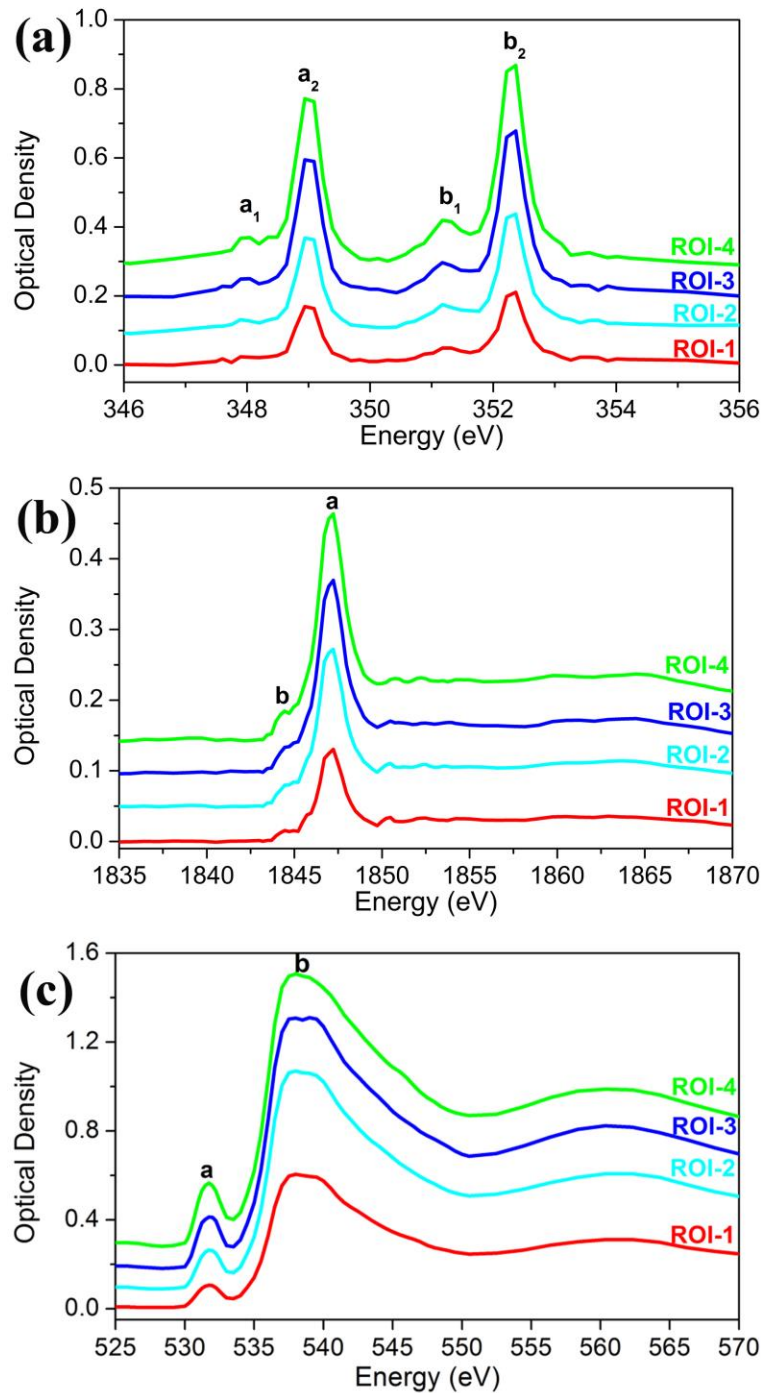


Figure 4-7 XANES spectra of individual CSH microsphere after IBU loading at Ca L_{3,2}-edge (a), Si K-edge (b) and O K-edge (c). (ROI 1-4 are the same regions as shown in Fig. 4-6(d)).

Several interesting features are noticeable. First, at the Ca L_{3,2}-edge (Figure 4-7(a)), no significant difference in the XANES was observed for different ROIs. After IBU loading, the XANES spectra of the four ROIs from thin areas (ROI-1 and ROI-2) to thick areas (ROI-3 and ROI-4) show the same features at all three edges, which means that the CSH microspheres remain chemically uniform after IBU loading. However, having compared the average spectra of CSH microspheres before and after IBU loading at the Ca L_{3,2}-edge, O K-edge and Si K-edge, we find discernible changes in the XANES at all edges, as illustrated in Figure 4-8.

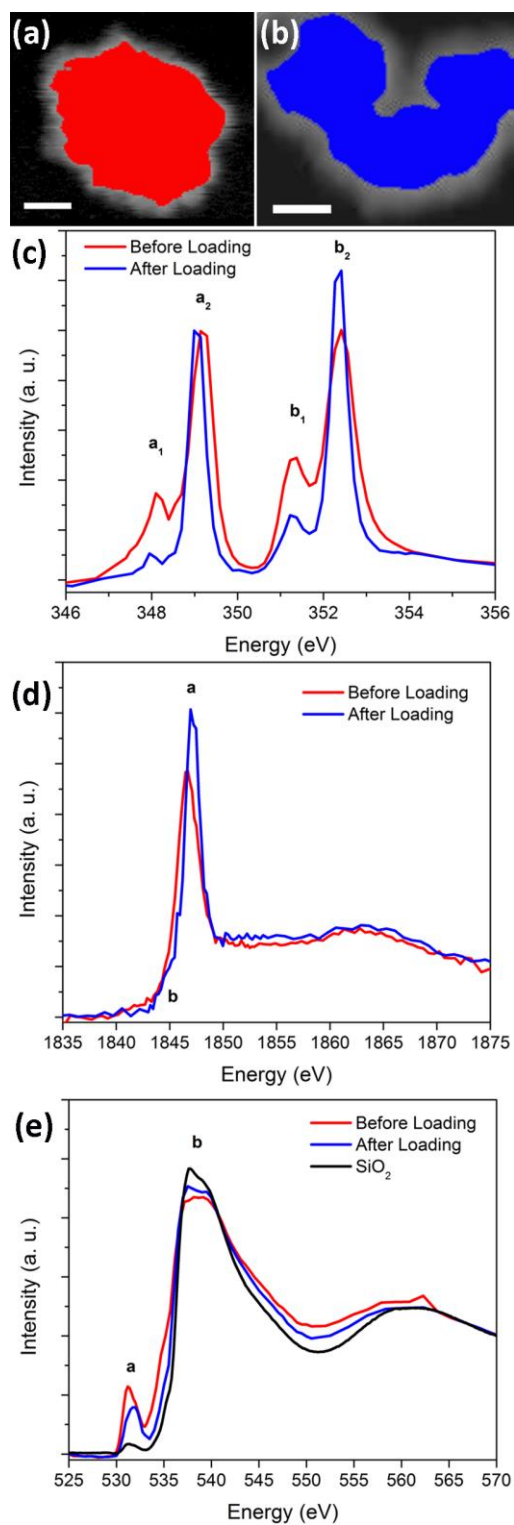
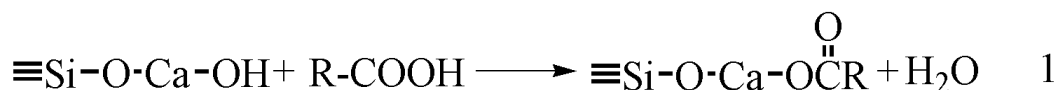


Figure 4-8 Comparison of average XANES spectra before (a) and after (b) IBU loading at (c) Ca L_{3,2}-edge, (d) Si K-edge and (e) O K-edge.

The presence of Ca-OH groups in CSH has been widely reported in the literature. They are more abundant on the surface or interlayers in order to balance the charge or neutralize the non-bridging oxygens (NBOs) [37-40]. In our previous study, we also illustrated that Ca-OH groups located on the surface or interlayer sites react with the carboxyl groups of IBU directly (Scheme 4-1) [41].



Scheme 4-1 Interaction between CSH and IBU at the Ca local environment.

This interaction between Ca and IBU results in the local environment of Ca is similar to that of calcium acetate after IBU loading. In Figure 4-8(c), there is around 0.1 eV energy shift between the spectra before and after IBU loading. It can be ascribed to the formation of Ca-O-C bonds after IBU loading, which distorts the structure of CSH locally by lowering the symmetry of Ca [23]. The energy differences of ΔL_3 ($E_{a2} - E_{a1}$), ΔL_2 ($E_{b2} - E_{b1}$) and intensity ratios of a_1 to a_2 , b_1 to b_2 of the Ca $L_{3,2}$ -edge (see Figure 4-8(c)), are listed in Table 4-1.

Table 4-1 ΔL_3 and ΔL_2 of CSH microspheres before and after IBU loading*

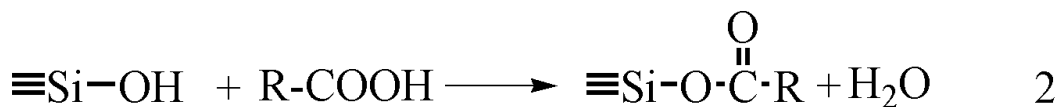
	ΔL_3 ($a_2 - a_1$) (eV)	$\frac{a_1}{a_2}$	ΔL_2 ($b_2 - b_1$) (eV)	$\frac{b_1}{b_2}$
Before Loading	1.0	0.35	1.0	0.49
After Loading	1.0	0.11	1.1	0.21

* The energy fine step before loading is 0.25 eV and the energy fine step after loading is 0.15 eV

It can be seen that, after IBU loading, there is no significant change in the splitting of a_1 and a_2 (b_1 and b_2 as well). That is because the CSH microsphere we synthesized is composed of $\text{Ca}_3\text{Si}_2\text{O}_7$, which has the crystal structure of rankinite as has been confirmed in previous studies [20, 37, 42]. The calcium atom in CSH is coordinated by seven oxygen atoms while the average coordination number of Ca in calcium acetate is reported to be 7.5 [43-45]. Although we cannot get much information from the energy differences, the intensity ratio of a_1 to a_2 (as well as b_1/b_2) is informative and it decreases after IBU loading, which indicates that the magnitude of crystal field decreases after IBU loading.

Compared to calcium silicate, the crystal field of calcium acetate is weaker because of the difference in ligand electronegativity [22, 25]. As proposed above, the number of Ca–O–C groups in CSH increases during the IBU loading process, which leads to the decrease of the crystal field (decrease in the intensities of a_1/a_2 and b_1/b_2).

Figure 4-8(d) shows the comparison of Si K-edge XANES spectra of the CSH mesoporous microspheres before and after IBU loading. Interestingly, before IBU loading, the main peak “a” is relatively broad; this is due to the differences in chemical environment at Si (IV) sites in the presence of Ca^{2+} . However, after IBU loading, there is a new peak “b” emerges at ~ 2 eV below the main peak and the main peak became sharper and shifted about 0.5 eV toward higher energy. These observations are in excellent agreement with our previous work (XANES collected on a large area of the specimen) [41]. It is proposed that CSH forms some silanol groups (Si–OH) on the surface which interacts with IBU (Scheme 4-2).



Scheme 4-2 Interaction between CSH and IBU at the Si local environment.

In the new structure (Si–O–C), due to the presence of the alkyl groups and the distortion of silicate tetrahedron [46, 47]; we observe that the new peak b appears at lower photon energy. On the other hand, most of the Si atoms of calcium silicate in the bulk are still in a SiO_4 tetrahedral environment and after drug loading, most of the silanol groups on the surface could react with the carboxyl groups of IBU. As a result of this interaction, the rest of Si atoms would be in a more “regular” SiO_4 environment leading to that peak “a” turns sharper and shifts to higher energy (the spectra are similar to that of SiO_2 (Figure 4-9)).

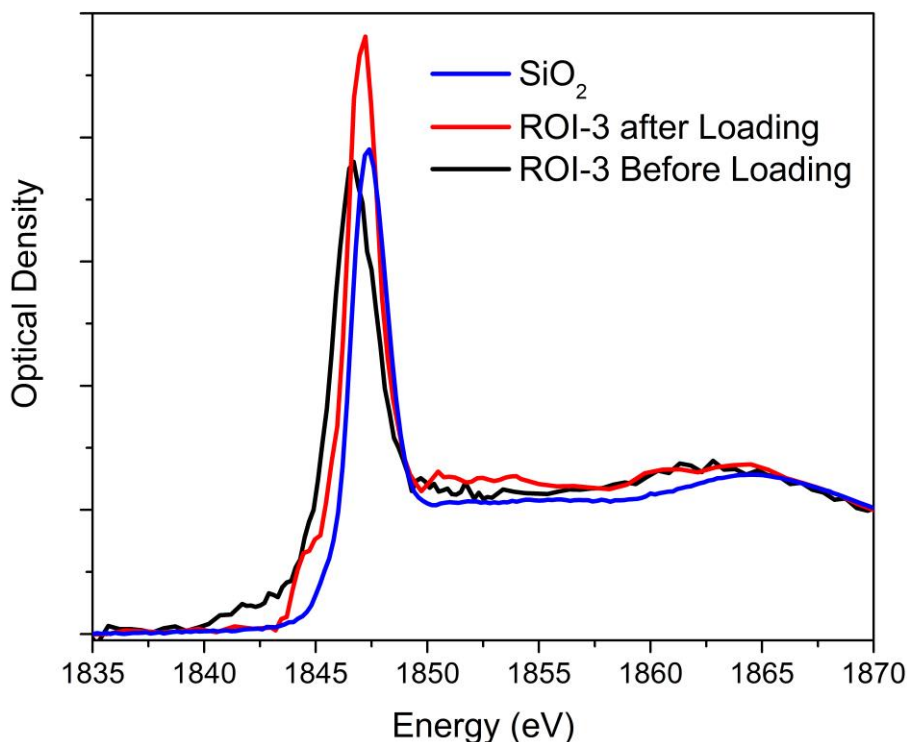


Figure 4-9 XANES spectra comparisons of individual mesoporous CSH microsphere before/after IBU loading and SiO₂.

Figure 4-8(e) shows the XANES spectra comparison at O K-edge. First, the pre-edge peak “a” shifts from 531.2 eV (due to the Ca–O crystal field effects) to 531.9 eV, which is assigned to the transition from O 1s to π^* states (O–C=O, from IBU) [27-29]; second, the main resonance “b” exhibits splitting into a doublet. When we compare the XANES of CSH loaded with IBU and silicon dioxide (black profile), one can see that the first peak of main resonance of CSH loaded with IBU is similar to that of SiO₂; the Si atoms are in a tetrahedral SiO₄ environment. Based on these observations, we can conclude that the O K-edge XANES spectra of CSH after IBU loading exhibit the chemical characteristics of both CSH and IBU. Besides, the O K-edge results are supplementary to the proposed interactions deduced from the Ca L_{3,2}-edge and Si K-edge XANES.

4.3.4 Thickness Mapping of Individual CSH Microsphere Before and After IBU Loading

Since STXM can determine the absolute thickness of the sample, which means that saturation does not occur, thickness distribution maps of the CSH microsphere before and

after IBU loading at the Si K-edge and C K-edge can be obtained. The thickness was obtained from stack fitting with the quantitatively scaled reference spectra of 1 nm thickness. Silicon and carbon reference spectra were obtained by fitting the original XANES spectra to match its calculated elemental linear X-ray absorption profile: calcium silicate (CaSiO_3 : density = 2.900 g/cm^3 , and thickness = 1 nm, ibuprofen ($\text{C}_{12}\text{H}_{18}\text{O}_2$: density = 1.030 g/cm^3 , and thickness = 1 nm) in the pre-edge and continuum ((Figure 4-10).

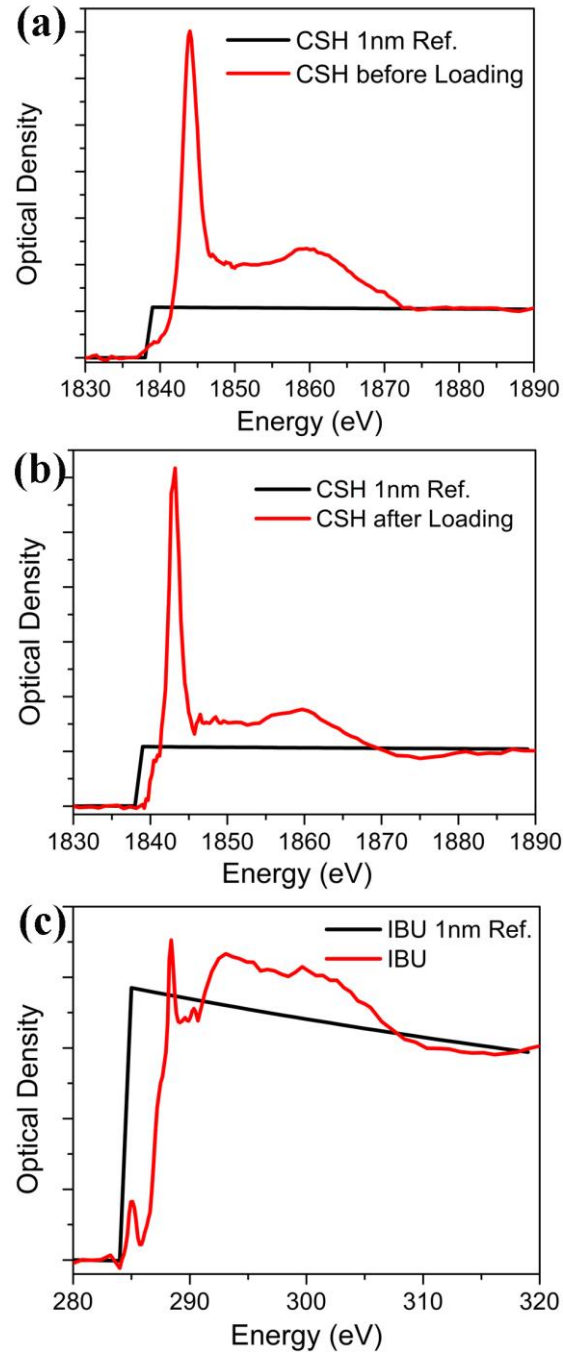


Figure 4-10 Reference spectra and elemental linear X-ray absorption profiles of CSH and IBU. (a) and (b) CSH Si K-edge before and after IBU loading (black profile: optical density spectrum of 1 nm thickness based on formula CaSiO_3 ; red profile: elemental linear X-ray absorption profile); (c) IBU C K-edge (black profile: optical density spectrum of 1 nm thickness based on formula $\text{C}_{12}\text{H}_{18}\text{O}_2$; red profile: elemental linear X-ray absorption profile).

Figure 4-11 shows the Si thickness map of single CSH microsphere before IBU loading. The stripes across the microsphere, which are due to the beam vibration during the STXM measurement, are not real structures of individual CSH microsphere. The thickness of the condensed core of the CSH microsphere is determined to be about 235 nm, while the thickness of the outer surface area is around 24 nm ($\pm 10\%$). This result confirms that under the ultrasonic irradiation, the CSH first forms a condensed core by stacking up nanosheets as building blocks, then more nanosheets aggregate and self-assemble to bird's nest like 3D hierarchical networks with mesopores and macropores [20].

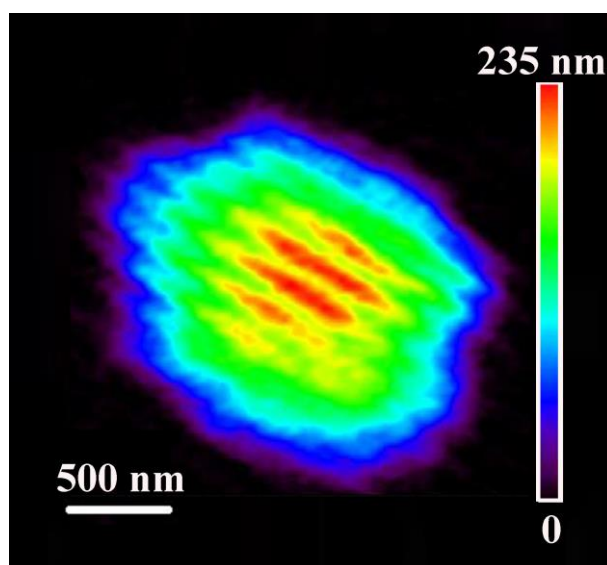


Figure 4-11 Thickness distribution of individual CSH microsphere at the Si K-edge; the vertical color bar illustrates the thickness of the microsphere.

The thickness distribution maps of the CSH microsphere after IBU loading at Si K-edge and C K-edge are shown in Figure 4-12(a) and (b), respectively. After drug loading, the material thickness of the centre areas of CSH microsphere is equivalent to ~ 160 nm ($\pm 10\%$) of crystalline CSH and that of the surface is around 18 nm ($\pm 10\%$). This thickness of CSH derived from the absorption is smaller than the actual size of the microspheres in TEM (~ 1 μm), which is due to the highly porous structure of the microspheres [20]. Besides, the thickness distribution map of IBU (Figure 4-12(b)) is more interesting and significant because the carbon signal is only from IBU molecules and it illustrates the

distribution of the drug molecules loaded in the drug carriers (and how much drug molecules can be loaded into the drug carriers by quantitatively comparing the thickness of CSH and IBU). The thickness ratios of CSH to IBU in the thick and thin regions are given in Table 4-2.

Table 4-2 Thickness and thickness ratio of CSH to IBU in different regions*

	Thickness (nm)		Ratio
	Si Map	C Map	
Region 1 (Red)	160	26	6.15
Region 2 (Green)	102	17	6.00
Region 3 (Purple)	18	3	6.00

*There is $\pm 10\%$ thickness deviation according to Figure 4-12.

IBU were observed on the entire CSH microspheres, and they are more abundant in thick areas (IBU thickness: ~ 26 nm) as compared to the outer surface (IBU thickness is around 2-3 nm); however thickness ratio of Si to C (also representing the thickness ratio of CSH to IBU) remains the same in different regions, which suggests that IBU molecules were uniformly loaded in the mesoporous CSH microspheres.

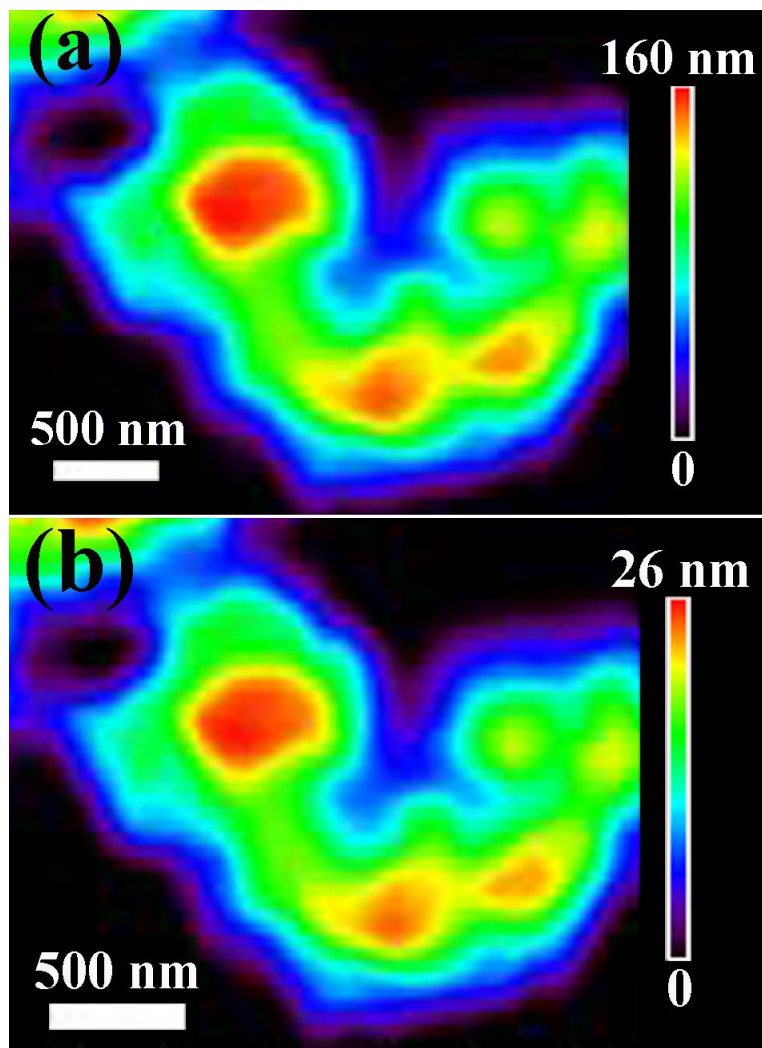


Figure 4-12 Thickness distribution maps of an individual CSH microsphere after IBU loading at (a) the Si K-edge and (b) the C K-edge. The vertical bar illustrates the color code of the material thickness.

4.4 Conclusions

In summary, we have reported the chemical imaging (with thickness distribution) and interactions between individual CSH microsphere and IBU on an individual meso-microsphere using STXM. Our results suggest that IBU interacts with both Ca-OH and Si-OH groups via its carboxylic acid functional group; this observation confirms previous analysis that based on a large collection of many individual CSH nanostructures in the drug delivery system. We find that the drug loading process has no diverse effect on the

integrity of IBU molecules. Moreover, it is of great interest and significance that one can obtain the drug loading distribution in an individual mesoporous CSH microsphere; also, IBU molecules are loaded homogenously into CSH drug carriers.

4.5 References

1. Sawyer, A.N., Nikonov, S.Y., Pancio, A.K., Niu, L.N., Agee, K.A., Loushine, R.J., Weller, R.N., Pashley, D.H., and Tay, F.R., *J. Endod.* **2012**, *38*, 680-683.
2. Dou, Y.D., Wu, C.T., and Chang, J., *Acta Biomater.* **2012**, *8*, 4139-4150.
3. Wei, J., Chen, F.P., Shin, J.W., Hong, H., Dai, C.L., Su, J.C., and Liu, C.S., *Biomaterials* **2009**, *30*, 1080-1088.
4. Rodriguez-Lorenzo, L.M., Garcia-Carrodeguas, R., Rodriguez, M.A., De Aza, S., Jimenez, J., Lopez-Bravo, A., Fernandez, M., and Roman, J.S., *J. Biomed. Mater. Res. A* **2009**, *88A*, 53-64.
5. Wu, C.T. and Chang, J., *Biomed. Mater.* **2013**, *8*, 032001.
6. Arcos, D. and Vallet-Regi, M., *Acta Mater.* **2013**, *61*, 890-911.
7. Balas, F., Manzano, M., Horcajada, P., and Vallet-Regi, M., *J. Am. Chem. Soc.* **2006**, *128*, 8116-8117.
8. Vallet-Regi, M., *Chem. Eur. J.* **2006**, *12*, 5934-5943.
9. Guttman, P., Bittencourt, C., Rehbein, S., Umek, P., Ke, X., Van Tendeloo, G., Ewels, C.P., and Schneider, G., *Nature Photonics* **2012**, *6*, 25-29.
10. Bittencourt, C., Hitchcock, A.P., Ke, X., Van Tendeloo, G., Ewels, C.P., and Guttman, P., *Beilstein J. Nanotechnol.* **2012**, *3*, 345-350.
11. de Smit, E., Swart, I., Creemer, J.F., Hoveling, G.H., Gilles, M.K., Tyliczszak, T., Kooyman, P.J., Zandbergen, H.W., Morin, C., Weckhuysen, B.M., and de Groot, F.M.F., *Nature* **2008**, *456*, 222-U239.

12. Felten, A., Bittencourt, C., Pireaux, J.-J., Reichelt, M., Mayer, J., Hernandez-Cruz, D., and Hitchcock, A.P., *Nano Lett.* **2007**, *7*, 2435-2440.
13. Schultz, B.J., Patridge, C.J., Lee, V., Jaye, C., Lysaght, P.S., Smith, C., Barnett, J., Fischer, D.A., Prendergast, D., and Banerjee, S., *Nat. Commun.* **2011**, *2*, 372.
14. Wang, Z., Wang, J., Sham, T.-K., and Yang, S., *J. Phys. Chem. C* **2012**, *116*, 10375-10381.
15. Henzler, K., Guttman, P., Lu, Y., Polzer, F., Schneider, G., and Ballauff, M., *Nano Lett.* **2013**, *13*, 824-828.
16. Sham, T.-K., *Int. J. Nanotechnol.* **2008**, *5*, 1194-1246.
17. Zhou, J., Zhou, X., Sun, X., Li, R., Murphy, M., Ding, Z., Sun, X., and Sham, T.-K., *Chem. Phys. Lett.* **2007**, *437*, 229-232.
18. Ushiro, M., Uno, K., Fujikawa, T., Sato, Y., Tohji, K., Watari, F., Chun, W.-J., Koike, Y., and Asakura, K., *Phys. Rev. B* **2006**, *73*, 144103.
19. Zhou, J., Wang, J., Liu, H., Banis, M.N., Sun, X., and Sham, T.-K., *J. Phys. Chem. Lett.* **2010**, *1*, 1709-1713.
20. Wu, J., Zhu, Y.-J., Cao, S.W., and Chen, F., *Adv. Mater.* **2010**, *22*, 749-753.
21. Zhu, Y.F., Shi, J.L., Li, Y.S., Chen, H.R., Shen, W.H., and Dong, X.P., *Micropor. Mesopor. Mater.* **2005**, *85*, 75-81.
22. de Groot, F.M.F., Fuggle, J.C., Thole, B.T., and Sawatzky, G.A., *Phys. Rev. B* **1990**, *42*, 5459-5468.
23. Himpsel, F.J., Karlsson, U.O., Mclean, A.B., Terminello, L.J., Degroot, F.M.F., Abbate, M., Fuggle, J.C., Yarmoff, J.A., Thole, B.T., and Sawatzky, G.A., *Phys. Rev. B* **1991**, *43*, 6899-6907.
24. Fleet, M.E. and Liu, X.Y., *Am. Mineral.* **2009**, *94*, 1235-1241.

25. Naftel, S.J., Sham, T.-K., Yiu, Y.M., and Yates, B.W., *J. Synchrotron Radiat.* **2001**, *8*, 255-257.
26. Ha, J., Chae, S., Chou, K.W., Tyliczszak, T., and Monteiro, P.J.M., *J. Mater. Sci.* **2012**, *47*, 976-989.
27. Zubavichus, Y., Shaporenko, A., Grunze, M., and Zharnikov, M., *J. Phys. Chem. A* **2005**, *109*, 6998-7000.
28. Plekan, O., Feyer, V., Richter, R., Coreno, M., de Simone, M., Prince, K.C., and Carravetta, V., *J. Electron Spectros. Related Pheno.* **2007**, *155*, 47-53.
29. Kuznetsova, A., Popova, I., Yates, J.T., Bronikowski, M.J., Huffman, C.B., Liu, J., Smalley, R.E., Hwu, H.H., and Chen, J.G.G., *J. Am. Chem. Soc.* **2001**, *123*, 10699-10704.
30. Demirkiran, H., Hu, Y., Zuin, L., Appathurai, N., and Aswath, P.B., *Mater. Sci. Eng. C* **2011**, *31*, 134-143.
31. Li, D., Bancroft, G.M., Kasrai, M., Fleet, M.E., Feng, X.H., Tan, K.H., and Yang, B.X., *Solid State Commun.* **1993**, *87*, 613-617.
32. Zhou, J.G., Wang, J., Sun, C.L., Maley, J.M., Sammynaiken, R., Sham, T.-K., and Pong, W.F., *J. Mater. Chem.* **2011**, *21*, 14622-14630.
33. Zhou, J., Wang, J., Fang, H., Wu, C., Cutler, J.N., and Sham, T.-K., *Chem. Commun.* **2010**, *46*, 2778-2780.
34. Jokic, A., Cutler, J.N., Ponomarenko, E., van der Kamp, G., and Anderson, D.W., *Geochim. Cosmochim. Acta* **2003**, *67*, 2585-2597.
35. Banerjee, S., Hemraj-Benny, T., Balasubramanian, M., Fischer, D.A., Misewich, J.A., and Wong, S.S., *Chem. Commun.* **2004**, *7*, 772-773.
36. Brandes, J.A., Cody, G.D., Rumble, D., Haberstroh, P., Wirick, S., and Gelinas, Y., *Carbon* **2008**, *46*, 1424-1434.

37. Kusachi, I., Henmi, C., Kawahara, A., and Henmi, K., *Mineral. J.* **1975**, *8*, 38-47.
38. Nonat, A., *Cem. Concr. Res.* **2004**, *34*, 1521-1528.
39. Cong, X.D. and Kirkpatrick, R.J., *Adv. Cem. Based Mater.* **1996**, *3*, 144-156.
40. Chen, J.J., Thomas, J.J., Taylor, H.F.W., and Jennings, H.M., *Cem. Concr. Res.* **2004**, *34*, 1499-1519.
41. Guo, X., Wu, J., Yiu, Y.-M., Hu, Y., Zhu, Y.-J., and Sham, T.-K., *Phys. Chem. Chem. Phys.* **2013**, *15*, 15033-15040.
42. Qian, F.J., Fu, R.L., Agathopoulos, S., Gu, X.G., and Song, X.F., *J. Lumin.* **2012**, *132*, 71-75.
43. Klop, E.A., Schouten, A., Vandersluis, P., and Spek, A.L., *Acta Crystallogr. C* **1984**, *40*, 51-53.
44. Sowrey, F.E., Skipper, L.J., Pickup, D.M., Drake, K.O., Lin, Z., Smith, M.E., and Newport, R.J., *Phys. Chem. Chem. Phys.* **2004**, *6*, 188-192.
45. Vandersluis, P., Schouten, A., and Spek, A.L., *Acta Crystallogr. C* **1987**, *43*, 1922-1924.
46. Hu, Y.F., Boukherroub, R., and Sham, T.-K., *J. Electron Spectros. Related Pheno.* **2004**, *135*, 143-147.
47. Chaboy, J., Barranco, A., Yanguas-Gil, A., Yubero, F., and González-Elipe, A., *Phys. Rev. B* **2007**, *75*, 075205.

Chapter 5

5 Tracking Drug Loading Capacities of Calcium Silicate Hydrate Carrier Loaded with Various Drugs: A Comparative X-ray Absorption Near Edge Structures Study

5.1 Introduction

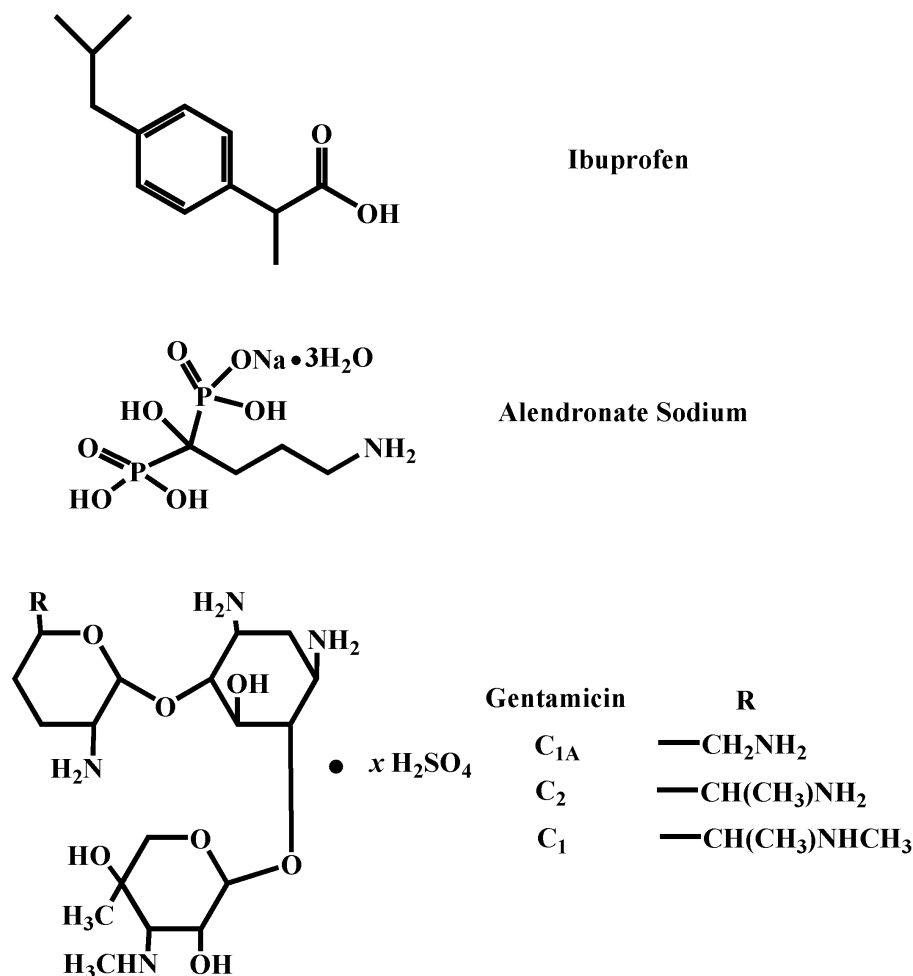
In recent years, the number of medications to treat musculoskeletal disorders such as osteoporosis and osteoarthritis is growing [1]. Conventionally, treatments are either by oral intake or injection, however, the efficiency for drug access to specific bone sites is poor, especially for bone implants for regenerations [2]. Thus, research efforts on drug delivery systems, one of the most promising applications for medical purposes, have significantly increased in the past decades. Many types of materials, including organic polymers, bioactive glasses, ceramics, and organic-inorganic composites, have been tested so far for drug delivery [3-6]. More recently, calcium silicate hydrate (CSH), a type of bioceramics cement, has gained growing attention for applications in bone tissue [7-10]. CSH not only is able to incorporate high dosages of drug molecules, but it also exhibits impressive bioactivity by transforming into hydroxyapatite in simulated body fluid (SBF). More importantly, their stimulatory effect on osteogenic differentiation of stem cells is quite satisfactory [11]. Till now, a wide range of drugs (antibiotics [12], anticancer drug [13], anti-inflammatory drug [14] and proteins [15] *etc.*) have been successfully loaded into bioceramics drug carriers. However, high drug loading capacities is still one of the key issues in drug delivery systems, which are affected by the routes and the stabilities of the drug loading in drug carriers [16]. Yang *et al.* [17] summarized possible types of drug adsorption mechanisms in mesoporous silica, which are dependent on two factors: one is the structure of the drug carriers, including pore size, surface area, and pore volume; the other is the functional groups present in drug molecules [5, 6].

* A version of this chapter has been accepted by *J. Phys. Chem. B* **2015**, *119*, 10052–10059. Reproduced by permission of The American Chemical Society. DOI:

[10.1021/acs.jpcc.5b04115](https://doi.org/10.1021/acs.jpcc.5b04115)

Similar to mesoporous silica, CSH possesses abundant silanol groups (Si-OH) on the surface [18-20]. Additionally CSH has better bioactivities because of the incorporation of Ca-O layers into SiO₂ tetrahedra [21-23]. Wu *et al.* successfully incorporated various types of drug and protein into CSH drug carriers [24, 25]; however, few studies systematically focus on the drug incorporation mechanisms in calcium silicate hydrate.

In Chapter 3, we revealed the interaction between ibuprofen (IBU) and CSH drug carriers with different morphologies with the help of XANES at the Ca and Si K-edge [26]. Herein, we further choose two more important drug compounds with their unique functional groups (Scheme 5-1): alendronate sodium (ALN), a bisphosphonate that inhibits bone resorption by osteoclasts [27]; and gentamicin sulfate (GS), a typical antibiotic drug that is extremely effective in treating bone infections [28]. In this chapter, a comparative XANES study of the interactions between the mesoporous spheres of CSH (MS-CSH) and three different drug molecules is reported, together with their drug loading capacities (DLCs) in MS-CSH, from which the relationship between DLCs and drug-carrier interactions emerges. This comparative study demonstrates that XANES is a versatile and powerful technique for tracking the effects of drug loading, and opens wider opportunities for the mechanical study of various types of biomaterials on the molecular level in drug delivery, drug release in the future. The findings provide theoretical foresights and guidance into further surface modifications or functionalization of CSH carriers to strengthen the interactions with drug molecules, and then enhance the drug loading capacities, control the drug release kinetics. It should be of interest to a wide readership in a variety of fields, such as materials engineering, biomaterials, drug delivery, surface chemistry and spectroscopy.



Scheme 5-1 Chemical structures of ibuprofen (IBU), alendronate sodium (ALN) and gentamicin sulfate (GS).

5.2 Experimental

5.2.1 Preparation of Mesoporous Spheres of CSH (MS-CSH)

MS-CSH were prepared by the self-assembly of CSH nanosheets via a sonochemical method [29]. 5 mL of a 4 M NaOH aqueous solution and 2 mL of tetraethyl orthosilicate (TEOS) were added into 500 mL of 0.03 M Ca(NO₃)₂ aqueous solution under magnetic stirring at room temperature. The resulting mixture was ultrasonically irradiated for 1 hour under ambient conditions using a high-intensity ultrasonic probe with the power of 200 W (Ti-horn, 27 kHz, Hangzhou Success, China) immersed directly in the solution. The product was collected by centrifugation and washed with deionized water and

absolute ethanol three times, respectively. Then, the powder was dried in air at 60 °C overnight.

5.2.2 Ibuprofen (IBU), Alendronate Sodium (ALN), and Gentamicin Sulfate (GS) Drug Incorporations into MS-CSH

Ibuprofen was purchased from Shanghai Yuanji Chemical Co., Ltd, alendronate sodium was purchased from Huaian San Ming Chemical Co., Ltd., and gentamicin sulfate was purchased from Wuhan Hezhong Chemical Co., Ltd. All the chemicals were used as received without further purifications. IBU was dissolved in hexane solution, ALN or GS was dissolved in deionized water, to make 3 types of drug solution with the same concentration of 40 mg·mL⁻¹. Then 1 g of as-synthesized MS-CSH powder was added into a 50 mL of IBU hexane solution, 0.4 g of MS-CSH powder was added into 20 mL of ALN aqueous solution, and 0.2 g MS-CSH was added into 10 mL of GS aqueous solution at room temperature, respectively. The flasks were immediately sealed, and the three mixtures were treated ultrasonically for 2 minutes. The three containers were oscillated at a constant rate of 160 rpm at 37 °C for 24 hours. After that the products were separated by centrifugation, washed with hexane or deionized water, respectively, and dried in air at 60 °C overnight.

5.2.3 Characterizations

The morphologies of MS-CSH before/after IBU, ALN, and GS loading were obtained by TEM (Philips CM-10 TEM). FTIR spectra of drug carriers before/after different drug loading were obtained on a FTIR spectrometer (Lambda FTIR-7600, Australia), and the loading capacities of the three drugs in MS-CSH were determined on a STA 409/PC simultaneous thermal analyzer (Netzsch, Germany) with a heating rate of 10 °C min⁻¹ in blowing air (via thermogravimetric (TG) curves).

5.2.4 XANES Measurements

XANES measurements were conducted at the Canadian Light Source (CLS) using the Soft X-ray Microcharacterization Beamline (SXRMB), which is equipped with a double crystal monochromator with two sets of interchangeable crystals operating with an energy range of 1.7 to 10 keV. The InSb (111) crystals were used for the Si K-edge

XANES measurements while the Si (111) crystals were used for the Ca K-edge XANES. The integrity of drug molecules (against radiation damage) was tested by fast XANES scans at the C K-edge with reduced beam dwell time (120 seconds for each fast XANES measurement) at the high resolution Spherical Grating Monochromator (SGM) beamline with an energy range of 250-2000 eV. At SGM beamline in the Canadian Light Source, the flux is about 10^{12} photons/s; under the slit size of 20 μm , the beam dose on the samples per area after 120 seconds fast scan is around 3×10^{11} photons/ μm^2 . The detection modes are total electron yield (TEY) and X-ray fluorescence yield (FLY) recorded with a Si drift solid state detector, tracking with surface and bulk sensitivities, respectively. XANES data were analyzed using the Athena XAS analysis software (<http://cars9.uchicago.edu/ifeffit/Ifeffit>), which is an interactive program for XAFS (X-ray absorption fine structure) analysis (spectral background removal, normalization, and linear combination fitting (LCF)).

5.2.5 FEFF Calculation

The modelling of crystal structure of CSH ($\text{Ca}_3\text{Si}_2\text{O}_7$) has been verified and reported in Chapter 3 and our previous publications [26, 29], and it has space group symmetry of $P_{2_1/a}$ with lattice constant of $a=10.557\text{\AA}$, $b=8.885\text{\AA}$, and $c=7.858\text{\AA}$, $\alpha=90^\circ$, $\beta=119.586^\circ$, $\gamma=90^\circ$. The locations of the atoms in $\text{Ca}_3\text{Si}_2\text{O}_7$ are listed in Table 5-1.

Table 5-1 Atomic coordinates of rankinite.

Site	x	y	z
Ca ₁	0.0071	0.0552	0.2893
Ca ₂	0.1677	0.5745	0.2083
Ca ₃	0.3403	0.9034	0.2839
Si ₁	0.2948	0.2357	0.4314
Si ₂	0.0903	0.2145	0.9843
O ₁	0.3579	0.4038	0.4229
O ₂	0.1782	0.2344	0.5033
O ₃	0.4105	0.1016	0.5523
O ₄	0.2007	0.1629	0.2120
O ₅	0.0970	0.3857	0.9810
O ₆	0.1451	0.1487	0.8437
O ₇	0.9299	0.1536	0.9394

The XANES (X-ray absorption near edge structure) spectra of the cluster of the $\text{Ca}_3\text{Si}_2\text{O}_7$ compounds with this crystal model are calculated by the multiple scattering theory using the FEFF9 code [30]. This theory is based on the real-space Green's function approach [31].

5.3 Results and Discussion

5.3.1 Morphologies of MS-CSH Loaded with Different Drug Molecules

The morphologies of mesoporous spheres of CSH before and after drug loading are shown in Figure 5-1. CSH spheres with diameter around 1 μm are formed by the self-assembly of nanosheets (Figure 5-1(a)) [29]. After the loading of IBU, ALN, and GS drugs, it should be noted that the general microsphere shape remains. However, the contrast of CSH microspheres changed to some extent (Figure 1(b) to 1(d)), which is due to the drug incorporation, leading to the increase in the thickness of CSH microspheres.

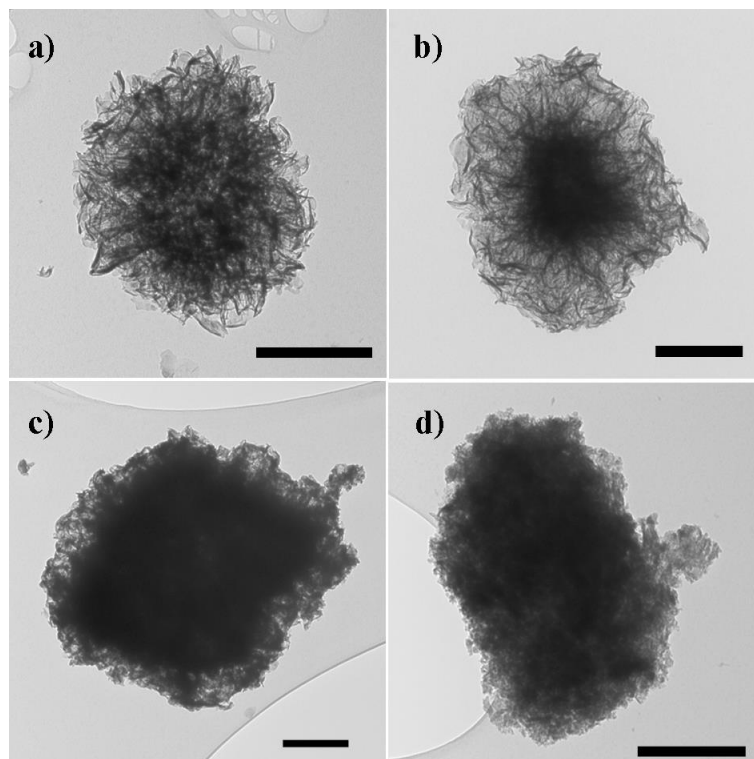


Figure 5-1 TEM images of CSH before/after drug loading: (a) mesoporous spheres of CSH (MS-CSH); (b) MS-CSH-IBU; (c) MS-CSH-ALN; (d) MS-CSH-GS; contrast change means the thickness increase of CSH microspheres, indicating the drug incorporations (scale bar = 500 nm).

5.3.2 Stabilities of Drug Molecules under the Collimated X-ray Beam

We have shown that IBU is stable under the collimated beam in Chapter 4 [32]. In order to examine the possibility of noticeable radiation damage of the ALN and GS drug molecules, fast XANES scan tests at the C K-edge (120 seconds for each fast scan spectrum measurement, the time of normal XANES collection is around 15 minutes) were performed, as shown in Figure 5-2(a). It is apparent from Figure 5-2(a) that there are no noticeable spectral changes observed for ALN and GS drug molecules after the exposure to the X-ray beam, indicating that the structures of ALN and GS are stable under the collimated X-ray beam. In order to confirm the integrity of the three types of drug molecules after their loading, Figure 5-2(b) compares the XANES spectra before and after drug loading at the C K-edge. There are several distinct spectral features need to

mention: For CSH alone, the peak (a) at 290.3 eV is the “fingerprint” feature of CO₂, which is normal to see when CSH is stored in the atmosphere for a long time; peak (b) at 285.2 eV is related to the C 1s-π* transition from aryl ring of ibuprofen; the peak at 288.5 eV (c) is from the 1s-π* (C=O) of carboxylic acid as in the case of IBU. The peaks at around 289 eV (d and e) is from C 1s-σ* (C-OH/C-NH₂) of ALN and GS drug molecules [33-36]. From the spectral comparisons at the C K-edge before and after the loading of various drug molecules, there are no noticeable changes to the above spectral features which are directly related to the functional groups of different drug molecules. Hence, it indicates that the structures of three drugs are intact after drug loading.

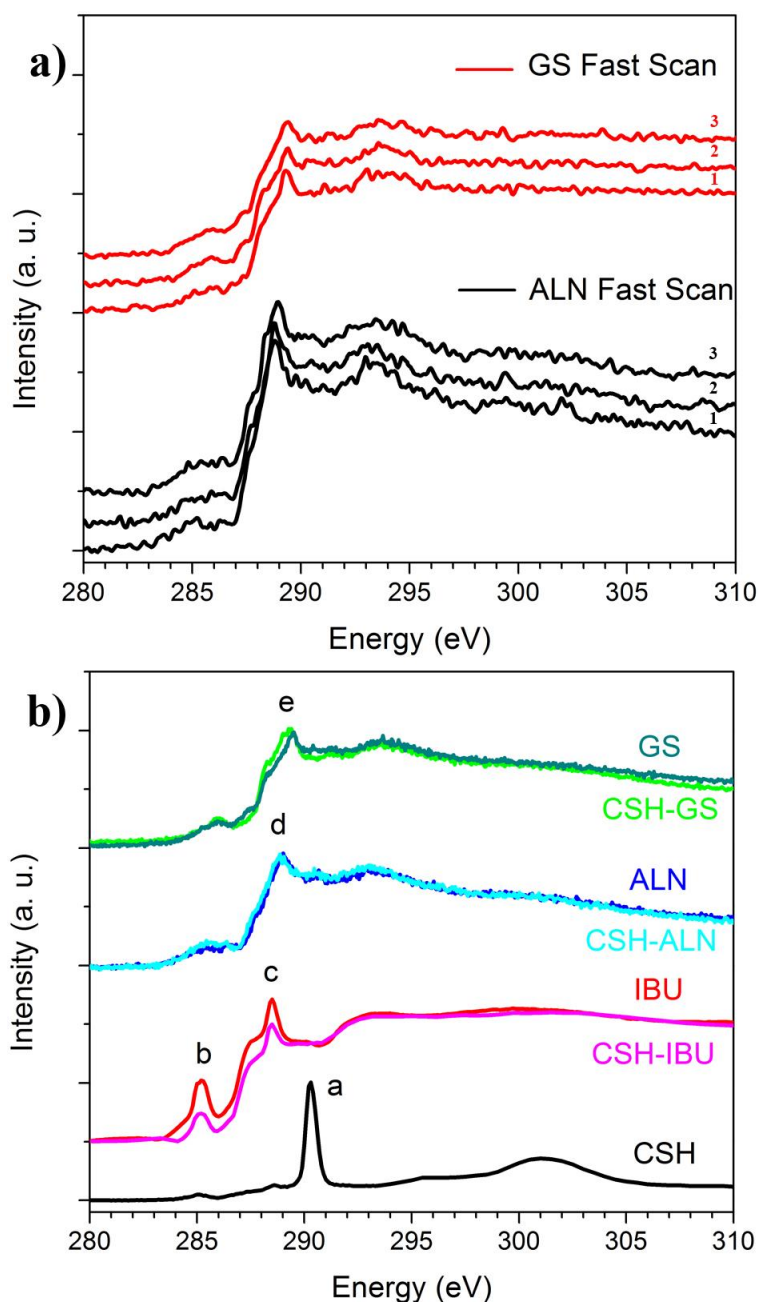


Figure 5-2 (a) Fast scan XANES spectra of ALN and GS drug molecules at the C K-edge (spectra were obtained sequentially), and (b) C K-edge XANES comparisons before and after the loading of IBU, ALN and GS into CSH mesoporous microspheres (feature “a” at 290.3 eV is for CO₂ adsorption in CSH; “b” at 285.2 eV is the feature of aryl ring of IBU; “c” at 288.5 eV is 1s- π* transition from carboxylic acid as in the case of IBU; “d” and “e” at around 289 eV is from C 1s-σ* (C-OH/C-NH₂) of ALN and GS drug molecules, respectively).

5.3.3 Studies of Interactions between MS-CSH and Different Drug Molecules by XANES

Before we compare the interactions between different drug molecules and CSH, we recall the crystal structure of CSH; CSH has a layered structure, shown in Figure 5-3.

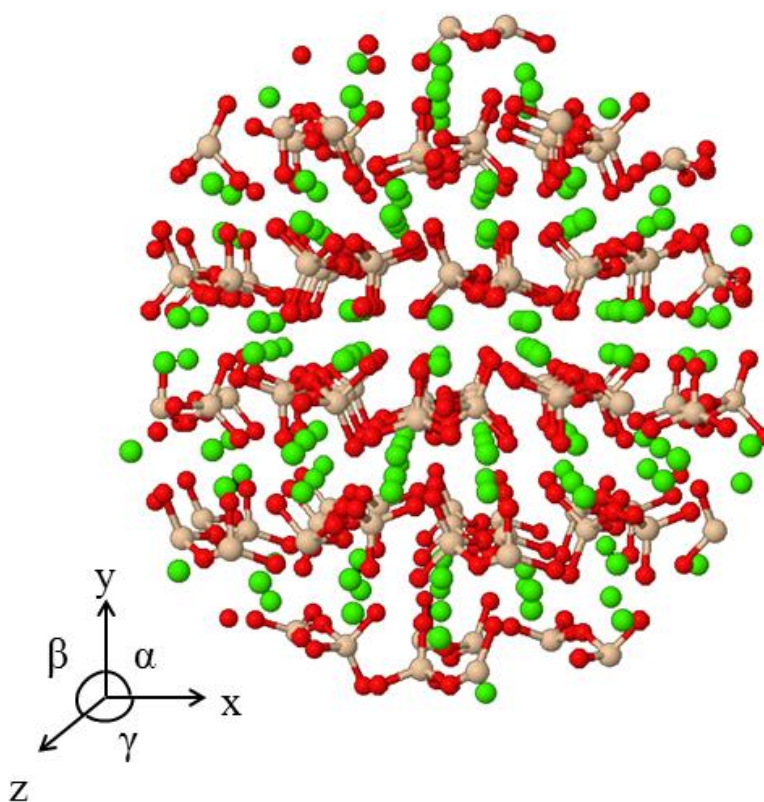


Figure 5-3 Crystal structure of CSH (green, beige and red dots represent for Ca, Si and O atoms, respectively; $\alpha=90^\circ$, $\beta=119.586^\circ$, and $\gamma=90^\circ$).

It contains silicate “dreierkette” linear chains, in which every two of three silicate tetrahedra share two oxygen atoms with central Ca ions, and we call the central part Ca-O structure Ca-O layer. These layers are separated by an intermediate layer where water, excess Ca^{2+} , OH^- and other ions are inserted to balance the charge [18-20, 37, 38]. In this chapter, only the TEY spectra were shown because both TEY and FLY are very similar, suggesting these samples are homogeneous (Figure 5-4). XANES spectra comparisons of

different drug-CSH delivery systems at the Ca K-edge were shown in Figure 5-5 to illustrate the carrier-drug interactions.

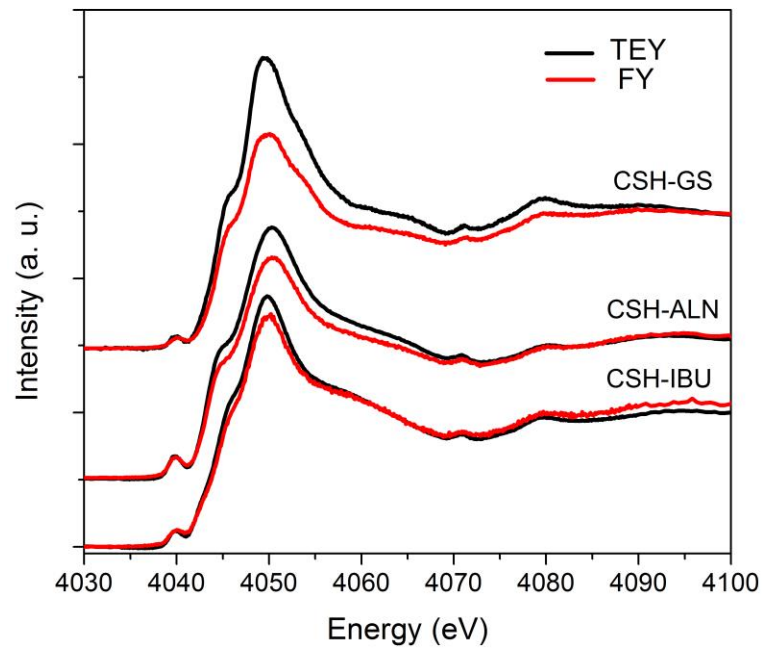


Figure 5-4 Comparisons of Ca K-edge TEY and FY XANES spectra of MS-CSH loaded with different drug molecules.

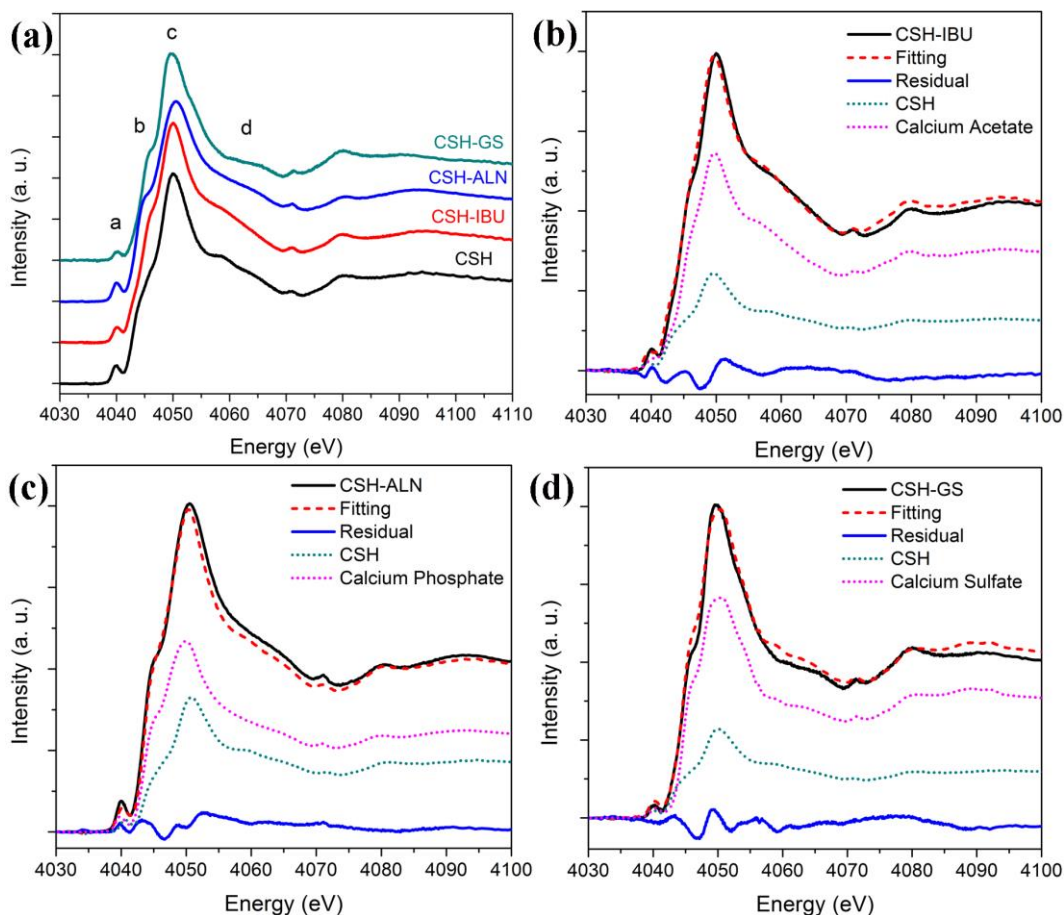


Figure 5-5 Ca K-edge total electron yield (TEY) XANES spectra (a) and linear combination fitting (b to d) of MS-CSH loaded with IBU, ALN and GS.

Figure 5-5(a) shows the Ca K-edge XANES of MS-CSH before and after loading of three types of drug molecules. There are four discernible XANES features, labelled “a”, “b”, “c”, and “d” with increasing photon energy. The pre-edge peak (feature “a”) can be ascribed to Ca $1s \rightarrow 3d$ transition; the shoulder “b” is assigned to the $1s \rightarrow 4s$ transition. Although they are dipole forbidden, both features “a” and “b” can be still observed because of the hybridization of Ca with ligand states of np-character. The most intense peak (feature “c”) is due to Ca $1s \rightarrow 4p$ dipole transition. The shoulder after the main resonance (feature “d”) is mainly from multiple scattering processes [39-41]. By comparing with the spectrum of MS-CSH (black), the differences from the features of b and c in the CSH-IBU (red), CSH-ALN (blue) and CSH-GS (dark cyan) spectra can be observed (more noticeable from the comparisons in the first derivative spectra at the Ca

K-edge in Figure 5-6), showing the change of the Ca local structures by the interaction between different drug molecules and Ca-OH groups. Based on the functional groups of different drug molecules, XANES spectra of standard samples (calcium acetate ($\text{Ca}(\text{C}_2\text{H}_3\text{O}_2)_2$), calcium phosphate ($\text{Ca}_3(\text{PO}_4)_2$), and calcium sulfate (CaSO_4)) were also recorded (Figure 5-6), and a linear combination fitting (LCF) (Figure 5-5(b) to 5-5(d)) were analyzed by Athena software, and the results are listed in Table 5-2.

Table 5-2 Ca K-edge linear combination fitting results of MS-CSH loaded with IBU, ALN and GS drug.

	Percentage (%)				R-factor
	CSH	$\text{Ca}(\text{C}_2\text{H}_3\text{O}_2)_2$	$\text{Ca}_3(\text{PO}_4)_2$	CaSO_4	
CSH-IBU	31	69	-	-	0.001430
CSH-ALN	41	-	59	-	0.002171
CSH-GS	29	-	-	71	0.001805

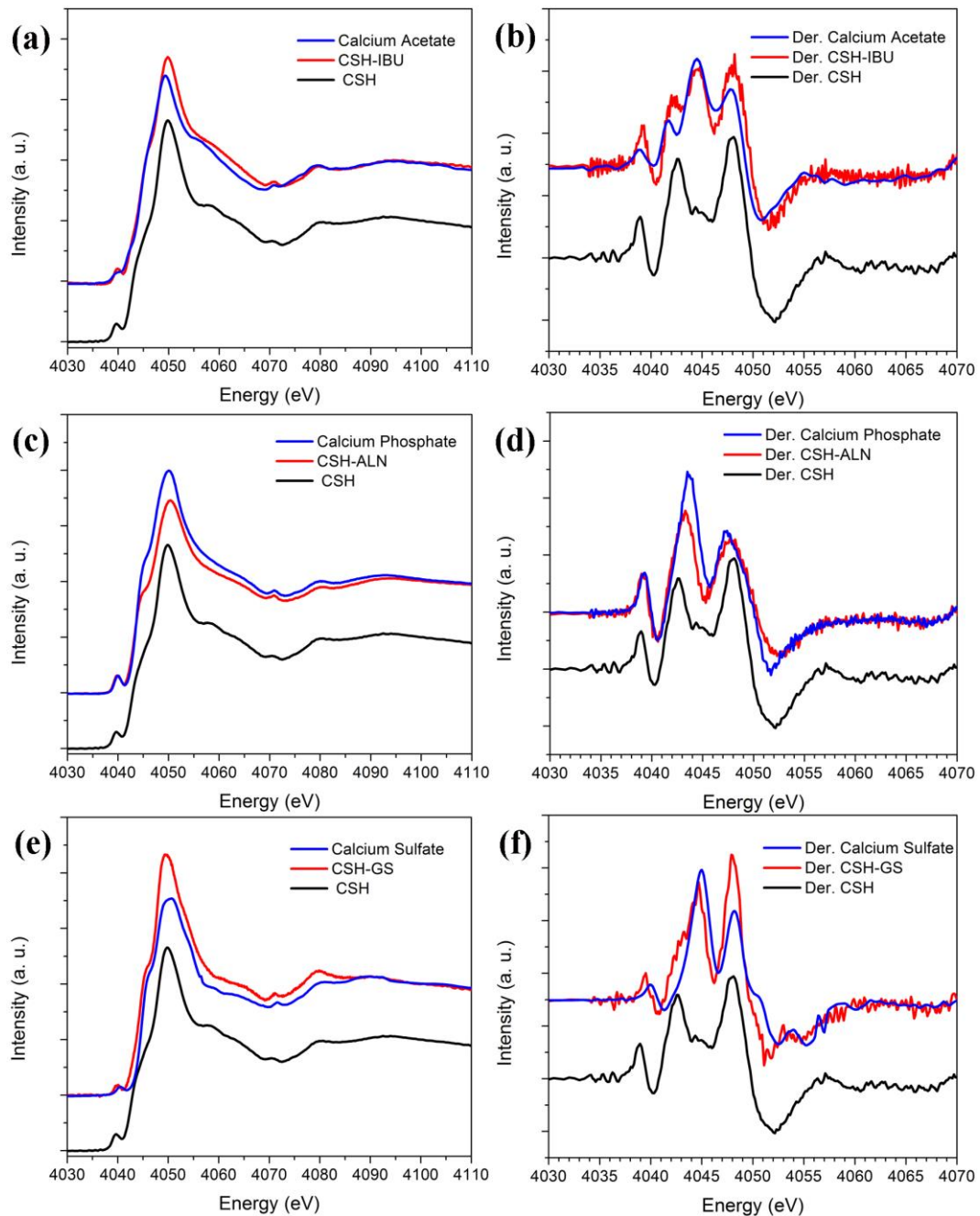
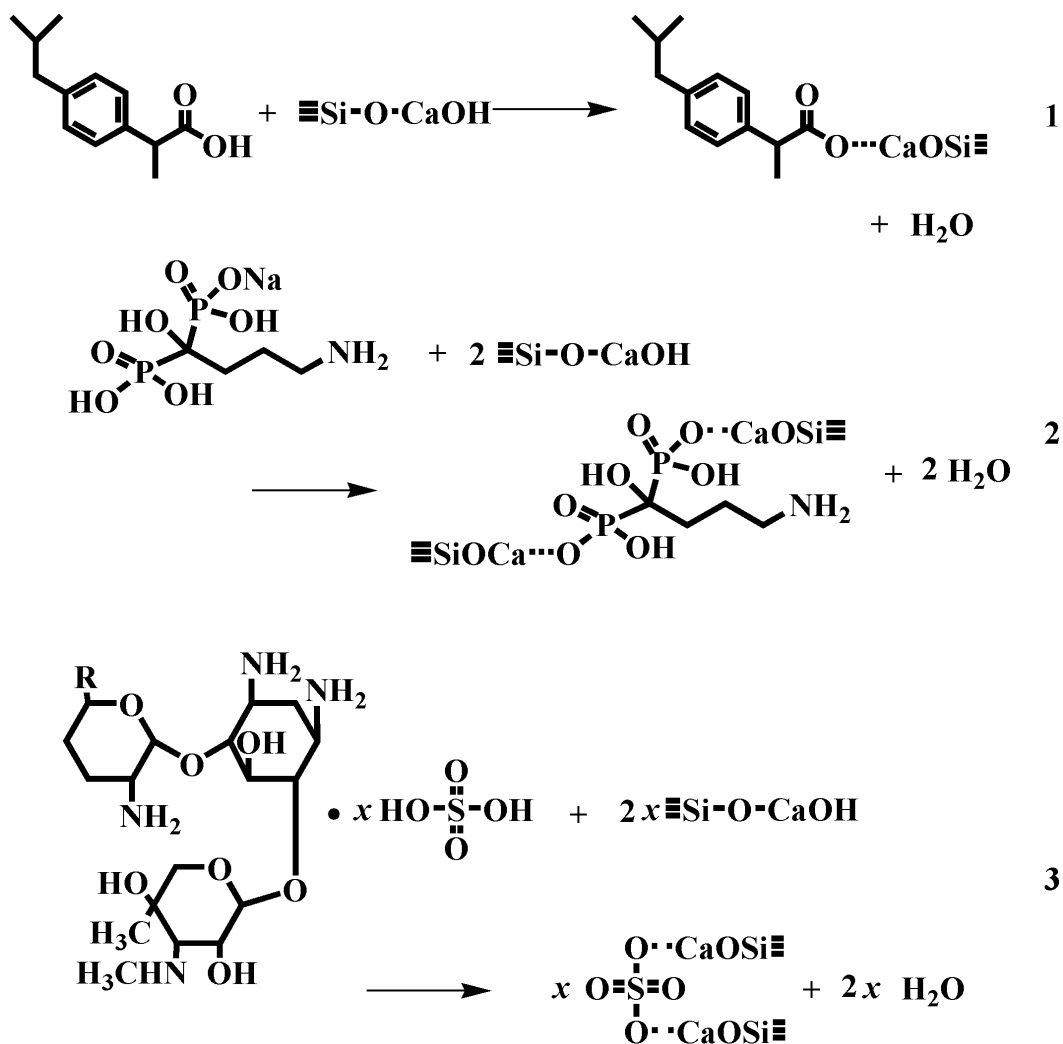


Figure 5-6 XANES (a, c, e) and their first derivative (b, d, f) spectra comparisons of MS-CSH before, after loaded with ibuprofen (IBU), alendronate sodium (ALN) and gentamicin sulfate (GS) and relative standard samples.

From both LCF results and XANES spectra comparisons (Figure 5-6), we can infer that the Ca K-edge XANES spectra of CSH-IBU, CSH-ALN and CSH-GS are more similar to those of calcium acetate, phosphate and sulfate, respectively, indicating significant

changes of the local environment of Ca occurred after drug loading. Because CSH microspheres are three-dimensional network structures assembled by tiny CSH nanosheets, it is highly possible that there are many Si-OH and Ca-OH groups ending on the surface of nanosheets as the building blocks throughout the network of CSH carriers. Thus, we conclude that IBU, ALN and GS molecules are linked to Ca-OH groups by primarily electrostatic interactions; more specifically via the interactions between carboxylic acid groups, phosphonic acid groups and sulfuric acid groups, respectively (Scheme 5-2).



Scheme 5-2 Electrostatic interactions between Ca-OH groups and different drug molecules.

In Figure 5-7(a) (Si K-edge), before drug loading, there is only one broad peak (labelled “a”, black), which is due to the Si 1s to 3p transition [40, 42], while IBU, ALN and GS drug loadings lead to significant changes to the local structure of silicate. First, the width of main resonance became narrower and the peak shifted to higher energy (~ 0.5 eV). Second, a noticeable new feature (labelled “b”) was evolved, which is observed in TEY spectra and absent in the FLY. These observations indicate that strong interactions between different functional groups of drug molecules and silicate layers mostly took place on the surface of MS-CSH.

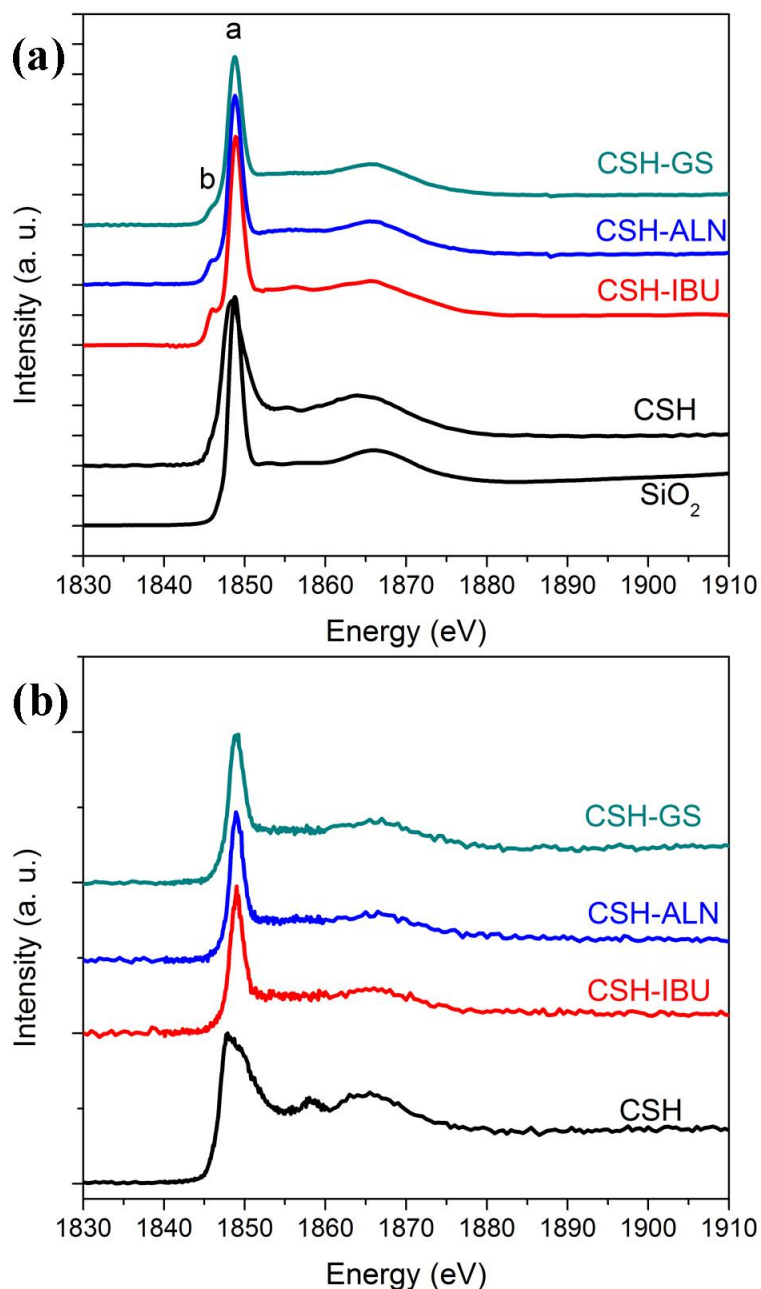
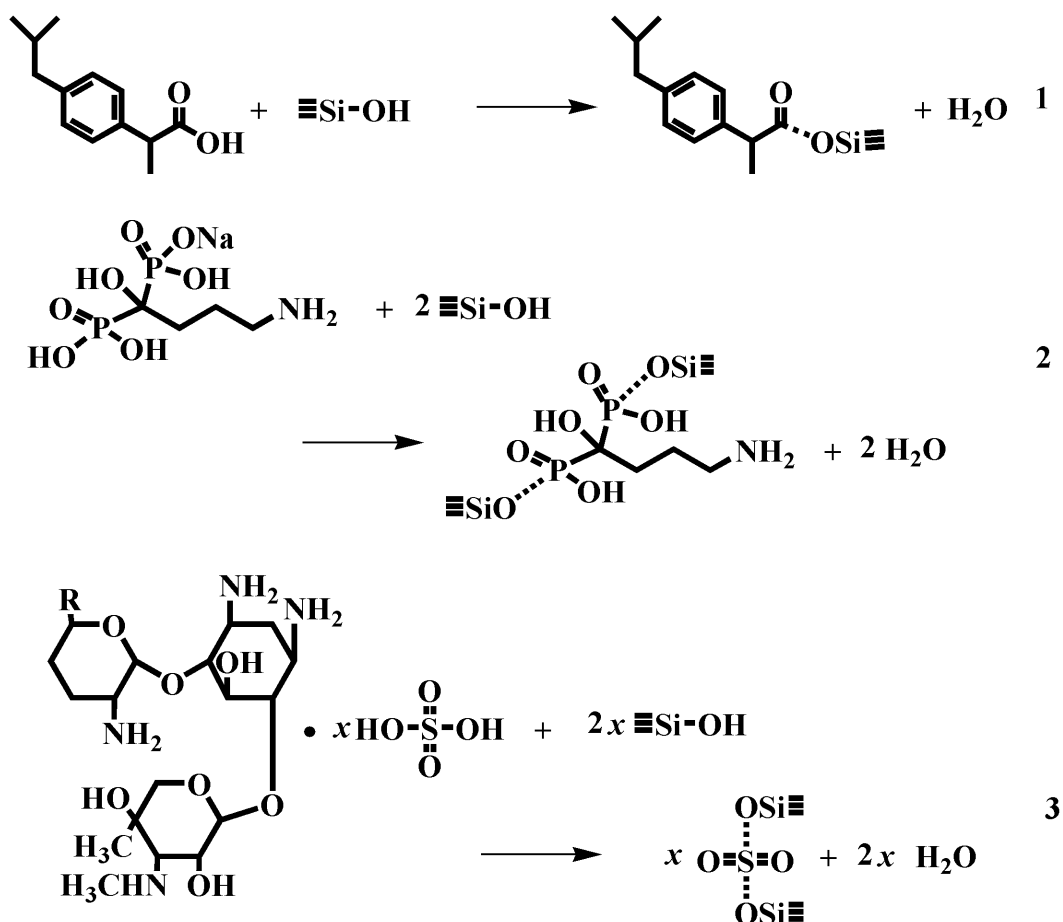


Figure 5-7 Si K-edge total electron yield (TEY) (a) fluorescence yield (FLY) (b) XANES spectra of MS-CSH and MS-CSH loaded with different types of drug molecules.

Silanol groups (Si-OH) on the surface provide the active sites for the interactions between MS-CSH drug carrier and different drug molecules (Scheme 5-3). Compared with the original silicate structure, the introduction of new drug molecules induces the

distortion of the silicate tetrahedron on the surface [43-45]; hence a new peak “b” emerged at the lower photon energy range only from TEY spectra. However, most of silicates in the bulk of MS-CSH are still in the tetrahedral environment after drug loading. Besides, MS-CSH in our study has a higher Ca/Si ratio (Ca/Si=1.5) [26, 29], leading to a higher concentration of Ca-OH groups on the surface or in the interlayer, relative to Si-OH groups (Figure 5-3) [19, 20, 38]. Hence, the electrostatic interactions more likely take place between Ca and drug molecules (due to the higher Ca-OH concentration and activity of Ca-OH, Si-OH to carboxylic acid), making silicate chains “isolated”; more like the regular “SiO₄” tetrahedral environment, hence the main resonances at the Si K-edge TEY and FY are similar to that of SiO₂ (Figure 5-7(a), sharp peak, located at higher photon energy).



Scheme 5-3 Electrostatic interactions between silanol groups and different drug molecules on the surface.

5.3.4 Studies of Interactions between MS-CSH and Different Drug Molecules by FTIR Spectroscopy

To further provide evidence for the existence of the interactions between different drug molecules and MS-CSH, FTIR spectra of the MS-CSH before and after loading with different drug molecules were obtained, as shown in Figure 5-8. For the MS-CSH, the absorption around 970 cm^{-1} is attributed to the Si-O stretching vibration of silicate. Similar to the case of XANES analysis, several changes are apparent. First, after IBU loading, the characteristic peak of C=O of IBU shifted from 1720 cm^{-1} to 1560 cm^{-1} , which is attributed to the polarity changes of -COOH group (linked to CSH). Besides, the Si-O stretching is blue shifted, which is ascribed to polarity change of Si-O-Si (formation of Si-O-C, magenta arrows) [26, 29, 46]. Second, the characteristic absorption peaks of pure ALN molecules at 1020 cm^{-1} and 1050 cm^{-1} (P=O stretching vibration, indicated by the navy arrows) are present [47], and after ALN loading, new absorption peaks were observed at 961 cm^{-1} and 1084 cm^{-1} (in cyan arrows), which are assigned to P-O stretching (PO_4^{3-}) [48]. Third, major absorption peaks of pure GS were at 619 cm^{-1} and $\sim 1100\text{ cm}^{-1}$ (dark cyan arrows) [49], and compared with the CSH FTIR spectrum (black), a new broad peak was observed at $\sim 1115\text{ cm}^{-1}$ (green), which belongs to the bands of sulfate ions. All these observations are in a good agreement with the XANES results discussed above; however, only parts of interactions can be confirmed because of the overlapping of absorption bands.

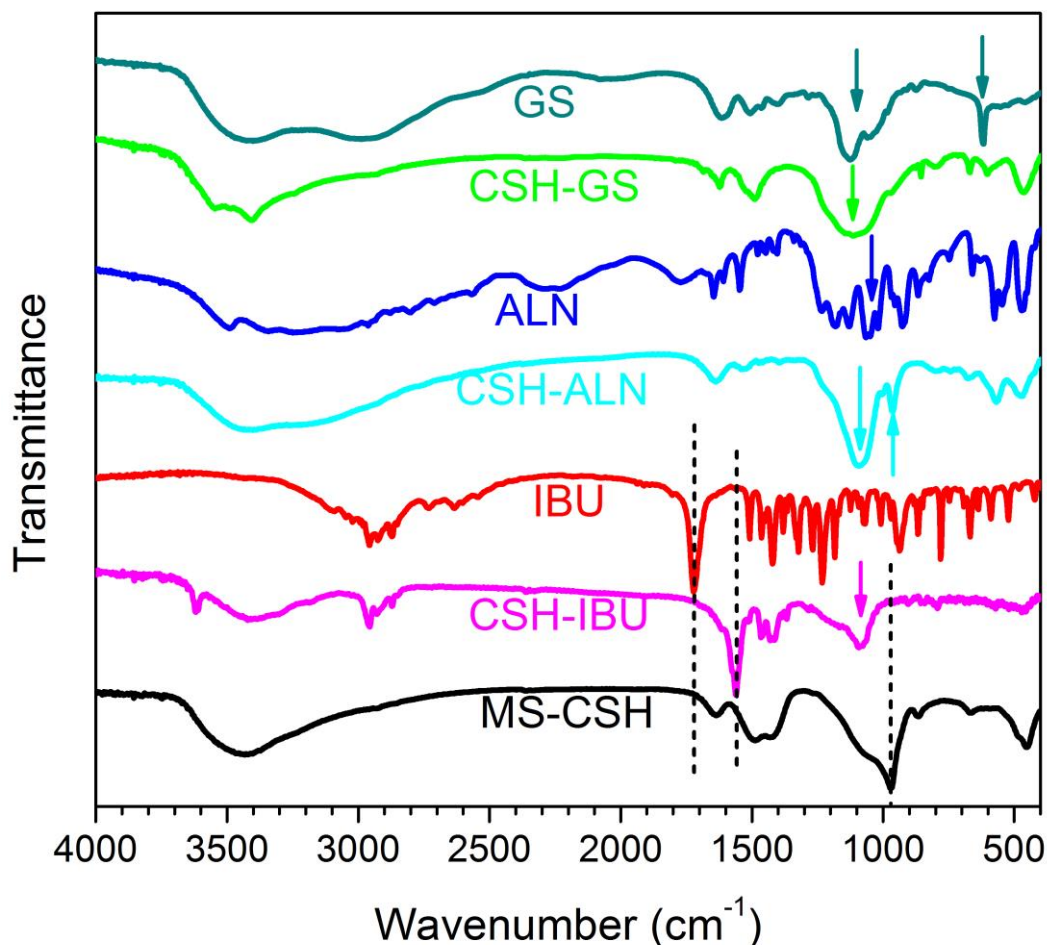


Figure 5-8 FTIR spectra of CSH mesoporous microspheres before and after loading of different drug molecules, and pure IBU, ALN, GS are also shown for comparisons (magenta arrows: Si-O-C stretching; navy arrow: P=O stretching vibration; cyan arrows: P-O stretching; dark cyan arrows: major representative absorption peaks of pure GS; green arrow: bands of sulfate ions).

5.3.5 Relationship between Drug Loading Capacities and Interactions of CSH and Different Drug Molecules

In order to compare the drug loading capacities (DLCs) of MS-CSH for the three types of drugs, thermogravimetric (TG) analysis of MS-CSH has been carried out as shown in Figure 5-9. A two-level step profiles were observed from different drug loading systems (IBU, ALN and GS). The first step occurring at around 80-180 °C is from the evaporation of water and the second step of weight loss is from the drug burning in air. The drug

loading capacities (DLCs) and efficiencies of different drug delivery systems are listed in Table 5-3. Compared with ALN and GS drug molecules, MS-CSH has an extremely high drug loading capacity with IBU drug molecules.

Table 5-3 Drug loading capacities for MS-CSH drug delivery systems.

Drug Delivery System	DLCs (wt. %) ^[a]	Loading Efficiencies (%) ^[b]
CSH-IBU	185.4	92.5
MS-CSH-ALN	15.4	19.2
MS-CSH-GS	8.9	22.2

^[a] Drug Loading Capacities = $m_{\text{drug}}/m_{\text{CSH}}$ wt. %.

^[b] Loading Efficiencies: the ratio of loaded amount of drug to the initial amount of drug before loading.

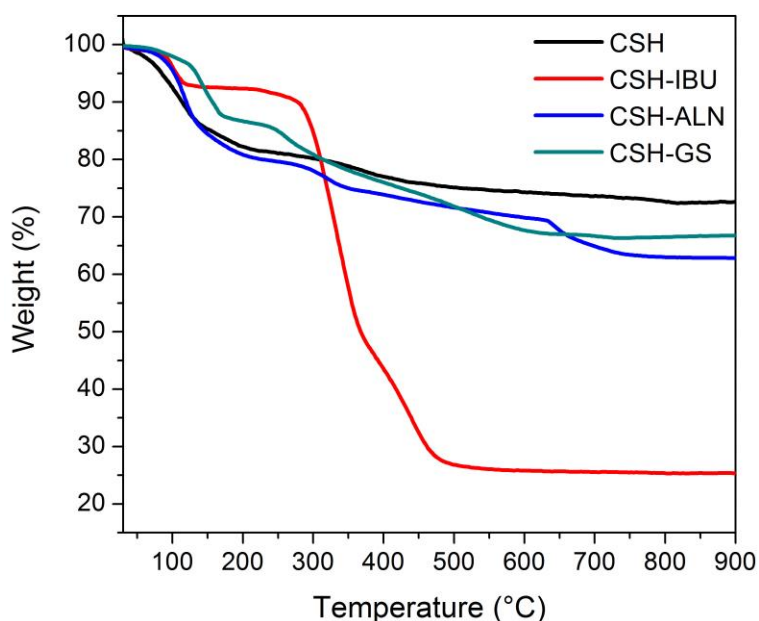


Figure 5-9 TG curves of MS-CSH and MS-CSH-Drug delivery systems (more weight change observed after loading, more drugs are incorporated into CSH).

Since the sizes of the drug molecules are in the range of one nanometer [2, 27], the nature of drug molecules (functional groups) must play a vital role in the drug loading capacities. Hence, the interactions between drug molecules and drug carriers are crucial for the enhancement of DLCs. According to the XANES analysis, only acidic functional groups of the drug molecules can be linked to abundant Ca-OH and Si-OH groups of CSH mesoporous microspheres by electrostatic interactions. It is interesting to note that

IBU has the highest drug loading amounts compared with the other two drugs. Shankland *et al.* [50] proved the existence of hydrogen-bonded dimers of IBU by single-crystal pulsed neutron diffraction. Babonneau *et al.* [51] demonstrated high mobility of IBU molecules, which allows the attachment of more IBU drug molecules by adsorption. Moreover, the electrostatic interaction between Ca^{2+} ions from the CSH carrier and the carboxylic acid groups from the IBU drug molecules is one main factor responsible for high IBU drug loading capacity. The IBU adsorption capacity on the CSH carrier nearly follows the stoichiometric ratio of Ca^{2+} ions from the CSH carrier and the $-\text{COOH}$ groups from the IBU drug molecules, as demonstrated in previous work [24].

On the other hand, MS-CSH has the lowest DLCs of GS which is caused by the strong interactions to some extent; although sulfate ions were linked to the Ca-OH and Si-OH groups in the aqueous solution, the alkyl part (gentamicin part) is not connected to the MS-CSH and this interaction may prevent further GS drug attachment to the MS-CSH. Besides, the gentamicin part may suffer from steric effect, which also hinders more GS drug molecules attachment. As a result, GS drug molecules are only loaded into MS-CSH by the physical adsorptions into the mesopores; leading to lowest DLCs than the other two CSH-Drug systems.

5.4 Conclusions

In this chapter, the interactions between different functional groups from three different drug molecules and MS-CSH have been studied by XANES and FTIR spectroscopy. The conclusions are summarized in Table 5-4. MS-CSH provides active linkage sites for acidic functional groups of drug molecules by electrostatic interactions; while they are not sensitive to the other groups such as amino and hydroxyl groups. Hence this result will provide some hints to scientists in drug delivery and materials fields: the acidic drug molecules can be loaded into CSH easily with higher DLCs; while further surface modifications of CSH such as with acidic groups on the surface, may provide further incorporation of basic drug molecules into CSH via the interactions, and may provide high DLCs and controlled drug release profiles. Besides, the ratio between Ca^{2+} ions from the CSH carrier and the $-\text{COOH}$ groups from the IBU drug molecules is one main factor responsible for high IBU drug loading capacity.

Table 5-4 Sensitivities of Ca-OH, Si-OH groups to different functional groups of drug molecules.

	Ca-OH	Si-OH
Carboxylic acid (R-COOH) groups	+	+
Phosphonic acid groups	+	+
Amino (R-NH ₃) groups	-	-
R-OH groups	-	-
Sulfuric acid groups	+	+

“+” means functional groups will have an interaction with either Ca-OH or Si-OH; while “-” means they will not.

5.5 References

- 1 Ginebra, M.P., Traykova, T., and Planell, J.A., *J. Control. Release* **2006**, *113*, 102-110.
- 2 Vallet-Regí, M., *Chem. Eur. J.* **2006**, *12*, 5934-5943.
- 3 Yoshida, R., Sakai, K., Okano, T., and Sakurai, Y., *Adv. Drug Deliver. Rev.* **1993**, *11*, 85-108.
- 4 Kataoka, K., Harada, A., and Nagasaki, Y., *Adv. Drug Deliver. Rev.* **2001**, *47*, 113-131.
- 5 Vallet-Regi, M., Balas, F., and Arcos, D., *Angew. Chem. Int. Edit.* **2007**, *46*, 7548-7558.
- 6 Wang, S.B., *Micropor. Mesopor. Mater.* **2009**, *117*, 1-9.
- 7 Liu, X.Y., Tao, S.Y., and Ding, C.X., *Biomaterials* **2002**, *23*, 963-968.
- 8 Siriphannon, P., Kameshima, Y., Yasumori, A., Okada, K., and Hayashi, S., *J. Eur. Ceram. Soc.* **2002**, *22*, 511-520.
- 9 Rodriguez-Lorenzo, L.M., Garcia-Carrodegua, R., Rodriguez, M.A., De Aza, S., Jimenez, J., Lopez-Bravo, A., Fernandez, M., and Roman, J.S., *J. Biomed. Mater. Res. A* **2009**, *88A*, 53-64.

10. Wei, J., Chen, F.P., Shin, J.W., Hong, H., Dai, C.L., Su, J.C., and Liu, C.S., *Biomaterials* **2009**, *30*, 1080-1088.
11. Wu, C.T. and Chang, J., *Biomed. Mater.* **2013**, *8*, 032001.
12. Zhu, Y.F. and Shi, J.L., *Micropor. Mesopor. Mater.* **2007**, *103*, 243-249.
13. Zhu, Y.F., Ikoma, T., Hanagata, N., and Kaskel, S., *Small* **2010**, *6*, 471-478.
14. Otsuka, M., Nakahigashi, Y., Matsuda, Y., Fox, J.L., Higuchi, W.I., and Sugiyama, Y., *J. Control. Release* **1998**, *52*, 281-289.
15. Blom, E.J., Klein-Nulend, J., Wolke, J.G.C., Kurashina, K., van Waas, M.A.J., and Burger, E.H., *Biomaterials* **2002**, *23*, 1261-1268.
16. Ramila, A., Munoz, B., Perez-Pariente, J., and Vallet-Regi, M., *J. Sol-Gel. Sci. Technol.* **2003**, *26*, 1199-1202.
17. Yang, P.P., Gai, S.L., and Lin, J., *Chem. Soc. Rev.* **2012**, *41*, 3679-3698.
18. Nonat, A., *Cem. Concr. Res.* **2004**, *34*, 1521-1528.
19. Cong, X.D. and Kirkpatrick, R.J., *Adv. Cem. Based Mater.* **1996**, *3*, 144-156.
20. Chen, J.J., Thomas, J.J., Taylor, H.F.W., and Jennings, H.M., *Cem. Concr. Res.* **2004**, *34*, 1499-1519.
21. Kusachi, I., Henmi, C., Kawahara, A., and Henmi, K., *Mineral. J.* **1975**, *8*, 38-47.
22. Hench, L.L., *J. Am. Ceram. Soc.* **1998**, *81*, 1705-1728.
23. Saravanapavan, P., Jones, J.R., Pryce, R.S., and Hench, L.L., *J. Biomed. Mater. Res. A* **2003**, *66A*, 110-119.
24. Wu, J., Zhu, Y.-J., and Chen, F., *Small* **2013**, *9*, 2911-2925.

25. Wu, J., Zhu, Y.-J., Chen, F., Zhao, X.Y., Zhao, J., and Qi, C., *Dalton Trans.* **2013**, *42*, 7032-7040.
26. Guo, X., Wu, J., Yiu, Y.-M., Hu, Y., Zhu, Y.-J., and Sham, T.-K., *Phys. Chem. Chem. Phys.* **2013**, *15*, 15033-15040.
27. Balas, F., Manzano, M., Horcajada, P., and Vallet-Regi, M., *J. Am. Chem. Soc.* **2006**, *128*, 8116-8117.
28. Sivakumar, M. and Panduranga Rao, K., *Biomaterials* **2002**, *23*, 3175-3181.
29. Wu, J., Zhu, Y.-J., Cao, S.W., and Chen, F., *Adv. Mater.* **2010**, *22*, 749-753.
30. Rehr, J.J., Kas, J.J., Prange, M.P., Sorini, A.P., Takimoto, Y., and Vila, F., *C. R. Phys.* **2009**, *10*, 548-559.
31. Rehr, J.J. and Albers, R.C., *Rev. Mod. Phys.* **2000**, *72*, 621-654.
32. Guo, X., Wang, Z., Wu, J., Wang, J., Zhu, Y.-J., and Sham, T.-K., *Nanoscale* **2015**, *7*, 6767-6773.
33. Solomon, D., Lehmann, J., Kinyangi, J., Liang, B., Heymann, K., Dathe, L., Hanley, K., Wirick, S., and Jacobsen, C., *Soil Sci. Soc. Am. J.* **2009**, *73*, 1817-1830.
34. Benzerara, K., Yoon, T.H., Tyliszczak, T., Constantz, B., Spormann, A.M., and Brown, G.E., *Geobiology* **2004**, *2*, 249-259.
35. Zubavichus, Y., Shaporenko, A., Grunze, M., and Zharnikov, M., *J. Phys. Chem. A* **2005**, *109*, 6998-7000.
36. Tivanski, A.V., Hopkins, R.J., Tyliszczak, T., and Gilles, M.K., *J. Phys. Chem. A* **2007**, *111*, 5448-5458.
37. Megaw, H.D. and Kelsey, C.H., *Nature* **1956**, *177*, 390-391.
38. Richardson, I.G., *Cem. Concr. Res.* **2008**, *38*, 137-158.

39. Eichert, D., Salome, M., Banu, M., Susini, J., and Rey, C., *Spectrochim. Acta B* **2005**, *60*, 850-858.
40. Demirkiran, H., Hu, Y., Zuin, L., Appathurai, N., and Aswath, P.B., *Mater. Sci. Eng. C* **2011**, *31*, 134-143.
41. Cormier, L. and Neuville, D.R., *Chem. Geol.* **2004**, *213*, 103-113.
42. Li, D., Bancroft, G.M., Kasrai, M., Fleet, M.E., Feng, X.H., Tan, K.H., and Yang, B.X., *Solid State Commun.* **1993**, *87*, 613-617.
43. Chaboy, J., Barranco, A., Yanguas-Gil, A., Yubero, F., and González-Elipe, A., *Phys. Rev. B* **2007**, *75*, 075205.
44. Hu, Y.F., Boukherroub, R., and Sham, T.-K., *J. Electron Spectros. Related Pheno.* **2004**, *135*, 143-147.
45. Sutherland, D.G.J., Kasrai, M., Bancroft, G.M., Liu, Z.F., and Tan, K.H., *Phys. Rev. B* **1993**, *48*, 14989-15001.
46. Stuart, B.H., *Infrared Spectroscopy: Fundamentals and Applications.* **2004**: Wiley.
47. Liu, X.M., Qu, S.X., Lu, X., Ge, X., and Leng, Y., *Biomed. Mater.* **2009**, *4*, 065008.
48. Zhang, G.L., Huang, R., Li, Z.C., Yang, X.Y., Chen, X.Y., Xia, W., Sun, X.L., Yang, G.J., Gao, C.Y., and Gou, Z.R., *J. Inorgan. Biochem.* **2012**, *113*, 1-8.
49. Sarabia-Sainz, A., Ramos-Clamont Montfort, G., Lizardi-Mendoza, J., Sánchez-Saavedra, M.D.P., Candia-Plata, M.D.C., Guzman, R.Z., Lucero-Acuña, A., and Vazquez-Moreno, L., *Int. J. Drug Deliver.* **2012**, *4*, 209-218.
50. Shankland, N., Wilson, C.C., Florence, A.J., and Cox, P.J., *Acta Crystallogr. C* **1997**, *53*, 951-954.

51. Babonneau, F., Yeung, L., Steunou, N., Gervais, C., Ramila, A., and Vallet-Regi, M., *J. Sol-Gel. Sci. Technol.* **2004**, *31*, 219-223.

Chapter 6

6 Tracking the Transformations of Mesoporous Microspheres of Calcium Silicate Hydrate in Nanoscale upon Ibuprofen Release: An XANES and STXM Study

6.1 Introduction

Nanostructured bioceramics nanomaterials, such as calcium phosphate ($\text{Ca}_3(\text{PO}_4)_2$, CaP) and calcium silicate (CS), have been widely applied as implants for the restoration of bone and tooth. The development of mesoporous bioceramics opens up new possibilities for drug delivery and bone therapies [1]. Since the discovery of Bioglass® by Hench and co-workers in 1971 [2], various kinds of silicates, and glasses have been investigated for hard tissue repair and replacement. Recently, CS material was proved to be excellently bioactive and a potential candidate for bone repair and therapies [3-9]. A common feature for all bioactive CS is that they can bond to living bones by forming hydroxyapatite ($\text{Ca}_{10}(\text{PO}_4)_6(\text{OH})_2$, HAp) on their surface when they are immersed into simulated body fluid (SBF) with ion concentrations similar to human blood plasma.

In previous studies, many characterization methods have been used in the study of the transformation mechanisms from CS to HAp. Among them, X-ray diffraction (XRD), infrared spectroscopy (IR), scanning electron microscopy (SEM), transmission electron microscopy (TEM) and energy-dispersive X-ray spectrometry (EDX) are the most common techniques to study the composition, structure and morphology of the products.

* A version of this chapter has been published in *CrystEngCommun.* **2015**, *17*, 4117 – 4124. Reproduced by permission of The Royal Society of Chemistry. DOI:

[10.1039/C5CE00500K](https://doi.org/10.1039/C5CE00500K)

However, the mechanism of biomineralization of CS is still not completely clear: one controversial issue is the presence of CaCO_3 ; Siriphannon *et al.* [3] and Wan *et al.* [6] reported that CaCO_3 were present during the HAp formation; while Gou *et al.* [5] reported that the final products would be carbonate-containing HAp; Li *et al.* [10] reported the absence of CaCO_3 after the *in vitro* test; the other problem is about the silica-rich layer during biomineralization. Although it is well accepted that the silica-rich layer provides favourable sites for HAp precipitation, there has been no direct evidence showing the presence of silica-rich layer using the above mentioned conventional techniques. X-ray absorption near edge structures (XANES) spectroscopy is an element specific technique, which probes the electronic states intimately associated with the absorbing atom in the vicinity of the X-ray absorption threshold (LUMO in molecules and the conduction band in semiconductor for example via dipole transitions) [11]. XANES provides information on the oxidation state, coordination and symmetry of the element of interest. Materials with different structures or compositions have their unique XANES spectra at specific absorption edges (e. g.: calcium silicate hydrate (CSH), amorphous calcium phosphate, HAp and CaCO_3 show different XANES features at the Ca K-edge), by which qualitative analysis is very reliable by “fingerprinting” [12-16]. Under favourable conditions (high quality data), quantitative information can be obtained by fitting the XANES data to a linear combination of XANES of standard components. Additionally, synchrotron source provides collimated and high photon flux that allows for detecting the minor components (even less than 0.1 wt. % [17]) in materials no matter they are crystalline, amorphous (XRD is only suitable for crystals) or in solution. Scanning transmission X-ray microscopy (STXM) [18, 19] provides spectromicroscopic information of nanomaterials; thus both electronic and spatial features of a single nanostructure can be revealed at nanoscale (~30 nm). Therefore, the combination of STXM and XANES can monitor the spectral change and image the transformation from CSH to HAp at nanoscale simultaneously, hence affords a comprehensive understanding of the biomineralization mechanism of CSH in connection with drug release.

Previous investigations reported the formation of HAp on CS in SBF without drug loading [3-6, 10]. Few researches illustrated the bioactivity of bioactive glasses (BG) and HAp when drug was released in SBF [20-22]. In this chapter, we investigated the drug

(ibuprofen, IBU) release from mesoporous CSH microspheres and the biomineralization of CSH during drug release in SBF using synchrotron based techniques (XANES and STXM). This study provides new insights into the mechanism of CSH biomineralization.

6.2 Experimental

6.2.1 Preparation of Mesoporous CSH Microspheres

CSH mesoporous microspheres were prepared by the self-assembly of CSH nanosheets via a sonochemical method [23]. 5 mL of a 4 M NaOH aqueous solution and 2 mL of tetraethyl orthosilicate (TEOS) were added into 500 mL of 0.03 M $\text{Ca}(\text{NO}_3)_2$ aqueous solution under magnetic stirring at room temperature. The resulting mixture was ultrasonically irradiated for 1 hour under ambient conditions using a high-intensity ultrasonic probe with the power of 200 W (Ti-horn, 27 kHz, Hangzhou Success, China) immersed directly in the solution. The product powder was collected after centrifugation and washed with deionised water and absolute ethanol three times, then dried in air at 60 °C overnight.

6.2.2 IBU Drug Loading

The as-synthesized powder (1.0 g of mesoporous CSH microspheres) was added into a 50 mL IBU hexane solution ($\sim 40 \text{ mg}\cdot\text{mL}^{-1}$) in a flask at room temperature. The flask was immediately sealed to prevent hexane from evaporation, and the mixture was treated by ultrasound for 2 minutes. Then the flask was oscillated at a constant rate of 160 rpm at 37 °C for 24 hours. After that the product was separated by centrifugation, washed with hexane, and dried in air at 60 °C overnight.

6.2.3 *In Vitro* Test

To investigate the kinetics of IBU release from CSH microspheres and the biomineralization of CSH and to mimic those processes in the human body, experiments were carried out in a simulated body fluid (SBF). The ion concentrations of the SBF, shown in Table 6-1, are similar to the physiological concentrations in the human blood plasma [24]. The pH of the SBF solution was buffered at 7.40 ± 0.02 with 1 mol/L HCl and tris-(hydroxymethyl)-aminomethane [$(\text{CH}_2\text{OH})_3\text{CNH}_2$]. 2 g of the as-synthesized

CSH-IBU powder was split equally into 10 specimens (0.2 g each), and then each of them was soaked in 200 mL of SBF solution at 36.5 °C for 1, 2, 3, 4, 5, 6, 12, 24, 36, 48 hours, respectively under constant shaking (120 rpm). A portion of the IBU-release medium (2.0 mL) was extracted for UV-Vis absorption analysis (Techcomp, UV2300) at the wavelength of 263 nm at given time intervals shown above. The solid products were separated by centrifugation, rinsed with absolute ethanol, and dried in air at 60 °C overnight for XRD, TEM and XANES studies.

Table 6-1 Ion concentrations of SBF and human blood plasma (mmol/L)

Ion	SBF	Human Blood Plasma
Na ⁺	142.0	142.0
K ⁺	5.0	5.0
Mg ⁺	1.5	1.5
Ca ²⁺	2.5	2.5
Cl ⁻	147.8	103.8
HCO ₃ ²⁻	4.2	27.0
HPO ₄ ²⁻	1.0	1.0

6.2.4 Characterization

The thermogravimetric (TG) curves were measured on a STA 409/PC simultaneous thermal analyzer (Netzsch, Germany) with a heating rate of 10 °C min⁻¹ in blowing air to measure the drug loading capacities of mesoporous CSH microspheres. The morphologies of the CSH microspheres before/after IBU loading, CSH-IBU microspheres after IBU releasing in SBF for various time periods were obtained by TEM (Philips CM-10 TEM). The compositions of biomineralization products for various time periods were characterized by XRD (Rigaku D/max 2550 V, Cu K α radiation, $\lambda = 1.54178 \text{ \AA}$). The concentrations of Ca, P and Si of the SBF after IBU releasing from CSH were determined using an inductively coupled plasma (ICP) instrument (JY 2000-2, Horiba, France).

6.2.5 XANES Measurements

XANES measurements were conducted at the Canadian Light Source (CLS) using the Soft X-ray Microcharacterization Beamline (SXRMB), which is equipped with a double crystal monochromator with two sets of interchangeable crystals operating with an

energy range of 1.7 to 10 keV. The InSb (111) crystals were used for the Si K-edge XANES measurements while the Si (111) crystals were used for the Ca K-edge and P K-edge XANES. The detection modes are total electron yield (TEY) and X-ray fluorescence yield (FLY), tracking with surface and bulk sensitivities, respectively. XANES data were analyzed using the Athena XAS analysis software

(<http://cars9.uchicago.edu/ifeffit/Ifeffit>), which is an interactive program for XAFS analysis, combining high-quality and well-tested XAFS analysis algorithms, tools for general data manipulation, and graphical display of data.

6.2.6 STXM Measurements

STXM measurement was conducted at the Soft X-ray Spectromicroscopy (SM) beamline at the CLS; SM is equipped with a 25 nm outermost-zone zone plate (CXRO, Berkeley Lab). The diffraction-limited spatial resolution for this zone plate is about 30 nm with a spectral resolution of 0.05 eV at the C K-edge. Image sequence (stack) scans over a range of photon energies were acquired for the same sample region at the C K-edge, Si K-edge and P K-edge. STXM data were analyzed using the aXis2000 software package (<http://unicorn.chemistry.mcmaster.ca/aXis2000.html>), which allows for detailed interactive processing of the images and fitting the image stacks with the reference X-ray absorption spectra. More details about STXM measurement and data analysis can be found elsewhere [25, 26].

6.3 Results and Discussion

6.3.1 Morphologies of CSH Microspheres Before and After IBU Loading

The morphologies of the mesoporous CSH microspheres before and after IBU loading were reported in our previous studies and chapters (Figure 6-1) [23, 27, 28].

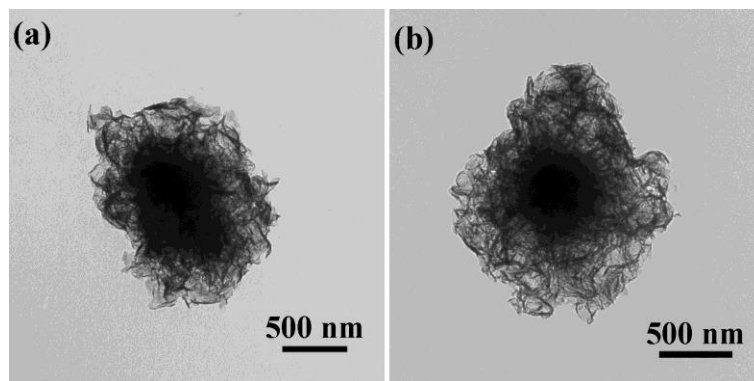


Figure 6-1 TEM images of mesoporous CSH microspheres before (a) and after (b) IBU loading.

6.3.2 IBU Loading Capacity of CSH Microspheres

To measure the drug loading capacity of CSH microspheres, the TG analysis of CSH and CSH loaded with IBU were carried out. As shown in Figure 6-2, there is a two-level-step profile for the weight loss of the CSH-IBU system; the weight losses at 80-100 °C and 280-480 °C originate from the evaporation of water and the clean burn of IBU in air, respectively. The drug loading capacity (DLC) ($m_{\text{IBU}}/m_{\text{CSH}}$ wt. %) of CSH microsphere is calculated based on the TG curves, showing a high value of 180 wt. % (i.e. 1.80 g IBU is loaded per gram of carriers), which agrees with our previous studies [23, 27].

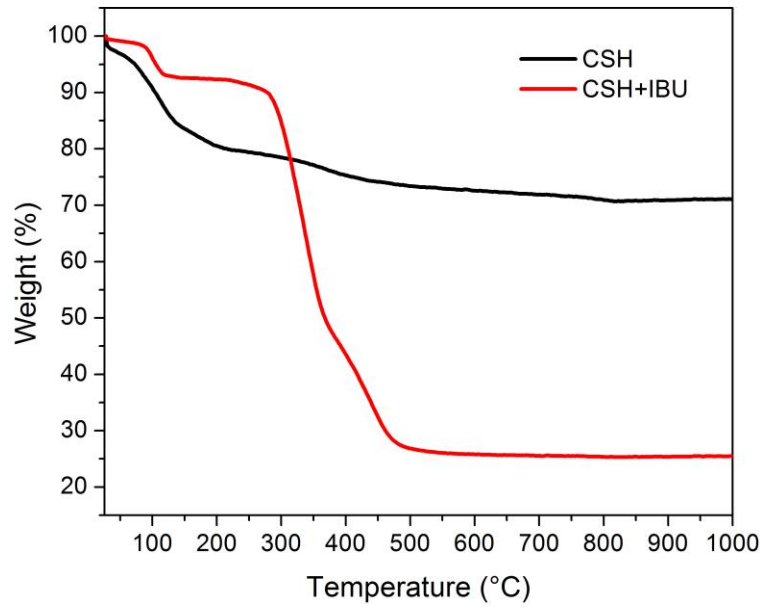


Figure 6-2 TG curves of mesoporous CSH microspheres and CSH loaded with IBU.

6.3.3 Morphologies Changes of CSH Microspheres in SBF upon IBU Release

Figure 6-3 shows the micrographs of the CSH microspheres after soaking in the SBF solutions for various time periods. In comparison with the microspheres before soaking, most of the carriers remained intact after the samples were soaked in the SBF for 1 hour. At 5 hours, some microspheres were broken down; sheets-like products can be found on the edge of microspheres. After longer soaking time (24 hours and 48 hours), microspheres can be barely observed, instead, most of the microspheres turned into the aggregation of particles and flakes.

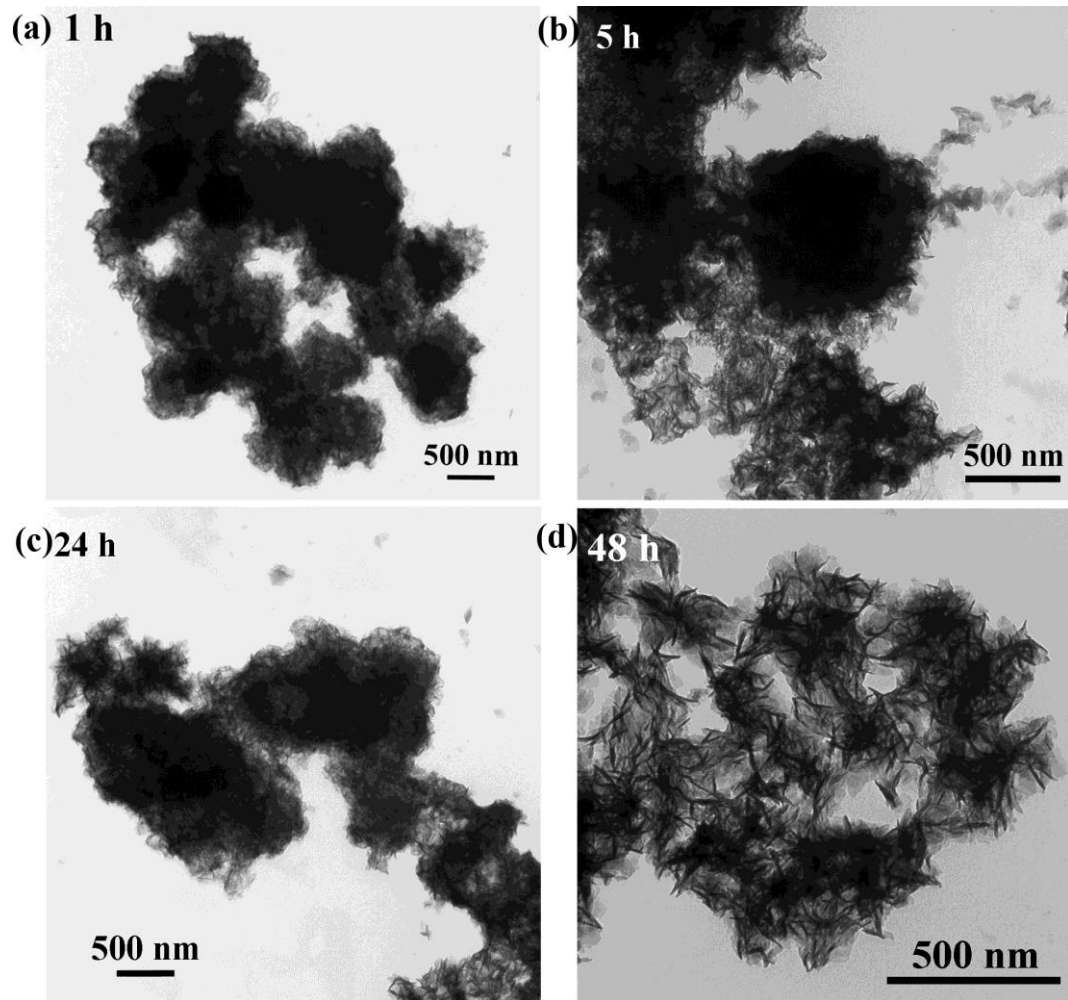


Figure 6-3 TEM micrographs of CSH-IBU microspheres soaked in SBF solution for different time: (a) 1 hours, (b) 5 hours, (c) 24 hours, and (d) 48 hours.

6.3.4 XRD Study of CSH Microspheres Phase Transformations in SBF upon IBU Release

To determine the compositions of the products having immersed in SBF solution for various period of time, XRD data of the CSH-IBU microspheres soaked in the SBF solution for various time periods were obtained as shown in Figure 6-4. One can see that starting from 4 h, the diffraction peaks (e.g. $2\theta = 26^\circ$ and 32° PDF number: 09-0432) of HAp emerge clearly in the XRD patterns. On the contrary, in the first 3 h, although weak crystalline CSH diffraction patterns can be still observed ($2\theta = 29^\circ$ PDF number: 33-0306), a broad peak is more prominent, indicating that some amorphous components

were formed, however, no further information can be revealed from XRD to illustrate the compositions of amorphous specimens.

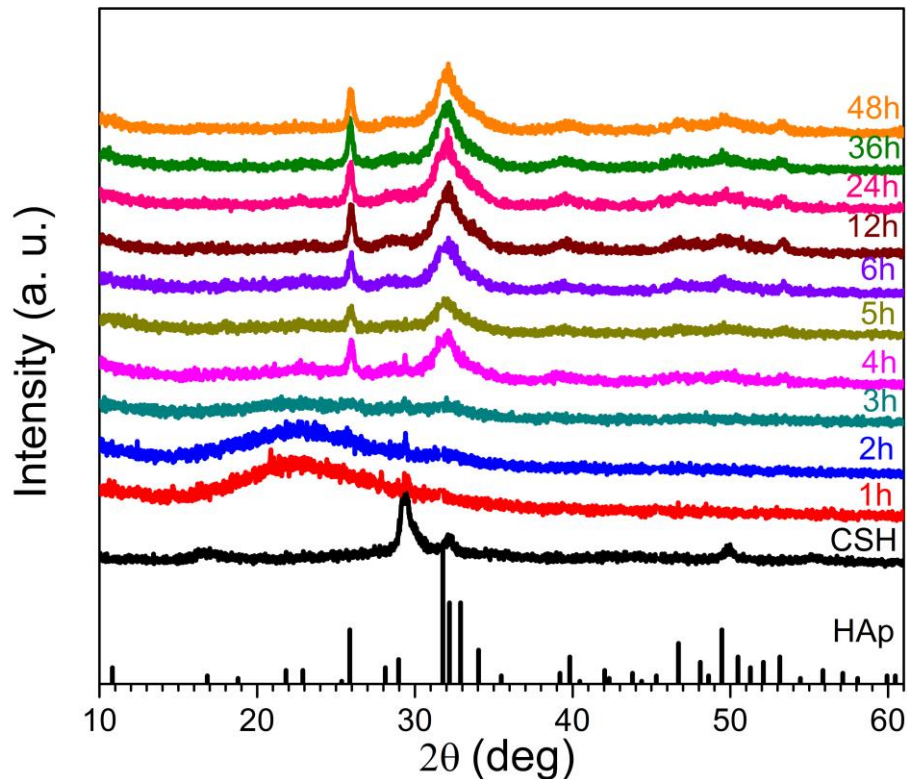


Figure 6-4 XRD patterns of CSH-IBU powder soaked in SBF solution for different time.

6.3.5 XANES Study of CSH Microspheres Phase Transformations in SBF upon IBU Release

In order to reveal the amorphous compositions of the products formed in the first several hours, XANES measurements at the Ca K-edge, P K-edge and Si K-edge were conducted (Figure 6-5). We only show TEY XANES for the discussions because both TEY and FLY are similar since the specimens are homogeneous and optically thin and FLY shows no detectable thickness effects.

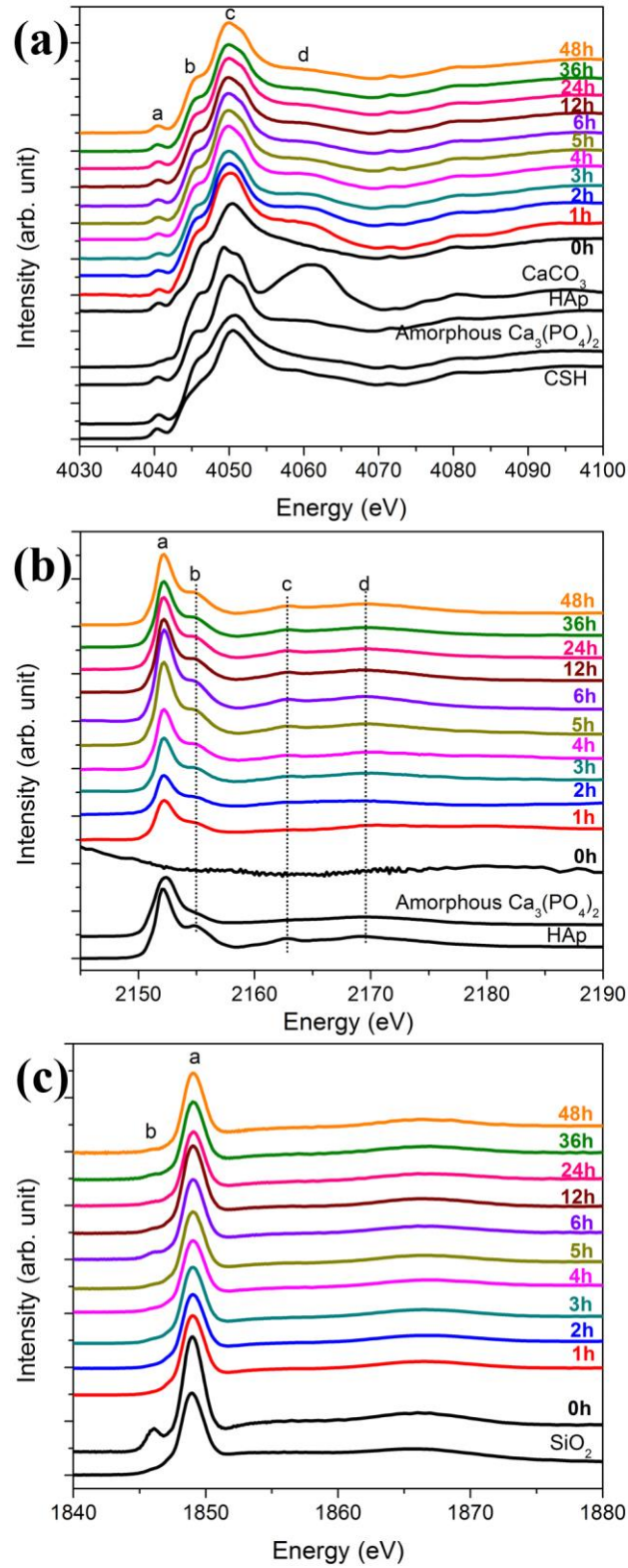


Figure 6-5 Ca (a), P (b) and Si (c) K-edge XANES spectra of CSH-IBU microspheres soaked in SBF solution for various time.

Figure 6-5(a) shows the Ca K-edge XANES of CSH-IBU microspheres after having been immersed in the SBF solution for different periods of time. There are four discernible XANES features, labelled as “a”, “b”, “c”, and “d” at increasing photon energy. The most intense peak (feature “c”) is due to Ca 1s → 4p transition. The pre-edge peak (feature “a”) can be ascribed to 1s → 3d transition; the shoulder “b” is assigned to the 1s → 4s transition, both of which can be observed are due to the hybridization of Ca with ligand states of np-character, leading to the departure from perfect crystal symmetry [29]. The shoulder after the main resonance (feature “d”) is mainly from multiple scattering processes [30-32]. By comparing the spectra of CSH, amorphous calcium phosphate and HAp standard samples, the main “fingerprint” differences between CSH and HAp clearly identifiable are the white line “c” and feature “d”. Starting from the spectrum of 3 h (dark cyan), the spectra are almost the same as that of HAp, indicating the formation of HAp on the surface of mesoporous CSH microspheres. After a linear combination fitting procedure using standard spectra of CSH, amorphous calcium phosphate, HAp and CaCO₃ (Figure 6-6), the compositions of amorphous samples in the first 4 hours can be clearly revealed, as shown in Table 6-2.

Table 6-2 Ca K-edge linear combination fitting results of samples after soaked in SBF solution in the first 4 hours.

	Percentage (%)				R-factor
	CSH	CaCO ₃	Amorphous CaP	HAp	
1 hour	8	6	13	73	0.00298
2 hour	3	11	9	77	0.000984
3 hour	0	7	1	92	0.000809
4 hour	0	0	0	100	0.000864

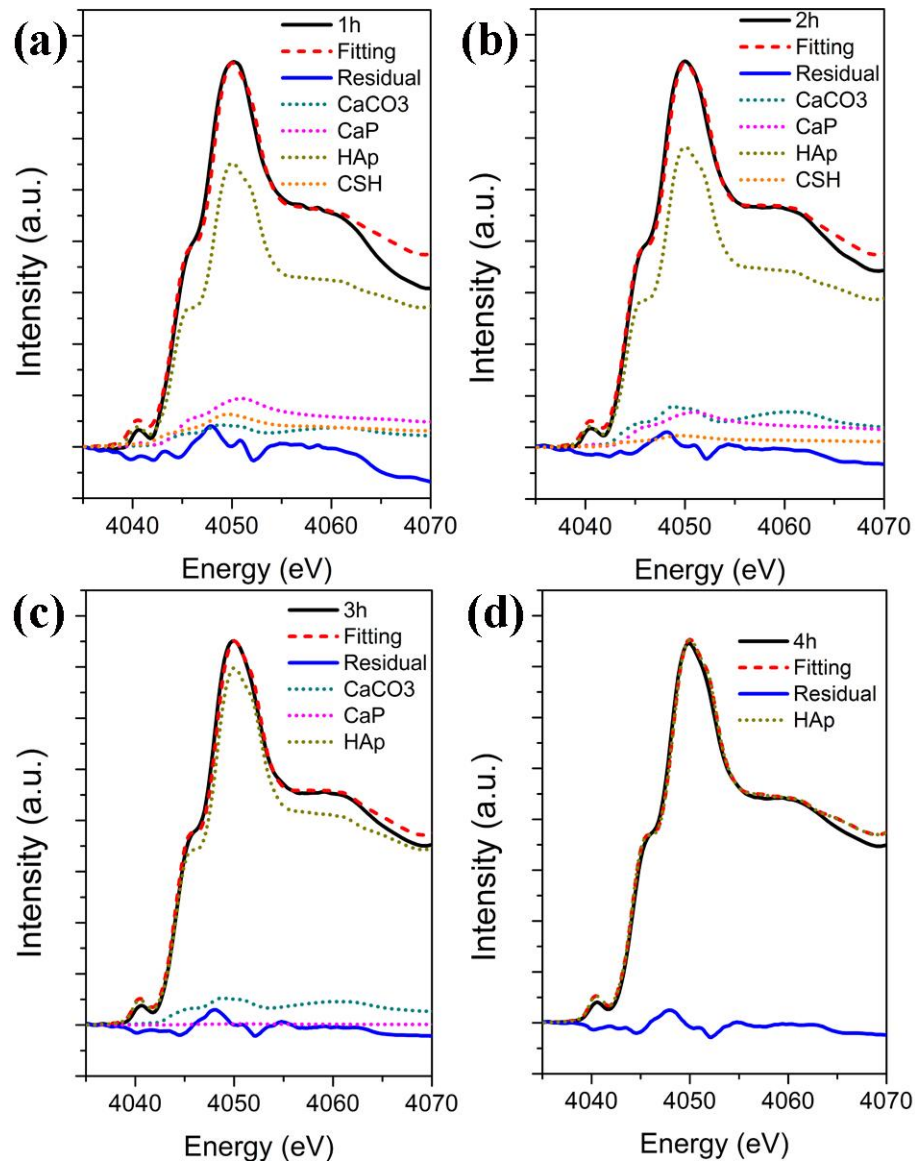


Figure 6-6 Comparison of Ca K-edge XANES spectra and linear combination fitting in the first 4 hours.

Combined with the results from XRD, we find that the dominant composition is amorphous HAp at the early stage of drug release, of which the percentage increase until the spectrum of 4 h which is identical to that of HAp, and it gradually becomes crystalline. Moreover, from the first several spectra, the contribution of amorphous CaCO_3 and calcium phosphate can also be observed, indicating that amorphous calcium phosphate was first formed then transformed into amorphous HAp rapidly, which is due to the stability of amorphous calcium phosphate in aqueous media: HAp has a lower

solubility in water than other form of calcium phosphate, and CaCO_3 was formed during the biomineralization.

The P K-edge XANES spectra also provide direct evidence for the formation of HAp. As seen in Figure 6-5(b), there is no P signal before the samples were immersed in the SBF solution (the curve labelled as 0 h); while a strong P signal was detected after the powder was soaked in the SBF for 1 h. The principal peak “a” results from P 1s \rightarrow 3p transitions. For the HAp minerals, there exhibits a distinctive post-edge shoulder “b” and higher-energy peaks at around 2163 eV (“c”) and 2170 eV (“d”) [15, 31, 33]. For the first 2 h, features b, c and d are less apparent, which are mixed with some amorphous $\text{Ca}_3(\text{PO}_4)_2$. While all of the features are similar to those of HAp after the CSH-IBU microspheres were soaked in the SBF solution for more than 3 h. The result of linear combination fitting at the P K-edge (Figure 6-7 and Table 6-3) is consistent with the Ca K-edge results.

Table 6-3 P K-edge linear combination fitting results of samples after soaked in SBF solution in the first 3 hours.

	Percentage (%)		R-factor
	Amorphous CaP	HAp	
1 hour	22	78	0.006551
2 hour	6	94	0.005300
3 hour	1	99	0.004686

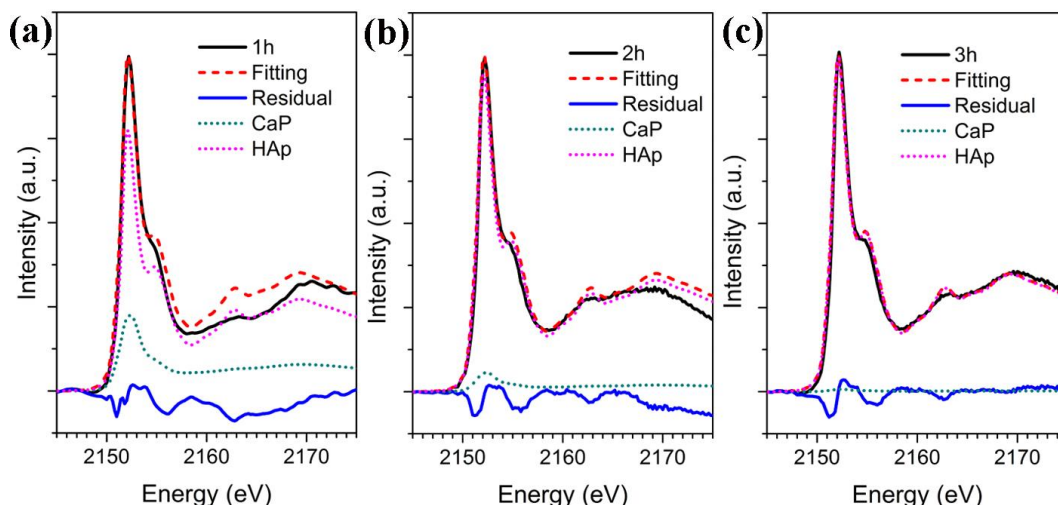


Figure 6-7 Comparison of P K-edge XANES spectra and linear combination fitting in the first 3 hours.

The observation at the Si K-edge is interesting (Figure 6-5(c)). During the IBU release process, there is only one prominent peak (labelled as “a”) in the Si K-edge XANES spectra, which is identified as the Si 1s to 3p transition for silicon (IV) in a tetrahedral oxygen ligand environment [31, 34]. Comparing to the spectrum of the CSH-IBU before IBU release (0 h), the peak at lower photon energy labelled as “b”, is due to the interaction between silanol groups (Si-OH) and carboxylic acid groups of IBU [27, 28] (less prominent in the FLY spectra, 0 h in Figure 6-8); it disappears nearly entirely in the spectra of CSH-IBU after IBU release. The disappearance of this peak once CSH-IBU microspheres were immersed in the SBF is likely due to the fast release of IBU from CSH carriers into SBF, resulting in the rapid decrease of the interaction between IBU and CSH. Compared to the standard sample SiO₂, the spectra of CSH-IBU microspheres after IBU release for different time periods are all identical to that of SiO₂, indicating that some mesoporous CSH microspheres have been hydrolyzed into SiO₂ during IBU release [35, 36]. Interestingly, the feature “b” can be detected again in the Si K-edge TEY spectra after 6 hours release although the intensities are much weaker than before (0 h spectrum).

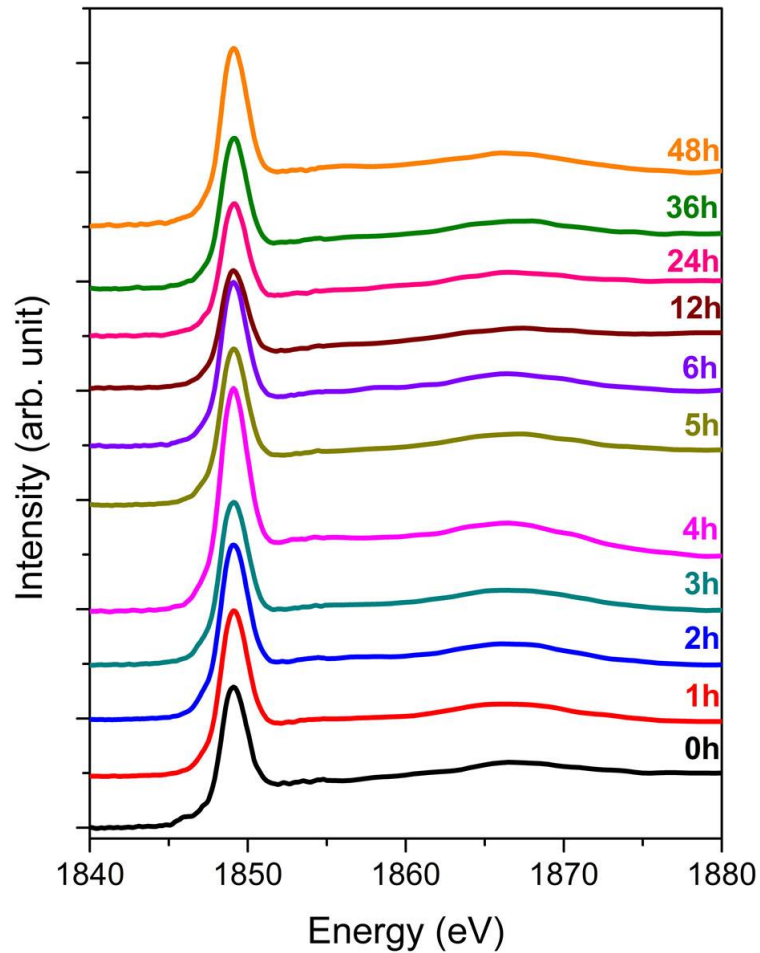


Figure 6-8 Si K-edge FLY XANES spectra of CSH-IBU microspheres soaked in SBF solution for various time periods.

The IBU release profile of mesoporous CSH microspheres in SBF is shown in Figure 6-9. Initially, there was a burst release effect at the early stage; about 85 % IBU were released in the first hour, and 97-98 % of loaded IBU were released after 4 hours. This type of release profile is suitable for an acute infection or inflammation, when an immediate high dosage is needed for a short period of time. Hence, according to the IBU release profile, the reappearance of feature “b” at the Si K-edge after 6h can be ascribed to the re-adsorption of IBU on the surface of the release products (SiO_2), since the equilibrium of IBU release was reached during that period of time. Since no SiO_2 phase was observed from XRD, all the SiO_2 components detected from XANES are amorphous.

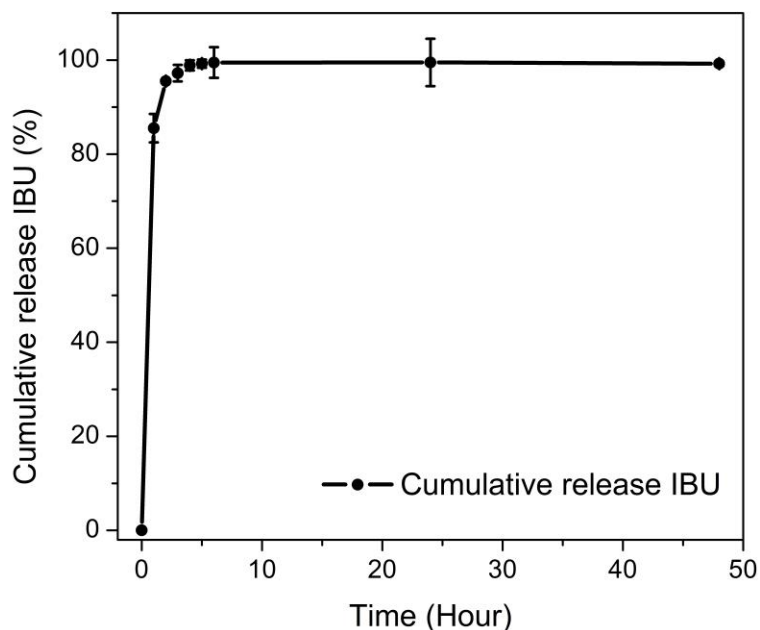


Figure 6-9 The cumulative IBU release of mesoporous CSH microspheres in SBF.

6.3.6 STXM Analysis of CSH-IBU System after Having Soaked in SBF for Five Hours

Since it is shown that the CSH-IBU system starts to transform into crystalline HAP after having been soaked in the SBF solution for more than 4 h, it would be desirable if we could identify and map the compositions of the *in vitro* samples after biomineralization at nanoscale. Figure 6-10(a) shows the STXM image of the CSH-IBU microspheres after having been soaked in the SBF solution for 5 h. No microspheres could be observed anymore; instead, an aggregation of flakes in several microns is seen. In order to monitor the components of the biomineralization product in details, we first obtain C K-edge XANES spectra isolated from 6 different regions of interest (ROIs) on the sample as shown in Figure 6-10(b). All the ROIs were selected randomly based on the optical densities (sample thickness) to illustrate the uniformity/heterogeneity of various components at different edges. Since STXM is a powerful technique to study carbon nanomaterials and provides high quality absorption spectra with submicron spatial resolution [37-39], C K-edge XANES from different ROIs could reveal the presence of residual IBU and carbon related compounds. From Figure 6-10(c), compared with the spectrum of IBU powder (black profile), there is no significant change or beam damage

to the residual IBU molecules on the drug release products: the sharp peak “a” located at 285 eV is from the carbon 1s to π^* transition for the aryl rings of IBU molecules; the peak “b” located at 288.3 eV is from the carbon 1s to π^* transition for carboxylic functional groups of IBU; the less apparent feature “c” became more prominent after having been soaked in SBF for 5h, and slightly shifted to higher photon energy, indicating the presence of carbonate ions [40-44].

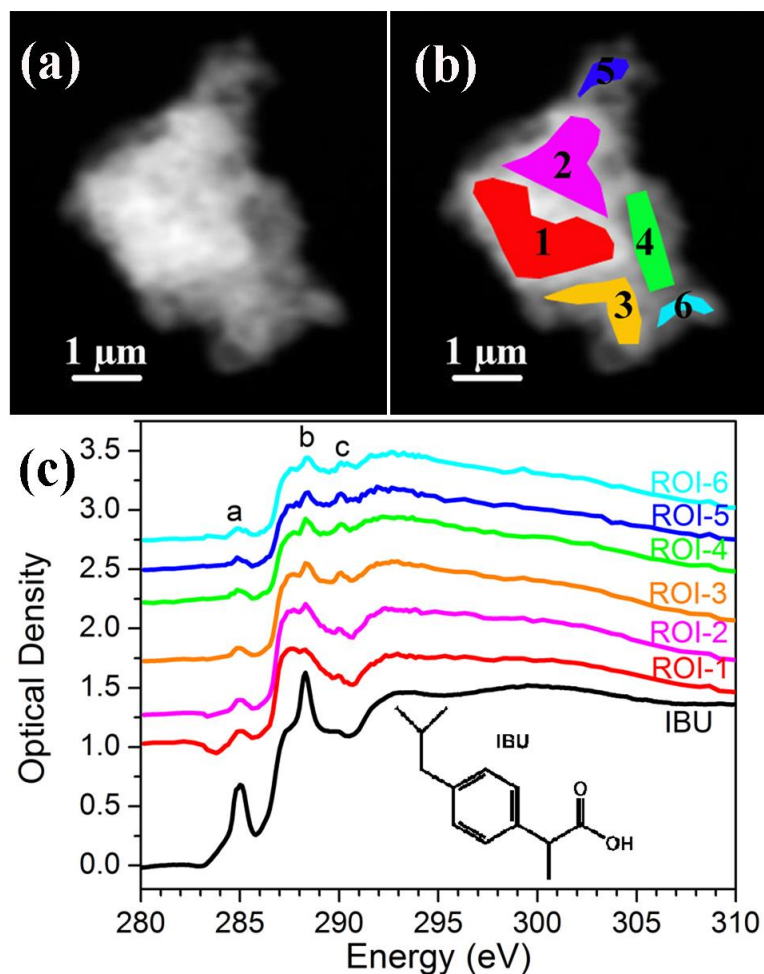


Figure 6-10 (a) STXM optical density image of CSH-IBU sample soaked in SBF for 5h (averaged from 280 to 2190 eV); **(b)** ROIs taken from the CSH-IBU sample: Red: ROI-1, Magenta: ROI-2, Orange: ROI-3, Green: ROI-4, Blue: ROI-5 and Cyan: ROI-6; **(c)** XANES spectra taken from each ROI displayed in (b) at the C K-edge.

We have also compared the XANES spectra isolated from different ROIs at the Si K-edge (Figure 6-11(c)) and the P K-edge (Figure 6-11(d)); it is interesting to note that the

strongest P signals were detected in ROI-1 and ROI-2 (red and magenta spectra of Figure 6-11(d)), where show the highest Si optical densities as well. Since STXM can determine the absolute thickness of the sample, SiO₂ and HAp thickness distributions are shown in Figure 6-11(a) and (b), respectively.

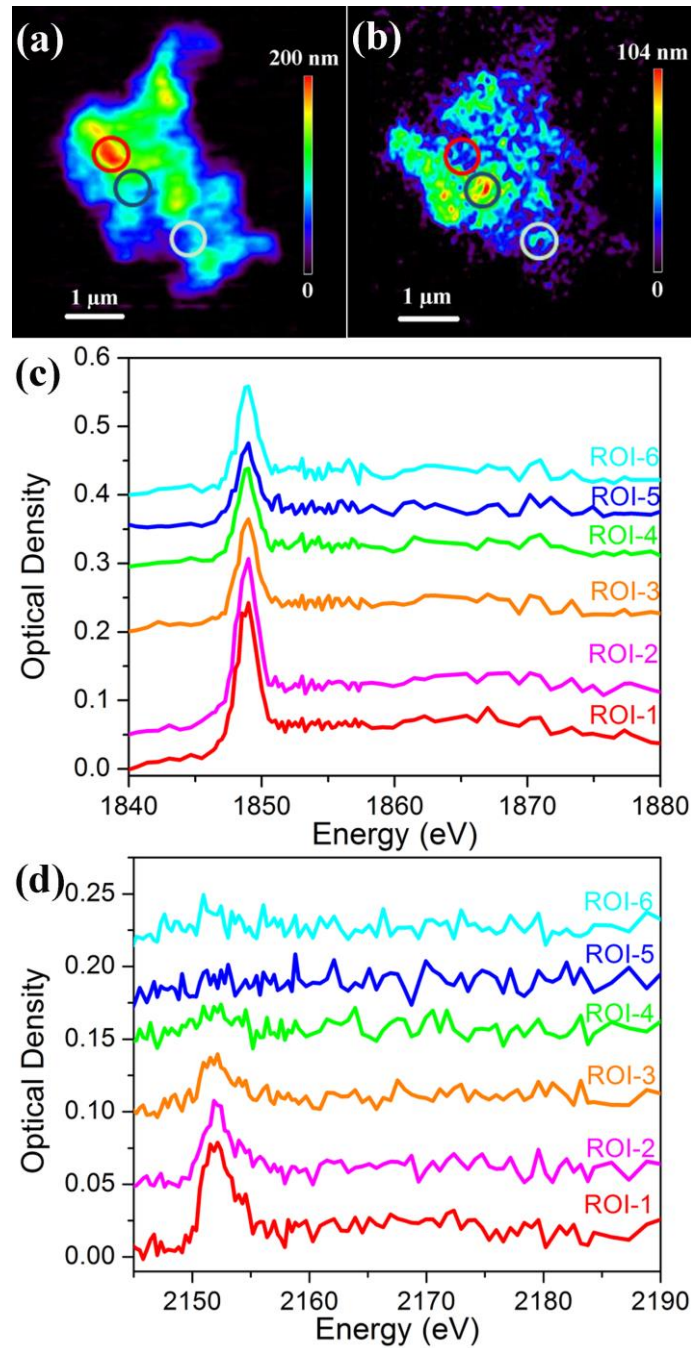


Figure 6-11 Thickness distribution maps of CSH-IBU sample soaked in SBF for 5h at (a) the Si K-edge and (b) the P K-edge. The vertical bar illustrates the color code of the material thickness; XANES spectra of CSH-IBU sample soaked in SBF for 5h at the Si K-edge (c) and P K-edge (d) (ROI 1-6 are the same regions as shown in Figure 6-10(b)).

For STXM thickness modelling procedure, XANES spectra were obtained by converting the signal to optical density (OD) based on Beer-Lambert Law:

$$OD = -\ln\left(\frac{I}{I_0}\right) = \mu \cdot \rho \cdot t \quad (6-1)$$

where I_0 and I are the incident and transmitted X-ray photon flux (photons), respectively. μ is the energy dependent mass absorption coefficient (cm^2/g), ρ is the density (g/cm^3) of the material, and t is the sample thickness (nm). Then these spectra were converted to absolute linear absorbance scales (optical density per nm thickness sample). The elemental linear X-ray absorption, which neglects interactions such as bonding among the atoms, is calculated by aXis2000 using Equation (6-1) and (6-2):

$$\mu = \frac{N_A}{MM} \sum_i x_i \cdot \sigma_{ai} \quad (6-2)$$

where N_A is the Avogadro's number, MM is the molecular weight of a compound containing x_i atoms of type i , σ_{ai} is the atomic photo absorption cross section (cm^2/atom) for type i atom. Then, the thickness was obtained by comparing the OD of each pixel in a STXM image and reference spectra. In this study, silicon and carbon reference spectra were obtained by fitting the original XANES spectra to match its calculated elemental linear X-ray absorption profile: hydroxyapatite ($\text{Ca}_5(\text{PO}_4)_3(\text{OH})$): density = $3.160 \text{ g}/\text{cm}^3$, and thickness = 1 nm, silicon dioxide (SiO_2): density = $2.650 \text{ g}/\text{cm}^3$, and thickness = 1 nm) in the pre-edge and continuum. The thickness was obtained from stack fitting with the quantitatively scaled reference spectra of 1 nm thickness (Figure 6-12).

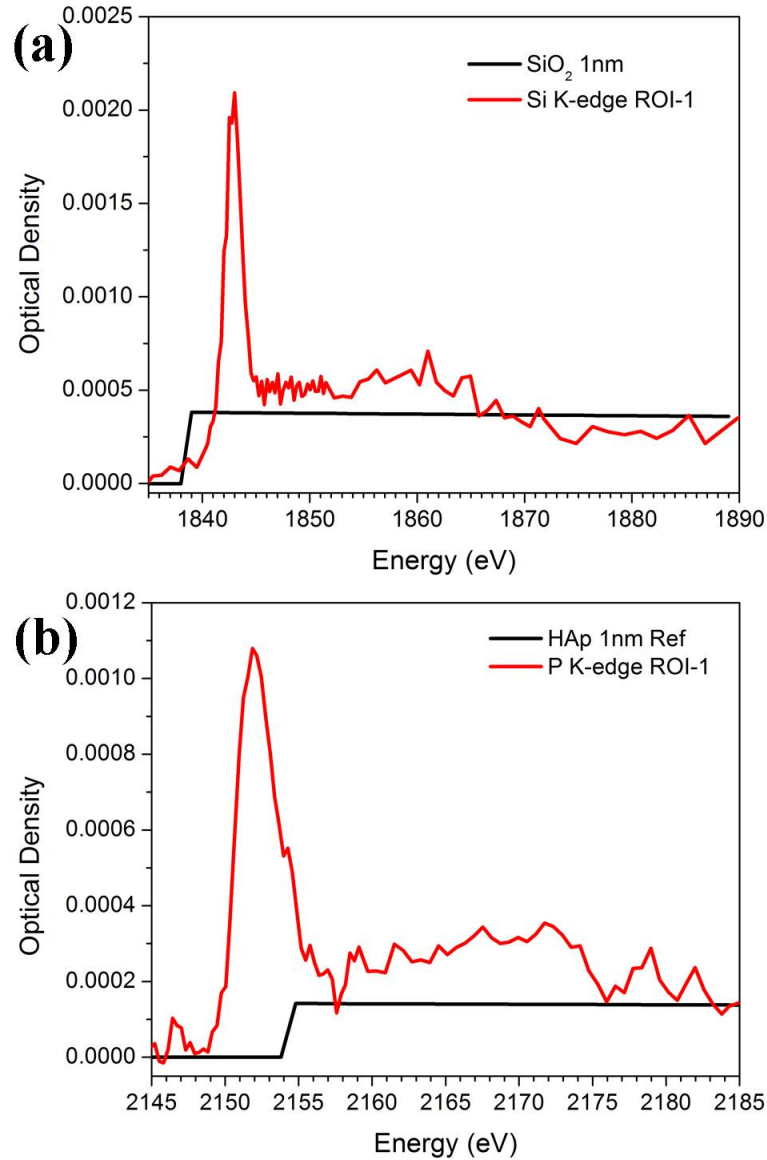


Figure 6-12 Reference spectra and elemental linear X-ray absorption profiles of SiO₂ (a) (black profile: optical density spectrum of 1 nm thickness based on formula SiO₂; red profile: elemental linear X-ray absorption profile) and HAp (b) (black profile: optical density spectrum of 1 nm thickness based on formula Ca₅(PO₄)₃(OH); red profile: elemental linear X-ray absorption profile).

After 5 h *in vitro* test, most of the SiO₂ were located in the top left area with the largest thickness around 200 nm ($\pm 10\%$). Moreover, one can see that from Figure 6-11(b), more HAp can be detected around the red areas. The average SiO₂, HAp thickness of selected

areas is given in Table 6-4 (the areas are shown in circles with different colors in Figure 6-11(a) and (b)).

Table 6-4 Thickness of SiO₂ and HAp in different regions.

	Average Thickness [nm]	
	SiO ₂ Map	HAp Map
Circle 1 (Red)	173	36
Circle 2 (Navy)	91	86
Circle 3 (White)	73	27

There is $\pm 10\%$ thickness deviation according to Figure 6-11(a) and 11 (b).

It is interesting to note that area 2 (navy circle) and 3 (white circle) have the similar thickness of SiO₂; however, the thicknesses of HAp in those areas are quite different. This is largely because area 2 is closer to area 1 (red circle) where most SiO₂ are located. During the biomineralization processes, some CSH microspheres (silanol abundant) [45-47] partially broke down and some silicate hydrolyzed into SiO₂ (area 1); this aggregation provides preferred further nucleation site for the growth of HAp [10, 48, 49]. That explains why we observe more HAp in area 2 rather than area 3.

6.3.7 Changes of Ca, Si and P during the Biomineralization

Figure 6-13 shows the change in concentration of Ca, Si and P in the SBF solution measured by ICP after soaking CSH-IBU microspheres in SBF for different time periods. At early stages, the Si concentrations in SBF increased when the IBU was released from CSH microspheres, indicating the dissolutions of CSH microspheres in the SBF solution. Meanwhile, there was a steep decrease of P concentration in the first 6 h of soaking, corresponding to the phosphate consumption in the SBF solution in order to form HAp on the surface of CSH microspheres. It should be noted that there is also a rapid drop of Ca concentrations in the first 6h of soaking and the concentration remained almost steady after 1 day. This observation is different from the Ca change in the previous studies [3, 5, 6, 10]. The reason why the rate is different is that the Ca dissolution rate of CSH microspheres is slower than the Ca precipitation rate from the SBF solution (the co-precipitation of Ca²⁺ and PO₄³⁻ from the SBF solution to form HAp on the surface of drug carriers).

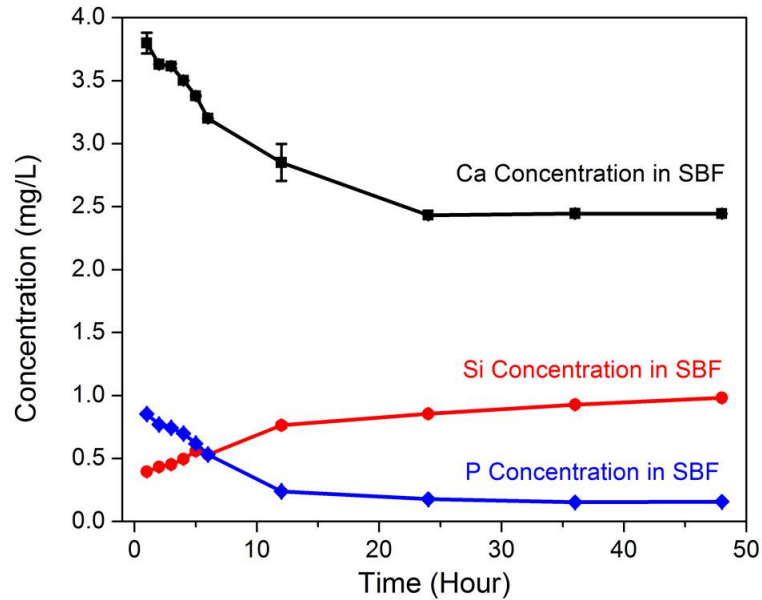


Figure 6-13 Concentration changes of Ca, P and Si after soaking CSH-IBU in SBF for different period of time.

6.4 Conclusions

Finally, based on all the above results, the processes of drug release and CSH biomineralization emerge. As illustrated in Figure 6-14, at the early stages of drug release, crystalline CSH microspheres disassemble into amorphous flake-like sheets, some silicate ions undergoes exchange into the SBF solution while others becomes hydrolyzed into amorphous silica. Both Ca (from CSH and SBF) and PO_4^{3-} ions (from SBF) (Figure 6-13) first form amorphous calcium phosphate at first 2h, then quickly transformed into amorphous HAp, and the finally products were crystalline HAp after the samples were soaked in the SBF solution for more than 3h. At the same time, some bicarbonate ions (HCO_3^-) co-precipitate from SBF, generating amorphous CaCO_3 . Moreover, from STXM data, more P were detected around the area where more Si were located; indicating the abundant silanol groups and the following hydrolyzed SiO_2 provided preference aggregation sites of HAp.

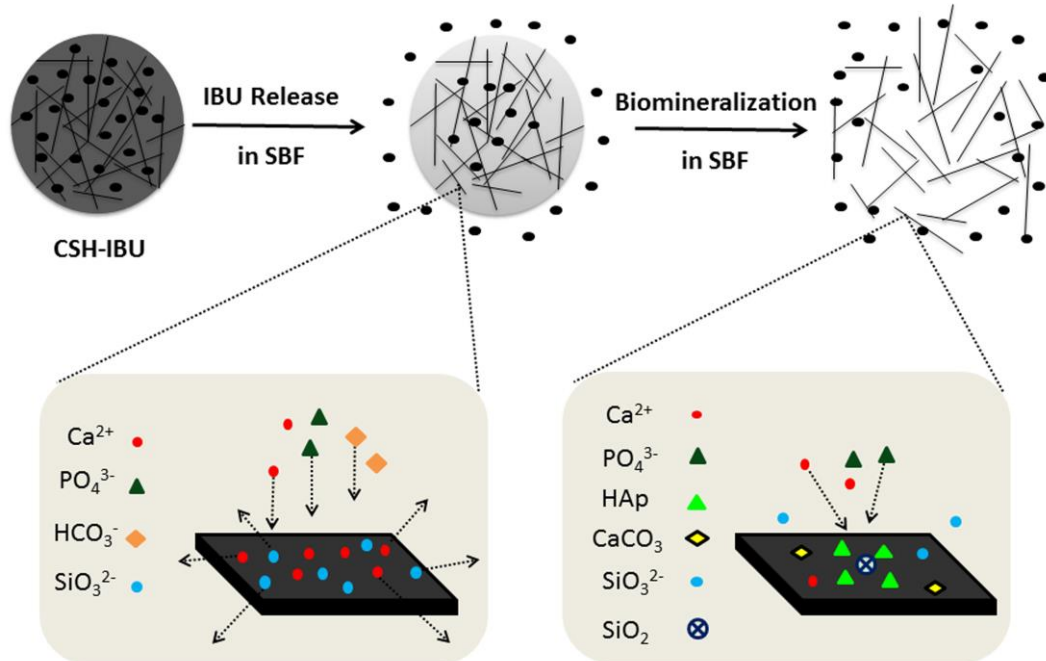


Figure 6-14 Illustration of the proposed mechanisms for the IBU (black dots) release from mesoporous CSH microspheres and biomineralization.

In this chapter we have illustrated that mesoporous CSH microspheres have very large drug loading capacities, which can reach as high as 1.80 g/g. The CSH-IBU system has a rapid drug release profile, which is suitable for acute disease (need of high drug dosage in a short period of time). The biomineralization mechanism for mesoporous CSH microspheres loaded with IBU in the SBF solution was elucidated via XANES and STXM. What's more important, we have demonstrated that synchrotron radiation is a very sensitive and powerful technique to study bioceramics: XANES has the ability to identify the chemical form of products (Si, P and Ca K-edge) even they are amorphous state. Using the highly-collimated STXM beam (best resolution: 30 nm), we provided spatial evidence of biomineralization formation (Si and P particularly).

6.5 References

1. Arcos, D. and Vallet-Regi, M., *Acta Mater.* **2013**, *61*, 890-911.

2. Hench, L.L., Splinter, R.J., Allen, W.C., and Greenlee, T.K., *J. Biomed. Mater. Res.* **1971**, *5*, 117-141.
3. Siriphannon, P., Kameshima, Y., Yasumori, A., Okada, K., and Hayashi, S., *J. Eur. Ceram. Soc.* **2002**, *22*, 511-520.
4. Siriphannon, P., Kameshima, Y., Yasumori, A., Okada, K., and Hayashi, S., *J. Biomed. Mater. Res.* **2002**, *60*, 175-185.
5. Gou, Z. and Chang, J., *J. Eur. Ceram. Soc.* **2004**, *24*, 93-99.
6. Wan, X.H., Chang, C.K., Mao, D.L., Jiang, L., and Li, M., *Mater. Sci. Eng. C* **2005**, *25*, 455-461.
7. Long, L.H., Chen, L.D., Bai, S.Q., Chang, J., and Lin, K.L., *J. Eur. Ceram. Soc.* **2006**, *26*, 1701-1706.
8. Coleman, N.J., Nicholson, J.W., and Awosanya, K., *Cem. Concr. Res.* **2007**, *37*, 1518-1523.
9. Gandolfi, M., Taddei, P., Tinti, A., De Stefano Dorigo, E., Rossi, P., and Prati, C., *Clin. Oral Invest.* **2010**, *14*, 659-668.
10. Li, X., Shi, J., Zhu, Y., Shen, W., Li, H., Liang, J., and Gao, J., *J. Biomed. Mater. Res. B* **2007**, *83B*, 431-439.
11. Sham, T.-K., *Inter. J. Nanotechnol.* **2008**, *5*, 1194-1246.
12. Takahashi, Y., Miyoshi, T., Yabuki, S., Inada, Y., and Shimizu, H., *Atmos. Environ.* **2008**, *42*, 6535-6541.
13. Naftel, S.J., Sham, T.-K., Yiu, Y.-M., and Yates, B.W., *J. Synchrotron Radiat.* **2001**, *8*, 255-257.
14. Fleet, M.E. and Liu, X.Y., *Am. Mineral.* **2009**, *94*, 1235-1241.

15. Ingall, E.D., Brandes, J.A., Diaz, J.M., de Jonge, M.D., Paterson, D., McNulty, I., Elliott, W.C., and Northrup, P., *J. Synchrotron Radiat.* **2011**, *18*, 189-197.
16. Liu, L., Kim, S., Chan, J., and Sham, T.-K., *MRS Online Proceedings Library* **2011**, *1352*, 63-68.
17. Tamenori, Y., Morita, M., and Nakamura, T., *J. Synchrotron Radiat.* **2011**, *18*, 747-752.
18. Tyliczszak, T., Kilcoyne, A.L.D., Liddle, J.A., Warwick, T., Hitchcock, A.P., Ade, H., and Shuh, D.K., *Microsc. Microanal.* **2004**, *10*, 1018-1019.
19. Hitchcock, A.P., Dynes, J.J., Johansson, G., Wang, J., and Botton, G., *Micron* **2008**, *39*, 311-319.
20. Sivakumar, M. and Panduranga Rao, K., *Biomaterials* **2002**, *23*, 3175-3181.
21. Xia, W. and Chang, J., *J. Control. Release* **2006**, *110*, 522-530.
22. Xia, W. and Chang, J., *J. Non-Cryst. Solids* **2008**, *354*, 1338-1341.
23. Wu, J., Zhu, Y.-J., Cao, S.W., and Chen, F., *Adv. Mater.* **2010**, *22*, 749-753.
24. Kokubo, T., *J. Non-Cryst. Solids* **1990**, *120*, 138-151.
25. Wang, Z., Wang, J., Sham, T.-K., and Yang, S., *J. Phys. Chem. C* **2012**, *116*, 10375-10381.
26. Wang, Z., Wang, J., Sham, T.-K., and Yang, S., *Nanoscale* **2014**, *6*, 9783-9790.
27. Guo, X., Wu, J., Yiu, Y.-M., Hu, Y., Zhu, Y.-J., and Sham, T.-K., *Phys. Chem. Chem. Phys.* **2013**, *15*, 15033-15040.
28. Guo, X., Wang, Z., Wu, J., Wang, J., Zhu, Y.-J., and Sham, T.-K., *Nanoscale* **2015**, *7*, 6767-6773.
29. Yamamoto, T., *X-Ray Spectrom.* **2008**, *37*, 572-584.

30. Eichert, D., Salome, M., Banu, M., Susini, J., and Rey, C., *Spectrochim. Acta B* **2005**, *60*, 850-858.
31. Demirkiran, H., Hu, Y., Zuin, L., Appathurai, N., and Aswath, P.B., *Mater. Sci. Eng. C* **2011**, *31*, 134-143.
32. Cormier, L. and Neuville, D.R., *Chem. Geol.* **2004**, *213*, 103-113.
33. Güngör, K., Jürgensen, A., and Karthikeyan, K.G., *J. Environ. Qual.* **2007**, *36*, 1856-1863.
34. Li, D., Bancroft, G.M., Kasrai, M., Fleet, M.E., Feng, X.H., Tan, K.H., and Yang, B.X., *Solid State Commun.* **1993**, *87*, 613-617.
35. Brinker, C.J., *J. Non-Crystal. Solids* **1988**, *100*, 31-50.
36. Motisuke, M., Santos, V., Bazanini, N., and Bertran, C., *J. Mater. Sci. Mater. Med.* **2014**, *25*, 2357-2363.
37. Zhou, J., Wang, J., Liu, H., Banis, M.N., Sun, X., and Sham, T.-K., *J. Phys. Chem. Lett.* **2010**, *1*, 1709-1713.
38. Zhou, J., Wang, J., Fang, H., Wu, C., Cutler, J.N., and Sham, T.-K., *Chem. Commun.* **2010**, *46*, 2778-2780.
39. Zhou, J.G., Wang, J., Sun, C.L., Maley, J.M., Sammynaiken, R., Sham, T.-K., and Pong, W.F., *J. Mater. Chem.* **2011**, *21*, 14622-14630.
40. Jokic, A., Cutler, J.N., Ponomarenko, E., van der Kamp, G., and Anderson, D.W., *Geochim. Cosmochim. Acta* **2003**, *67*, 2585-2597.
41. Benzerara, K., Yoon, T.H., Tyliczszak, T., Constantz, B., Spormann, A.M., and Brown, G.E., *Geobiology* **2004**, *2*, 249-259.
42. Zubavichus, Y., Shaporenko, A., Grunze, M., and Zharnikov, M., *J. Phys. Chem. A* **2005**, *109*, 6998-7000.

43. Ha, J., Chae, S., Chou, K.W., Tyliczszak, T., and Monteiro, P.J.M., *J. Mater. Sci.* **2012**, *47*, 976-989.
44. Brandes, J.A., Wirick, S., and Jacobsen, C., *J. Synchrotron Radiat.* **2010**, *17*, 676-682.
45. Nonat, A., *Cem. Concr. Res.* **2004**, *34*, 1521-1528.
46. Cong, X.D. and Kirkpatrick, R.J., *Adv. Cem. Based Mater.* **1996**, *3*, 144-156.
47. Chen, J.J., Thomas, J.J., Taylor, H.F.W., and Jennings, H.M., *Cem. Concr. Res.* **2004**, *34*, 1499-1519.
48. Tanizawa, Y. and Suzuki, T., *J. Chem. Soc. Faraday Trans.* **1995**, *91*, 3499-3503.
49. Li, P., Ohtsuki, C., Kokubo, T., Nakanishi, K., Soga, N., Nakamura, T., and Yamamuro, T., *J. Mater. Sci. Mater. Med.* **1993**, *4*, 127-131.

Chapter 7

7 Effects of Polymers on the Drug Loading Capacities and Drug Release of Calcium Silicate Hydrates: An X-ray Absorption Near Edge Structures (XANES) Study

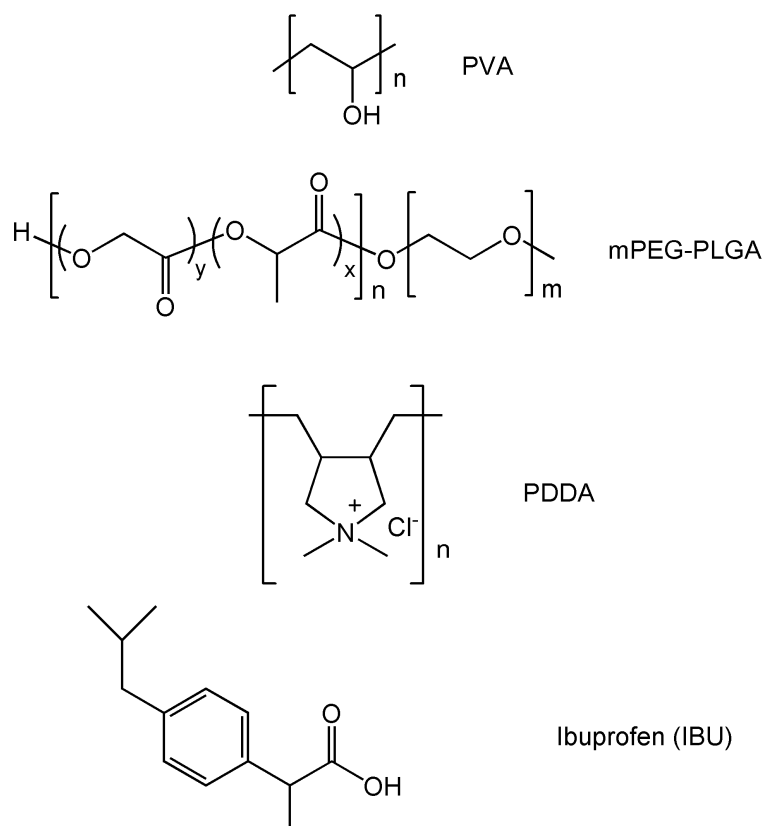
7.1 Introduction

Calcium silicate hydrate (CSH) has served as the component of glass or cement concrete for a long time; moreover, it was found to be an excellent candidate for bioceramics in bone regeneration and augmentation in recent two decades because of their impressive bioactivity, biocompatibility and biodegradability [1-4]. Furthermore, its stimulatory effect on osteogenic differentiation of stem cells makes CSH a new type of promising biomaterials in biomedical applications [5-7]. Currently, composite biomaterials comprising inorganic bioceramics and organic polymers are even more attractive because their combination improves their mechanical properties and stabilities, and further enhances tissue interaction [8]. With increasing demands for biomaterials to deliver drugs to local hard-tissue site in order to increase the effectiveness of therapy, efforts have been invested in developing composite biomaterials with a drug-delivery capacity [9-12]. However, high drug loading capacities and controlled drug release profiles are still key challenges in drug delivery systems, which are affected by both structures of drug carriers, including pore size, pore volume and surface areas, *etc.*, and interactions between drug carriers and drug molecules[13-15].

Previously, a variety of analytical techniques such as X-ray photoelectron spectroscopy (XPS) [16], nuclear magnetic resonance (NMR) [17] and Fourier transform infrared (FTIR) spectroscopy [18] have been applied in the structural investigation of heterogeneous cement materials. More recently, X-ray absorption spectroscopy (XAS) has also been used to study cement paste [19]. X-ray absorption near edge structure (XANES), a near edge region of the XAS (generally from 20 eV below to 50 eV above the absorption edge), is an elemental specific technique, because the binding energy of each core electron of each element is unique. XANES provides information about immediate surroundings of the absorbing atom and it is sensitive to the oxidation state,

local symmetry of elements of interest [20]. Hence, we not only can investigate the structure of the drug carriers CSH before and after polymer incorporation, but also track the interactions between drug molecules and CSH/polymer composites by the XANES spectral comparisons at different elements/edges; thus, we gain a comprehensive understanding of how polymers and drug molecules interact with different functional groups (calcium and silicate in this case) of drug carriers and deduce their drug loading capacities and release profiles.

Recently, Ha *et al.* investigated polymers on the structure and the carbonation of CSH using scanning transmission X-ray microscopy [19]; however, the use of X-ray absorption near-edge structure (XANES) to study CSH/polymers composites as drug carriers in drug delivery systems has yet to be reported. Herein, we report a controlled precipitation synthesis of CSH nanosheets, followed by a room-temperature solution preparation of three CSH/block copolymer composites by the incorporation of one each of the three different block copolymers: polyvinyl alcohol (PVA), monomethoxy (polyethyleneglycol)-block-poly(DL-lactide-co-glycolide) (mPEG-PLGA) and poly(diallyldimethylammonium chloride) (PDDA). Ibuprofen (IBU), a typical anti-inflammatory drug is further employed for the investigations of drug loading and release properties of these polymer incorporated composites (Scheme 7-1). XANES is utilized to study the structural change of CSH after the formation of CSH/polymer composite and the interactions between IBU and CSH/polymer composite to reveal the effects of polymer incorporation on drug loading capacities and drug release kinetics.



Scheme 7-1 Chemical structures of different polymers and ibuprofen.

7.2 Experimental

7.2.1 Materials

$\text{Na}_2\text{SiO}_3 \cdot 9\text{H}_2\text{O}$, $\text{Ca}(\text{NO}_3)_2 \cdot 4\text{H}_2\text{O}$, $\text{NH}_3 \cdot \text{H}_2\text{O}$, polyvinyl alcohol (PVA, $M_w = 1750 \pm 50$) were purchased from Sinopharm Chemical Reagent Co., Ltd. Monomethoxy (polyethyleneglycol)-block-poly(DL-lactide-co-glycolide) (mPEG-PLGA, $M_w = 8000$; the molecular weight of the mPEG segment was 5000 and the molar ratio of DL-lactide to glycolide was 75:25.) was purchased from Jinan Daigang Biomaterial Co., Ltd. Poly(diallyldimethylammonium chloride) (PDDA, M_w 100,000-200,000, 20 wt. % in H_2O) was purchased from Sigma-Aldrich. Ibuprofen (IBU) was purchased from Shanghai Yuanji Chemical Co., Ltd. The phosphate buffer saline (PBS, $\text{pH} = 7.4$ at 37°C) was purchased from Bio Basic Inc. All the purchased chemicals were used as received without further purification.

7.2.2 Preparation of CSH/polymer Composites

Calcium silicate hydrate nanosheets were prepared by a reaction rate-controlled solution precipitation method [21]. For the preparation of CSH/polymer composites, solution A was prepared by dissolving 0.853 g of $\text{Na}_2\text{SiO}_3 \cdot 9\text{H}_2\text{O}$ into 50 mL of deionized water, into which 5 mL of 0.6 M $\text{Ca}(\text{NO}_3)_2$ aqueous solution was injected at a constant rate of $2.5 \text{ mL} \cdot \text{h}^{-1}$ under magnetic stirring for 3 hours followed by addition of 1 mL of aqueous ammonia (~27%). Solution B was 10 mL of a 10% PDDA aqueous solution; Solution C and D were prepared by dissolving 0.5 g of mPEG-PLGA into 10 mL of deionized water and 1 g of PVA into 10 mL of deionized water, respectively. Then 25 mL each of solution A was added into solution B, C and D, under magnetic stirring for 8 days. The CSH/polymer composites were collected by centrifugation, washed with deionized water three times and absolute ethanol once, then dried at 60°C .

7.2.3 IBU Drug Loading and *In Vitro* Release

0.035 g of CSH/PVA, 0.1 g of CSH/mPEG-PLGA and 0.02 g CSH/PDDA as synthesized composites were added into 1.75 mL, 5 mL, and 1 mL of IBU hexane solution ($40 \text{ mg} \cdot \text{mL}^{-1}$) in three different flasks at room temperature, respectively. The flask was immediately sealed to prevent hexane from evaporation, and the mixture was treated by ultrasound for 2 minutes. Then the flask was oscillated at a constant rate of 160 rpm at 37°C for 24 hours. After that the product was separated by centrifugation, washed with hexane once, and dried in air at 60°C . Then each (20 mg) of the as-prepared IBU-loaded composites were immersed in a 40 mL phosphate buffered saline (PBS) at 37°C under shaking at a constant rate. The IBU release medium (2.0 mL) was extracted for UV-Vis analysis at the wavelength of 263 nm at given time intervals.

7.2.4 Characterization

The transmission electron microscopy micrographs were obtained with a transmission electron microscope (TEM, Philips CM-10) at Biotron Lab, University of Western Ontario. The thermogravimetric (TG) curves were measured on a STA 409/PC simultaneous thermal analyzer (Netzsch, Germany) with a heating rate of $10^\circ\text{C} \text{ min}^{-1}$ in blowing air to measure the drug loading capacities of mesoporous CSH microspheres.

Fourier transform infrared (FTIR) spectra were recorded on a FTIR spectrometer (FTIR-7600, Lambda, Australia). The compositions of CSH/polymer composites were characterized by XRD (Rigaku D/max 2550 V, Cu K α radiation, $\lambda = 1.54178 \text{ \AA}$).

7.2.5 XANES Measurement

XANES measurements were conducted at the Canadian Light Source (CLS) using the Soft X-ray Microcharacterization Beamline (SXRMB), which is equipped with a double crystal monochromator with two sets of interchangeable crystals operating with an energy range of 1.7 to 10 keV. The InSb (111) crystals were used for the Si K-edge XANES measurements while the Si (111) crystals were used for the Ca K-edge XANES. The detection modes are total electron yield (TEY) and X-ray fluorescence yield (FLY) recorded with a Si drift solid state detector, tracking with surface and bulk sensitivities, respectively.

7.2.6 FEFF Simulation

FEFF is a computer code based on real space multiple scattering theory - it allows the mathematical modeling of XANES and EXAFS. The crystal structure of the as-synthesized CSH nanosheets was reported to be consistent with the 1.4 nm tobermorite ($\text{Ca}_5\text{Si}_6\text{O}_{16}(\text{OH})_2 \cdot 8\text{H}_2\text{O}$) [21], and have space group symmetry of B_{11b} with a lattice constant of $a = 6.735 \text{ \AA}$, $b = 7.425 \text{ \AA}$, $c = 27.987 \text{ \AA}$, $\gamma = 123.25^\circ$. The locations of the atoms in $\text{Ca}_5\text{Si}_6\text{O}_{16}(\text{OH})_2$ are shown in Table 7-1 [22]. To set up a simulation, the positions of the atomic clusters above are input into the FEFF software. The positions can be generated by the crystal parameters, including the space group, unit cell parameters, and the atomic coordination in the unit cell, *etc.*

Table 7-1 Atomic coordinates of tobermorite.

Site	x	y	z
Ca ₁	0.737	0.425	0.2852
Ca ₂	0.879	0.994	0.0019
Ca ₃	0.251	0.428	0.2147
Si ₁	0.750	0.386	0.1752
Si ₂	0.895	0.750	0.1041
Si ₃	0.743	0.961	0.1751
O ₁	0.752	0.512	0.1248
O ₂	0.760	0.189	0.1542
O ₃	0.972	0.554	0.2070
O ₄	0.518	0.301	0.2065
O ₅	0.887	0.250	-0.0482
OH ₆	0.182	0.888	0.1175
O ₇	0.759	0.860	0.1252
O ₈	0.501	0.824	0.2067
O ₉	0.982	0.033	0.2069

7.3 Results and Discussion

7.3.1 Morphologies of CSH Nanosheets, CSH/polymer Composites and CSH/polymer-IBU

The morphologies of CSH nanosheets, various CSH/polymer composites before and after IBU loading have been characterized by transmission electron spectroscopy, shown in Figure 7-1. One can see that the specimens consist of warped nanosheets and these nanosheets stack together (Figure 7-1(a)). Different polymer incorporations and IBU loadings (Figure 7-1(b) to (h)) do not alter the morphology of CSH nanosheets significantly. Hence, we cannot obtain much information on the various polymers and IBU molecules based on the TEM micrographs.

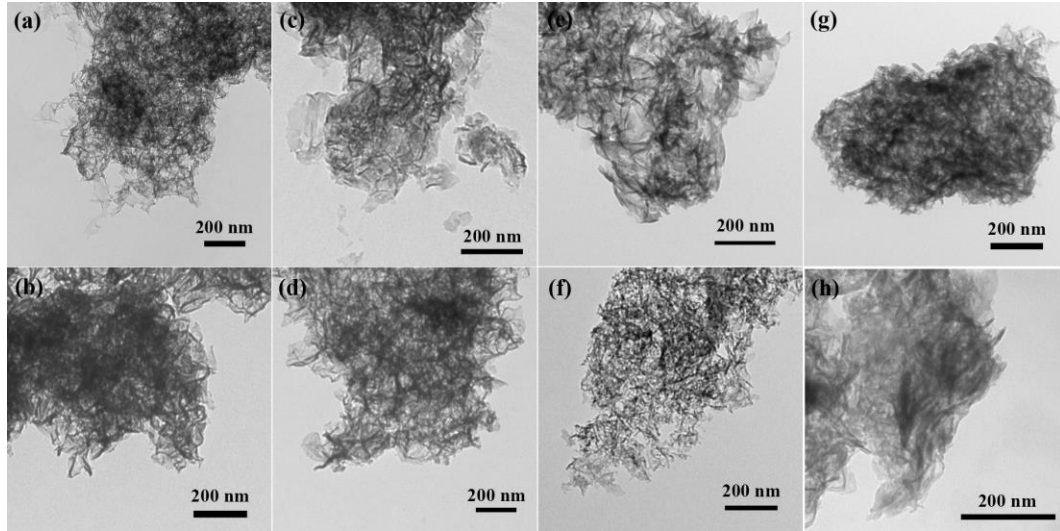


Figure 7-1 TEM images of CSH nanosheets and CSH/polymer composites before and after IBU loading: (a) CSH, (b) CSH-IBU, (c) CSH/PDDA, (d) CSH/PDDA-IBU, (e) CSH/mPEG-PLGA, (f) CSH/mPEG-PLGA-IBU, (g) CSH/PVA, (h) CSH/PVA-IBU.

7.3.2 Studies of Interactions between CSH and Different Block Polymers

The FTIR spectra of the CSH nanosheets and CSH/polymer composites are shown in Figure 7-2. For CSH nanosheets, the absorption bands in the range of $900\text{-}1100\text{ cm}^{-1}$ are the stretching vibration of Si-O bonds; the absorption at around 1630 cm^{-1} is assigned to the bending vibration of the adsorbed water, and the broad band at $3000\text{-}3700\text{ cm}^{-1}$ is due to stretching vibration of O-H groups in water or hydroxyls. After different polymers adsorption, there are no significant FTIR changes except the more noticeable absorptions at around $2800\text{-}2900\text{ cm}^{-1}$, which are due to C-H stretching from polymer molecules [23, 24]. From the above results, we cannot get much information of different polymers from FTIR spectra due to the low amount of polymer incorporation.

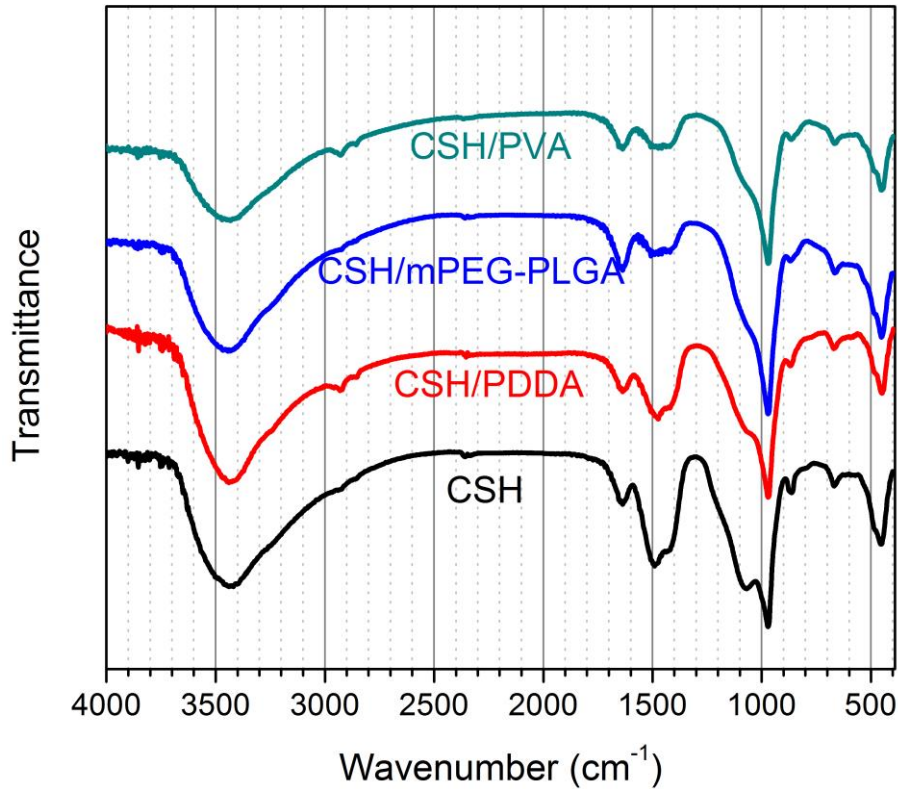


Figure 7-2 FTIR spectra of CSH nanosheets, and different CSH/polymer composites.

XRD data of CSH nanosheets and their polymer composites were obtained, as shown in Figure 7-3. The phase of CSH nanosheets is consistent with that of the 1.4 nm tobermorite structure ($\text{Ca}_5\text{Si}_6\text{O}_{16}(\text{OH})_2 \cdot 8\text{H}_2\text{O}$ JCPDS: 29-0331), which was reported in previous study [21]. Upon composites formation, there are no significant changes for CSH/PDDA (red) composite; however, for CSH/mPEG-PLGA (navy) and CSH/PVA (dark cyan) composites, there are new patterns at around 18-19°. Matsuyama *et al.* [25] reported that these new patterns can be ascribed to the precipitated polymers themselves.

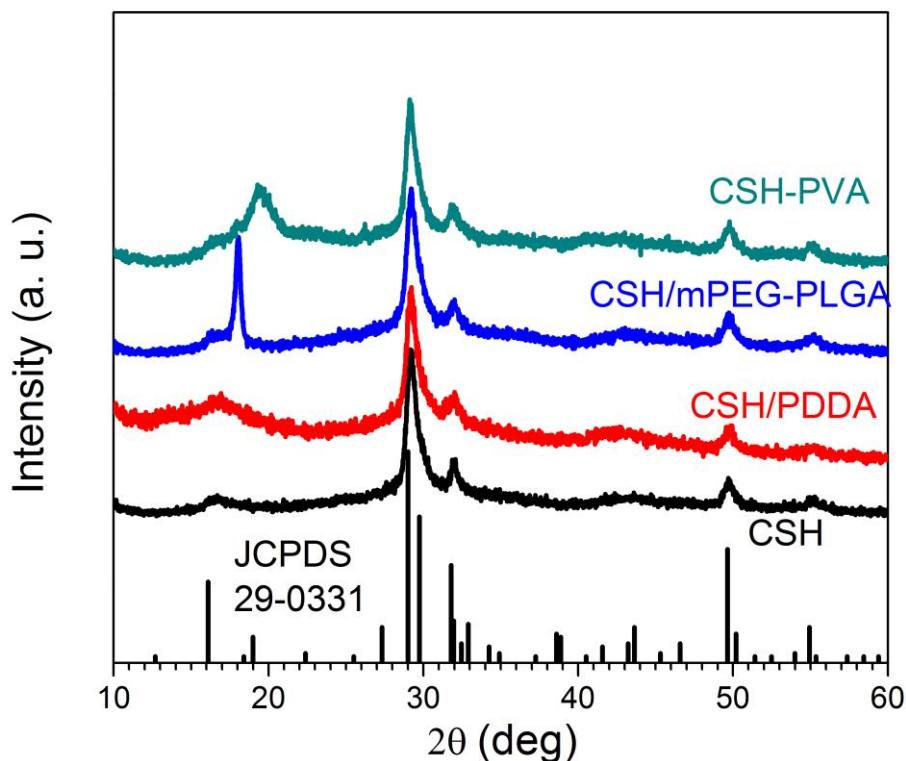


Figure 7-3 XRD patterns of CSH nanosheets and different CSH/polymer composites.

In order to confirm and extensively study the interaction between CSH nanosheets and different polymers, Figure 7-4 shows the Ca K-edge XANES spectra of CSH nanosheets and their polymers composites. The detection modes are total electron yield (TEY) and X-ray fluorescence yield (FLY), tracking surface and bulk sensitivity, respectively. Compare the TEY with the FLY spectra, there are no detectable differences between them, indicating that the specimens are homogeneous before and after different polymer composites formation and suffers little thickness effect. Herein we will use TEY XANES for the following discussion.

There are several discernible XANES features, labelled from “a” to “d”. The pre-edge peak (feature “a”) can be ascribed to Ca 1s to 3d transition; the shoulder “b” is assigned to the 1s to 4s transition. Although both of them are formally dipole forbidden, they can be still observed because of the hybridization of Ca with ligand states of np-character, leading to the departure from perfect Ca crystal symmetry. The most intense peak (feature “c”) is due to Ca 1s to 4p dipole transition. The shoulder after the main

resonance (feature “d”) is mainly from multiple scattering processes, which is very sensitive to the immediate surroundings of Ca [26-28].

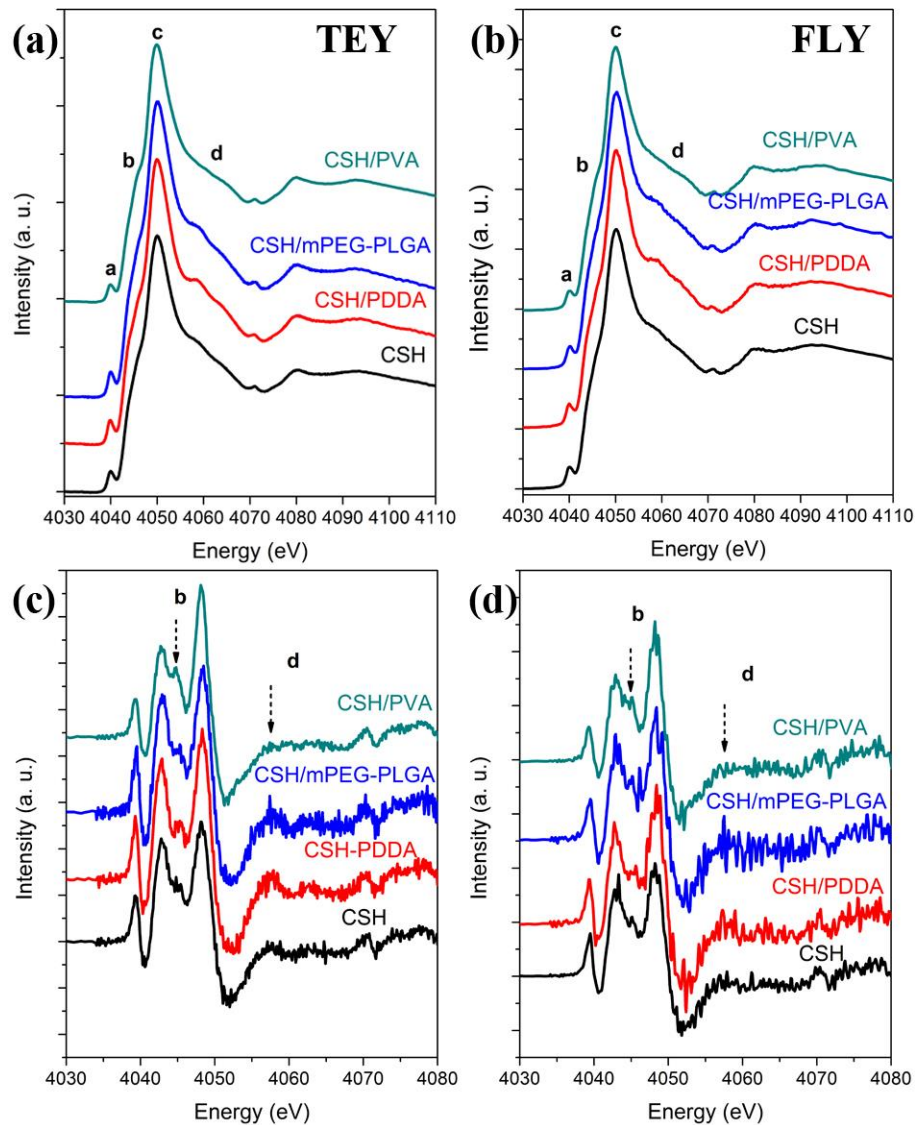


Figure 7-4 (a) Ca K-edge XANES total electron yield (TEY) and (b) fluorescence yield (FLY) spectra of CSH/polymer composites and their first derivative spectra (c) and (d), respectively (dashed arrows in (c) and (d) indicate the changes of CSH/PVA composites compared with CSH nanosheets).

Compared with the FTIR results, XANES spectra are more sensitive to the structure changes after the formation of CSH/polymer composites even though the amounts of polymers incorporations are relative low. Although the spectra of CSH/PDDA (red

profile) and CSH/mPEG-PLGA (navy) are very similar to that of CSH nanosheets (black), after close examination of the spectra of CSH/PVA (dark cyan), two subtle though clearly noticeable changes are observed: one is at the edge jump region (labelled “b”, 4040 - 4045 eV), which becomes more apparent in the first derivative of the spectrum (Figure 7-4(c) and (d)), indicated by the dashed arrows; the other is the change of feature “d”, which can be also observed in the derivative spectrum of CSH/PVA between 4055 - 4060 eV. Both of these changes can be detected both in TEY and FLY spectra. Matsuyama *et al.* [29, 30] found out that the more compact nature of the PVA chain (~0.45 nm) provided the possibility of intercalating into the structure of CSH (in this study, CSH has the structure of 1.4 nm (interlayer spacing) tobermorite, Figure 7-5). The 1.4 nm tobermorite is formed by central Ca-O sheets, connected on both sides to silicate chains. The space between two layers contains additional calcium cations and water molecules [22]. As a result, these changes at the Ca K-edge can be ascribed to the insertion of PVA molecules into the interlayer of CSH, changing the Ca local ordering (changes of feature “b”) and then alters the multiple scattering pathways (change of feature “d”). On the contrary, the reason why mPEG-PLGA and PDDA cannot intercalate into CSH structure may be due to the steric effects or larger chain diameter, and moreover for PDDA polymer, the cationic N⁺ ions interact with Ca ions repulsively and cannot further change the Ca local structure.

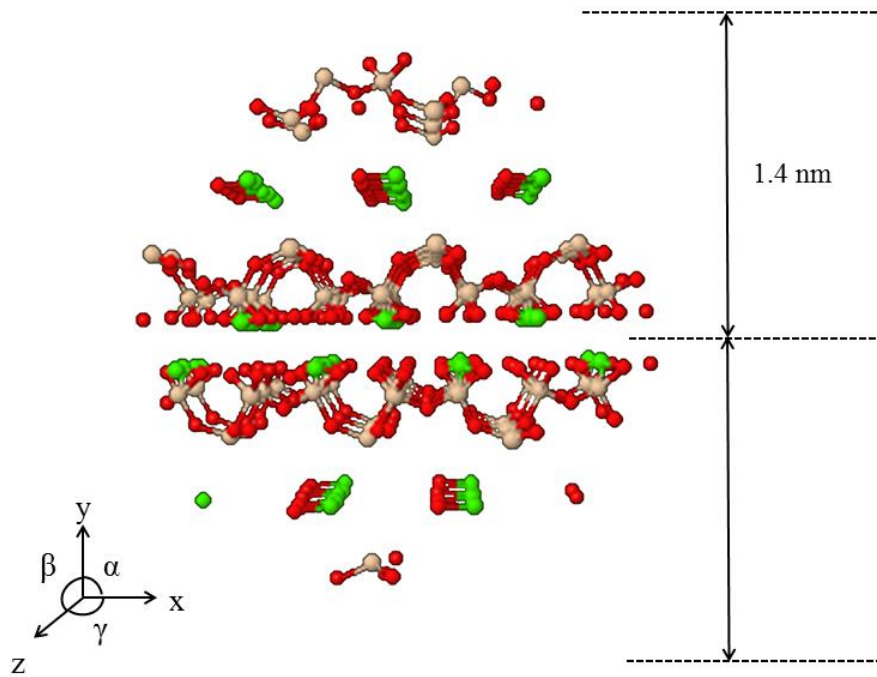


Figure 7-5 Crystal structure of 1.4 nm tobermorite (green, red and beige spheres stand for Ca, O and Si atoms, respectively; $\alpha=90^{\circ}$, $\beta=90^{\circ}$, and $\gamma=123.25^{\circ}$).

Hence mPEG-PLGA and PDDA can only adsorb on the surface of CSH nanosheets, resulting in the change of the local structure of tetrahedral silicate significantly, which are shown in Figure 7-6.

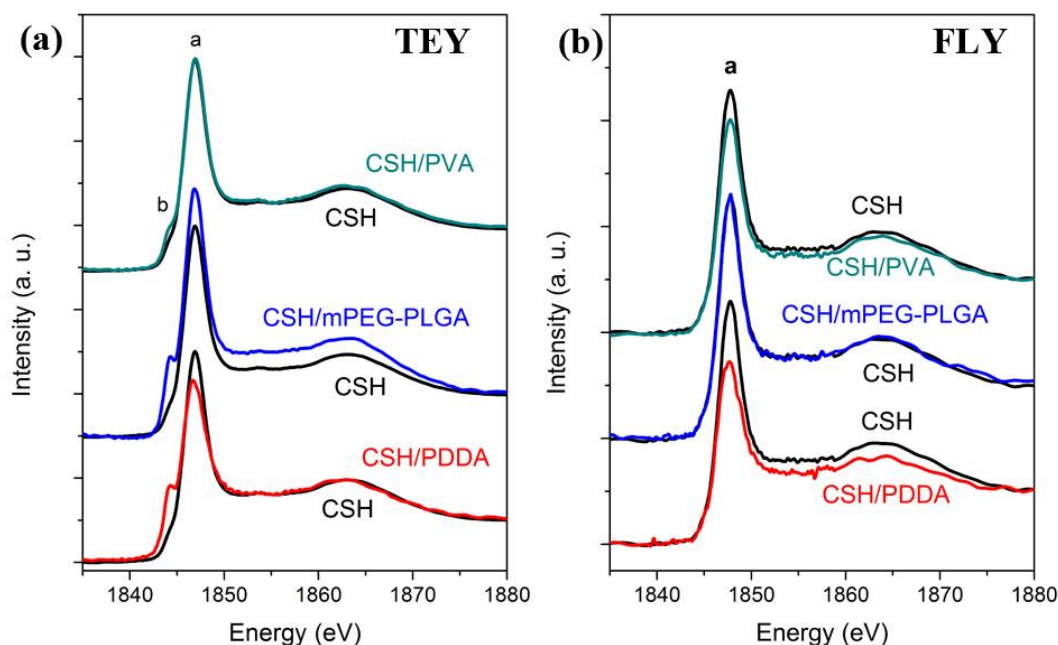


Figure 7-6 (a) Si K-edge XANES total electron yield (TEY) and (b) fluorescence yield (FLY) spectra of CSH/polymer composites.

At the Si K-edge, for the CSH nanosheets, there is only one peak (“a”, black), which is ascribed to the Si 1s to 3p transition in a Si-O tetrahedral environment [31, 32]. For all of the CSH/polymer composites spectra (red, navy, and dark cyan curves), it is interesting to note that a new feature “b” emerged at a lower energy of the main resonance in TEY spectra only (Figure 7-6(a)), while their FLY spectra are very similar (Figure 7-6(b)). This new feature is due to the adsorption of different polymers on the surface of the CSH nanosheets, inducing the distortion of silicate tetrahedra on the surface, which we have explained in previous chapters [33, 34]. Since PVA should be intercalated into interlayers of CSH structure based on the results from the Ca K-edge XANES, there is only subtle change at its Si K-edge XANES, indicating PVA molecules only change the local structure of Ca when they are intercalated into the structure of CSH.

Based on the results of the Ca and Si K-edge XANES, we propose the following interactions between CSH and different polymer molecules, as shown in Figure 7-7. All of the PDDA, mPEG-PLGA and PVA molecules may distort silicate tetrahedra by the adsorption on the surface or the defects of CSH nanosheets; only PVA can intercalate

into the interlayers of CSH structure and changes the Ca local structures because of the compact nature of PVA chains.

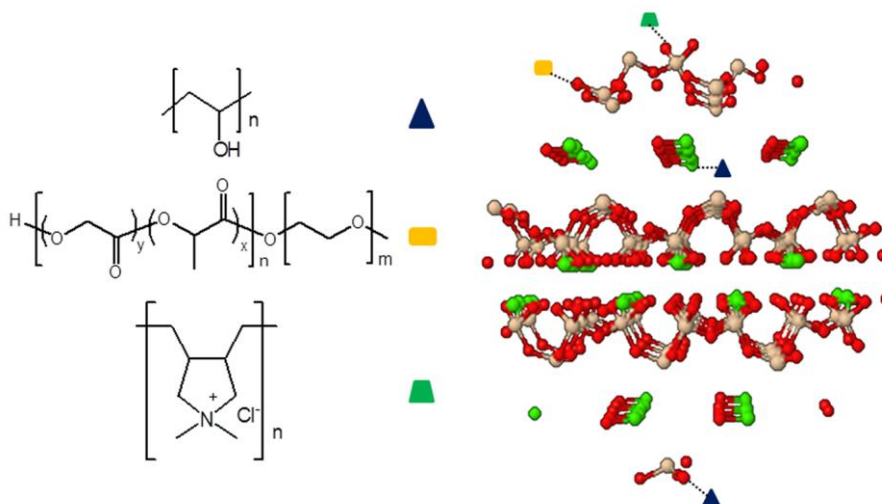
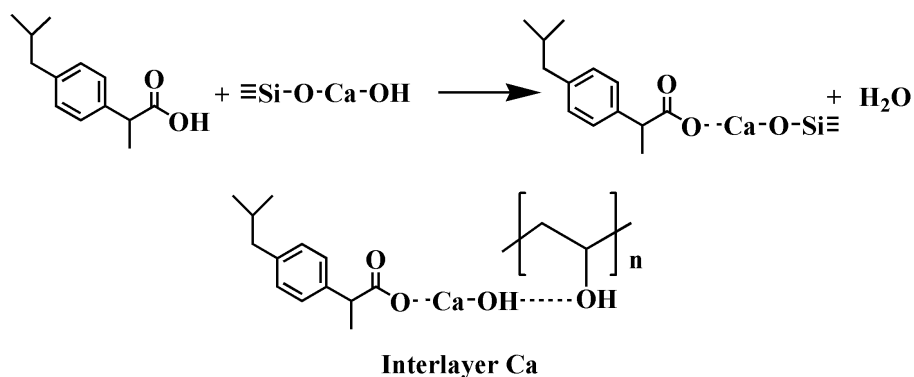


Figure 7-7 Schematic illustration of the interactions between CSH and different polymers (navy triangle, orange rectangle, green trapezoid stand for PVA, mPEG-PLGA and PDDA, respectively; and green, beige and red dots represent calcium, silicon and oxygen atoms, respectively).

7.3.3 Studies of Interactions between CSH/polymer Composites and IBU Molecules

Figure 7-8 shows the Ca K-edge XANES spectra of CSH nanosheets and their polymer composites before and after IBU loading. Similar to the situation before IBU loading, there are no detectable differences between TEY and FLY of CSH/polymer composites with IBU loading. However, compared with the spectra before IBU loading, there are several distinct changes; especially prominent at the features “b” and “d” in the first derivative spectra (Figure 7-8(c) and (d)). In the case of CSH nanosheets, CSH/mPEG-PLGA and CSH/PDDA composites, before IBU loading, there are only two peaks between 4040-4050 eV in the derivative spectra of feature “b”, but three peaks appear after the drug is loaded (both in TEY and FLY spectra); moreover, the shoulder features “d” smear out in all the spectra after IBU loading. These changes have been extensively studied as presented in Chapter 3 and 5 [35], which are due to the interactions between

Ca-OH groups and carboxylic acid groups of IBU molecules. What is more interesting is the observation that the spectra changes after IBU loading into CSH/PVA composites: the spectrum (dark cyan) after IBU loading is different from all the other three spectra. This may be due to the combined effects of IBU, PVA molecules to the local structure of Ca since PVA has been intercalated into the structure of CSH already (Scheme 7-2).



Scheme 7-2 Interactions between CSH, IBU and PVA on the local structure of Ca in the interlayer of CSH.

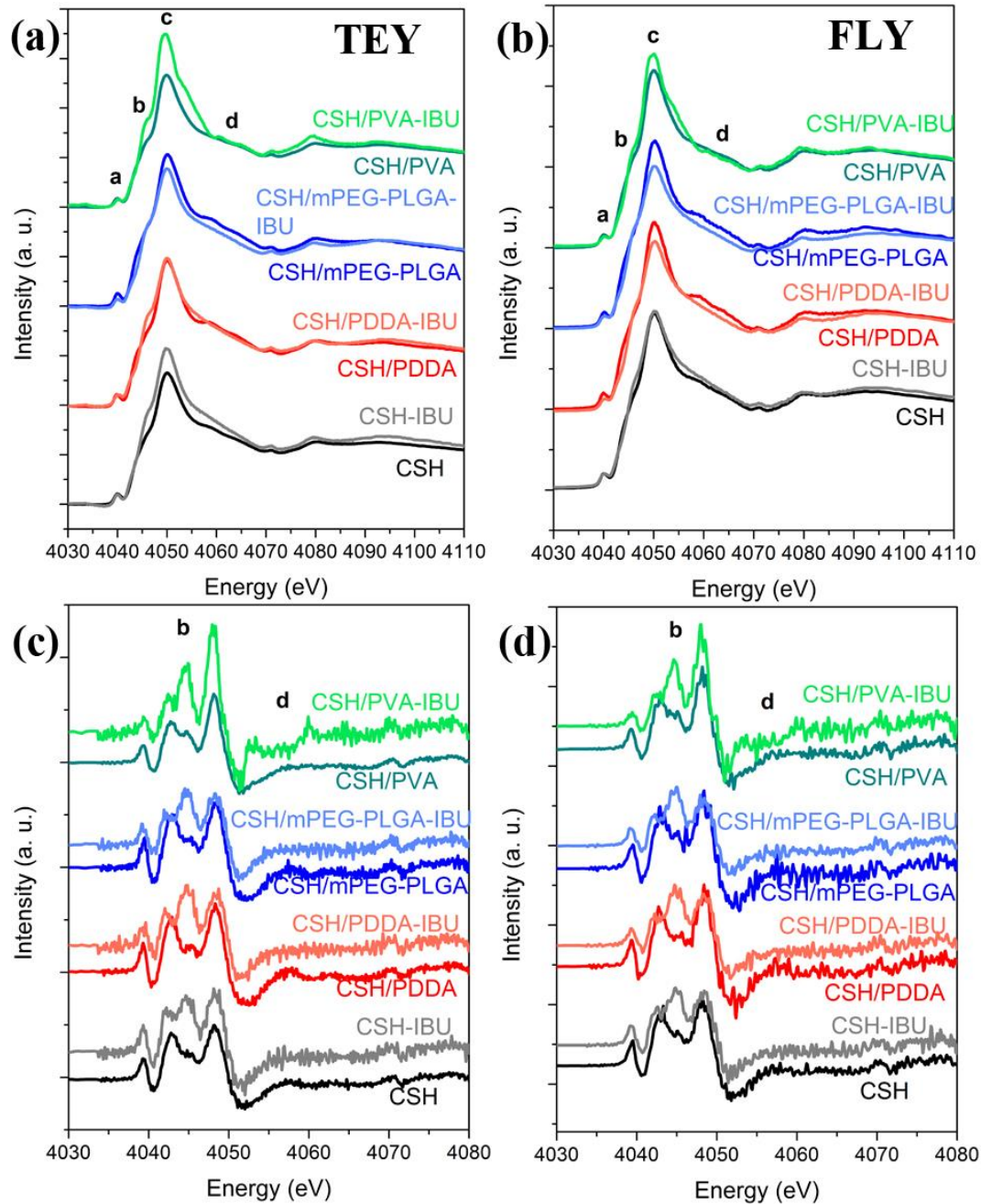
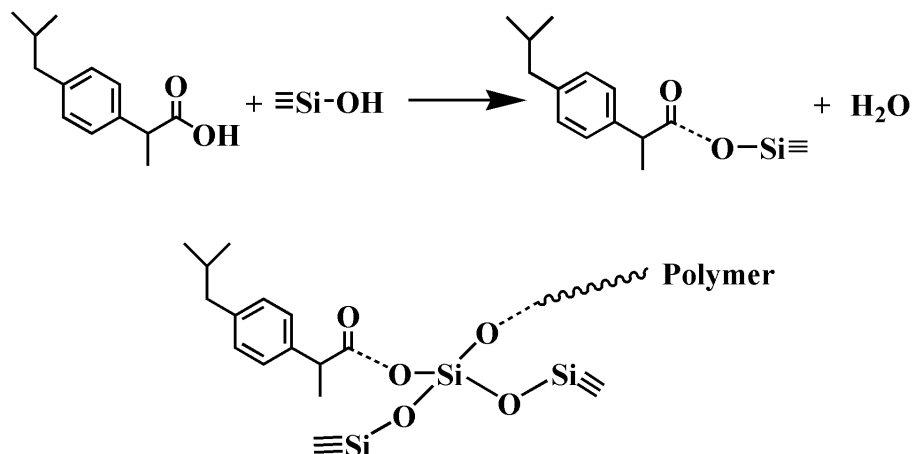


Figure 7-8 Comparisons of (a) Ca K-edge XANES total electron yield (TEY) and (b) fluorescence yield (FLY) spectra of CSH/polymer composites before and after IBU loading and their first derivative spectra (c) and (d), respectively.

The effect of IBU loading on the silicate environment has been studied via the Si K-edge XANES spectra, as shown in Figure 7-9. After IBU loading, feature “b” can only be observed in the TEY of IBU loading samples, which can be ascribed to the combined

interactions between different polymers, IBU molecules and silanol groups (-Si-OH), especially for the CSH/mPEG-PLGA-IBU, which has a more intense peak at around 1843 eV (scheme 7-3).



Silanol groups on the Surface of CSH

Scheme 7-3 Interactions between CSH, IBU and polymers on the local structure of silicate on the surface.

Additionally, the IBU loading changed the main resonance “a” as well, both in the TEY and FY spectra: the main resonance became sharper and shifted to higher energy by 0.2 eV. In chapter 5, we have illustrated that the electrostatic interaction is stronger between Ca and IBU (due to the activity of Ca-OH, Si-OH to carboxylic acid) than that between silanol groups and IBU, making original silicate environment a more “isolated” tetrahedral environment, hence the width of the main resonances at the Si K-edge TEY and FY became narrower and shifted.

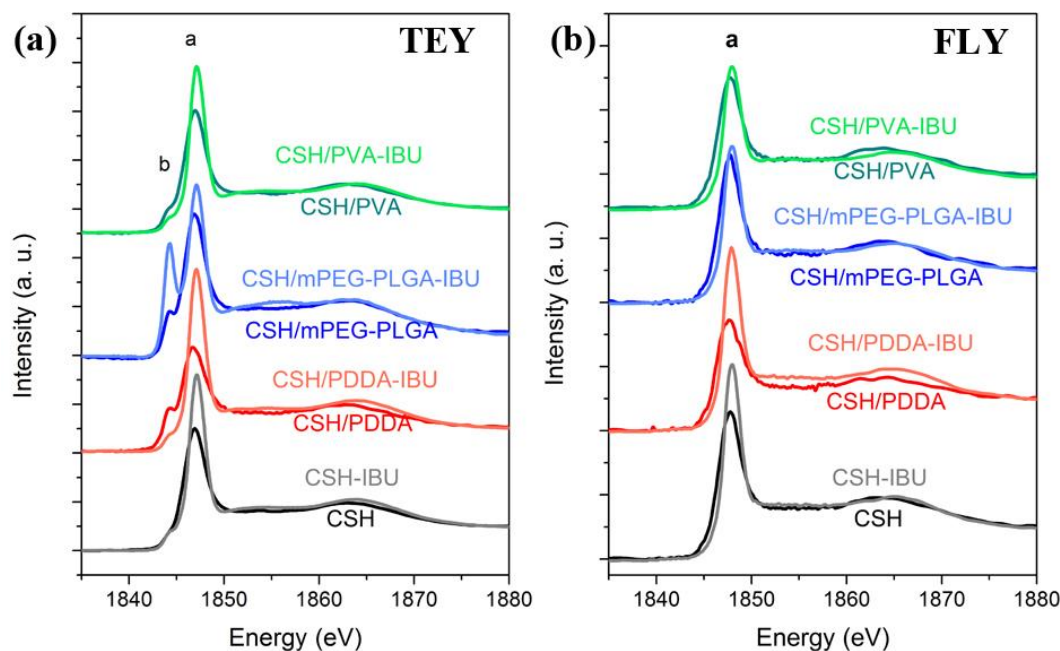


Figure 7-9 Comparisons of (a) Si K-edge XANES total electron yield (TEY) and (b) fluorescence yield (FLY) spectra of CSH/polymer composites after IBU loading.

The FTIR spectra of the CSH nanosheets and CSH/polymer composites before and after the IBU loading are shown in Figure 7-10 to support the XANES analysis. The more prominent C–H stretching ($\sim 2800\text{--}3000\text{ cm}^{-1}$), and the appearance of C=O ($\sim 1560\text{ cm}^{-1}$) stretching vibration peaks indicate that IBU has been loaded on the nanosheets and composites. Nevertheless C=O stretching vibrations are normally located around 1700 cm^{-1} [23], the red shift of C=O stretching vibration indicates the interactions between the CSH/polymer composites and the –COOH groups of IBU drug molecules. Besides, the blue shift of Si–O stretching vibration from 975 cm^{-1} to 1083 cm^{-1} also supports this IBU-silanol groups interaction. The formation of –Si–O–C can increase the polarity of the Si–O group while reduce the polarity of the C=O group, which results in the blue and red shifts in the FTIR spectra mentioned above.

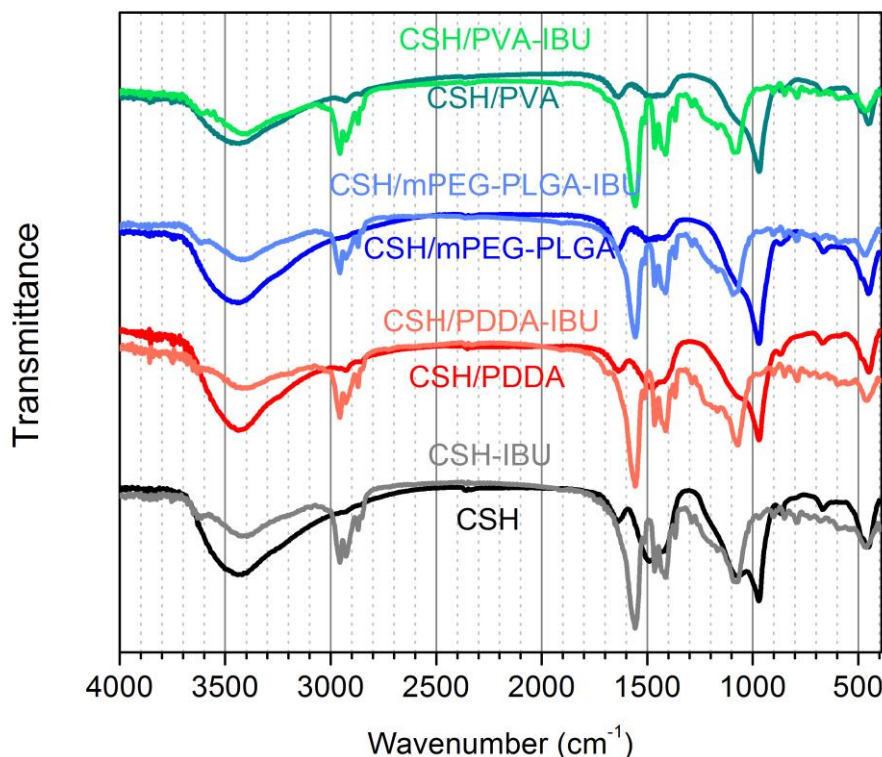


Figure 7-10 Comparisons of FTIR spectra of CSH nanosheets, CSH/polymer composites before and after IBU drug loading.

7.3.4 Effects of Different Polymer Incorporations on Drug Loading Capacities and Drug Release Kinetics

After we have demonstrated that the incorporations of different polymers change the structures of CSH by the analysis of XANES, especially that of the CSH/PVA composites, it would be necessary to investigate whether or not these interactions may influence the drug loading capacities (DLCs) and drug release kinetics. Hence, IBU loading capacities results into different CSH/polymer composites are shown in Figure 7-11. Compared with the CSH nanosheets alone, all the DLCs of IBU decrease to some extent after the formation of CSH/polymer composites. This is due to the interactions between different polymers and CSH nanosheets: parts of the active sites (Ca-OH and Si-OH groups) interact with different polymers molecules, leading to the reduction of the number of active sites for the IBU molecules' attachment. It should be noted that the IBU DLCs of CSH/mPEG-PLGA decrease significantly compared with that of CSH nanosheets. One reason is due to the interactions of CSH and polymers mentioned above,

the other is the steric and entropic effects, which is one of the key factors that prevents the IBU molecules' attachment on the surface of CSH composites.

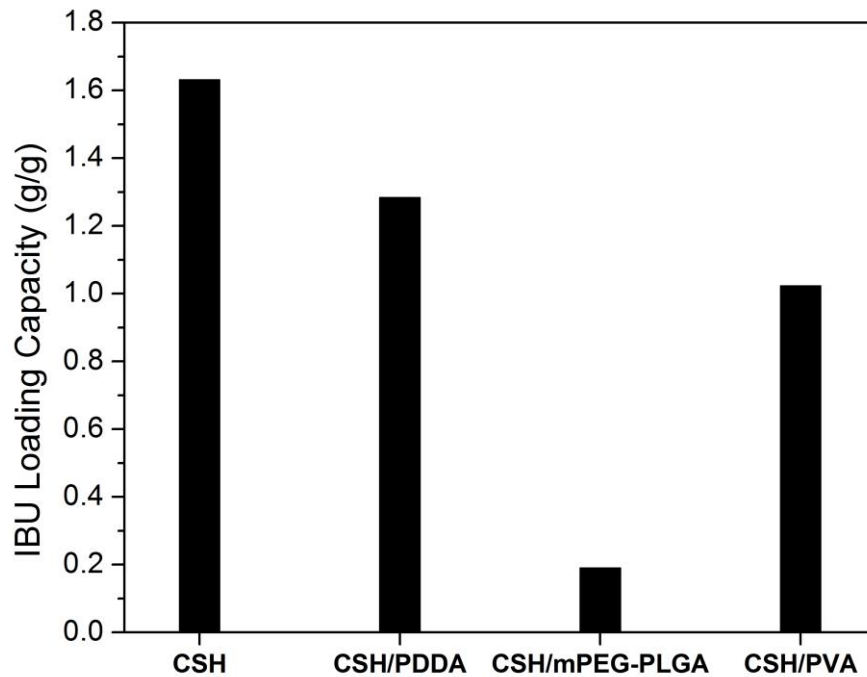


Figure 7-11 Drug loading capacities (DLCs) of different CSH/polymer composites (the DLC of CSH nanosheets for comparison).

Figure 7-12 shows the IBU drug release profiles of the IBU-CSH/polymer composites drug delivery systems in the PBS medium. In Chapter 6, it is shown that the CSH drug carriers alone do not provide good ability of controlled drug release: there was a burst drug release effect at the early stage; about 97-98 % of loaded IBU were released in the first several hours [36], and so are the situations of CSH/PDDA and CSH/mPEG-PLGA in this study. However, compared with the other two composites, the CSH/PVA-IBU system shows a relative controlled drug release kinetics, which is largely due to the intercalation of PVA into the CSH structures, and the combined effects of PVA and IBU on the structure changes of Ca ions which slowed down the IBU release from the CSH/PVA composite.

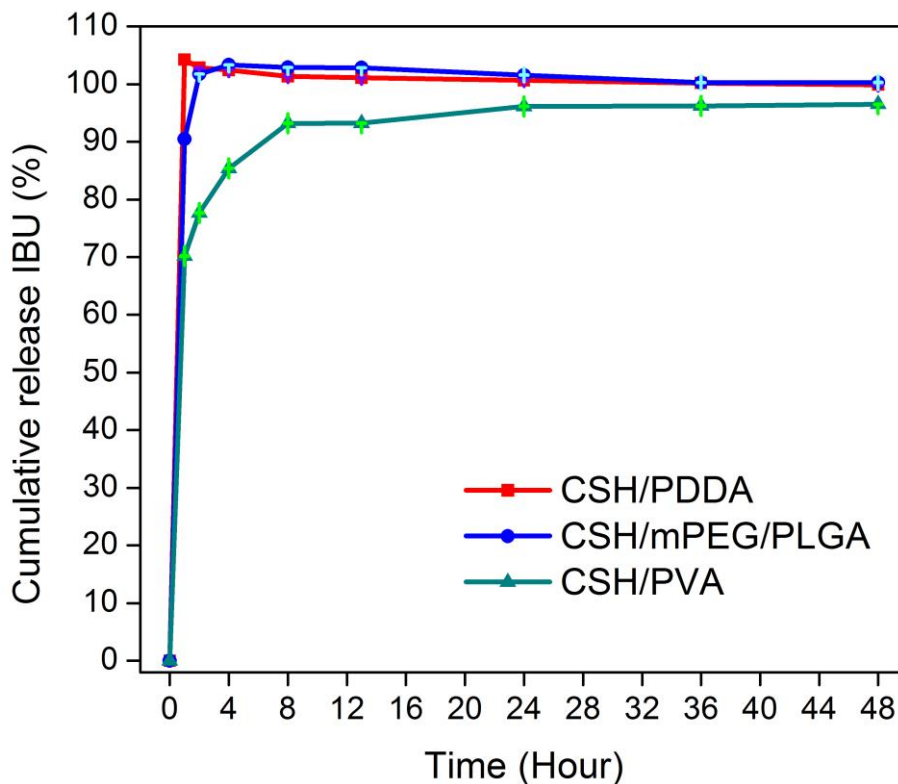


Figure 7-12 Drug release profiles of different CSH/polymer composites.

7.4 Conclusions

In this chapter, we have shown the structural changes of CSH nanosheets upon the formation of different polymers composites and the incorporations of IBU molecules by XANES spectra analysis as summarized below.

- PVA molecules can intercalate into to the interlayers of CSH structures and as a result modify the local structure of interlayer Ca ions and silicate tetrahedra on the surface; while mPEG-PLGA and PDDA can only adsorb on the surface of CSH nanosheets leading to the distortion the silicate tetrahedra chains on the surface because of steric effects.
- The IBU loading on these composites further changes the local structure of Ca and silicate simultaneously by the interactions between the carboxylic acid groups of IBU and the Ca-OH and Si-OH groups of CSH, which has been extensively studied in previous chapters already.

- However, the CSH/polymer composites do not enhance the drug loading capacities of IBU because the active sites for drug molecules' attachment have been reduced by the interaction CSH with polymers.
- Compared with the other two composite systems, the CSH/PVA composite has a relatively better controlled drug release profile (delayed release). In our opinions, this may be due to the PVA intercalation into CSH structures and has a combined effect with IBU on the structure of interlayer Ca ions after drug loading.

Finally, we have demonstrated that XANES is a sensitive tool to track these effects from different elemental point of view, and opens up future possibilities for the study of drug delivery and drug release of bioceramics and their composites.

7.5 References

1. Gou, Z. and Chang, J., *J. Eur. Ceram. Soc.* **2004**, *24*, 93-99.
2. Rodriguez-Lorenzo, L.M., Garcia-Carrodegas, R., Rodriguez, M.A., De Aza, S., Jimenez, J., Lopez-Bravo, A., Fernandez, M., and Roman, J.S., *J. Biomed. Mater. Res. A* **2009**, *88A*, 53-64.
3. Siriphannon, P., Kameshima, Y., Yasumori, A., Okada, K., and Hayashi, S., *J. Eur. Ceram. Soc.* **2002**, *22*, 511-520.
4. Li, H. and Chang, J., *J. Control. Release* **2005**, *107*, 463-473.
5. Ding, S.-J., Shie, M.-Y., and Wang, C.-Y., *J. Mater. Chem.* **2009**, *19*, 1183-1190.
6. Wu, C.T. and Chang, J., *Biomed. Mater.* **2013**, *8*, 032001.
7. Hughes, E., Yanni, T., Jamshidi, P., and Grover, L.M., *Adv. Appl. Ceram.* **2015**, *114*, 65-76.
8. Rezwan, K., Chen, Q.Z., Blaker, J.J., and Boccaccini, A.R., *Biomaterials* **2006**, *27*, 3413-3431.

9. Dou, Y.D., Wu, C.T., and Chang, J., *Acta Biomater.* **2012**, 8, 4139-4150.
10. Wei, J., Chen, F.P., Shin, J.W., Hong, H., Dai, C.L., Su, J.C., and Liu, C.S., *Biomaterials* **2009**, 30, 1080-1088.
11. Wu, J., Zhu, Y.-J., Chen, F., Zhao, X.Y., Zhao, J., and Qi, C., *Dalton Trans.* **2013**, 42, 7032-7040.
12. Cheng, W., Li, H.Y., and Chang, J., *Mater. Lett.* **2005**, 59, 2214-2218.
13. Ramila, A., Munoz, B., Perez-Pariente, J., and Vallet-Regi, M., *J. Sol-Gel. Sci. Technol.* **2003**, 26, 1199-1202.
14. Wang, S.B., *Micropor. Mesopor. Mater.* **2009**, 117, 1-9.
15. Vallet-Regi, M., Balas, F., and Arcos, D., *Angew. Chem. Int. Edit.* **2007**, 46, 7548-7558.
16. Black, L., Garbev, K., and Gee, I., *Cem. Concr. Res.* **2008**, 38, 745-750.
17. Wang, S.D. and Scrivener, K.L., *Cem. Concr. Res.* **2003**, 33, 769-774.
18. Rees, C.A., Provis, J.L., Lukey, G.C., and van Deventer, J.S.J., *Langmuir* **2007**, 23, 9076-9082.
19. Ha, J., Chae, S., Chou, K.W., Tyliczszak, T., and Monteiro, P.J.M., *J. Mater. Sci.* **2012**, 47, 976-989.
20. Sham, T.-K., *Int. J. Nanotechnol.* **2008**, 5, 1194-1246.
21. Wu, J., Zhu, Y.-J., and Chen, F., *Small* **2013**, 9, 2911-2925.
22. Bonaccorsi, E., Merlino, S., and Kampf, A.R., *J. Am. Ceram. Soc.* **2005**, 88, 505-512.
23. Stuart, B.H., *Infrared Spectroscopy: Fundamentals and Applications.* **2004**: Wiley.

24. Yu, P., Kirkpatrick, R.J., Poe, B., McMillan, P.F., and Cong, X.D., *J. Am. Ceram. Soc.* **1999**, *82*, 742-748.
25. Matsuyama, H. and Young, J.F., *J. Mater. Res.* **1999**, *14*, 3379-3388.
26. Yamamoto, T., *X-Ray Spectrom.* **2008**, *37*, 572-584.
27. Eichert, D., Salome, M., Banu, M., Susini, J., and Rey, C., *Spectrochim. Acta B* **2005**, *60*, 850-858.
28. Cormier, L. and Neuville, D.R., *Chem. Geol.* **2004**, *213*, 103-113.
29. Matsuyama, H. and Young, J.F., *J. Mater. Res.* **1999**, *14*, 3389-3396.
30. Matsuyama, H. and Young, J.F., *Chem. Mater.* **1999**, *11*, 16-19.
31. Li, D., Bancroft, G.M., Kasrai, M., Fleet, M.E., Feng, X.H., Tan, K.H., and Yang, B.X., *Solid State Commun.* **1993**, *87*, 613-617.
32. Li, D., Bancroft, G.M., Fleet, M.E., and Feng, X.H., *Phys. Chem. Miner.* **1995**, *22*, 115-122.
33. Sutherland, D.G.J., Kasrai, M., Bancroft, G.M., Liu, Z.F., and Tan, K.H., *Phys. Rev. B* **1993**, *48*, 14989-15001.
34. Chaboy, J., Barranco, A., Yanguas-Gil, A., Yubero, F., and Gonzalez-Elipe, A.R., *Phys. Rev. B* **2007**, *75*, 075205.
35. Guo, X., Wu, J., Yiu, Y.-M., Hu, Y., Zhu, Y.-J., and Sham, T.-K., *Phys. Chem. Chem. Phys.* **2013**, *15*, 15033-15040.
36. Guo, X., Wang, Z., Wu, J., Hu, Y., Wang, J., Zhu, Y.-J., and Sham, T.-K., *CrystEngComm.* **2015**, *17*, 4117-4124.

Chapter 8

8 Summary, Conclusions, and Future Work

8.1 Summary and Conclusions

In this thesis, the interactions of drug carriers and drug molecules, which play crucial roles in the determinations of drug loading capacities and drug release kinetics have been explored. Hence, the focus of this thesis has been on the investigation of the interaction between calcium silicate hydrate (CSH) and different drug molecules by X-ray absorption near edge structure (XANES) and scanning transmission X-ray microscopy (STXM) to understand the local structure change after drug molecules incorporations. It is also demonstrated that XANES and STXM are so powerful tools with element and chemical site specificity that they should be widely applied in structural and mechanisms studies of various biomaterials in the drug delivery fields in the future.

In chapter 3, Ca and Si K-edge XANES studies of CSH with different morphologies before and after ibuprofen (IBU) loading were presented. It is found that there are significant interactions of the drug molecules with the carriers from XANES spectra, accompanied by the local ordering of the system. First, calcium ions interact with carboxyl groups, generating calcium acetate like compounds. Second, besides hydrogen bonding between silicates and drug molecules, the most amazing observation is the strong interaction between silicates and carboxylic groups, forming Si-O-C bonds via esterification-like reaction. Moreover, drug loading leads to better ordering of silicates locally. Third, we have demonstrated that the morphology and the presence of hydrates of drug carriers may influence the drug loading capacities. The CSH drug delivery systems exhibit high drug loading capacities and excellent sustained drug release behaviors, which can be potentially applied in various biomedical fields.

In chapter 4, CSH microspheres formed by the self-assembly of nanosheets were prepared according to a sonochemical method reported previously. The chemical imaging (with thickness distribution) and interactions between individual CSH microsphere and IBU on an individual microsphere were studied by STXM at the C and Si K-edges. The

results suggest that IBU interacts with both Ca-OH and Si-OH groups via its carboxylic acid functional group; this observation confirms previous analysis that based on a large collection of many individual CSH nanostructures in the drug delivery system in chapter 3. We find that the drug loading process has no diverse effect on the integrity of IBU molecules. Moreover, it is of great interest and significance that one can obtain the drug loading distribution in an individual mesoporous CSH microsphere; IBU molecules are loaded homogenously into CSH drug carriers.

In chapter 5, the comparative studies of interactions between different functional groups of ibuprofen, alendronate sodium and gentamicin sulfate, and mesoporous spheres of CSH were performed by XANES and FTIR spectroscopy in order to establish the relationship between carrier-drug interactions and drug loading capacities. MS-CSH provides active linkage sites for acidic functional groups of drug molecules by electrostatic interactions; while they are not sensitive to the other groups such as amino and hydroxyl groups. Hence this result will provide some hints to scientists in drug delivery and materials fields: the acidic drug molecules can be loaded into CSH easily with higher DLCs; while further surface modifications of CSH such as with acidic groups on the surface, may provide further incorporation of basic drug molecules into CSH via the interactions, and may provide high DLCs and controlled drug release profiles. Besides, the ratio between Ca^{2+} ions from the CSH carrier and the $-\text{COOH}$ groups from the IBU drug molecules is one main factor responsible for high IBU drug loading capacity.

In chapter 6, the mechanisms studies of CSH microspheres biomineralization upon IBU release in the simulated body fluid (SBF) were elucidated by XANES via linear combination fittings. At the early stages of drug release, crystalline CSH microspheres disassemble into amorphous flake-like sheets, some silicate ions undergoes exchange into the SBF solution while others becomes hydrolyzed into amorphous silica. Both Ca (from CSH and SBF) and PO_4^{3-} ions (from SBF) first form amorphous calcium phosphate at first 2h, then quickly transformed into amorphous hydroxyapatite (HAp), and the finally products were crystalline HAp after the samples were soaked in the SBF solution for more than 3h. At the same time, some bicarbonate ions (HCO_3^-) co-precipitate from SBF,

generating amorphous CaCO_3 . Moreover, from STXM data, more P were detected around the area where more Si were located; indicating the abundant silanol groups and the following hydrolyzed SiO_2 provided preference aggregation sites of HAp.

In chapter 7, CSH/polymer composites were synthesized using a controlled precipitation reaction between calcium salt and silicate salt, followed by the addition of various polymer solutions at room temperature. We have shown the structural changes of CSH nanosheets upon the formation of different polymers composites and the incorporations of IBU molecules by XANES spectra analysis as summarized below. Polyvinyl alcohol (PVA) molecules can intercalate into to interlayers of CSH structures and as a result modify the local structure of interlayer Ca ions and silicate tetrahedra on the surface; while monomethoxy (polyethyleneglycol)-block-poly(DL-lactide-co-glycolide) (mPEG-PLGA) and poly(diallyldimethylammonium chloride) (PDDA) can only adsorb on the surface of CSH nanosheets by distortion the silicate tetrahedral chains on the surface because of the steric effects. The IBU loading further changes the local structure of Ca and silicate simultaneously by the interactions between the carboxylic acid groups of IBU and the Ca-OH and Si-OH groups of CSH, which has been extensively studied in previous chapters. However, the CSH/polymer composites do not enhance the drug loading capacities of IBU because the active sites for drug molecules attachment have been reduced by the interactions with different polymers. Compared with the other two composite systems, the CSH/PVA composite has a relatively better controlled drug release profile. In our opinions, this may be due to the PVA intercalation into CSH structures and has a combined effect with IBU on the structure of interlayer Ca ions after drug loading.

8.2 Future Work

Calcium silicate is a new type of bioceramics which has gained considerable attentions in hard-tissue medical treatment because of its satisfactory osteoblast proliferation and differentiation. It has been shown in this thesis that XANES and STXM are powerful and sensitive techniques to help understand the carrier-drug interactions and phase transformation of drug carriers during drug release by correlation with structural changes of drug carriers before and after drug loading; or by analysis the drug release *in vitro*

products after several time intervals. These findings provide theoretical foresights and guidance into further surface modifications or functionalization of calcium silicate carriers to enhance the drug loading capacities, control the drug release kinetics and open up new possibilities to apply calcium silicate into various fields in future.

Continuing along the results in chapter 5; calcium silicates are only sensitive to the acidic functional groups of drug molecules, due to the active sites of Ca-OH and Si-OH groups, thus calcium silicate modified with polyacids (such as acetic acid) on the surface, which may provide acidic ends on the surface to further attach drug molecules only possess basic functional groups will be good candidates for XANES study in the next step. It would be interesting to investigate the structural changes of calcium silicate after surface modifications and monitor the interactions between basic drug molecules and drug carriers, which may increase the drug loading capacities of basic drugs and control the drug release kinetics to some extent.

For the work presented in chapter 7, and that we have successfully mapped the IBU distribution in individual CSH microsphere in chapter 4, it would be significant to track the polymers and IBU distributions in the CSH/polymer composites by the analysis the STXM images and comparison the polymers and IBU spectra at the C K-edge, respectively.

Europium (Eu) is known as the phosphors because of its intra orbital electronic transition, which can be applied into biological imaging. What is more important is that it is functional mimics of Ca ions and can affect the bone remodelling cycle [1]. As a result, there is an increasing interest in Eu³⁺ doped HAp and CSH as drug carriers because of the multi-functionalities [2, 3]. X-ray excited optical luminescence (XEOL) which is an X-ray photon-in, optical photon-out technique is more powerful than conventional methods for studying the optical properties of light emitting materials, because it allows more pathways for optical decay and elemental specific [4]. Hence, on the basis of XANES studies, it would be interesting to investigate the structural changes after Eu doping, and compare the optical properties of drug carriers before and after drug loading using XEOL.

Industrial activities generate large quantities of heavy metal bearing wastes every year, and most of them are toxic, mutagenic, and carcinogenic. Cement is found and is used for stabilization and solidification of waste materials containing heavy metals [5, 6].

However, the mechanisms of fixation of heavy metals are not completely clear, and EXAFS has been investigated successfully in the study the Zn sorption mechanism into CSH [7]. So it would be significant to systematically study the adsorption mechanisms of different heavy metal ions (such as Ni^{2+} , Cr^{3+} , Cu^{2+} , *etc.*) into calcium silicate by XANES, EXAFS, FEFF simulation and linear combination fitting. This study is maybe going to elucidate some key factors to be considered that will influence the ions adsorptions, such as atomic diameter, ionic charge, *etc.*

8.3 References

1. Barta, C.A., Sachs-Barrable, K., Jia, J., Thompson, K.H., Wasan, K.M., and Orvig, C., *Dalton Trans.* **2007**, *43*, 5019-5030.
2. Kang, X., Huang, S., Yang, P., Ma, P.a., Yang, D., and Lin, J., *Dalton Trans.* **2011**, *40*, 1873-1879.
3. Chen, F., Huang, P., Zhu, Y.-J., Wu, J., Zhang, C.-L., and Cui, D.-X., *Biomaterials* **2011**, *32*, 9031-9039.
4. Sham, T.-K. and Rosenberg, R.A., *ChemPhysChem.* **2007**, *8*, 2557-2567.
5. Chen, Q.Y., Tyrer, M., Hills, C.D., Yang, X.M., and Carey, P., *Waste Manage.* **2009**, *29*, 390-403.
6. Wu, J., Zhu, Y.-J., and Chen, F., *Small* **2013**, *9*, 2911-2925.
7. Ziegler, F., Scheidegger, A.M., Johnson, C.A., Dähn, R., and Wieland, E., *Environ. Sci. Technol.* **2001**, *35*, 1550-1555.

Appendix A: Copyright Release from The Royal Society of Chemistry

RSC | Advancing the
Chemical Sciences

Royal Society of Chemistry
Thomas Graham House
Science Park
Milton Road
Cambridge
CB4 0WF

Tel: +44 (0)1223 420 066
Fax: +44 (0)1223 423 623
Email: contracts-copyright@rsc.org

www.rsc.org

Acknowledgements to be used by RSC authors

Authors of RSC books and journal articles can reproduce material (for example a figure) from the RSC publication in a non-RSC publication, including theses, without formally requesting permission providing that the correct acknowledgement is given to the RSC publication. This permission extends to reproduction of large portions of text or the whole article or book chapter when being reproduced in a thesis.

The acknowledgement to be used depends on the RSC publication in which the material was published and the form of the acknowledgements is as follows:

- For material being reproduced from an article in *New Journal of Chemistry* the acknowledgement should be in the form:
 - [Original citation] - Reproduced by permission of The Royal Society of Chemistry (RSC) on behalf of the Centre National de la Recherche Scientifique (CNRS) and the RSC
- For material being reproduced from an article *Photochemical & Photobiological Sciences* the acknowledgement should be in the form:
 - [Original citation] - Reproduced by permission of The Royal Society of Chemistry (RSC) on behalf of the European Society for Photobiology, the European Photochemistry Association, and RSC
- For material being reproduced from an article in *Physical Chemistry Chemical Physics* the acknowledgement should be in the form:
 - [Original citation] - Reproduced by permission of the PCCP Owner Societies
- For material reproduced from books and any other journal the acknowledgement should be in the form:
 - [Original citation] - Reproduced by permission of The Royal Society of Chemistry

The acknowledgement should also include a hyperlink to the article on the RSC website.

The form of the acknowledgement is also specified in the RSC agreement/licence signed by the corresponding author.

Except in cases of republication in a thesis, this express permission does not cover the reproduction of large portions of text from the RSC publication or reproduction of the whole article or book chapter.

A publisher of a non-RSC publication can use this document as proof that permission is granted to use the material in the non-RSC publication.

VAT Registration Number: GB 342 1764 71

Registered Charity Number: 207890

Dear Xiaoxuan Guo

The Royal Society of Chemistry (RSC) hereby grants permission for the use of your paper(s) specified below in the printed and microfilm version of your thesis. You may also make available the PDF version of your paper(s) that the RSC sent to the corresponding author(s) of your paper(s) upon publication of the paper(s) in the following ways: in your thesis via any website that your university may have for the deposition of theses, via your university's Intranet or via your own personal website. We are however unable to grant you permission to include the PDF version of the paper(s) on its own in your institutional repository. The Royal Society of Chemistry is a signatory to the STM Guidelines on Permissions (available on request).

Please note that if the material specified below or any part of it appears with credit or acknowledgement to a third party then you must also secure permission from that third party before reproducing that material.

Please ensure that the thesis states the following:

Reproduced by permission of The Royal Society of Chemistry

and include a link to the paper on the Royal Society of Chemistry's website.

Please ensure that your co-authors are aware that you are including the paper in your thesis.

Regards

Gill Cockhead

Publishing Contracts & Copyright Executive

Royal Society of Chemistry

Dear Gill Cockhead,

I would like to request for a permission to reproduce three articles in the following journal in their entirety for my Ph.D. thesis.

1. Guo, X., Wang, Z., Wu, J., Wang, J., Zhu, Y.-J., and Sham, T.-K., Imaging of drug loading distributions in individual microspheres of calcium silicate hydrate - an X-ray spectromicroscopy study. *Nanoscale* 2015, 7, 6767-6773.
2. Guo, X., Wang, Z., Wu, J., Hu, Y., Wang, J., Zhu, Y.-J., and Sham, T.-K., Tracking the transformations of mesoporous microspheres of calcium silicate hydrate at the nanoscale upon ibuprofen release: a XANES and STXM study. *CrystEngComm*. 2015, 17, 4117-4124.
3. Guo, X., Wu, J., Yiu, Y.-M., Hu, Y., Zhu, Y.-J., and Sham, T.-K., Drug-nanocarrier interaction-tracking the local structure of calcium silicate upon ibuprofen loading with X-ray absorption near edge structure (XANES). *Phys. Chem. Chem. Phys.* 2013, 15, 15033-15040.

Sincerely,

Xiaoxuan Guo

Appendix B: Copyright Release from The American Chemical Society



RightsLink®

Home

Create Account

Help



ACS Publications
Most Trusted. Most Cited. Most Read.

Title: Tracking Drug Loading Capacities of Calcium Silicate Hydrate Carrier: A Comparative X-ray Absorption Near Edge Structures Study

Author: Xiaoxuan Guo, Zhiqiang Wang, Jin Wu, et al

Publication: The Journal of Physical Chemistry B

Publisher: American Chemical Society

Date: Aug 1, 2015

Copyright © 2015, American Chemical Society

LOGIN

If you're a [copyright.com](#) user, you can login to RightsLink using your [copyright.com](#) credentials. Already a [RightsLink](#) user or want to [learn more?](#)

PERMISSION/LICENSE IS GRANTED FOR YOUR ORDER AT NO CHARGE

This type of permission/license, instead of the standard Terms & Conditions, is sent to you because no fee is being charged for your order. Please note the following:

- Permission is granted for your request in both print and electronic formats, and translations.
- If figures and/or tables were requested, they may be adapted or used in part.
- Please print this page for your records and send a copy of it to your publisher/graduate school.
- Appropriate credit for the requested material should be given as follows: "Reprinted (adapted) with permission from (COMPLETE REFERENCE CITATION). Copyright (YEAR) American Chemical Society." Insert appropriate information in place of the capitalized words.
- One-time permission is granted only for the use specified in your request. No additional uses are granted (such as derivative works or other editions). For any other uses, please submit a new request.

BACK

CLOSE WINDOW

Copyright © 2015 [Copyright Clearance Center, Inc.](#) All Rights Reserved. [Privacy statement.](#) [Terms and Conditions.](#) Comments? We would like to hear from you. E-mail us at customercare@copyright.com

Curriculum Vitae

Name:	Xiaoxuan Guo
Post-secondary Education and Degrees:	Nankai University Tianjin, China 2006-2010 B.Sc. University of Western Ontario London, Ontario, Canada 2010-present Ph.D. Candidate
Honors and Awards:	ASPIRE Travel Award, \$1,000 (2012) Ph.D. project was a news item reported by the media - London Metro, The London Free Press and Canadian Light Source News
Related Work Experience	Teaching Assistant and Lab Demonstrator Chemistry, University of Western Ontario 2010-2015

Publications:

1. **Guo, X.**, Wang, Z., Wu, J., Yiu, Y.-M., Hu, Y., Zhu, Y.-J., and Sham, T.-K., Tracking Drug Loading Capacities of Calcium Silicate Hydrate Carrier: A Comparative X-ray Absorption Near Edge Structures Study. *J. Phys. Chem. B*, **2015**, *119*, 10052–10059.
2. **Guo, X.**, Wang, Z., Wu, J., Wang, J., Zhu, Y.-J., and Sham, T.-K., Imaging of drug loading distributions in individual microspheres of calcium silicate hydrate - an X-ray spectromicroscopy study. *Nanoscale* **2015**, *7*, 6767-6773.
3. **Guo, X.**, Wang, Z., Wu, J., Hu, Y., Wang, J., Zhu, Y.-J., and Sham, T.-K., Tracking the transformations of mesoporous microspheres of calcium silicate hydrate at the nanoscale upon ibuprofen release: a XANES and STXM study. *CrystEngComm*. **2015**, *17*, 4117-4124.

4. Hou, D., **Guo, X.**, Liu, C., Sham, T.-K., Liang, H., Gao, J., Sun, X., Zhang, B., Zhan, F., Huan, Y., and Tao, Y., Hydrothermal synthesis, X-ray absorption and luminescence properties of Tb³⁺ doped LaPO₄. *J. Lumin.* **2015**, *165*, 23-29.
5. Wang, Z., **Guo, X.**, and Sham, T.-K., 2D XANES-XEOL mapping: observation of enhanced band gap emission from ZnO nanowire arrays. *Nanoscale* **2014**, *6*, 6531-6536.
6. Chen, Y., **Guo, X.**, Tse, W.H., Sham, T.-K., and Zhang, J., Magnetic anisotropy induced in NiCo granular nanostructures by ZnO nanorods deposited on a polymer substrate. *RSC Adv.* **2014**, *4*, 47987-47991.
7. **Guo, X.**, Wu, J., Yiu, Y.-M., Hu, Y., Zhu, Y.-J., and Sham, T.-K., Drug–nanocarrier interaction—tracking the local structure of calcium silicate upon ibuprofen loading with X-ray absorption near edge structure (XANES). *Phys. Chem. Chem. Phys.* **2013**, *15*, 15033-15040.
8. **Guo, X.**, Sham, T.-K., Zhu, Y.-J., and Hu, Y., Interaction of Nanostructured Calcium Silicate Hydrate with Ibuprofen Drug Molecules: X-ray Absorption Near Edge Structure (XANES) Study at the Ca, Si and O K-edge. 15th International Conference on X-Ray Absorption Fine Structure (XAFS15), *J. Phys. Conf. Series* **2013**, *430*, 012064.
9. Chen, L., Razavi, F.S., Mumin, A., **Guo, X.**, Sham, T.-K., and Zhang, J., Multifunctional nanoparticles for rapid bacterial capture, detection, and decontamination. *RSC Adv.* **2013**, *3*, 2390-2397.

Conferences Presentations:

1. Tracking the Transformations of Mesoporous Microspheres of Calcium Silicate Hydrate in Nanoscale upon Ibuprofen Release: An XANES and STXM Study (poster) *Centre for Advanced Materials and Biomaterials Research (CAMBR) Conference*, London, Canada (**2015**)

2. Chemical Imaging and Spectroscopy of Individual Mesoporous Calcium Silicate Hydrate Microspheres loaded with Ibuprofen (oral) *Centre for Advanced Materials and Biomaterials Research (CAMBR) Conference*, London, Canada (2013)
3. Chemical Imaging and Spectroscopy of Individual Mesoporous Calcium Silicate Hydrate Microspheres loaded with Ibuprofen (oral) *38th International Conference on Vacuum Ultraviolet and X-ray Physics*, Hefei, Anhui, China (2013)
4. Interaction of Nanostructured Calcium Silicate Hydrate with Drug Molecules, Ibuprofen (IBU): XANES study at the Ca, Si and O K-edge (poster) *15th International Conference on X-ray Absorption Fine Structures*, Beijing, China (2012)
5. Interaction of Nanostructured Calcium Silicate Hydrate with Ibuprofen (oral, invited speaker) *Canadian Light Source 15th Annual Users' Meeting and Related Workshops*, Saskatoon, Canada (2012)